Integrating Advanced Dosimetry and Experimental Radiobiology for Mechanistic Understanding of Proton Therapy Efficacy

Groenendijk, C.F.

DOI
10.4233/uuid:a2705912-8f85-46ff-b8dc-951db4cf3bea

Publication date
2025

Document Version
Final published version

Citation (APA)
Groenendijk, C. F. (2025). *Integrating Advanced Dosimetry and Experimental Radiobiology for Mechanistic Understanding of Proton Therapy Efficacy*. [Dissertation (TU Delft), Delft University of Technology]. https://doi.org/10.4233/uuid:a2705912-8f85-46ff-b8dc-951db4cf3bea

Important note
To cite this publication, please use the final published version (if applicable).
Please check the document version above.

Integrating Advanced Dosimetry and Experimental Radiobiology for Mechanistic Understanding of Proton Therapy Efficacy

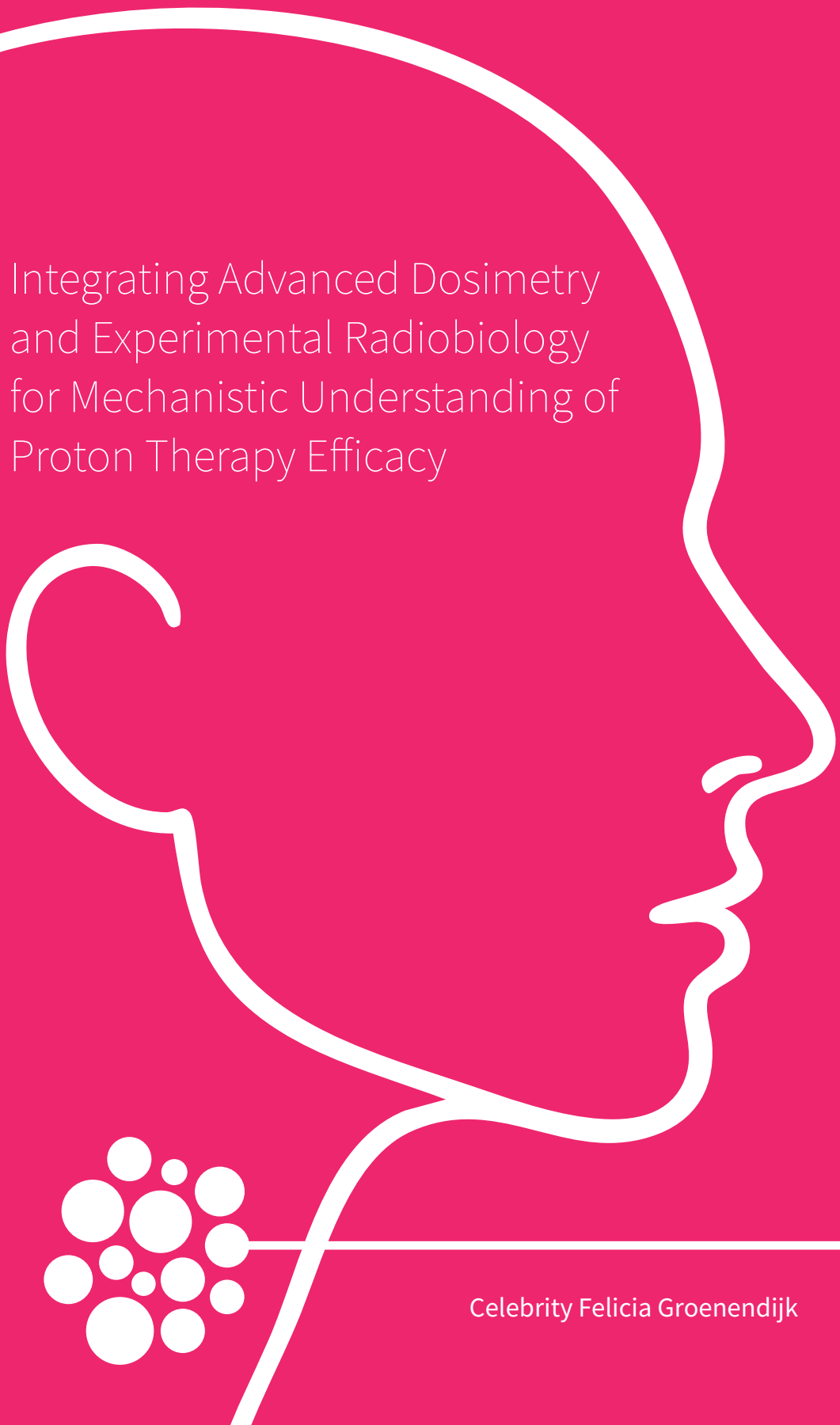

Celebrity Felicia Groenendijk

Integrating Advanced Dosimetry and Experimental Radiobiology for Mechanistic Understanding of Proton Therapy Efficacy

Integrating Advanced Dosimetry and Experimental Radiobiology for Mechanistic Understanding of Proton Therapy Efficacy

Dissertation

for the purpose of obtaining the degree of doctor
at Delft University of Technology
by the authority of the Rector Magnificus, Prof. dr. ir. T.H.J.J. van der Hagen;

Chair of the Board for Doctorates
to be defended publicly on
Tuesday 9, December 2025 at
10:00 o'clock

by

Celebrity Felicia GROENENDIJK

Master of Science in Biomedical Engineering,
Delft University of Technology, Delft, the Netherlands
born in Rotterdam, the Netherlands

This dissertation has been approved by the promotors.

Composition of the doctoral committee:

Rector Magnificus	chairperson
Dr. ir. D. Lathouwers	Delft University of Technology, promotor
Dr. J.M.C. Brown	Swinburne University of Technology, Australia, promotor
Independent members	
Prof. dr. M.S. Hoogeman	Delft University of Technology / Erasmus University Medical Center
Prof. dr. ir. A.G. Denkova	Delft University of Technology
Prof. dr. P. Dorenbos	Delft University of Technology
Dr. S. Incerti	Centre national de la recherche scientifique (CNRS), France
Dr. E. van der Kolk	Delft University of Technology, reserve member
Other member	
Dr. M.E. Capala	Erasmus University Medical Center

Keywords: Proton therapy; beamline characterization; proton dosimetry; microdosimeter; microdosimetric measurements; lineal energy; Monte Carlo simulations; GEANT4; GEANT4-DNA; experimental radiobiology; DNA damage modeling; cell survival; head and neck squamous cell carcinoma; personalized patient selection; mechanistic insights.

ISBN: 978-94-6496-509-4
Printed by: Gildeprint – Enschede

The research described in this thesis was developed in the Medical Physics and Technology section of the department of Radiation, Science and Technology of the Delft University of Technology, Delft, the Netherlands. The work described in this thesis has been financially supported by Varian, a Siemens Healthineers Company.

An electronic version of this dissertation is available at
http://repository.tudelft.nl/.

Contents

Summary

Proton therapy has gained popularity for its ability to precisely deposit energy at a specific depth, allowing for higher tumor doses while minimizing radiation exposure to surrounding healthy tissue. This advantage is particularly relevant for head and neck squamous cell carcinoma (HNSCC), the seventh most common cancer globally, where radiotherapy is challenging due to the tumor's location near critical organs. Despite advances in conventional photon-based radiotherapy, treatments still expose nearby critical organs, often resulting in severe side effects that significantly impact patients' quality of life. However, robust clinical evidence supporting the superiority of proton therapy for HNSCC remains limited, partly due to the tumor's heterogeneity and variations in treatment response driven by intrinsic biological factors and the tumor microenvironment. Furthermore, differences in energy deposition at the molecular level between protons and photons may influence DNA repair mechanisms, potentially affecting treatment efficacy in tumors with DNA repair deficiencies. Understanding these variations in biological effects is essential for improving HNSCC patient selection for proton and photon therapy and optimizing personalized radiotherapy strategies.

This dissertation aims to develop and establish a comprehensive radiobiological testing platform at the Research & Development experimental proton beamline of the Holland Proton Therapy Centre (HollandPTC) in Delft, The Netherlands. The platform serves two main objectives: (1) to improve the mechanistic understanding of biological effects induced by proton irradiation, and (2) to enable ex vivo assays using patient-derived HNSCC tissue to assess radiation responses and facilitate their implementation in clinical settings. As part of a broader HollandPTC R&D consortium project, conducted in collaboration with the Department of Molecular Genetics at Erasmus Medical Center in Rotterdam, this research contributes to advancing the efficacy of proton therapy. Ultimately, these efforts aim to support clinicians in comparing individual tumor sensitivity to proton versus photon therapy and to optimize personalized treatment strategies for HNSCC patients. The project is structured around four key milestones, which are described in Chapters 3, 4, 5, and 6.

To establish a comprehensive radiobiological testing platform and understand tissue responses to radiation, it is crucial to look into the interactions and dynamics of protons with matter across different scales. Chapter 2 provides the necessary background theory, beginning with proton interactions at the tissue level and progressing to proton dosimetry and key dosimetric quantities, such as Linear Energy Transfer (LET), which

is commonly used to assess radiobiological effects. The chapter highlights LET's limitations and emphasizes the use of lineal energy as a more suitable metric for studying proton energy deposition in small volumes, such as cells. It also covers lineal energy measurement techniques, including the use of a 3D silicon-on-insulator microdosimeter. Given the importance of computer simulations in understanding biological outcomes, the Monte Carlo radiation transport toolkit GEANT4 is introduced, explaining particle transport and its relevance in radiotherapy. Finally, the chapter explores the low-energy extension GEANT4-DNA, detailing its value in simulating early DNA damage and its contribution to advancing proton therapy research.

Chapter 3 presents the first milestone, focusing on the development and characterization of two proton irradiation platforms at the HollandPTC R&D experimental proton beamline. The proton beamline was characterized for both pencil beam and double passive scattering configurations, with key beam properties and behaviors documented to ensure accurate system performance and precise dose delivery. The double passive scattering configuration incorporates various beamline components, including scatterers and a dual-ring system, to expand the initial proton pencil beam, creating a large field with homogeneous dose distribution across its area. This configuration is especially advantageous for radiobiological experiments that require uniform irradiation of larger areas, such as cell culture flasks or well-plates, allowing for more accurate and consistent biological assessments. A key component of this milestone is the development of both a water phantom configuration and a water-equivalent polystyrene (RW3) slab phantom configuration with a flipper system. These setups are optimized at an energy of 150 megaelectronvolts (MeV) using the double passive scattering configuration and generate a large, homogeneous dose distribution across a 10×10 cm^2 field. This ensures the effective irradiation of cell culture flasks or well-plates containing cell lines or patient-derived tissue samples for radiobiological studies.

To effectively plan and optimize these radiobiological experiments, predict beam characteristics, and validate experimental results, the availability of a simulation platform is essential. Chapter 4 presents the development of a GEANT4 based simulation platform, G4HPTC-R&D, specifically designed for the HollandPTC R&D experimental proton beamline. G4HPTC-R&D accurately reproduces both pencil beam and large field characteristics, achieving an accuracy of within $\pm$5% across different proton beam energies. Most importantly, the large field reproducibility is evaluated by the field uniformity, which varies by less than 1% along both axes, and the γ-index global pass rate – a key metric to compare the accuracy of measured and calculated dose distributions by evaluating spatial and dose differences – which reaches 96.6% (3 mm, 3% criteria),

surpassing the 90% threshold required for radiobiological studies. The independent experimental benchmarking confirms that G4HPTC-R&D reliably replicates the physical behavior of the proton beamline in both pencil beam and passively scattered configurations, ensuring its suitability for clinical and radiobiological applications.

Building on the validated simulation platform G4HPTC-R&D, the next step is to perform a three-dimensional microdosimetric characterization of both proton irradiation platforms. This process, detailed in Chapter 5, follows the same approach as before – integrating experimental measurements with GEANT4 simulations – and is essential for understanding proton energy deposition patterns at the cellular level, a key factor in interpreting biological outcomes. Utilizing a 3D silicon-on-insulator microdosimeter, lineal energy spectra and the corresponding dose-mean lineal energy values ($\overline{y_D}$) are obtained. Measurements are conducted in the water phantom configuration along the 150 MeV passively scattered Bragg curve and in the RW3 slab phantom setup at various points across the $10 \times 10\,\mathrm{cm}^2$ field, as well as along the Bragg curve. The full integration of the microdosimeter geometry and proton irradiation platforms into G4HPTC-R&D enabled benchmarking against experimental measurements. Key detector limitations, such as the low detection threshold, are addressed through spectral unfolding in combination with a dead time correction model. The resulting experimentally-informed simulated lineal energy spectra and $\overline{y_D}$ values are crucial for understanding how $\overline{y_D}$ evolves along the Bragg curve across different irradiation configurations. This combined experimental and simulation approach not only validates the G4HPTC-R&D platform but also provides deeper insights into proton lineal energy distributions, laying the foundation for future correlations with biological outcomes. This final step marks the completion of a comprehensive radiobiological testing platform, facilitating more precise investigations into proton effects at the cellular level.

Chapter 6 demonstrates the application of the established comprehensive radiobiological testing platform, integrating clonogenic survival assays and DNA damage complexity analysis of the FaDu HNSCC cell line. Utilizing the water phantom configuration, FaDu cells are irradiated at three distinct positions along the Bragg curve: the plateau region, P_{36} (36% proximal to the maximum dose), P_{80} (80% proximal to the maximum dose), and D_{20} (20% distal to the maximum dose). At each position, a clonogenic survival assay is conducted to evaluate the survival fraction of FaDu cells following proton irradiation. Additionally, the formation of p53-binding protein 1 (53BP1) foci – a key marker of DNA double-strand break (DSB) repair – is assessed, providing further insight into DNA damage responses at different points along the Bragg curve. The results demonstrate a significant decrease in FaDu cell survival at D_{20} compared to P_{36} and

P_{80}, corresponding to $\overline{y_D}$ values of 1.10 keV/µm at P_{36}, 1.80 keV/µm at P_{80}, and 7.25 keV/µm at D_{20}. Furthermore, 53BP1 foci analysis reveals a higher number of 53BP1 foci immediately after irradiation, slower foci resolution, and a greater number of residual foci 24 hours post-irradiation at D_{20} relative to P_{36} and P_{80}. To further interpret these experimental findings, GEANT4-DNA simulations are employed to mechanistically model DNA damage induction, including the amount, type and complexity of DNA strand breaks. The simulations highlight a greater contribution of DSBs and an increased proportion of clustered, complex DSBs relative to the total number of strand breaks at the distal end of the Bragg curve. When these findings are linked to the higher $\overline{y_D}$, elevated 53BP1 foci post-irradiation, delayed foci resolution, and more residual foci after 24 hours at D_{20}, they suggest the presence of complex DNA damage that is more challenging for cells to repair, leading to persistent damage and reduced cellular survival. In contrast, irradiation at the plateau and P_{80}, where $\overline{y_D}$ is lower, produces nearly identical biological outcomes. This correlation between Bragg curve position, $\overline{y_D}$, and DNA damage complexity provides novel insights into the cellular and molecular effects of proton radiation, offering valuable knowledge to enhance the efficacy of proton therapy in cancer treatment.

Chapter 7 summarizes the key findings of this dissertation and presents the potential for developing a predictive framework for individual tumor responses to radiotherapy through three complementary approaches. The cellular mechanistic approach focuses on predicting radiation responses at the molecular and cellular levels. The tissue biological approach uses patient-derived tissue samples and identified biomarkers to evaluate and predict radiation response. The patient clinical approach involves real-time irradiation of tumor biopsies prior to and during treatment to guide personalized patient selection. The chapter concludes that the comprehensive radiobiological testing platform developed in this dissertation provides essential tools for predicting tumor responses, thereby supporting personalized patient selection and ultimately enhance patient outcomes.

Samenvatting

Protonentherapie heeft aan populariteit gewonnen vanwege het vermogen om energie precies af te geven op een specifieke diepte, waardoor hogere tumordoses mogelijk zijn met minimalisatie van stralingsblootstelling aan omliggend gezond weefsel. Dit voordeel is bijzonder relevant voor hoofd- en halskanker (HNSCC), de zevende meest voorkomende vorm van kanker wereldwijd, waarbij radiotherapie uitdagend is vanwege de nabijheid van kritische organen. Ondanks vooruitgangen in conventionele foton-gebaseerde radiotherapie, blijft behandeling nabijgelegen kritische organen blootstellen, wat vaak leidt tot ernstige bijwerkingen die de levenskwaliteit van patiënten aanzienlijk beïnvloeden. Er is echter nog steeds beperkt klinisch bewijs ter ondersteuning van de superioriteit van protonentherapie voor HNSCC, deels vanwege de heterogeniteit van de tumor en variaties in de behandelingsrespons die worden aangedreven door intrinsieke biologische factoren en het tumormicromilieu. Verder kunnen verschillen in energie afgifte op moleculair niveau tussen protonen en fotonen de DNA-herstelmechanismen beïnvloeden, wat mogelijk de behandelresultaten beïnvloedt bij tumoren met DNA-hersteldeficiënties. Het begrijpen van deze variaties in biologische effecten is essentieel voor het verbeteren van de patiëntselectie voor protonen- en fotonentherapie en het optimaliseren van gepersonaliseerde radiotherapiestrategieën.

Dit proefschrift heeft als doel een veelomvattend radiobiologisch testplatform te ontwikkelen en te implementeren aan de Research & Development experimentele protonenbundel van het Holland Protonen Therapie Centrum (HollandPTC) in Delft, Nederland. Dit platform heeft twee hoofddoelstellingen: (1) het verbeteren van het mechanistisch inzicht in de biologische effecten die optreden na bestraling met protonen, en (2) het mogelijk maken van ex vivo analyses met patiënt afkomstig HNSCC-weefsel om stralingsresponsen te evalueren en de implementatie ervan in klinische toepassingen te faciliteren. Als onderdeel van een breder R&D-consortiumproject van HollandPTC, uitgevoerd in samenwerking met de afdeling Moleculaire Genetica van het Erasmus Medisch Centrum in Rotterdam, levert dit onderzoek een bijdrage aan de verdere verbetering van de effectiviteit van protonentherapie. Uiteindelijk beogen deze inspanningen clinici te ondersteunen bij het vergelijken van de individuele tumorsensitiviteit voor protonen- versus fotonentherapie en het optimaliseren van gepersonaliseerde behandelstrategieën voor HNSCC-patiënten. Het project is opgebouwd rond vier kernmijlpalen, welke worden beschreven in de Hoofdstukken 3, 4, 5 en 6.

Om een veelomvattend radiobiologisch testplatform op te zetten en de weefselresponsen op straling te begrijpen, is het essentieel om de interacties en dynamiek van protonen met materie op verschillende schalen te onderzoeken. Hoofdstuk 2 biedt de noodzakelijke achtergrondtheorie, beginnend met protoneninteracties op weefselniveau en verdergaand naar protonendosimetrie en belangrijke dosimetrische grootheden, zoals lineaire energie overdracht (LET), die vaak worden gebruikt om radiobiologische effecten te beoordelen. Het hoofdstuk benadrukt de beperkingen van LET en legt de nadruk op het gebruik van lineale energie als een meer geschikte maatstaf voor het bestuderen van protonenergieafzetting in kleine volumes, zoals cellen. Het behandelt ook technieken voor het meten van lineale energie, inclusief het gebruik van een 3D silicium-op-isolator microdosimeter. Gezien het belang van computersimulaties bij het begrijpen van biologische uitkomsten, wordt de Monte Carlo toolkit voor stralingstransport GEANT4 geïntroduceerd, met uitleg over deeltjestransport en het belang ervan in de radiotherapie. Ten slotte onderzoekt het hoofdstuk de lage energie extensie GEANT4-DNA, waarbij wordt toegelicht welke meerwaarde deze biedt voor het simuleren van vroege DNA schade en hoe zij bijdraagt aan de vooruitgang van protonentherapie onderzoek.

Hoofdstuk 3 presenteert de eerste mijlpaal, gericht op de ontwikkeling en karakterisering van twee protonenbestralingplatforms bij de HollandPTC R&D experimentele protonenbundel. De protonenbundel is gekarakteriseerd voor zowel een staafbundel als dubbel passieve verspreiding configuraties, waarbij belangrijke straaleigenschappen en -gedragingen worden gedocumenteerd om nauwkeurige systeemprestaties en precieze dosislevering te waarborgen. De dubbel passieve verspreiding configuratie bevat verschillende elementen, waaronder verspreidingselementen en een dual-ring systeem, waarmee de initiële protonen staafbundel wordt vergroot, wat resulteert in een groot veld met een homogene dosisverdeling over dat gebied. Deze configuratie is bijzonder nuttig voor radiobiologische experimenten die uniforme bestraling van grotere gebieden vereisen, zoals cellen in flesjes of well-platen, wat een meer nauwkeurige en consistente biologische beoordeling mogelijk maakt. Een belangrijk onderdeel van deze mijlpaal is de ontwikkeling van zowel een water fantoom configuratie als een water-equivalente polystyreen (RW3) platen fantoom configuratie met een flippersysteem. Deze opstellingen zijn geoptimaliseerd op een energie van 150 mega-elektronvolts (MeV) met de dubbel passieve verspreiding configuratie en genereren een grote, homogene dosisverdeling over een 10×10 cm^2 veld. Dit zorgt voor de effectieve bestraling van cellen in flesjes of well-platen met celculturen of patiënt afkomstige weefselmonsters voor radiobiologische studies.

Om deze radiobiologische experimenten effectief te plannen en optimaliseren, straaleigenschappen te voorspellen en experimentele resultaten te valideren, is de beschikbaarheid van een simulatieplatform essentieel. Hoofdstuk 4 presenteert de ontwikkeling van een GEANT4 gebaseerd simulatieplatform, G4HPTC-R&D, specifiek ontworpen voor de HollandPTC R&D experimentele protonenbundel. G4HPTC-R&D reproduceert nauwkeurig zowel staafbundel- als grote veldkenmerken, met een nauwkeurigheid van binnen $\pm$5% voor verschillende protonenbundelenergieën. Het belangrijkste is dat de reproduceerbaarheid van het grote veld wordt geëvalueerd door de velduniformiteit, die langs beide assen met minder dan 1% varieert, en de γ-index globale passpercentage – een belangrijke maatstaf om de nauwkeurigheid van gemeten en berekende dosisverdelingen te vergelijken door ruimtelijke en dosisverschillen te evalueren – die een waarde van 96.6% bereikt (3 mm, 3% criteria), en daarmee de vereiste 90%-drempel voor radiobiologische studies overschrijdt. De onafhankelijke experimentele validatie bevestigt dat G4HPTC-R&D betrouwbaar het fysische gedrag van de protonenbundel in zowel staafbundel- als dubbel passieve verspreiding configuraties repliceert, en bevestigt de geschiktheid voor klinische en radiobiologische toepassingen.

Gebaseerd op het gevalideerde simulatieplatform G4HPTC-R&D, wordt de volgende stap gezet door een driedimensionale microdosimetrische karakterisering van beide protonenbestralingplatforms uit te voeren. Dit proces, gedetailleerd in Hoofdstuk 5, volgt dezelfde aanpak als eerder – het integreren van experimentele metingen met GEANT4 simulaties – en is essentieel voor het begrijpen van protonenergieafzetting patronen op cellulair niveau, een sleutelcomponent voor het interpreteren van biologische uitkomsten. Met behulp van een 3D silicium-op-isolator microdosimeter worden lineale energie spectra en de bijbehorende dosis-gemiddelde lineale energie waarden ($\overline{y_D}$) verkregen. Metingen worden uitgevoerd in de water fantoom configuratie langs de 150 MeV passief verspreidde Bragg curve en in de RW3 platen fantoom configuratie op verschillende punten over het 10×10 cm^2 veld, evenals langs de Bragg curve. De volledige integratie van de microdosimetergeometrie en protonenbestralingplatforms in G4HPTC-R&D maakt validatie tegen experimentele metingen mogelijk. Belangrijke detectorbeperkingen, zoals de lage detectiedrempel, worden aangepakt door spectrale reconstructie in combinatie met een dode tijd correctiemodel. De resulterende experimenteel-geïnformeerde gesimuleerde lineale energie spectra en $\overline{y_D}$ waarden zijn cruciaal voor het begrijpen van de evolutie van $\overline{y_D}$ langs de Bragg curve over verschillende bestralingconfiguraties. Deze gecombineerde experimentele- en simulatieaanpak valideert niet alleen het G4HPTC-R&D platform, maar biedt ook diepere inzichten in protonen lineale energieverdelingen, en legt de basis voor toekomstige correlaties met biologische uitkomsten. Deze laatste stap markeert de voltooiing van een veelomvattend radiobiologisch

testplatform, dat het mogelijk maakt om meer precieze onderzoeken naar protoneffecten op cellulair niveau uit te voeren.

Hoofdstuk 6 toont de toepassing van het ontwikkelde, veelomvattende radiobiologische testplatform, door clonogene overlevingsanalyse en DNA schadecomplexiteitsanalyse van de FaDu HNSCC cellijn te integreren. Met behulp van de water fantoom configuratie worden FaDu cellen bestraald op drie verschillende posities langs de Bragg curve: het plateau, P_{36} (36% proximaal van de maximale dosis), P_{80} (80% proximaal van de maximale dosis), en D_{20} (20% distaal van de maximale dosis). Bij elke positie wordt een clonogene overlevingsanalyse uitgevoerd om de overlevingsfracties van FaDu cellen na protonenbestraling te evalueren. Bovendien wordt de vorming van p53-bindend eiwit 1 (53BP1) foci geëvalueerd – een belangrijke indicator voor DNA dubbelstrengsbreuk (DSB) herstel – wat verder inzicht biedt in DNA schaderesponsen op verschillende punten langs de Bragg curve. De resultaten tonen een significante afname van de FaDu celoverleving bij D_{20} in vergelijking met P_{36} en P_{80}, wat overeenkomt met $\overline{y_D}$ waarden van 1.10 keV/µm bij P_{36}, 1.80 keV/µm bij P_{80}, en 7.25 keV/µm bij D_{20}. Bovendien toont 53BP1 foci analyse een hoger aantal 53BP1 foci direct na bestraling, tragere foci resolutie, en een groter aantal residuele foci 24 uur na bestraling bij D_{20} in vergelijking met P_{36} en P_{80}. Om deze experimentele bevindingen verder te interpreteren, worden GEANT4-DNA simulaties gebruikt om DNA schade inductie mechanistisch te modelleren, inclusief de hoeveelheid, het type en de complexiteit van DNA strengbreuken. De simulaties benadrukken een grotere bijdrage van DSB's en een verhoogd percentage van geclusterde, complexe DSB's in verhouding tot het totale aantal breuken aan de distale kant van de Bragg curve. Wanneer deze bevindingen worden gekoppeld aan de hogere $\overline{y_D}$, verhoogde 53BP1 foci post-bestraling, vertraagde foci resolutie en meer residuele foci na 24 uur bij D_{20}, suggereren ze de aanwezigheid van complexe DNA schade die moeilijker voor cellen te herstellen is, wat leidt tot persistente schade en verminderde celoverleving. In tegenstelling tot bestraling bij het plateau en P_{80}, waar $\overline{y_D}$ lager is, resulteert dit in vrijwel identieke biologische uitkomsten. Deze correlatie tussen Bragg curve positie, $\overline{y_D}$ en DNA schadecomplexiteit biedt nieuwe inzichten in de cellulaire en moleculaire effecten van protonenstraling, wat waardevolle kennis biedt om de effectiviteit van protonentherapie in kankerbehandeling te verbeteren.

Hoofdstuk 7 vat de belangrijkste bevindingen van dit proefschrift samen en bespreekt de mogelijkheden voor de ontwikkeling van een voorspellend kader voor de individuele tumorrespons op radiotherapie, gebaseerd op drie complementaire benaderingen. De cellulaire mechanistische benadering richt zich op het voorspellen van bestralingsresponsen op moleculair en cellulair niveau. De weefsel biologische benadering maakt

gebruik van patiënt afkomstige weefselmonsters en geïdentificeerde biomarkers om de bestralingsrespons te evalueren en te voorspellen. De patiënt klinische benadering omvat real-time bestraling van tumorbiopten voorafgaand aan en tijdens de behandeling, met als doel gepersonaliseerde behandelkeuzes te ondersteunen. Het hoofdstuk concludeert dat het in dit proefschrift ontwikkelde en geïmplementeerde radiobiologische testplatform essentiële hulpmiddelen biedt voor het voorspellen van tumorresponsen. Daarmee draagt het bij aan gepersonaliseerde patiëntselectie en beoogt het uiteindelijk de behandeluitkomsten te verbeteren.

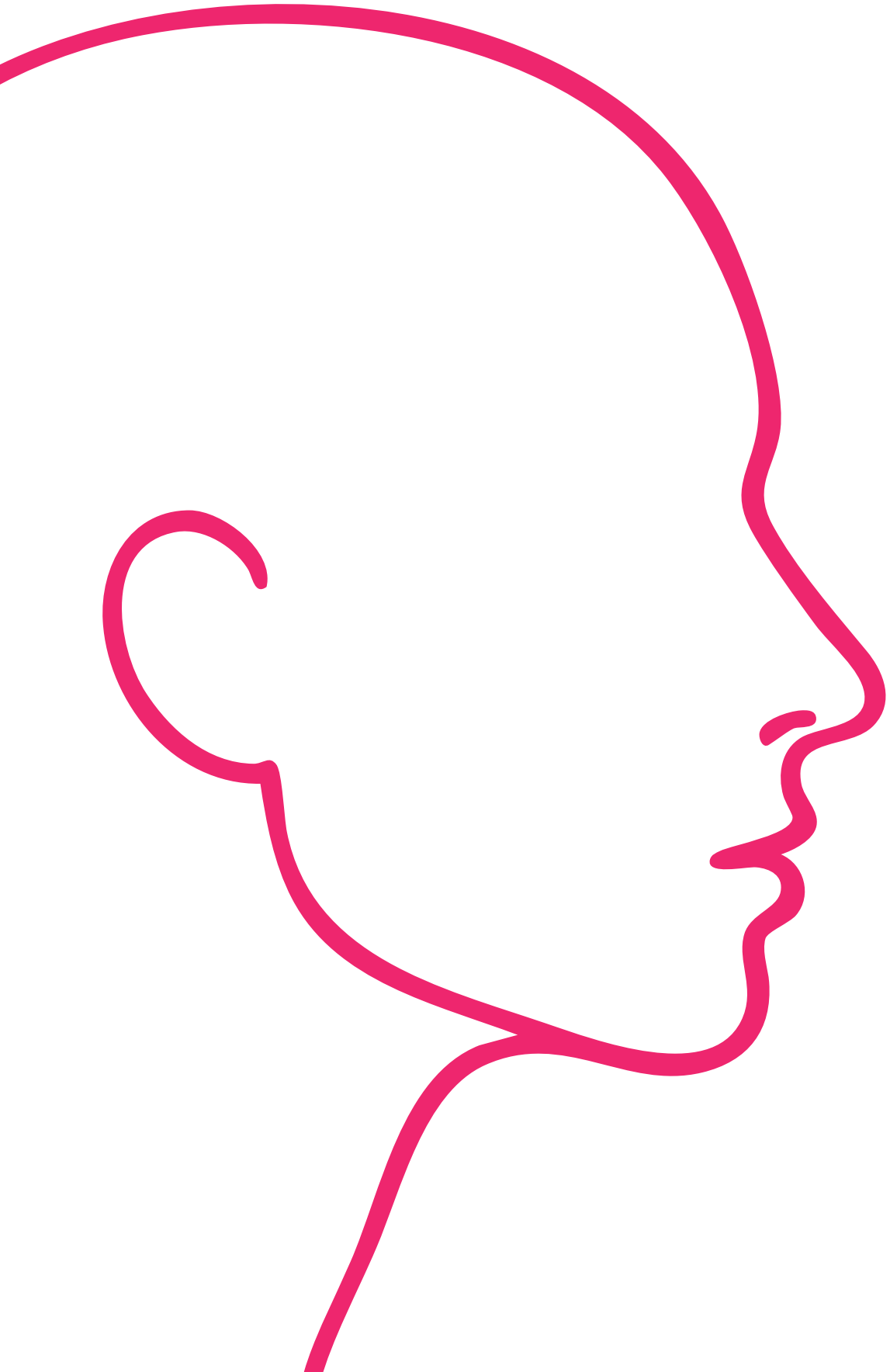

Chapter 1

Motivation of the Dissertation

1.1 Towards Improved Personalized Patient Selection in Radiotherapy

Despite significant advances in cancer research and treatment over the last decades, cancer continued to account for nearly one in six deaths globally in 2022. Amongst the most prevalent cancer types, head and neck squamous cell carcinoma (HNSCC) ranks as the seventh most common cancer worldwide [1, 2]. Early-stage HNSCC is often treated with surgery and/or radiotherapy, but for advanced inoperable cases, radiotherapy remains standard, used in 70-75% of patients [3]. Treating HNSCC patients with radiotherapy is particularly challenging due to the tumor's close proximity to critical organs at risk (OARs), such as the parotid glands, the spinal cord and the brain. While intensity-modulated radiation therapy (IMRT), the state-of-the-art radiotherapy for HNSCC, has improved tumor targeting and reduced OAR exposure, its photon dose distribution inevitably irradiates nearby critical organs, leading to acute and long-term toxicities that severely impact quality of life [4]. To this end, proton radiotherapy has gained popularity for its finite range in tissue, enabling precise energy deposition at a specific depth. This characteristic enables escalation of the dose to the tumor to improve local tumor control, while simultaneously minimizing dose to surrounding healthy tissue to reduce acute and long-term radiation-induced side effects. As a consequence, proton therapy demonstrates considerable potential to improve HNSCC patients quality of life [5, 6].

Even though clinical experience with proton therapy for HNSCC is growing, robust evidence of its efficacy remains limited [7, 8]. A major challenge lies in the significant heterogeneity of HNSCC, observed both at the cellular level in controlled in vitro studies using different cell lines and at the clinical level, where tumor heterogeneity complicates the identification of factors influencing patient outcomes and responses to radiation therapy [9, 10]. This variability in response is driven by intrinsic tumor characteristics and the complexities of the tumor microenvironment, which vary between patients [11, 12, 13]. Despite numerous studies, the understanding of predictive biomarkers remains insufficient, complicating the ability to predict responses to photon and proton therapy. Additionally, current data on the variation in linear energy transfer (LET) and relative biological effectiveness (RBE) of protons across different tissues and cell lines is still scarce [4]. Furthermore, the unique physical properties of protons and photons may result in different interactions with DNA, potentially influencing the DNA repair pathways triggered by radiation-induced damage [14]. Tumors with DNA repair deficiencies, common in many cancers, may exhibit greater sensitivity to high-LET radiation such as protons compared to low-LET radiation like photons, highlighting the importance of understanding variations in DNA damage induction [15, 16].

In the context of radiotherapy, patient selection refers to the process of determining the most suitable treatment approach for each patient. This personalized approach optimizes the choice between proton and photon therapy, ensuring that patients receive the treatment most likely to provide the greatest therapeutic benefit [17]. Elucidating the precise mechanisms driving the biologically distinct effects in individual tumors is therefore crucial for improving personalized patient selection, enabling both proton and photon therapies to be more precisely tailored to the unique biological characteristics of each tumor. To address this need, this dissertation aims to develop and establish a comprehensive radiobiological testing platform at the Research & Development experimental proton beamline of the Holland Proton Therapy Centre (HollandPTC) in Delft, The Netherlands, to support personalized patient selection. The following sections offer background information on HNSCC (Sec. 1.2), conventional photon radiotherapy (Sec. 1.3), proton radiotherapy (Sec. 1.4), and HollandPTC (Sec. 1.5). Section 1.6 reviews the state-of-the-art radiobiological approaches for proton therapy evaluation, while Section 1.7 presents the aim of this dissertation, along with its key objectives and the dissertation structure.

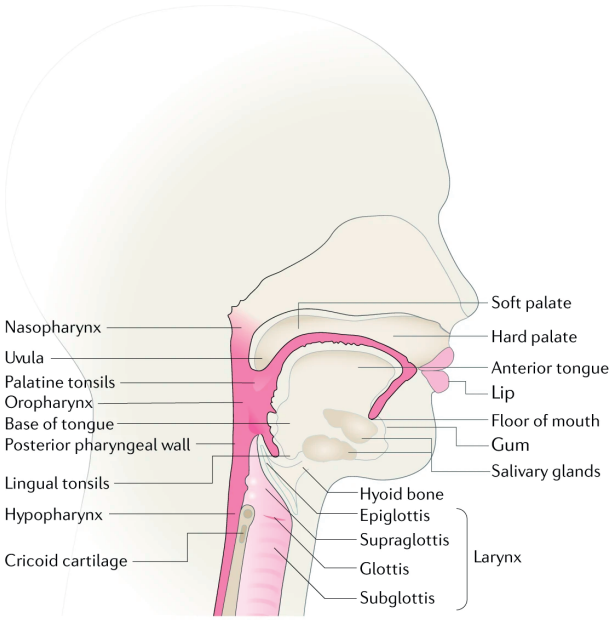

FIGURE 1.1: Head and Neck Squamous Cell Carcinoma (HNSCC) develops from the mucosal epithelium of the oral cavity, nasopharynx, oropharynx, hypopharynx, and larynx. Adjusted from [18].

1.2 Head and Neck Squamous Cell Carcinoma

HNSCC originates from the mucosal epithelium, which acts as a protective barrier for the underlying tissues of the oral cavity, nasopharynx, oropharynx, hypopharynx, and larynx (Fig. 1.1). The incidence of HNSCC is rising and is expected to increase by 30% by 2030, reaching around 1.08 million new cases each year [18]. Although the incidence of HNSCC has been on the rise, survival outcomes have shown improvement over recent decades with the HNSCC 5-year relative survival rate increasing from 52.7% in 1982-1986 to 65.9% in 2002-2006 [19]. These improvements in HNSCC survival rates may be attributed to several factors. One factor is the rise in human papillomavirus (HPV) associated tumors, which tend to respond more favorably to chemotherapy and radiotherapy compared to non-HPV-associated tumors, thereby enhancing prognosis for some head and neck cancer patients and contributing to improved survival rates [20]. In addition, HPV-related tumors are more prevalent among younger patients, potentially explaining the greater survival improvements observed in this group. Furthermore, the improved treatment options, especially the combination of concurrent chemotherapy plus radiotherapy, along with advances in screening and staging, has also likely contributed to improved survival outcomes in head and neck cancer patients [19]. Despite the improved survival outcomes, head and neck cancers generally remain challenging to cure due to the complex anatomy and critical structures in the head and neck area.

1.3 Photon Radiotherapy

The most widely used form of external beam radiation therapy utilizes megavoltage photon beams generated by linear accelerators (LINACs), which are standard equipment in most hospitals. From an electron source, electrons are accelerated and directed to strike a target, typically made from tungsten. These collisions generate high-energy photons, which are then guided through a beam delivery system. The beam delivery system is mounted on a rotating gantry which allows the patient to be irradiated from various angles [21]. Photons, as uncharged massless particles, consist of a dose – the average energy imparted per unit mass (Sec. 2.2.1) – distribution characterized by a moderate dose at the surface, followed by an initial peak at a shallow depth below the skin after a brief dose build-up phase. After reaching this peak, the dose gradually declines with increasing tissue depth due to attenuation of the photon beam, as illustrated in Figure 1.2. This process describes the gradual reduction of the number of photons available to deposit energy as a result of Compton scattering and photoelectric absorption. Compton scattering involves the interaction of a photon with a free or weakly bound electron, resulting in a change of the photon's direction with a reduced energy

and the creation of a recoil electron. In contrast, photoelectric absorption occurs when a photon is absorbed by an atom, transferring its full energy to a bound electron, which is subsequently ejected from one of the atom's electron shells as a photoelectron [22].

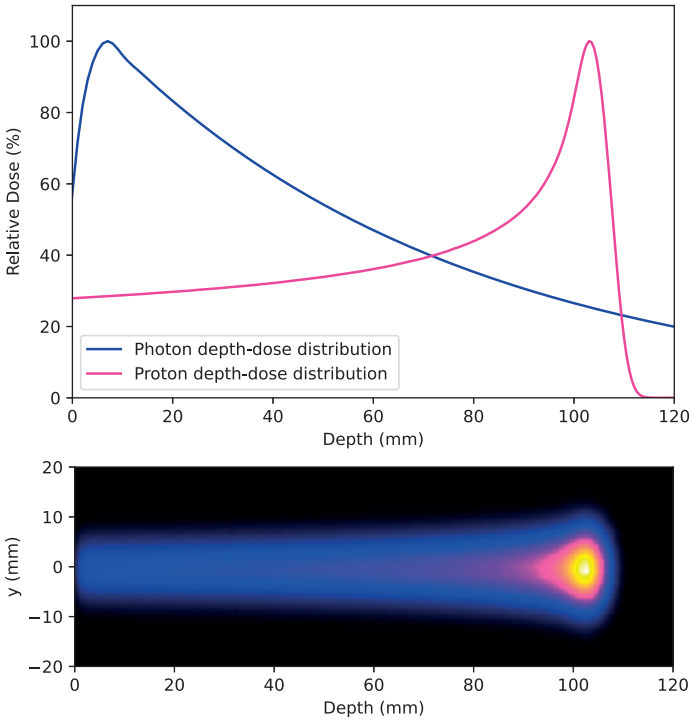

FIGURE 1.2: Top figure: relative depth-dose distributions (%) in water (mm) for a mono-energetic photon beam (blue) and mono-energetic proton beam (pink) with the direction of the beam from left to right. The photon depth-dose distribution displays a peak dose near the entrance, followed by an exponential decrease in energy deposition with depth due to attenuation of the beam. The proton depth-dose distribution shows an increase in dose with depth, leading to a Bragg peak right before protons reach the end of their range. Bottom figure: the proton depth-dose profile in the yz-plane, illustrating the lateral broadening of the proton beam due to multiple Coulomb scattering. The white dot represents the maximum of the dose.

1.3.1 Intensity-Modulated Radiation Therapy

Over many years, significant advances in radiotherapy planning and delivery have been made which has driven the development of advanced three-dimensional conformal radiation therapy (3D-CRT) [23]. The aim of 3D-CRT is to shape the prescribed dose to match the three-dimensional target volume, which includes both the cancerous cells

and an added margin for spatial uncertainties, while simultaneously minimizing exposure to surrounding healthy tissues. The current state-of-the-art in 3D-CRT is intensity-modulated radiation therapy (IMRT), which uses multiple optimized, non-uniform photon beam intensities to achieve a uniform dose distribution at the tumor site. By tailoring the beam intensity to the specific shape and size of the tumor, clinicians can maximize treatment effectiveness while minimizing side effects. An example of an IMRT treatment plan is shown in Figure 1.3. Although IMRT provides a relatively high degree of target conformity and spares surrounding healthy tissues, the continuous dose distribution of photons throughout the body (Fig. 1.2) inevitably results in the irradiation of several critical healthy organs located near the tumor in the head and neck region. Over time, this exposure can lead to serious side effects for HNSCC patients including difficulties in swallowing, a dry mouth, and changes in taste, significantly diminishing the quality of life post-treatment [24]. Additionally, this unwanted dose distribution restricts the maximum dose that can be safely delivered to the tumor due to the need to protect surrounding healthy tissues, ultimately resulting in decreased tumor control [25, 26]. For these reasons, there has been increasing interest in exploring tissue sparing radiation treatment methods such as proton therapy to mitigate treatment related complications and improve patient outcomes.

1.4 Proton Radiotherapy

Proton therapy, first proposed by Wilson in 1946 [27], is an advanced form of radiation therapy that utilizes protons to deliver a highly localized dose to the tumor, simultaneously sparing surrounding healthy tissue, due to the unique physical properties of protons. As positively charged subatomic particles with relatively large mass, protons undergo frequent interactions as they travel through tissue resulting in the characteristic proton depth-dose distribution shown in Figure 1.2. Upon entering the body, protons deliver a relatively low entrance dose in the plateau region. In this region, protons mainly lose energy through electromagnetic interactions which gradually decelerate them. As the protons slow down, protons deposit the majority of their energy near the end of their range, creating a distinct ”Bragg peak” (Fig. 1.2), leading to a sharp increase in energy deposition at the end of the proton’s path [21, 28]. This sharp energy delivery potentially allows for targeted tumor irradiation while sparing OARs, and improved control of the maximum dose to the tumor. To deliver this precise dose distribution, two primary beam delivery techniques have been developed: pencil beam scanning and passive scattering.

1.4.1 Pencil Beam Scanning

A pencil beam refers to a highly focused, narrow beam of protons, typically a few millimeters in diameter, used to precisely target a tumor. To fully irradiate a tumor, the proton beam is moved in a controlled, point-by-point manner across the tumor, dividing the treatment area into small spots, each of which is precisely irradiated by the narrow beam. By adjusting the beam's energy and position, the protons are directed to varying depths with varying intensities, allowing coverage of the entire tumor volume. This technique, also known as intensity-modulated proton therapy (IMPT), pencil beam scanning (PBS) or active scanning, effectively "paints" the tumor layer by layer, achieving a homogeneous dose distribution [21, 28]. IMPT, unlike conventional photon-based IMRT, achieves superior dose localization due to the unique finite range of protons. This property minimizes the deposition of unnecessary dose to surrounding healthy tissues, as demonstrated in the example IMPT treatment plan depicted in Figure 1.3. The figure also highlights the dose distribution differences between IMRT and IMPT, emphasizing how protons enable higher, more precise doses to the tumor while sparing adjacent normal tissues [6, 29, 30, 31].

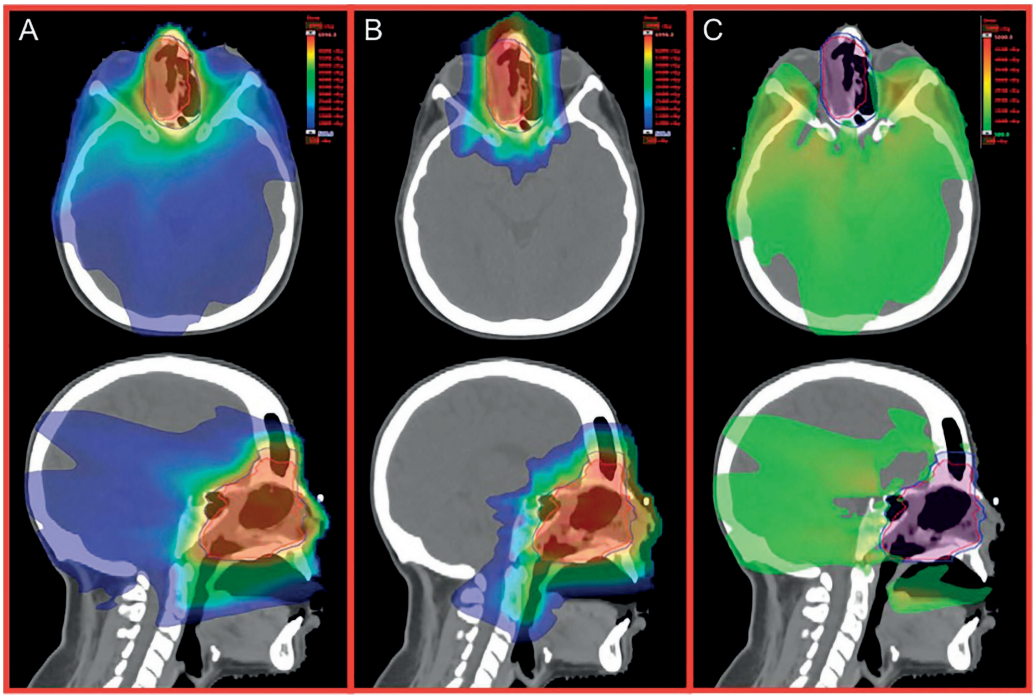

FIGURE 1.3: Treatment plans for a HNSCC patient showing representative axial and sagittal images for (A) IMRT treatment plan, (B) IMPT treatment plan, and (C) the difference between an IMRT and IMPT treatment plan, taken from Moreno et al. [29].

1.4.2 Passive Scattering

Passively scattered proton therapy (PSPT) utilizes a single proton pencil beam which is then modified to deliver a dose distribution that conforms to the shape and depth of the tumor. The modulation of the beam occurs both laterally, to uniformly cover the tumor area, and along the beam's depth. This is achieved using devices such as scattering foils, range modulators, and collimators. Lateral broadening of the beam is typically accomplished through a double scattering system, where the proton beam is passed through two scattering materials of varying thicknesses and compositions. These materials of high and low atomic numbers ensure that the beam spreads uniformly across the target area. The depth modulation is achieved using range modulators of varying thicknesses, creating multiple Bragg peaks at different depths. The combination of these peaks results in a Spread-Out Bragg Peak (SOBP), providing a uniform dose to the tumor volume at different depths. To further refine the beam and ensure it conforms to the tumor's shape before entering the patient, collimators or custom designed field-specific apertures are employed. While PSPT offers certain clinical advantages, IMPT is considered as the state-of-the-art method due to its flexibility in delivering a dose that conforms tightly to complex tumor shapes. This makes it particularly effective for treating HNSCC, where sparing OARs is critical [24].

1.5 Holland Proton Therapy Centre

The Holland Proton Therapy Centre (HollandPTC) is one of three proton radiotherapy centers in the Netherlands (Fig. 1.4). Located in Delft, HollandPTC is a collaborative initiative involving three institutions: the Erasmus University Medical Center Rotterdam (Erasmus MC), the Leiden University Medical Center (LUMC), and the Delft University of Technology (TU Delft). Together, these institutions have established the HollandPTC R&D consortium research program focused on investigating and enhancing the superior efficacy of proton therapy over conventional photon therapy through cross-disciplinary research. The program further aims to test new treatment strategies and improve proton therapy by developing and implementing innovative technologies and methodologies, and perform physics and biological experiments. In addition, the consortium's goal is to evaluate combinations of proton therapy with other treatment methods including immunotherapy, hyperthermia, and targeted drugs, to optimize its clinical effectiveness and efficiency. The last critical aspect is to assess the cost-effectiveness of proton therapy. Given the higher costs associated with building and maintaining proton therapy facilities, research at HollandPTC seeks to determine whether the benefits of proton therapy

justify these higher costs, especially when considering long-term outcomes and quality of life [32].

FIGURE 1.4: The Holland Proton Therapy Centre, Delft, The Netherlands.

1.5.1 ProBeam Isochronous Cyclotron

HollandPTC is a ProBeam (Varian, A Siemens Healthineers Company [33]) isochronous cyclotron-based facility. A cyclotron is a particle accelerator designed to produce charged particle beams for various applications. At HollandPTC, the ProBeam isochronous cyclotron features a central source where hydrogen gas is ionized to produce protons. These protons are extracted and directed into a circular trajectory by a chamber equipped with multiple electromagnets. A radio frequency system applies a high-frequency alternating voltage to accelerate the protons, causing them to spiral outward as they gain energy until they reach the outer edge of the chamber. An extraction system then directs these accelerated protons into a beam transport system that guides them to the appropriate room. Figure 1.5 presents a top-view layout of the HollandPTC facility, which includes two patient treatment rooms featuring pencil beam scanning through large rotating gantries for multi-angle proton beam delivery. A third room serves as a treatment

room dedicated to eye treatments, while an additional fixed horizontal beamline serves the Research & Development (R&D) room, dedicated to advanced research activities.

1.5.2 HNSCC Patient Selection

Proton therapy at HollandPTC is primarily used to treat cancers where precision is critical. HollandPTC has treated cancer patients that qualify for proton radiotherapy since 2018 [34]. For HNSCC, the process of patient selection for proton therapy follows the Dutch National Indication Protocol Proton therapy for Head and Neck Cancer patients (NIPP-HNC) to determine which head and neck cancer patients are most likely to benefit from proton therapy by minimizing late radiation-induced side effects compared to photon therapy [35]. The NIPP-HNC uses a model-based approach which involves calculating the Normal Tissue Complication Probability (NTCP) for both photon and proton therapy plans. NTCP models incorporate dose-volume variables alongside other independent predictors to enhance the accuracy of complication risk predictions. Patients are selected for proton therapy if the predicted reduction in NTCP exceeds specific thresholds, indicating a significant benefit in minimizing potential side effects.

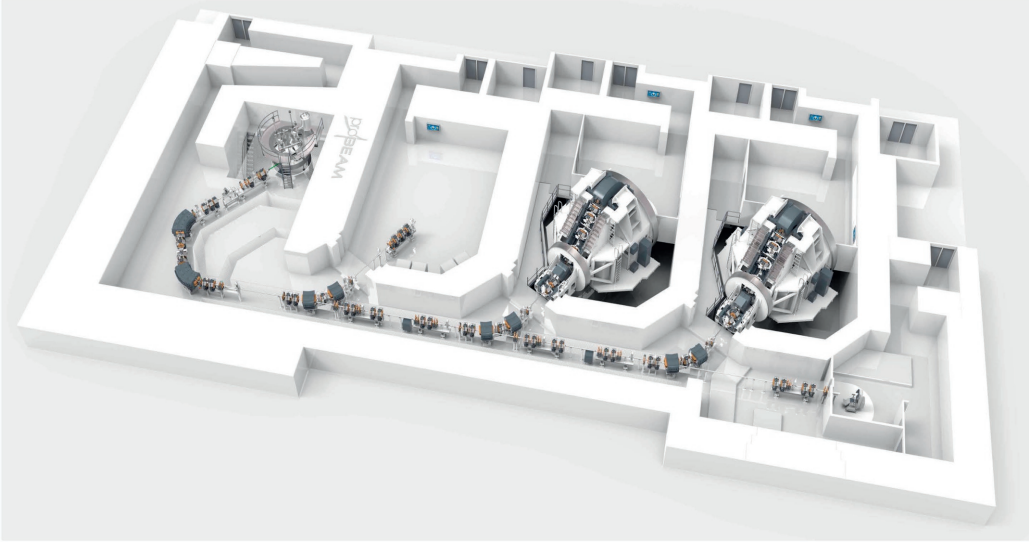

FIGURE 1.5: HollandPTC's architecture with from left to right the ProBeam (Varian, a Siemens Healthineers Company) isochronous cyclotron, the R&D experimental room, gantry I, gantry II, and the eye treatment room.

1.5.3 Research & Development

The investigation into proton versus photon therapy primarily focuses on Randomized Clinical Trials (RCTs), retrospective studies, and long-term follow-ups that examine various aspects of treatment outcomes. In addition to serving as a treatment facility, HollandPTC functions as a research and development hub, collaborating closely with its three founding institutions to advance proton therapy research. The R&D room, also known as the experimental bunker, is equipped with a fixed horizontal beamline that allows all sorts of physics and biology studies, including the refinement of proton's therapy physical processes, such as the measurement and optimization of radiation doses. Furthermore, numerous radiobiological studies can be conducted to explore the biological effects of proton radiation, examining differences in the response of cancer cells versus normal cells, as well as comparisons with photon therapy carried out at Erasmus MC and LUMC. Additionally, other research activities such as radioprotection studies for space applications can also be conducted.

1.6 State-of-the-Art Radiobiological Approaches for Proton Therapy Evaluation

The presence of a dedicated experimental proton beamline within a clinical proton therapy center provides a significant advantage by enabling direct collaboration between clinicians and researches. This unique capability not only facilitates state-of-the-art radiobiological approaches for evaluating proton therapy but also enables personalization of treatment strategies by combining biological data from ex vivo assays with patient-specific clinical information.

In Europe, 28 proton therapy facilities are currently in operation. Among these, several include dedicated experimental proton beamlines, such as the Heavy Ion Therapy Centre (Heidelberg, Germany) [36], the University Proton Therapy Dresden (Dresden, Germany) [37, 38], the MedAustron Ion Therapy Facility (Wiener Neustadt, Austria) [39], the Danish Centre for Particle Therapy (Aarhus, Denmark) [40], the Christie Proton Therapy Center (Manchester, United Kingdom) [41], the Trento Proton Therapy Center (Trento, Italy) [42, 43], and the Paul Scherrer Institute (Villigen, Switzerland) [44]. Among these, only the facilities in Dresden [37, 38] and Trento [42, 43] consists of a passively scattered configuration [45]. Additionally, many other facilities have non-clinical experimental rooms that support radiobiological research. The passive scattering configuration is particularly valuable for radiobiological experiments, as it generates large

irradiation fields with homogeneous dose distributions, making it well-suited for the irradiation of tissue samples and cell lines. However, despite these research capabilities, no facility currently provides a radiobiological platform that integrates high-resolution advanced dosimetry methods within a fully characterized clinical-level system while also enabling ex vivo assays with patient-derived tumor biopsies for clinical integration [46].

In radiotherapy, LET is used to quantify radiation quality, representing the amount of energy deposited by radiation per unit length of tissue traversed. Along the proton Bragg curve, LET varies significantly, increasing sharply near the Bragg peak. This rise in LET has critical implications for patients undergoing proton therapy, as regions of high LET are associated with enhanced biological damage [47]. Therefore, thorough characterization along the entire depth-dose profile is essential for understanding biological response. Most proton therapy facilities primarily rely on Monte Carlo simulations to determine dose-averaged LET (LET_d) [48, 49, 50, 51, 52]. However, research of Guan et al. demonstrated that lineal energy (y) distributions better explain variations in RBE compared to LET_d [53]. They revealed that identical LET_d values from different proton energy spectra resulted in distinct survival rates in lung cancer cells, highlighting the limitations of LET_d alone. Microdosimetry, which captures the stochastic nature of energy deposition at microscopic scales – such as within individual cells – provides crucial insights into how these variations influence biological effects. Microdosimetric measurements are therefore crucial in correlating physical dose distributions with biological responses and have been integrated into various clinical proton beamlines, including both spot-scanning proton beams [54, 55, 56] and passive scattering proton beams [56, 57, 58, 59, 60]. A range of detectors were employed for these measurements, including the gold standard Tissue Equivalent Proportional Counters (TEPCs), solid-state microdosimeters, crystal diamond-based detectors, and mini-TEPCs [57, 61, 62, 63]. While these experimental studies have primarily focused on one-dimensional measurements along the proton Bragg curve, irradiating biological samples using a passive scattering setup over large fields necessitates three-dimensional microdosimetric mapping, representing a critical gap in the field.

Despite significant advancements in radiobiological setups and microdosimetric characterizations, a fully biologically-driven mechanistic model that accurately links radiation-induced DNA damage to cellular outcomes has not yet been established [64]. Achieving this requires the use of Monte Carlo toolkits capable of track-structure simulations to model early DNA damage and provide detailed insights into DNA strand breaks and

their complexity. Several Monte Carlo codes have been developed for this purpose, including PARTRAC [65], KURBUC [66], RITRACKS [67], NOREC [68], TOPAS-nBIO [69], and GEANT4-DNA [70, 71, 72, 73, 74]. Recent advancements in GEANT4-DNA have notably enhanced its capability to simulate DNA damage at nanoscopic scales, offering a powerful framework for end-to-end modeling of radiation-induced DNA damage. This includes the integration of realistic cell geometries, with a nucleus encapsulated by a cytoplasm-like water environment, enabling the precise simulation of energy depositions. The simulation parameters have been accurately refined to capture both direct and indirect DNA damage, achieving validation within a 13.3% error margin for proton-induced double-strand breaks (DSBs) [75].

A key innovation within GEANT4-DNA is the development of the "molecularDNA" application, which has been employed to investigate DNA damage yields induced by ionizing radiation in various biological systems, including human fibroblast cells, bacterial cells, and other human cell types [76, 77, 78, 79, 80]. However, a comprehensive platform that integrates mechanistic insights at the subcellular level with biological outcomes at the macroscopic tissue level has yet to be developed.

1.7 Aim of the Dissertation and Structure

This dissertation aims to develop and establish a comprehensive radiobiological testing platform that serves two primary objectives: (1) to enhance the mechanistic understanding of biological outcomes following proton irradiation, and (2) to enable ex vivo assays for evaluating HNSCC patient-derived tissue responses to proton irradiation and support their integration into clinical practice. These approaches will help clinicians assess the relative sensitivity of individual tumors to proton versus photon therapy, ultimately improving personalized patient selection. To achieve these objectives, four key milestones have been defined. This project is part of the broader HollandPTC initiative aimed at advancing the efficacy of proton therapy. It was launched alongside several Varian-funded research projects to strengthen collaboration between HollandPTC, Erasmus MC, LUMC, and TU Delft. This dissertation presents one such project within the HollandPTC R&D consortium research program, conducted with the Department of Molecular Genetics at Erasmus MC in Rotterdam.

Milestones

1. The characterization of the HollandPTC R&D experimental proton beamline and the development of two proton irradiation platforms utilizing a double passive

scattering configuration. Characterizing the beamline is essential not only to ensure the system operates as intended, delivers precise doses and maintains reproducibility, but also to gain insights into its fundamental properties and behaviors. This characterization involves a comprehensive set of measurements to understand, document, and optimize the proton's trajectory through air, a process crucial for ensuring the accuracy, reliability, and outcomes of experiments involving cells and tissues.

2. Development of a simulation platform of the HollandPTC R&D experimental proton beamline using the Monte Carlo radiation transport modeling toolkit GEANT4. The availability of a simulation platform is highly valuable in the planning and optimization of radiobiological experiments, the prediction of beam characteristics which are challenging to measure experimentally, and the validation of experimental results to ensure accuracy.

3. Three-dimensional microdosimetric characterization of the two proton irradiation platforms at the HollandPTC R&D experimental proton beamline. This characterization is conducted through a combined approach including experimental measurements of proton energy deposition using the 3D silicon-on-insulator Mushroom microdosimeter, alongside GEANT4 simulations for validation. This milestone is essential for understanding proton energy deposition and lineal energy spectra at the cellular level along the proton Bragg curve across both platforms, and provides an essential basis for analyzing biological effects.

4. Employment of the radiobiological testing platform for a HNSCC cell line and linking mechanistic insights to biological outcomes. The study of in vitro clonogenic survival and DNA damage foci kinetics of a HNSCC cell line is performed along various positions along the proton Bragg curve. Additionally, with the use of GEANT4-DNA a mechanistic understanding of DNA damage induction, its yield and complexity is obtained and its impact on HNSCC cell survival and foci kinetics is linked to lineal energy and dose.

Dissertation Structure

To support the understanding of this dissertation, Chapter 2 provides essential background information on the macro-to-nano dynamics in proton radiobiology, offering insights into their influence on biological outcomes. It covers proton interactions with matter across different scales to elucidate their physical characteristics, along with an

overview of proton dosimetry and the important role of microdosimetry in understanding proton energy deposition at the cellular-level. The chapter also outlines various detectors used in microdosimetry, with a particular focus on the solid-state microdosimeter employed in this dissertation. Additionally, it addresses the importance of computational simulations in radiotherapy, specifically the application of the radiation transport Monte Carlo toolkit GEANT4 and its low-energy extension, GEANT4-DNA, in enhancing the mechanistic understanding of biological responses to proton irradiation.

The development and establishment of a comprehensive radiobiological testing platform are structured around four key milestones, detailed in Chapters 3, 4, 5, and 6. The first milestone, presented in Chapter 3, involves the characterization of the HollandPTC R&D experimental proton beamline and the development of two proton irradiation platforms. The second milestone, introduced in Chapter 4, focuses on the development of a GEANT4 based simulation platform for modeling the HollandPTC R&D experimental proton beamline. Chapter 5 details the third milestone, which consists of a three-dimensional microdosimetric characterization of the proton irradiation platforms. Finally, the fourth milestone, described in Chapter 6, demonstrates the platform's implementation through proof-of-viability experiments using the FaDu HNSCC cell line, establishing correlations between mechanistic estimates of DNA damage and biological outcomes.

Chapter 7 concludes this dissertation by summarizing its key findings and emphasizing the significance of the developed radiobiological testing platform. It also explores future research directions, including the potential to establish a predictive framework for tumor responses and its integration into clinical workflows. These advancements lay the foundation for more precise, personalized patient selection in radiotherapy.

Chapter 2

Unraveling Proton Macro-to-Nano Dynamics for Biological Insights

Understanding the proton macro-to-nano dynamics to elucidate their biological effects refers to examining how protons interact with matter at different scales, from the macroscopic scale (tissue level) down to the nanoscopic scale (cellular and molecular levels). This involves understanding the physical characteristics of proton interactions with matter (Sec. 2.1), including how protons deposit their energy in terms of dose (Sec. 2.2). At the microscopic scale, the emphasis lies on how energy deposition patterns translate to lineal energy, referred to as microdosimetry (Sec. 2.3). The use of a 3D silicon-on-insulator Mushroom microdosimeter allows for the measurement of cellular-level energy deposition and is detailed in Section 2.4. The crucial role of Monte Carlo simulations is described in Section 2.5, making use of the Monte Carlo transport modeling toolkit GEANT4 (Sec. 2.6). Upon understanding of cellular-level energy deposition patterns, the emphasis shifts to understanding the interaction with DNA, specifically DNA damage induction mechanisms and DNA damage complexity, where the use of GEANT4-DNA (Sec. 2.7) plays an essential role in mechanistically enhancing the interpretation of biological experiments.

2.1 Proton Interactions in Matter

When protons traverse biological tissue, their interactions with the medium can be classified into two primary physical processes: electromagnetic interactions and nuclear interactions.

2.1.1 Electromagnetic Interactions

Protons lose the majority of their energy through electromagnetic interactions with atomic electrons due to the Coulomb forces exerted by the atom's electric field. These continuous inelastic Coulombic interactions lead to ionizations, in which an electron is completely removed from an atom (Fig. 2.1), and excitations, which is the transfer of an electron to a higher energy shell within the atom. Together with the production of secondary particles, all energy is eventually lost and protons stop [22, 28]. The stopping depth of protons, the proton's range, depends on both their initial energy and the material they traverse. A critical factor determining the proton's gradual deceleration and eventual halt is the stopping power S, defined as $S \equiv -dE/dx$ (MeV/cm), which describes the increasing rate of energy loss per unit path length [81]. The energy loss rate is primarily governed by inelastic collisions with target electrons (electronic stopping), which is described by the Bethe-Bloch formula. Corrected for density, the mass stopping power of protons is described by

$$\frac{S}{\rho} \equiv -\frac{1}{\rho}\frac{dE}{dx} = 0.3072\frac{Z}{A}\frac{1}{\beta^2}\left(\ln\frac{W_m}{I} - \beta^2\right) \quad \frac{\text{MeV}}{\text{g/cm}^2} \tag{2.1}$$

with atomic number Z, relative atomic mass A, density ρ of the stopping material, $\beta \equiv v/c$ is the proton's velocity, $W_m = \frac{2m_e c^2\beta^2}{1-\beta^2}$ with $2m_e c^2 \approx 0.511$ MeV being the electron rest energy, and I the mean ionization energy of the target material [28, 81].

Multiple Coulomb Scattering

In addition to protons eventually stopping, its generally linear trajectory is altered when collisions occur with atomic nuclei due to the Coulombic force, a phenomenon known as scattering (Fig. 2.1). This scattering process is typically characterized by numerous random, small-angle deviations, referred to as Multiple Coulomb Scattering (MCS) and results in lateral broadening of the beam, shown in Figure 1.2. The spatial distribution of MCS approaches a Gaussian distribution. This is explained by the Central Limit Theorem which states that when an adequate number of random samples is taken, the distribution of the sample will be approximately Gaussian distributed [22]. The angle under which the deflections take place is only a few degrees dependent on the material that is being traversed. The proton angular deviation θ_0 is described by Highland's formula as

$$\theta_0 = \frac{14.1\text{MeV}}{pv}\sqrt{\frac{L}{L_R}}\left[1 + \frac{1}{9}\log\left(\frac{L}{L_R}\right)\right] \text{ rad} \tag{2.2}$$

with p as the proton's momentum, v as the proton's velocity, L is the thickness of the material, and L_R is the accompanying radiation length. Materials with a high atomic number have increased electron density and thus an increased probability of interaction, resulting in a larger angular deviation [28].

Proton's Mean Range

The penetration depth of protons in a given material is described by the mean projected range, R, and is the average straight line distance a proton travels until stopping. R can be derived by integrating the mass stopping power over the path and is defined as the depth at which half of the protons have stopped [28]. Within the context of the Bragg peak, this corresponds to the distal 80% point (D_{80}) of the Bragg peak. Proton's range R is given by

$$R(E_0) = \int_{E_0}^{E_f}\left(\frac{dE}{dx}\right)^{-1} dE \tag{2.3}$$

where $\frac{dE}{dx}$ is described by equation 2.1, E_0 is the initial kinetic energy of the proton when entering the material and E_f the final energy, approaching zero. The range is, however, not the same for every proton due to the stochastic nature of proton interactions within the medium. As a result, statistical fluctuations lead to deviations in the range for individual protons due to scattering, called energy range straggling. Consequently, this process contributes to an increased width of the Bragg peak [82].

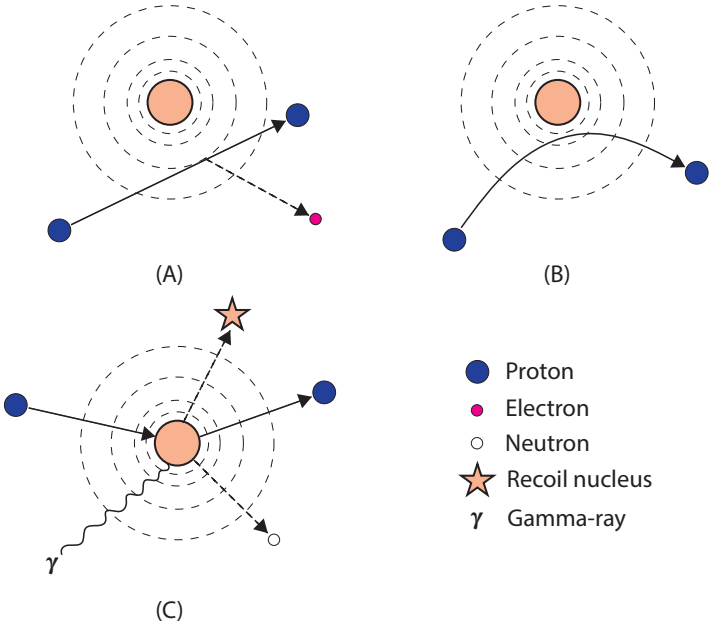

FIGURE 2.1: A graphical representation of three types of proton interactions with atoms, showing three atoms (orange nuclei) surrounded by their electron shells: (A) ionization caused by Coulomb interactions with the atom's electrons, (B) deflection of the proton's trajectory due to Coulomb scattering, and (C) a nuclear reaction where the primary proton is removed, accompanied by the emission of a secondary particle (γ-ray), and the formation of a recoil nucleus. Mimicked from [83].

2.1.2 Nuclear Interactions

Besides the electromagnetic interactions, protons can undergo less occasional nuclear interactions, where a proton collides with an atomic nucleus and imparts significant momentum to the nucleus. This phenomenon can result in the formation of a recoil nucleus when part of the kinetic energy of the primary proton is transferred to the target nucleus (Fig. 2.1). Furthermore, a nuclear interaction can cause nuclear fragmentation in which, when the energy transfer is high enough, the interaction results into the break-up of the nucleus in smaller fragments [22]. The most relevant aspect of these reactions is that these nuclear reactions initiate the production of secondary particles being either

protons, neutrons, γ-rays or heavy fragments. Nuclear interactions become increasingly significant as protons travel deeper into tissue, leading to a gradual reduction in the number of primary protons as they travel from the entrance toward the end of their range. Near the end of their range, there is a sharp drop in fluence – the number of protons per area – due to the protons losing energy and being absorbed by the medium. In this region of the Bragg peak, nuclear interactions contribute to the formation of a low-dose tail (Fig. 1.2), caused by secondary particles produced in nuclear reactions [28, 83].

2.2 Proton Dosimetry

As a result of proton interactions with matter, energy is transferred and deposited into the tissue. This process is quantified as the physical absorbed dose D. Proton dosimetry refers to the measurement, calculation, and analysis of the absorbed dose delivered by protons to tissues during proton therapy. The following sections provide a detailed explanation of the concepts of energy deposited, energy imparted and absorbed dose, as defined by the ICRU [84].

2.2.1 Energy Deposited, Energy Imparted and Absorbed Dose

Energy Deposited

The energy deposited ε_i is related to a single event i where ε_i represents a stochastic quantity and is described by

$$\varepsilon_i = \varepsilon_{in} - \varepsilon_{out} + Q \tag{2.4}$$

where ε_{in} is the kinetic energy of the incoming proton, ε_{out} is the total kinetic energy of all particles leaving the event, and Q represents the alterations in the rest mass energy of the atoms and all particles participating in that event. It is thus the energy transferred locally at specific points along the particle's track through ionization or excitation. Additionally, energy leaving the region by secondary radiation, known as delta rays, is not included in the deposited energy within that region.

Energy Imparted

In contrast to energy deposited, the energy imparted ε to matter refers to a broader concept in that it is volume-based and describes the sum of all energy depositions ε_i in a defined volume. ε is a stochastic quantity and is described by

$$\varepsilon = \sum_i \varepsilon_i \tag{2.5}$$

including all energy depositions through ionization, excitation, or other interactions, and subtracts energy carried away by secondary radiation that escape the defined volume.

Absorbed Dose

Absorbed dose D is defined as the average energy imparted per unit mass of the irradiated medium and is measured in the unit of Gray (Gy), where 1 Gy equals 1 Joule of energy imparted per kilogram of mass. D is a non-stochastic quantity and is expressed as

$$D = \frac{d\bar{\varepsilon}}{dm} \tag{2.6}$$

where $d\bar{\varepsilon}$ presents the average energy imparted in mass dm. The amount of energy absorbed by a material depends on its properties and the type of radiation it is exposed to. Different materials absorb energy differently, even when exposed to the same type of radiation. In proton therapy, the absorbed dose is used to evaluate the radiation delivered to both the tumor and the surrounding tissues, commonly referred to as dose.

2.2.2 Linear Energy Transfer

While absorbed dose quantifies the average energy imparted per unit mass, it lacks information about the microscopic distribution of that energy along the particle's track, which is important for understanding specific biological effects. To describe this amount of energy lost along the track, the term Linear Energy Transfer (LET) was introduced, defined as the average energy dE transferred through ionization and excitation over a distance dx of a particle's track, expressed as dE/dx (keV/µm) and is illustrated in Figure 2.3 [85, 86]. A lower LET is associated with a lower ionization density, typically resulting in fewer interactions per micrometer. This is referred to as low-LET radiation, which accounts for photons, shown in Figure 2.2. In contrast, high-LET radiation, such as protons, produces denser ionization events along the particle's track. This results in more complex track structures, which are characteristic of high-LET radiation (Fig. 2.2). Such radiation types are generally more effective in inducing biological damage due to their higher ionization density, making them particularly important in therapies like proton therapy [87].

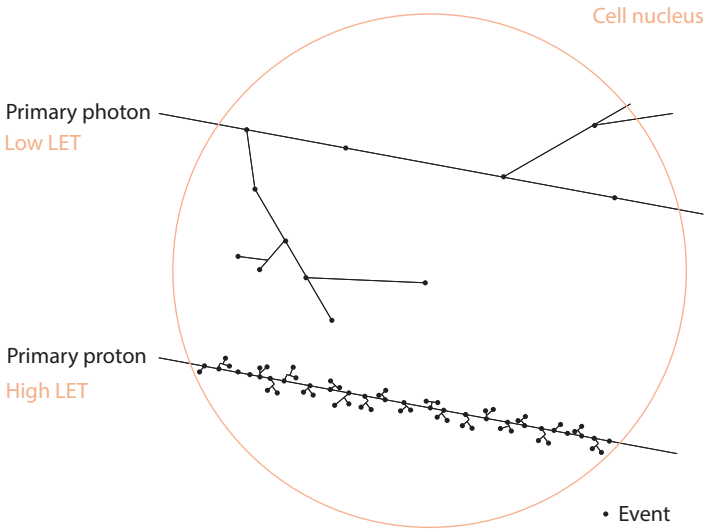

FIGURE 2.2: An illustration of the track structure of a primary photon and primary proton through a cell nucleus. The track structure of a photon consists of sparsely dense ionizations along its track and is referred to as low LET. The track structure of a proton consists of a higher ionization density along its track and is referred to as high LET.

Definitions of LET

LET accounts for energy lost through ionization and excitation, as well as through the production of high-energy secondary electrons (delta rays). This is referred to as unrestricted LET (L_∞), which is equivalent to the electronic stopping power S (Sec. 2.1.1). In contrast, restricted LET (L_Δ) accounts only for the energy lost by the primary particle, excluding energy transferred to delta rays that have less biological impact, providing a more accurate measure of energy deposition relevant to biological effects. Several studies proposed two methodologies to derive the average LET [49, 88]. The first approach is averaging over the fluence Φ_i, which represents the number of tracks produced by charged particles, also called track-averaged LET, LET_t, and is given by

$$\text{LET}_t(z) = \frac{\int_0^\infty S_{\text{el}}(E)\Phi(E,z)\,dE}{\int_0^\infty \Phi(E,z)\,dE}, \tag{2.7}$$

where $S_{\text{el}}(E)$ refers to the primary charged particle electronic stopping power at a given kinetic energy E, with $\Phi(E,z)$ as the primary charged particle fluence as a function of kinetic energy E and position z. The second approach is dose-averaged LET, LET_d, and weights the stopping power of each individual primary charged particle according to its relative contribution to the local dose deposition, and is given by

$$\mathrm{LET}_d(z) = \frac{\int_0^\infty S_{\mathrm{el}}^2(E)\Phi(E,z)\,dE}{\int_0^\infty S_{\mathrm{el}}(E)\Phi(E,z)\,dE}. \tag{2.8}$$

2.2.3 LET Limitations

The kinetic energy loss of charged particles as they travel through a medium occurs in discrete events, leading to statistical fluctuations in energy deposition. As a result, the actual LET of a particle may deviate from the average LET [49]. Additionally, the microscopic size of biological targets amplifies the significance of these fluctuations in energy deposition at the cellular or molecular level. Furthermore, since LET represents an average value, two different types of radiation with the same LET can exhibit different energy deposition distributions due to variations in energy straggling, finite range of particles and their track structure, potentially leading to varying biological effects [55]. Therefore, LET does not capture the detailed radial distribution of energy around the particle track, limiting its ability to fully explain the mechanisms of biological damage at the cellular and molecular levels. To address this, the field of microdosimetry was introduced [85].

2.3 The Role of Microdosimetry

Microdosimetry, introduced by Rossi and Rosenzweig in the mid-1950s [89], investigates the spatial, temporal, and spectral characteristics of the stochastic energy deposition processes in microscopic structures. Two fundamental quantities, specific energy (z) and lineal energy (y), serve as the microscopic, stochastic counterparts to dose and LET, respectively. Both are random variables that can be measured experimentally under certain conditions.

2.3.1 Specific Energy

Specific energy z represents the energy imparted by ionizing radiation in an individual microscopic volume per unit mass. z is defined by

$$z = \frac{\varepsilon}{m} \tag{2.9}$$

where ε is the energy imparted and m is the mass. Unlike absorbed dose, which is a macroscopic quantity where statistical fluctuations in energy deposition are negligible, specific energy is a microscopic, stochastic quantity that captures significant statistical

fluctuations in energy deposition. While both are measured in Gy (J/kg), specific energy varies from one microscopic volume to another due to these statistical fluctuations [90].

2.3.2 Lineal Energy

Lineal energy, y, represents the energy imparted within a defined microscopic volume of a single event divided by the mean chord length of that volume, providing a stochastic and volumetric perspective on the energy deposition. Unlike LET, which averages over a continuous track, lineal energy accounts for the discrete and random nature of energy transfer events within a microscopic volume, as shown in Figure 2.3, and is given by

$$y = \frac{\varepsilon}{\bar{l}} \tag{2.10}$$

with ε the energy imparted to the medium of a single event in the volume of interest, and $\bar{l}$ the mean chord length of that volume. According to Cauchy's theorem, the mean chord length can be calculated according to the formula $\bar{l} = 4V/S$, where V represents the volume and S denotes its surface area [90]. y is extensively used in microdosimetry and can be experimentally measured, making it an important tool for understanding and improving the efficacy of proton therapy. The core differences between LET and lineal energy are summarized in Table 2.1.

2.3.3 Microdosimetric Distributions

Due to the stochastic nature of particle interactions, the energy imparted to microscopic volumes varies from event to event. To capture this variability, microdosimetric distributions of lineal energy are used. These distributions offer a more comprehensive description of the radiation field by reflecting the spread of energy deposition events, which is crucial for assessing biological effects.

The probability density function of lineal energy $f(y)$ is the y distribution of all individual energy deposition events, weighted by the frequency. The frequency-mean lineal energy, $\overline{y_F}$, is the first moment of this distribution and equals

$$\overline{y_F} = \int_0^\infty y f(y)\, dy. \tag{2.11}$$

While $\overline{y_F}$ describes the average lineal energy of individual events weighted by their occurrence, it does not directly reflect the biological impact of energy deposition, which depends on how much energy is actually transferred to the target. To capture this, the dose-mean lineal energy is introduced, weighting lineal energy by the energy imparted

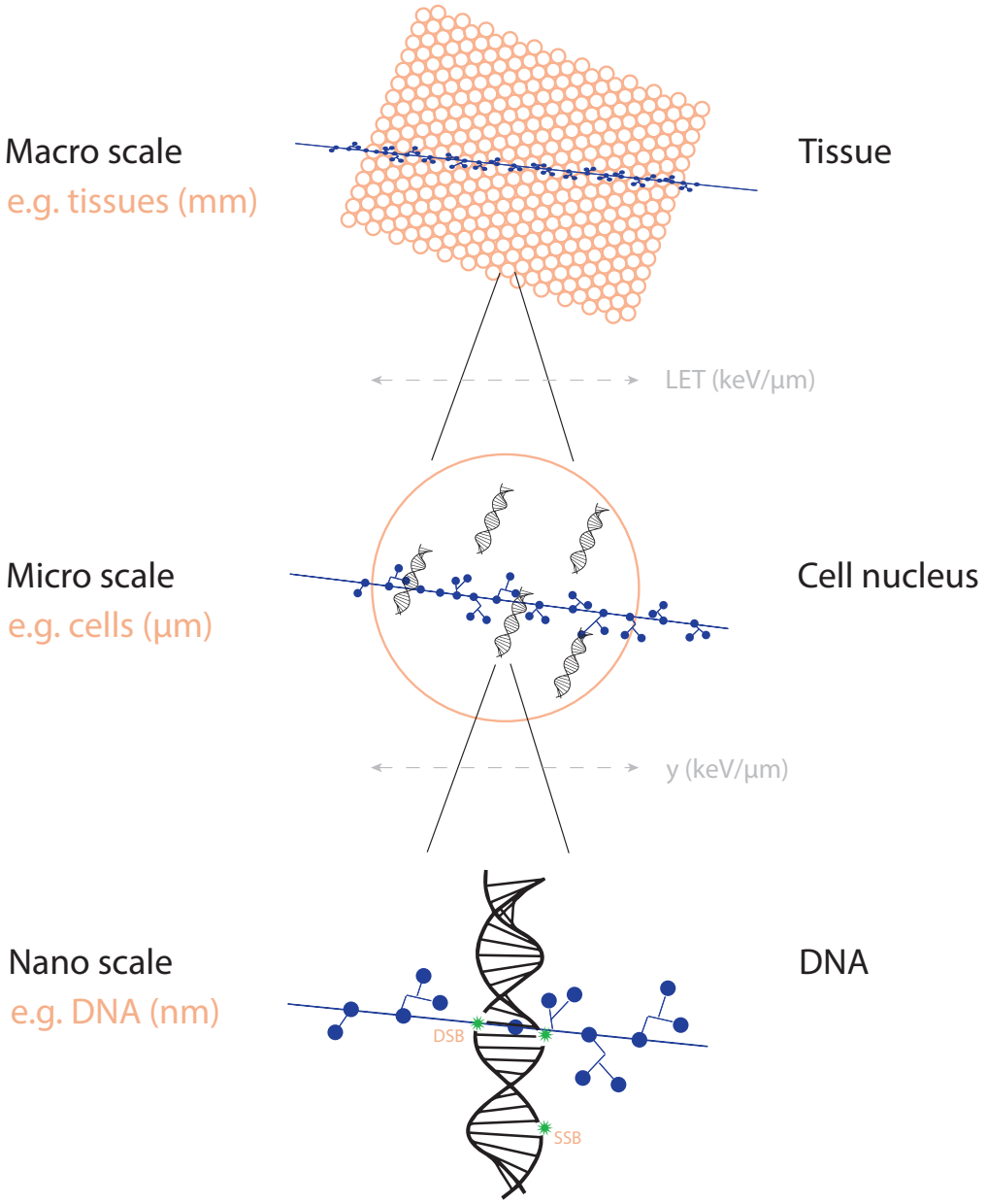

FIGURE 2.3: Three different scales in proton dosimetry: the macro-, micro-, and nanoscale. The macroscale refers to the tissue level in mm, in which LET describes the average amount of energy transferred per unit distance. The microscale refers to the cellular level where lineal energy y represents the amount of energy imparted within a defined volume (e.g., a cell). The nanoscale refers to radiation-induced DNA damage at the chromosomal level, visualized in terms of a single-strand break (SSB) and a double-strand break (DSB).

during each event. This shift from event frequency to energy deposition is reflected in the dose-weighted y-distribution $d(y)$, given by

$$d(y) = \frac{yf(y)}{\overline{y_F}}. \tag{2.12}$$

The dose-mean lineal energy, $\overline{y_D}$, is then given by

$$\overline{y_D} = \int_0^\infty y d(y)\, dy. \tag{2.13}$$

Further details on the microdosimetric quantities can be found in [90, 91].

TABLE 2.1: Comparison between Linear Energy Transfer (LET) and lineal energy (y). RB = radiation biology, sims = simulations.

Feature	LET	y
Definition	Energy deposited per unit path length in a medium.	Energy deposited per unit chord length in a volume.
Formula	$LET = \frac{dE}{dx}$	$y = \frac{\varepsilon}{l}$
Units	keV/µm	keV/µm
Nature	Deterministic, based on S.	Stochastic, depends on ε within finite volumes.
Scale	Macroscopic (continuous property of particle tracks).	Microscopic (random quantity in small volumes).
Dep. on Geometry	Independent of microscopic target shape or size.	Strongly dependent on target geometry.
Role of δ-rays	Considers only primary particle energy loss.	Includes stochastic effects of δ-ray energy deposition.
Relevance RB	Indicates general radiation quality.	Assessing microscopic radiation effects.
Measurement	Derived from S calculations or track structure sims.	Measured using microdosimetric detectors.

2.3.4 Microdosimetric Measurements

The field of experimental microdosimetry aims to experimentally measure the stochastic distribution of energy deposition at the microscopic level to gain insights into the impact of radiation on biological cells. Devices capable of measuring energy depositions at the microscopic scale are known as microdosimeters. Such microdosimeters typically use gas or solid-state counters.

Tissue Equivalent Proportional Counters

The first constructed microdosimeter, known as the tissue-equivalent proportional counter (TEPC), consisted of a hollow sphere made of tissue equivalent plastic and was filled with a gas that mimicked the properties of human tissue. The pressure of the gas was adjusted so that the cavity exhibited the mass stopping power of a 1-2 micrometer sphere of solid tissue at unit density. The proportional counter utilized an externally applied high electric field to amplify the ionization generated by charged particles passing through the gas, so that the energy deposited was roughly proportional to the charge collected of the counter [92, 93]. In such TEPCs, the dose absorbed by the gas closely matches the dose that would be absorbed by tissue, allowing it to serve as a reliable substitute

for tissue. Although TEPCs are commonly used as microdosimeters, they have several limitations. A significant factor is the wall effect, which introduces measurement uncertainties. The chamber wall can cause the reentry effect, where an electron produced by the incident radiation exits the active volume and later reenters, increasing the measured dose. Additionally, electron scattering by the wall can create extra events, further raising the dose. Finally, delta rays produced outside the active volume are more likely to enter the chamber than in actual tissue, also leading to higher dose measurements. Along with the wall effect, density issues can arise when the chemical composition of the wall is not identical to that of the gas, which is required according to the Bragg-Gray principle to preserve the secondary particle fluence [94]. Finally, the large physical size of TEPCs reduces lateral spatial resolution and limits their use in certain applications. To improve performance, it is necessary to reduce the geometrical size of the TEPC's sensitive volume, which lowers the counting rate in high intensity particle beams. Smaller detectors also provide higher spatial resolution in regions with steep gradients, thus enhancing the accuracy of measurements [55, 95].

Since the development of the TEPC, various types of microdosimeters have been developed to overcome their limitations, such as solid-state microdosimeters, crystal diamond-based detectors, and mini-TEPCs [61, 62, 63]. While mini-TEPCs, such as the one successfully tested at the 62 MeV proton beam of CATANA, offer advantages like the ability to sustain higher fluence rates without significant pile-up and eliminating the need for continuous gas flow [58], solid-state detectors have emerged as a more effective solution to address the limitations of TEPCs.

Solid-State Microdosimeters

Solid-state detectors utilize solid semiconductor materials, such as silicon, and are also referred to as semiconductor detectors. The advantage of using a solid material is that the detector dimension can become smaller due to increased densities of solid materials compared to gas [22]. Additionally, the silicon detector generates electron-hole pairs upon interaction with ionizing radiation, requiring significantly less energy in silicon (3.65 eV) compared to the 30 eV needed to create an ion pair in a gas-filled ionization chamber. This reduced energy requirement enables silicon detectors to achieve superior energy resolution compared to ionization chambers [96]. Unlike TEPCs, which simulate a single biological cell using a gas-filled volume, solid-state microdosimeters feature arrays of micron-sized silicon sensitive volumes (SVs). This configuration more accurately mimics a collection of biological cells, offering improved spatial resolution and enabling more detailed studies of radiation interactions at the microscopic level. Their compact

size, improved spatial resolution and their operation without the need for gas flow systems make them highly effective for microdosimetry applications. Further information and an in-depth explanation of the solid-state microdosimeter used in this work will be explained in the next section.

2.4 3D Silicon-On-Insulator Mushroom Microdosimeter

The 3D silicon-on-insulator (SOI) Mushroom microdosimeter is a solid-state detector fabricated using a semiconductor structure that consists of a thin silicon layer housing the electronic components, on top of an insulating silicon dioxide (SiO_2) layer, resting on a bulk silicon substrate. The availability of planar and Micro-Electro-Mechanical Systems (MEMS) 3D detector technology has led to the fabrication of 3D cylindrical SVs embedded in PolyMethyl MethAcrylate (PMMA), of which a general design can be seen in Figure 2.4, introduced by the Centre for Medical Radiation Physics (CMRP), University of Wollongong, Australia [97, 98].

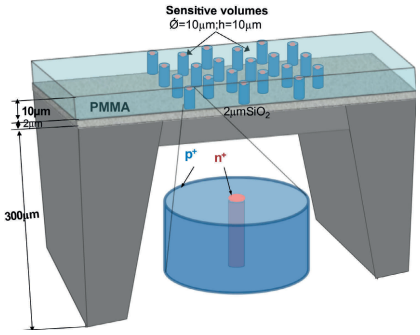

FIGURE 2.4: A schematic representation of a general design of a 3D SOI Mushroom microdosimeter. Taken from Rosenfeld et al. [97].

.

2.4.1 Microdosimeter Design

The 3D SOI Mushroom microdosimeter is a solid-state microdosimeter designed to measure the stochastic nature of energy deposition at microscopic scales. It operates by measuring energy imparted within cell-like SVs, allowing for the characterization of microdosimetric quantities relevant to understanding radiation interactions at cellular and subcellular levels. It features a 2×2 mm^2 active detecting area, visible as the central black chip in Figure 2.5a. This area contains 1520 cylindrical SVs arranged in a 38×40 array, as shown in the microscopic image in Figure 2.5d. Each SV is precisely structured, with a diameter of 18 µm, a thickness of 10 µm, and a center-to-center pitch of 56 µm.

The design of each SV consists of an n-type (negative charge carriers, n^+) polysilicon electrode core (Fig. 2.4), a p-type (positive charge carriers, p^+) polysilicon electrode surrounding ring (Fig. 2.4), and aluminum contacts placed over the n+ and p+ electrodes. The microdosimeter is housed in a dual in-line (DIL) package, mounted on a printed circuit board, referred to as the MicroPlus probe or μ^+ probe, which is shown in Figure 2.5b. To protect the microdosimeter from light, it is covered with black polyethylene film. To facilitate measurements in water, the μ^+ probe is typically enclosed within a watertight PMMA sheath (Figure 2.5c). To minimize background noise and electromagnetic interference, the PMMA sheath is often wrapped in aluminum foil, leaving a small exposed window where the μ^+ probe is positioned (Fig. 2.5e). The complete μ^+ probe assembly, including the shaping amplifier, is shown in Figure 2.5e.

2.4.2 Calibration of Microdosimeters Using Alpha Spectroscopy

Before exposing a microdosimeter to radiation fields, it is essential to calibrate the device through alpha spectroscopy, utilizing a well-characterized alpha-emitting source. Alpha particles, due to their short range in matter and high LET, are an ideal choice for assessing the microdosimeter's response to ionizing radiation. To ensure accurate calibration, the experimental setup typically involves positioning the alpha source at a distance of 1 to 2 cm above the microdosimeter with a custom 3D-printed holder. The entire assembly can be placed inside an aluminum-wrapped box to minimize external interference. The microdosimeter's response can then be analyzed by measuring the resulting pulses using an oscilloscope, allowing for the evaluation of the microdosimeter's performance.

2.4.3 Instrumentation and Data Acquisition in Microdosimetry

The measurement of energy deposition relies on precise instrumentation and data acquisition techniques. When a charged particle interacts with a silicon sensitive volume, electron-hole pairs are created along the charged particle's path, generating an electrical signal. A charge-sensitive preamplifier is then used to convert the electrical signal into a proportional voltage pulse. This allows the signal to be translated into a measurable format. To further refine the signal, a shaping amplifier is employed, which shapes the pulse to ensure that its amplitude is proportional to the energy deposited in the detector. A digital MultiChannel Analyzer (MCA), plays an important role in interpreting the data. It records the peak amplitude and generates a histogram that represents the number of events in each pulse height channel, serving as the primary output of the MCA. To accurately interpret the data, calibration is necessary. The calibration process involves determining fitting parameters that relate the observed pulse amplitudes to the actual energy deposited in the detector. These parameters are typically derived from a

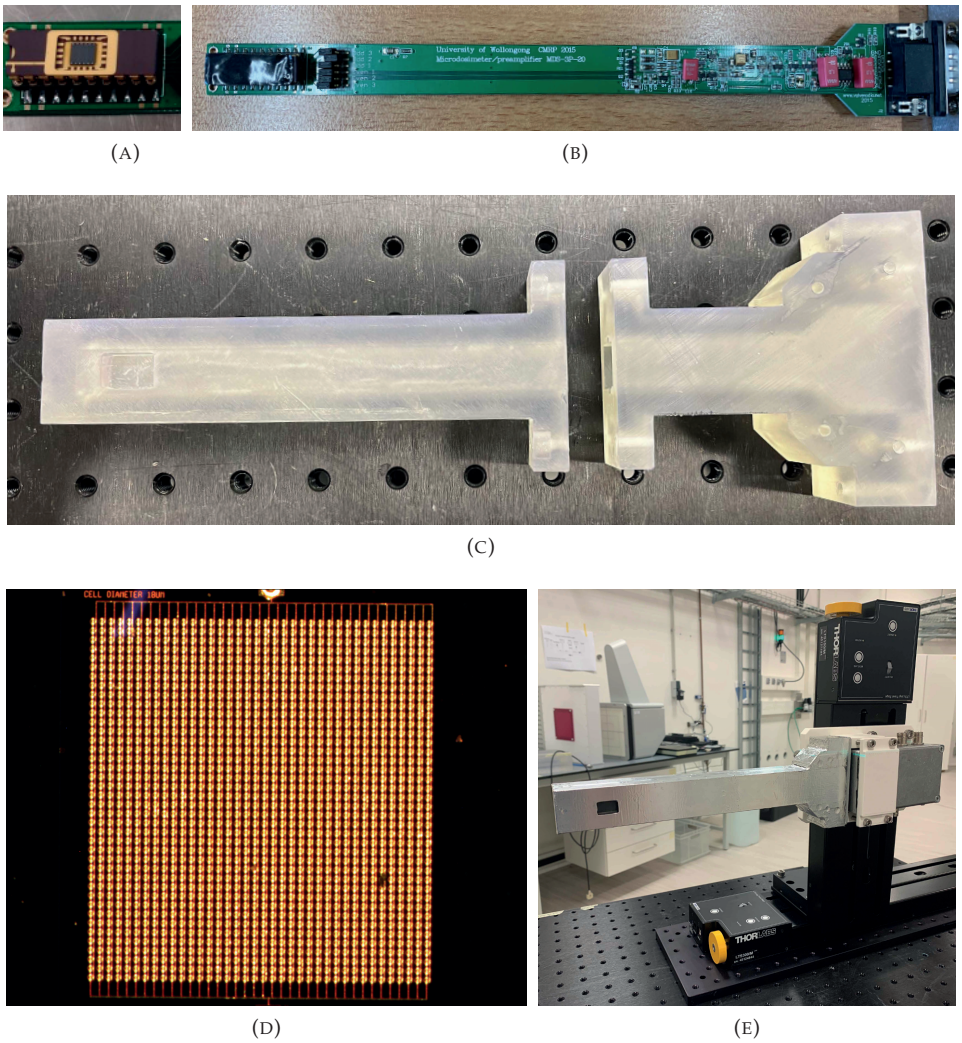

(A) (B)

(C)

(D) (E)

FIGURE 2.5: (A) The 3D SOI Mushroom microdosimeter with the 2×2 mm^2 active detecting area, (B) the microdosimeter attached to a printed circuit board, referred to as the μ^+ probe, (C) the watertight PMMA sheath to house the μ^+ probe, (D) a microscopic image of the 1520 cylindrical SVs arranged in a 38×40 array, and (E) the μ^+ probe assembly, including the shaping amplifier mounted on a motorized linear stage.

calibration spectrum obtained using a calibrated pulse generator, ensuring that the system can convert raw pulse data into meaningful energy measurements. Once calibration is complete, the raw pulse height spectrum can be converted into an energy deposition spectrum (ε) by multiplying it with the calibration parameters. Finally, the energy deposition spectrum is used to calculate the lineal energy spectrum. This is achieved by

dividing the energy deposition (ε) by the mean chord length ($\bar{l}$), which accounts for the geometry of the detector and the trajectory of the charged particles.

2.4.4 Silicon-to-Tissue Equivalence in Microdosimetry

Whereas TEPCs have the advantage of using tissue-equivalent gas in their sensitive regions, correction factors for silicon-to-tissue equivalence have been established to adapt SOI microdosimeter measurements for biological relevance. These corrections rely on the ratio of stopping powers between silicon and tissue, often using Monte Carlo simulations. The implementation of silicon-to-tissue correction methods ensures that the microdosimetric quantities derived from SOI detectors remain biologically meaningful and comparable to TEPC-based measurements [99, 100].

2.5 Computational Approaches in Radiotherapy

Computer simulations have gained significant importance over the last decades and are extensively used to solve complex problems in radiation therapy for a wide range of applications. These computer simulations make use of the Monte Carlo (MC) method, a computational technique that solves mathematical problems by simulating random variables to model the complex interactions between radiation and matter, further explained in Section 2.5.1. MC simulations play a key role in accurate dose calculations and verification of treatment plans to make sure the planned dose distribution is delivered with precision to the patient. Additionally, MC simulations are widely used to simulate complex geometries to optimize beamline configurations. They also contribute significantly in the field of radiobiology by simulating the biological effects on tissue structures, which aids in understanding the biological responses to different radiation qualities [101].

2.5.1 The Monte Carlo Method

After its first suggestion in 1940 [102], the MC method was used to study nuclear disintegrations caused by high-energy particles by employing random numbers between zero and one to determine the momentum of a target particle, with the probability of a collision being weighted by the corresponding cross-section [103]. In this way, the generation of random numbers determines the particle's trajectory, energy loss, and interactions. Since its introduction, several MC radiation transport modeling toolkits have been developed, such as EGS [104], MCNP [105, 106], FLUKA [107, 108], PENELOPE

[109], and GEANT4 [110, 111, 112]. The latter is employed in this dissertation and is discussed in greater detail in the next section.

2.6 Introducing GEANT4: A Monte Carlo Toolkit for Radiation Transport

GEANT4 is a toolkit designed for simulating the passage of particles through matter using Monte Carlo methods [110, 111, 112]. As the most widely used Monte Carlo radiation transport toolkit, it offers a full range of capabilities, including particle tracking, geometry, physics models, and hits detection. With its extensive range of physics transport models – covering electromagnetic, hadronic, and optical interactions – GEANT4 finds applications across various fields, including high-energy and nuclear physics experiments, as well as studies in accelerator, space and medical physics. The toolkit features a variety of example applications that illustrate both basic configurations, of which an example geometry is shown in Figure 2.6, and fully developed setups across various fields. Built in the object-oriented programming language C++, the GEANT4 source code is freely available from the project website under an open source license [113]. Developed through an international collaboration of physicists and software engineers, the GEANT4 Collaboration offers comprehensive documentation and user support for the toolkit, ensuring accessibility and guidance for its users across various applications.

2.6.1 Particle Transport

Particle transport in GEANT4 is modeled step by step, referred to as the condensed-history technique. In this method, each step refers to a specific distance traveled by the particle. After a series of steps, the cumulative effects of multiple collisions are simulated, representing the interactions that occur along the particle's trajectory. The length of the steps, the step length, plays an important role in determining the accuracy of the simulation. Users can define specific step length limits for particular particles or regions, regulated by production cuts. These production cuts are thresholds that define the minimum energy or range that secondary particles must have to be explicitly tracked in the simulation. These thresholds help optimize simulation performance by excluding secondary particles that would have negligible effects on the results, thereby balancing computational efficiency with simulation accuracy [114].

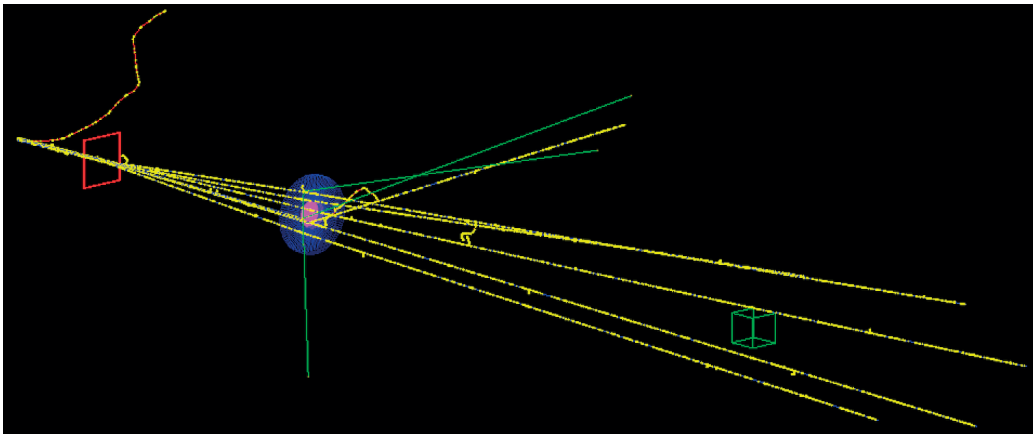

FIGURE 2.6: Example of a simple GEANT4 geometry showing the particles emitting from a source.

2.6.2 Physics in GEANT4

The selection of an appropriate physics model in GEANT4 depends on the particles of interest and the physical processes being studied. GEANT4 offers a comprehensive set of physics models, collectively referred to as a physics list, which defines the particles and their associated interactions. This allows users to select the most suitable configuration for their application. GEANT4 classifies most of its physics processes into two main categories: electromagnetic (EM) and hadronic. EM processes involve interactions with bound electrons or atomic fields, while hadronic processes include reactions that produce hadrons in the final state, such as neutrons, fission fragments, or unstable isotopes. This category also covers lepton- and gamma-induced nuclear reactions and radioactive decay [115].

Electromagnetic Physics

In GEANT4, electromagnetic physics processes are managed through base classes that incorporate one or more physics models to manage the energy loss, range and cross-sections tables. Each model applies to a specific energy range and designated region, allowing for the assignment of models from both low- and high-energy sub-packages to processes for different particle types. Electromagnetic physics constructors have become stable in the recent releases of GEANT4 [112], with *G4EmStandardPhysics_option4* being the most precise model for describing electromagnetic processes. This physics list handles a range of EM processes, including pair production, multiple Coulomb scattering, the photoelectric effect, Rayleigh scattering, bremsstrahlung, ionization, and positron annihilation, for various particles [114].

Hadronic Physics

GEANT4 provides total, inelastic, and elastic cross-sections for hadron-nucleus and nucleus-nucleus reactions up to and beyond 1 GeV, parameterized based on various datasets [112, 116, 117]. Total and elastic cross-sections are effectively infinite due to Coulomb interactions [114], but atomic screening reduces the effective nuclear charge as nuclei approach each other, limiting these cross-sections, causing small-angle sxattering, which will therefore be ignored in hadronic physics. Inelastic cross-sections remain the most significant due to their impact on hadronic physics [112, 115].

Sub-GeV inelastic hadronic interactions are complex and require multiple models. These interactions start with a hadron-nucleon collision, described by the intranuclear cascade model, which tracks multiple nucleon collisions. Three models represent this cascade: Bertini Intranuclear Cascade (BERT), Binary Cascade (BIC), and Liège Intranuclear Cascade (INCL++) model. The cascade generates and scatters secondary particles, resulting in a chain of collisions within the nucleus. The precompound/pre-equilibrium model describes this propagation, transitioning into the equilibrium phase. As particles lose energy, the residual nucleus de-excites through (1) nuclear evaporation, (2) fission, (3) Fermi break-up, or (4) fragmentation, reaching a stable state. If semi-stable radionuclides form, their decay is simulated via α, β^-, β^+, isomeric transition, and electron capture [114, 115].

Low Energy Physics

Electron transport below 1 keV is generally negligible in macroscopic proton dosimetry. However, this limitation prevents the modeling of particle tracks and energy deposition at microscopic and nanoscopic scales, which is essential for understanding radiation effects on cells and DNA. Specifically, low-energy electron interactions play a crucial role in chemical processes such as water radiolysis, responsible for the production of reactive oxygen species (ROS) that indirectly cause DNA damage, making them essential for mechanistic studies of celullar radiobiological effects. Traditional macroscopic MC codes, which rely on the condensed-history technique, are inadequate for such applications. To overcome this, track-structure capabilities were integrated into GEANT4, leading to the development of its low-energy extension designed to model particle interactions at microscopic and nanoscopic scales.

2.7 GEANT4-DNA and Simulating Early DNA Damage

GEANT4-DNA [70, 71, 72, 73, 74], introduced in 2007 (Geant4 v9.1), is the low-energy extension of the GEANT4 MC toolkit. Other general-purpose MC codes with track-structure capabilities include PARTRAC [65], KURBUC [66], RITRACKS [67], NOREC [68], and TOPAS-nBIO [69], reviewed by Kyriakou et al. [64]. GEANT4-DNA models low-energy particle interactions including all associated secondaries at the (sub)cellular and DNA levels [64, 118]. Unlike GEANT4, which uses the condensed-history technique, GEANT4-DNA employs a track-structure approach to simulate electron transport down to energies near the ionization threshold of tissue-like materials ($\pm$10 eV). This capability enables detailed energy deposition modeling in liquid water, the primary constituent of biological systems. While other track-structure codes focus solely on physical interactions, GEANT4-DNA also simulates physico-chemical and chemical stages of ionizing radiation. Users can choose from three validated physics models with different cross-sections for elastic and inelastic scattering (Option 2, Option 4 and Option 6). These models have been validated against reference data and, where possible, experimental results and other MC studies [64].

2.7.1 Physical, Physico-Chemical, and Chemical Stage

Physical Stage

The physical stage involves the individual interactions between charged particles and the atomic components of the tissue, which can result into ionizations and excitations of atoms, described by energy-loss models. These models consist of the interaction products, and final states of the physical interactions, while accounting for the molecular structure of liquid water [72]. Additional details on these models, developed by the GEANT4-DNA collaboration, are provided elsewhere [74, 75, 119, 120].

Physico-Chemical Stage

The physico-chemical or pre-chemical stage refers to the phase in which electronic alterations in water molecules, such as excited H_2O^* and ionized H_2O^+, result in the formation of highly reactive free radicals and other ROS due to water radiolysis within 1 ps after the irradiation.

Chemical Stage

The chemical stage describes the diffusion of generated reactive species within the medium. These species can interact with cellular components through rapid chemical reactions, such as DNA strand interactions, potentially leading to molecular damage.

2.7.2 DNA Damage Modeling

To calculate interactions with the DNA geometry, the IRT-sync model provides spatiotemporal data on reactive species at each time step. The induction of a DNA damage lesion depends on the amount of energy deposited, which must fall within a specific energy range according to a linear probability model during a physical interaction. Additionally, the interaction must occur within 3.5 Å of a DNA base, a distance equivalent to the radius of nucleotide molecules. Through these calculations, GEANT4-DNA facilitates the modeling and quantification of DNA strand break number, distribution and complexity. This capability is of significant value and serves as a useful tool for enhancing the understanding of biological outcomes.

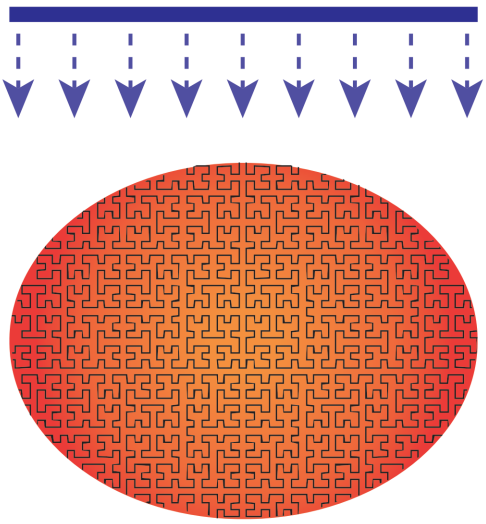

FIGURE 2.7: A simplified schematic representation of the human cell geometry in the GEANT4-DNA "molecularDNA" application. The orange ellipse represents the human cell, containing Hilbert curve fractals in black to illustrate a continuous DNA chain. The blue bar demonstrates the radiation source and its direction. Mimicked from Chatzipapas et al. [121].

2.7.3 The "molecularDNA" Application

The "molecularDNA" application, publicly released in GEANT4 version 11.1 [121], provides a user-friendly example for simulating radiation-induced DNA damage. This application version has undergone substantial enhancements from its previous development iterations [75, 78, 80, 122], specifically including the new chemistry model Synchronous Independent Reaction Time (IRT-sync) model. Most importantly, the simulation results are validated through comparison with previously published data [123].

"molecularDNA" includes several DNA geometries for various modeling purposes: the cylinders geometry, representing a cell with small DNA fragments modeled as cylindrical structures, mainly used for parameter studies. Additionally, a plasmid geometry is available, consisting of a cubic volume of liquid water containing 10000 plasmids. The application also consists of an E. coli bacterium geometry designed to simulate the bacterium genome. For human cell modeling, "molecularDNA" offers a simplified human fibroblast geometry, incorporating a cell nucleus containing a continuous DNA chain modeled using Hilbert curve fractals (Fig. 2.7), further discussed in Chapter 6.2.2. Next to geometry selection, users can define the particle source and specify DNA damage modeling parameters [121]. More detailed information about the features of "molecularDNA" and its applications can be found in its documentation and on the GEANT4-DNA website [124, 125].

Chapter 3

Characterization of the HollandPTC R&D Proton Beamline

Parts of this chapter have been published as "Rovituso, M., Groenendijk, C. F., Van der Wal, E., Van Burik, W., Ibrahimi, A., Prieto, H. R., Brown, J. M. C., Weber, U., Simeonov, Y., Fontana, M., Lathouwers, D., & Hoogeman, M. (2025). *Characterisation of the HollandPTC R&D proton beamline for physics and radiobiology studies*. Physica Medica, 130, 104883" [126].

3.1 Introduction

HollandPTC is one of three proton therapy centers in the Netherlands and has been treating eligible cancer patients with proton therapy since 2018 [34]. It is the only facility in the country with a dedicated clinical R&D experimental proton beamline, emphasizing the need to maximize scientific output during each beamtime session. The HollandPTC R&D experimental proton beamline, specifically designed and developed for the HollandPTC, is equipped with a passive scattering system capable of generating large proton fields of varying sizes. This configuration supports radiobiological studies using clinically relevant proton energies.

The HollandPTC R&D experimental proton beamline, shown in Figure 3.1, delivers therapeutic proton beams with energies ranging from 70 MeV to 240 MeV. The nominal beam current, which quantifies the amount of electric charge transported by the proton beam per unit time (measured in amperes) at cyclotron extraction, is adjustable from 1 nA to 800 nA. The end of the vacuum beam pipe consists of a Kapton window with a thickness of 0.125 mm, beyond which the proton beam enters a 3.8 m beamline target station in air. This station is constructed from modular tables of 750 mm $\times$ 750 mm, each featuring a Thorlabs plate, a type of mounting surface commonly used in experimental setups for precision alignment and mounting of components. The Thorlabs plates can be removed and replaced within $\pm$1 mm precision relative to the beam. Additionally, a fixed room laser system defines an isocenter, the reference point in the experimental room where the beam is focused, located 911 mm from the Kapton window at the exit of the vacuum pipe. The laser system extends along the entire target station, enabling accurate alignment at different distances from the Kapton vacuum pipe exit window.

Conducting a diverse range of experiments requires a beamline design that is versatile for pre-clinical studies while maintaining compatibility with clinical proton therapy applications. To ensure that the R&D experimental proton beamline system performs as expected, delivers accurate doses, and remains reproducible, characterization is crucial. This characterization process involves determining and describing its key properties and behaviors, which are essential for understanding its performance across various applications. Characterizing the physical properties of the proton pencil beam requires measuring several parameters, including beam shape, size, intensity, and the depth-dose distribution [28]. In addition to the pencil beam, a dual-ring passive scattering system was designed, constructed, and characterized to produce uniform lateral fields ranging from 2$\times$2 cm^2 to 20$\times$20 cm^2. These large fields were evaluated in terms of field uniformity, field shape, and dose rate, and are particularly important in radiobiological

experiments where consistent and reproducible irradiation is needed to evaluate cellular responses across a broader target region. For this purpose, two unique radiobiological endstations were developed that enable precise irradiation of biological samples, such as cell cultures and tumor tissue samples.

This chapter details the characterization of the HollandPTC R&D experimental proton beamline in both pencil beam and double passive scattering configuration for physics and radiobiological studies. These characterizations in terms of beam shape, size, intensity, and depth-dose distribution are essential to establish well-defined dosimetric conditions for conducting physics and radiobiological experiments, and offer reproducible experimental setups in order to study the underlying biological mechanisms of proton therapy. Section 3.2 describes the two different beamline configurations and the measured beamline characteristics. The experimental results for both configurations are presented in Section 3.3, followed by the discussion in Section 3.4 and the conclusion in Section 3.5.

FIGURE 3.1: The experimental room at HollandPTC.

3.2 Methods

3.2.1 Measurement Devices

To fully characterize the HollandPTC R&D experimental proton beamline, the following measurement devices were used.

- A beam monitor (BMI01, DETECTOR, Turin, Italy) consists of two planar integral chambers and is capable of online proton beam monitoring in terms of beam intensity and time with a 1 ms resolution. The BMI01 is placed 100 mm downstream of the Kapton vacuum pipe exit window and consists of a sensitive area of 300 $\times$ 300 mm^2 and a water-equivalent (WE) thickness of 0.6 mm. Moreover, the BMI01 is connected to the Varian ProBeam system, serving as a trigger for a customized delivery system to control the irradiation based on either delivery time or the number of protons delivered.

- The Lynx® detector (IBA Dosimetry, Schwarzenbruck, Germany) comprises a scintillating screen coupled to a CCD camera, featuring an active surface area of 300 $\times$ 300 mm^2 and an effective spatial resolution of 0.5 mm in both the x and y directions. The detector was utilized to measure the beam spot at the isocenter, as well as at various distances from the Kapton vacuum pipe exit window to characterize the beam envelope. Additionally, it was employed to measure the shape and profile of large fields.

- The BC-75 Faraday cup (Pyramid Technical Consultants, Inc.) is a charge beam collector used to provide direct measurements of the proton beam current, optimized for proton energies up to 250 MeV, with a maximum current readout capacity of 4µA. Featuring a sensitive area with a diameter of 70.5 mm, the Faraday Cup was utilized in this study as a reference device to calibrate BMI01 and to characterize the beam current at the isocenter.

- The Qubenext (DETECTOR, Turin, Italy) is a device utilized to measure depth-dose distributions using air vented multi-layer ionization chambers. It features a sensitive area of 127 $\times$ 127 mm^2 and consists of 128 channels, each with a pitch of 2.34 mm WE, enabling measurement of proton ranges up to a total of 310 mm WE. In this study, the Qubenext was employed to evaluate depth-dose distributions.

- The Advanced Markus® ionization chamber of type 34045 (PTW Freiburg, Germany) is a vented plane-parallel ionization chamber equipped with a thin entrance window and a waterproof protective cap for measurements in water. It has a sensitive volume of 0.02 cm^3 and is used to measure absorbed dose. In this study, the

Advanced Markus® chamber was used for absorbed dose and absorbed dose rate measurements.

- The OCTAVIUS Detector 1500XDR (PTW Freiburg, Germany) consists of a matrix of vented plane-parallel ion chambers, each measuring $4.4 \times 4.4 \times 3$ mm^3, with a center-to-center spacing of 7.1 mm. The matrix contains a total of 1405 ion chambers, arranged to provide a maximum field size of 27×27 cm^2. In this study, the OCTAVIUS was used to measure absorbed dose and absorbed dose rate measurements across large fields.

3.2.2 Pencil Beam Measurements

Beam Spot Measurements

The pencil beam spot size for energies ranging from 70 to 240 MeV was measured at the isocenter using the Lynx® detector. A 2D intensity distribution was obtained, and a 2D Gaussian function was fitted to account for the elliptical, rather than symmetric, spread of the beam and to determine the beam spot size. The 2D Gaussian function $f(x, y)$ was described by:

$$f(x,y) = A \cdot e^{-\left(\frac{\mu_x - x}{2\sigma_x}\right)^2 + \left(\frac{\mu_y - y}{2\sigma_y}\right)^2} \tag{3.1}$$

where A is the height of the distribution, μ_x and μ_y are the mean values in x and y, respectively, and σ_x and σ_y are the standard deviations of the distributions in x and y, respectively. $\mu_{x,y}$ was used to confirm that the beam was correctly directed and centered relative to the reference points provided by the room's laser alignment system and the detector setup, while $\sigma_{x,y}$ was used to determine the beam spot size in terms of the Full Width at Half Maximum ($\text{FWHM}_{x,y} = 2.355 \cdot \sigma_{x,y}$) for both x and y.

Beam Envelope Measurements

The beam envelope refers to the spatial distribution of the beam as it propagates through air. To determine the beam envelope, intensity distributions were measured using the Lynx® detector at seven positions along the beam path, at distances of 230, 530, 911, 1230, 1530, 1830, and 2045 mm from the Kapton vacuum pipe exit window, schematically illustrated in Figure 3.2. These measurements were conducted at proton energies of 70, 120, 150, 200, and 240 MeV. For each position and energy, a 2D Gaussian fit (Eq. 3.1) was applied to calculate the beam spot sizes. The resulting beam envelope provided insights into the beam optics and beam's trajectory through air at varying proton energies.

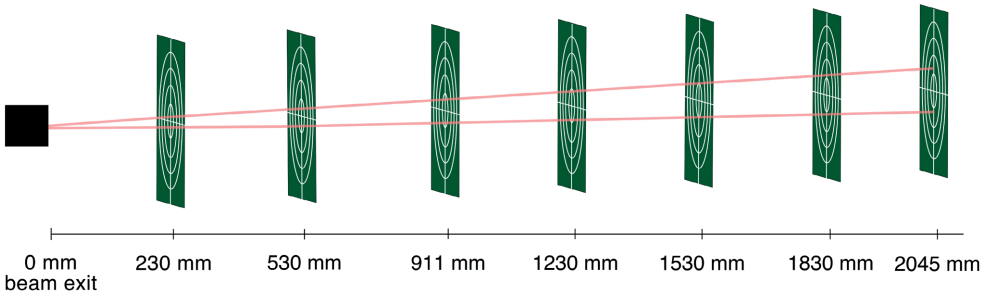

FIGURE 3.2: Schematic illustration of beam envelope measurements. The black square represents the beam exit at 0 mm, with the subsequent Lynx® detector positions indicated as green squares, illustrating the beam's propagation through air in pink.

Beam Spot Asymmetry

Beamline components such as focusing magnets can introduce asymmetry in the beam spot due to non-uniform beam optics. Additionally, interactions with materials like vacuum windows or beam monitors, along with misalignment of the detector can lead to variations in the beam spread. These factors can contribute to asymmetry of the beam spot. The asymmetry (AS) of the beam spot was calculated as:

$$\mathrm{AS}(\%) = 100 \cdot \frac{\sigma_x - \left(\frac{\sigma_x+\sigma_y}{2}\right)}{\frac{\sigma_x+\sigma_y}{2}} \tag{3.2}$$

with σ_x the beam spot size in the x-direction, and σ_y the beam spot size in y-direction [42].

Transmission Efficiency and BMI01 Calibration

The actual beam current at the isocenter can be reduced due to various factors, such as traveling through the Kapton vacuum pipe exit window, the BMI01, and interactions that occur as the beam travels through air. This discrepancy means the nominal current does not directly reflect the beam current at the location where measurements are taken, and is defined as the transmission efficiency (TE). Measurements to assess the TE of the beam were carried out using the BC-75 Faraday cup, which is reported to have an uncertainty of less than 2% in charge readout. TE was measured for different beam energies, with a readout time of 100 ms for the BC-75, and a readout range spanning from 1 nA to 50 nA. To quantify the uncertainty in the BC-75 readout values, each measurement was repeated three times, with each run lasting 20 seconds. For each run the data points were averaged, and a standard deviation was calculated. The TE is defined as the ratio

of the measured beam current at the isocenter to the nominal beam current, as expressed in the following formula:

$$\mathrm{TE}\,(\%) = 100 \cdot \left(\frac{I_{iso}}{I_{nom}} \right) \tag{3.3}$$

with I_{iso} as the beam current at the isocenter, and I_{nom} representing the nominal beam current at cyclotron extraction.

Depth-Dose Measurements

Depth-dose distributions for proton energies ranging from 70 to 240 MeV were measured at the isocenter using the QUBEnext detector, with measurements taken in 10 MeV increments, as schematically illustrated in Figure 3.3. The distributions were analyzed by fitting them with a Bortfeld function [127]. From the fitted data, the R100 (the depth at which the dose reaches 100% of its maximum value), the peak width, R80 (the depth at which the dose reaches 80% of its maximum value), and the peak-to-entrance (P-E) ratio were determined. The P-E ratio was calculated by dividing the maximum dose value by the dose value at the first entrance channel [42].

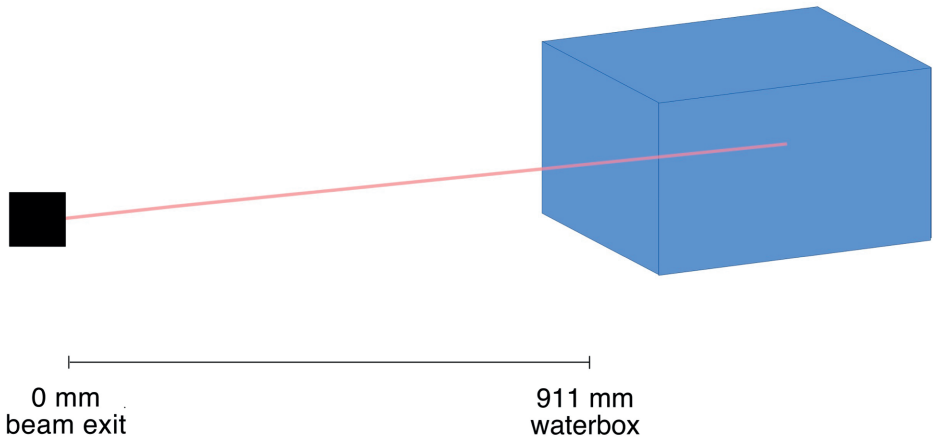

FIGURE 3.3: Schematic illustration of depth-dose measurements. The black square represents the beam exit at 0 mm, with the blue box representing the Qubenext detector at the isocenter (911 mm).

3.2.3 Double Passive Scattering Measurements

Passive Scattering Approach

Various passive scattering (Sec. 1.4.2) techniques are available to broaden the initial pencil beam to achieve a large field with a uniform dose distribution. At HollandPTC, a double passive scattering system with a dual-ring configuration was developed and optimized for an energy of 150 MeV [128, 129]. This system incorporates a flat scattering foil, made of lead, to spread the initial pencil beam into a profile resembling a Gaussian distribution. Following this, a dual-ring structure, consisting of a central disk constructed from a high-Z material (lead), surrounded by a ring made of a lower-Z material (aluminum), further shapes the beam. The central disk generates a Gaussian-like profile, while the surrounding ring produces an annular-shaped profile. Together, these combine to create a uniform beam profile [28].

Two dual-ring systems were designed to accommodate different field sizes and dose rates. The "thick ring" system is optimized for fields up to 20×20 cm^2 with lower dose rates, while the "thin ring" system is tailored for fields up to 8×8 cm^2 with higher dose rates. The thick ring system utilizes a 3.4 mm scattering foil, whereas the thin ring system employs a thinner 0.8 mm scattering foil. The thicknesses and dimensions of the rings are reported in Table 3.1. These dimensions were taken from the work of Tommasino et al. [43]. The dual-ring setups were mounted on a specialized support system designed to allow easy insertion and removal from the beamline without compromising their alignment relative to the beam. Each support system is made in such a way to enable precise alignment adjustments in the order of 0.05 mm steps. The support system is shown in Figure 3.4a.

TABLE 3.1: Specifications of the dual-ring systems in terms of diameter (mm) and thickness (mm) for the outer ring (aluminum) and inner ring (lead) for the thick ring and thin ring system.

Setup	**Outer ring (Al)**		**Inner ring (Pb)**	
	Diameter (mm)	Thickness (mm)	Diameter (mm)	Thickness (mm)
Thick ring	200	16	45	5.5
Thin ring	200	5	11	1.5

Longitudinal Beam Spreading and Collimation

In order to spread the monoenergetic beam and create a uniform dose distribution in the longitudinal direction, a 2D polymer range-modulator was used. It is composed of numerous thin pins, each with a precisely defined shape and varying lengths, designed to achieve the required modulation to produce a Spread-Out Bragg Peak (SOBP) [130, 131].

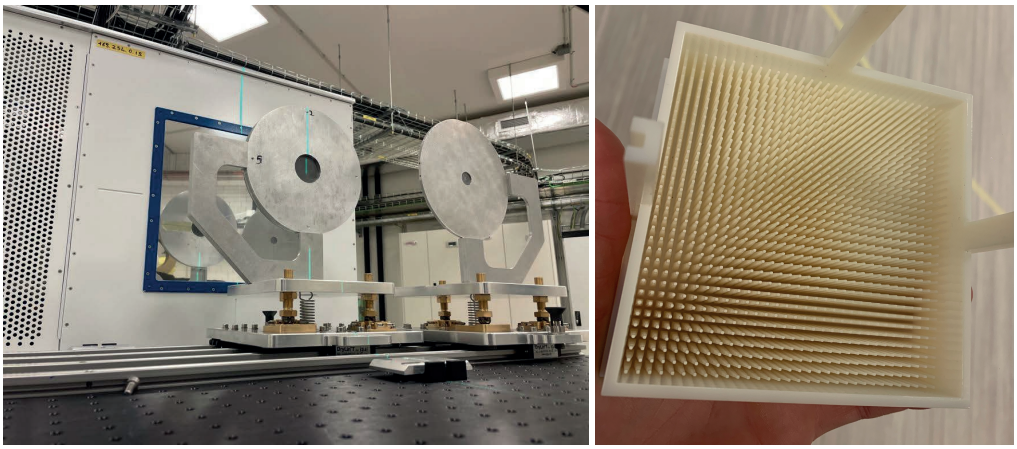

(A) (B)

FIGURE 3.4: (A) The dual-ring systems mounted on the specialized support system, and (B) the 2D range-modulator.

The 2D range-modulator was optimized for an initial energy of 150 MeV to produce a SOBP of a specific width and is shown in Figure 3.4b. To shape and control the generated large field, a two-stage brass collimator system was implemented. Its primary function was to define a squared field size by laterally restricting the proton beam, ensuring that the dose is delivered only within the desired field boundaries. The first collimator provides an initial rough shaping of the beam and blocks the majority of the spread protons caused by the passive scattering elements. This prevents the spread protons from bombarding the second collimator, which would otherwise increase the generation of high-energy neutrons in the brass material. By mitigating neutron production in the second collimator, the system reduces the impact on the target [132]. The second collimator, placed 85 cm downstream and 12 cm upstream of the target, finalizes the beam shaping and further stops unwanted secondaries to ensure a uniform dose distribution across the large field. The two-stage system can accommodate different collimator sizes to create a variety of square field sizes of 2×2, 4×4, 10×10, 16×16, and 20×20 cm^2. To address elevated intensity at the field edges, caused by increased scattering from the passive scattering system and collimators, all collimators were designed with slightly larger apertures than the nominal field size. This compensatory design enhanced dose uniformity across the field, minimizing variations between the center and edges.

Figure 3.5 shows a photo and schematic representation of the dual-ring passive scattering configuration. The proton beam exits (1) the Kapton vacuum pipe window, passes through (2) the first scattering foil, and is monitored by (3) the BMI01. The beam then

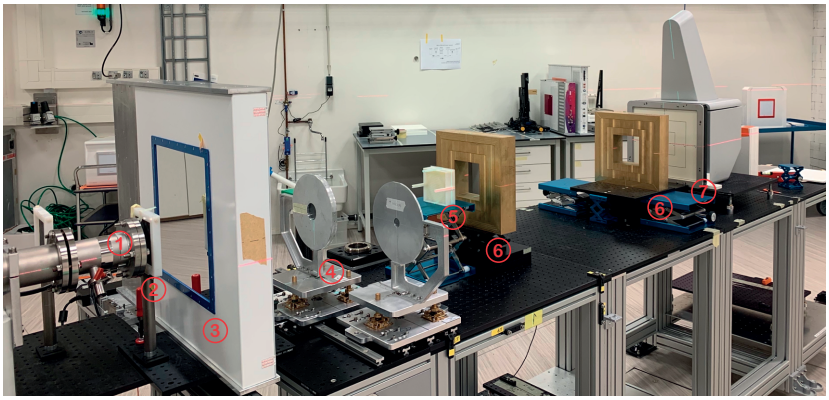

(A)

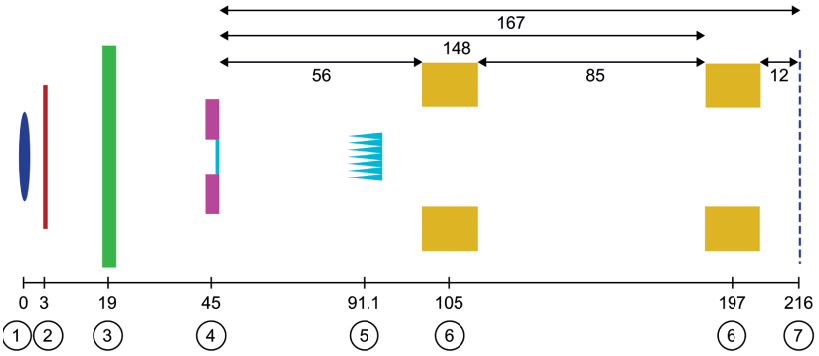

(B)

FIGURE 3.5: (A) The experimental setup, and (B) schematic representation (not to scale) of the dual-ring passive scattering configuration with the distances from Kapton vacuum pipe exit window in cm. From left to right: the Kapton vacuum pipe exit window (1), the first scattering foil (2), BMI01 (3), dual-ring (4), 2D range-modulator (5), collimator system (6) and detector or target (7).

traverses (4) the dual-ring, interacts with (5) the 2D range-modulator, and is shaped by (6) the two-stage brass collimator system, which defines field size.

Large Field Uniformity

To achieve maximum beam uniformity across the large field, the distances between the first scattering foil, dual-ring, and target position were optimized. For this purpose, GEANT4 simulations were performed to determine the optimal spacing between these components. The shape and uniformity of the passively scattered field were measured using the Lynx® detector. The Lynx® was placed at target position, as shown in Figure 3.5. From the obtained 2D beam cross-sections, the uniformity (U) across the field was calculated as:

$$\mathrm{U}(\%) = \left(1 - \frac{I_{max} - I_{min}}{I_{max} + I_{min}}\right) \cdot 100\%, \tag{3.4}$$

where I_{max} is the maximum intensity across the field of interest, and I_{min} is the minimum intensity. A uniformity with a maximum deviation of 5% is desired for both pre-clinical radiobiological experiments and detector characterization in order to mimic the clinical standards.

Depth-Dose Measurements

Once the field uniformity was assessed, depth-dose distributions for both the thin and thick ring systems were measured in a water phantom using the Advanced Markus® chamber. The Advanced Markus® chamber used in the R&D room was cross-checked against the one used for clinical practice, which is calibrated against a primary standard. An agreement of 0.5% was observed between the two chambers. To verify the absolute dose uniformity across the field, measurements with the Advanced Markus® chamber were performed at the center of the field and at several points along the x and y direction. Maximum dose rate measurements were conducted along the Bragg peak, and at the midpoint of the SOBP. To enable BP experiments at various depths, dose rates were measured at the entrance, at 80% of the maximum dose proximal to the BP (P80), and at 20% of the maximum dose distal to the BP (D20). The irradiation time ranged between 10 and 60 seconds, and the dose rate was calculated by dividing the total measured dose by the corresponding irradiation time. To fully characterize the total 3D depth-dose distribution across the large field both laterally and longitudinally, the OCTAVIUS Detector 1500XDR was used. Slabs of WE polystyrene (RW3) were placed in front of the detector, and x-y dose profiles were measured at each depth. Larger step sizes (1 cm) were used in the plateau region, while 5 mm steps were employed in the spread-out Bragg peak (SOBP) region. The 3D dose distribution was then reconstructed by calculating the total dose at each depth.

3.2.4 Two Endstations for Radiobiological Experiments

At the R&D experimental proton beamline at HollandPTC, clinically relevant conditions for radiobiological experiments were established. Two unique radiobiological endstations were designed specifically for radiobiological studies:

- A water phantom configuration was developed to enable precise irradiation of cell samples within a 10 $\times$ 10 cm^2 field. In this setup, 3D-printed holders were designed to accommodate either cell culture flasks or well-plates. The holders were mounted on a motorized linear stage, which allowed for movement along the x, y,

and z axes to position the samples at the desired depth within the Bragg Peak (BP) or SOBP. Additionally, the holder includes a slot to position an Advanced Markus® chamber directly behind the cell sample, allowing for real-time dosimetric measurements during irradiation. The BP and SOBP curves were measured using the Advanced Markus® chamber with and without the cell sample in place to determine the corrected water-equivalent thickness of the sample. The configuration for the cell culture flask holder is shown in Figure 3.6.

- A water-equivalent polystyrene (RW3) slab phantom configuration was developed that uses RW3 phantom slabs to achieve the desired BP or SOBP depth for cell sample irradiation. This configuration makes use of a dedicated cell irradiation flipper system designed and built in-house, enabling cells to remain in a horizontal position until just before irradiation. The technical drawings of the system are presented in Figure 3.7. A remote-controlled motor then flips the culture flask to a vertical position when the beam is ready to be delivered. After irradiation, the flask is returned to the horizontal position. This system allows cells to be irradiated either immersed in culture medium or not, with no significant biological impact. Additionally, 3D-printed supports for cell culture flasks, well-plates, and Petri dishes were created to accommodate various sample types for irradiation using this flipper system.

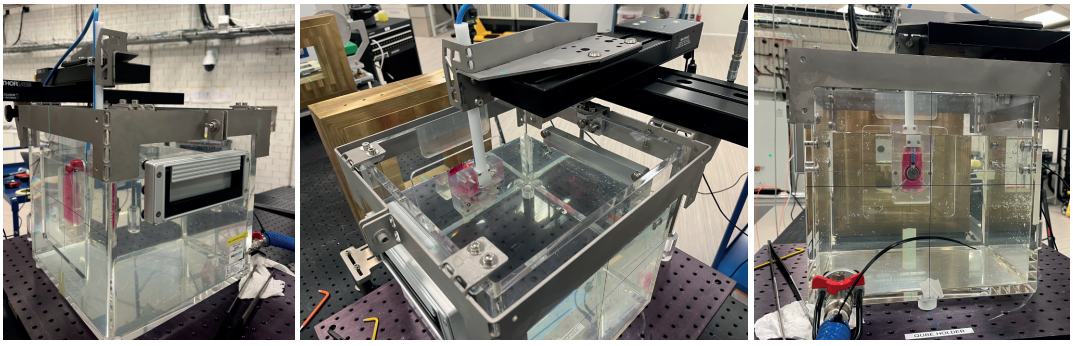

(A) (B) (C)

FIGURE 3.6: The water phantom configuration used for cell irradiations and absolute dosimetry measurements. A cell culture flask with culture medium is placed in the 3D-printed holder, mounted to the motorized linear stages. (A) and (B) show a side and top view of the configuration showing the motorized linear stages and 3D-printed holder, and (C) a view from the back where the Advanced Markus® chamber is visible.

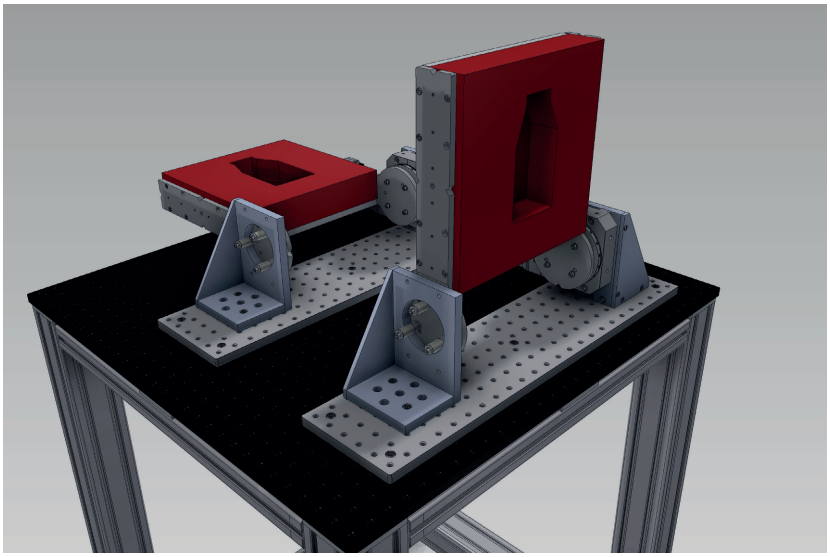

FIGURE 3.7: Three-dimensional technical drawings of the cell irradiation flipper system realized for the HollandPTC R&D experimental proton beamline. The sample holder shown in the drawings is for a T25 cell culture flask. In the figure both the vertical and horizontal positions are shown.

3.3 Results

3.3.1 Pencil Beam Characterization

Beam Spot Size

The beam spot sizes measured at the isocenter with the Lynx® detector for energies ranging from 70 to 240 MeV with 10 MeV steps is shown in Figure 3.8, and are listed in Table 3.2. The beam spot sizes are expressed as the FWHM, obtained from the 2D Gaussian fit on the 2D beam cross-sections (Eq. 3.1). The beam spot size decreases with increasing proton energy due to the reduced effect of multiple Coulomb scattering at higher energies. As proton energy increases, the beam undergoes less scattering in air, leading to a more focused beam and a smaller beam spot size. At lower energies, the beam spot size in the x direction is larger than in the y direction. This asymmetry at the isocenter decreases as the energy increases up to 160 MeV where the asymmetry is 0%, and then increases again for energies greater than 160 MeV. The AS percentages are listed in Table 3.2. Figure 3.9 presents the lateral beam profile in the x direction for energies of 70, 150, and 240 MeV, demonstrating a Gaussian distribution and highlights the decrease in beam spot size at 240 MeV compared to 70 MeV. This effect is also observed when comparing the 2D beam cross-sections, shown in Figure 3.10.

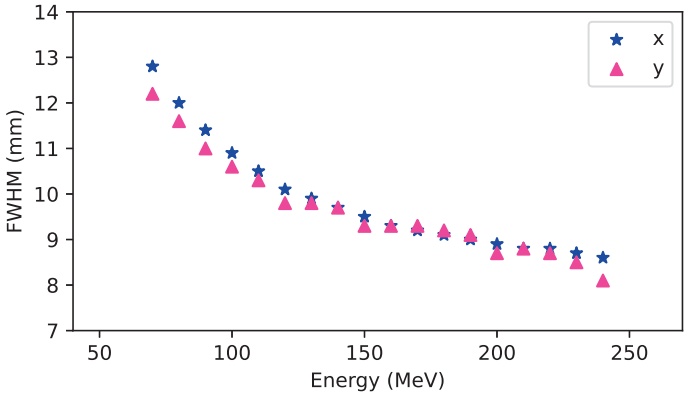

FIGURE 3.8: The beam spot size expressed as the FWHM (mm) in x and y at isocenter, obtained using Eq. 3.1, as a function of nominal beam energy (MeV).

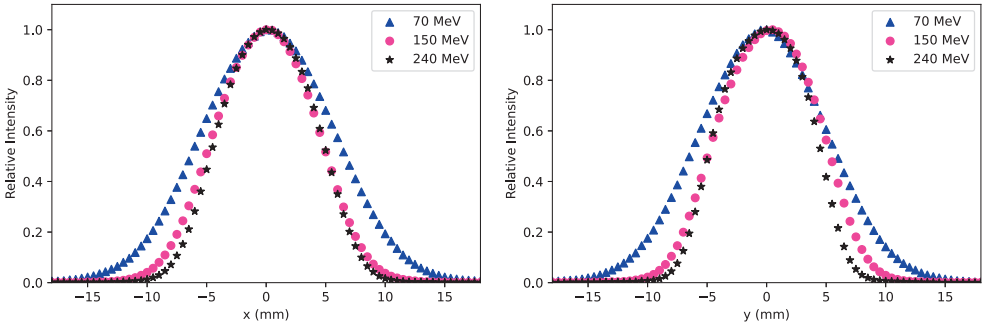

FIGURE 3.9: Lateral profiles at isocenter for the x (left) and y (right) direction for 70, 150 and 240 MeV.

Beam Envelope

Result of the beam envelope measurements for 70, 120, 150, 200 and 240 MeV are shown in Figure 3.11, presenting the beam spot size expressed as the FWHM in the x direction and y direction through air at the seven positions. At lower energies, the beam exhibits a larger beam envelope due to the combined effects of its initially larger spot size and more pronounced multiple Coulomb scattering in air. This scattering causes the beam to diverge more as it travels. At higher energies, the beam envelope is smaller, because higher energy protons undergo less multiple Coulomb scattering, maintaining a more focused trajectory. Furthermore, at all proton energies, the beam spot exhibits the greatest asymmetry ($\pm$12%) at short distances from the Kapton vacuum pipe exit window, with FWHM_x consistently larger than FWHM_y. The beam spot asymmetry decreases

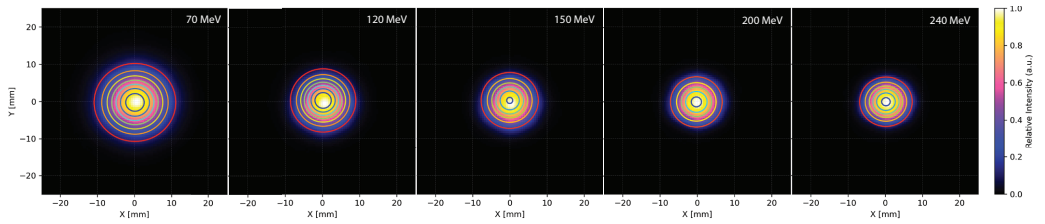

FIGURE 3.10: The 2D beam cross-sections measured at the isocenter with the Lynx® detector at 70, 120, 150, 200 and 240 MeV.

as the beam travels through air, achieving greater symmetry (±1%) around the isocenter (911 mm). However, asymmetry increases again at distances beyond the isocenter (±3%). The observed differences between $FWHM_x$ and $FWHM_y$ suggest the influence of non-linear beam optics, likely caused by the quadrupole magnets along the beamline [133].

Transmission Efficiency

Table 3.2 presents the TE at various energies. TE increases with increasing beam energy due to the configuration of the ESS. To achieve lower energies, such as 70 MeV, the ESS uses a greater amount of degrader material to reduce the beam's energy. This results in increased scattering within the degrader, leading to a higher loss of protons through the beam transport system and a reduction in beam quality. Conversely, at higher energies, the energy degrader is largely retracted, maintaining beam quality more effectively. As a result, the measured beam current at the isocenter more closely resembles the nominal beam current. The variation in TE reflects the corresponding difference in proton flux per 1 nA of nominal beam current at different energies, as shown in Table 3.2. At higher TE values, thus for higher energies, a significantly greater number of protons reach the isocenter, delivering a higher proton flux for the same nominal beam current.

Depth-Dose Distributions

The depth-dose distributions obtained with the Qubenext detector for energies between 70 and 240 MeV with 10 MeV steps are shown in Figure 3.12. The effective energy at isocenter position with respect to the nominal energy at cyclotron extraction is reported in the second column of Table 3.2. Moreover, for 70, 100, 130, 150, 180, 200, and 240 MeV, the peak position, the peak width, the R80 and the peak to plateau ratio were extracted modeling the experimental data with a Bortfeld function [127], reported in Table 3.3. Higher nominal energies lead to deeper proton penetration in water, resulting in

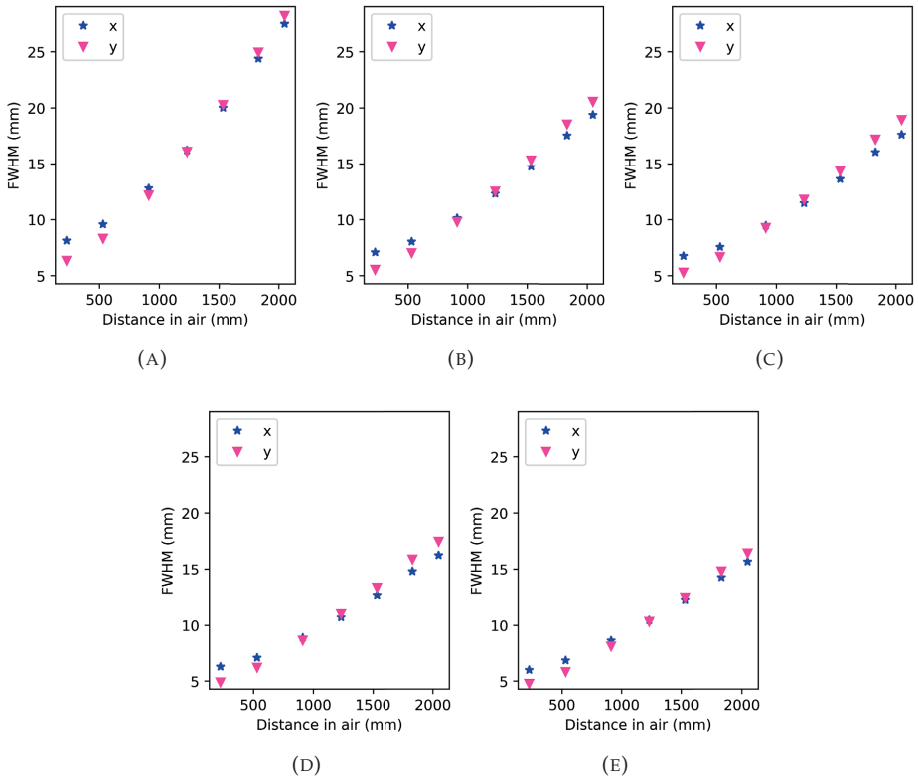

FIGURE 3.11: Beam envelope experimental data. The sigma values extracted from the Gaussian fit expressed in mm are shown as function of depth in air (cm) for (A) 70 MeV, (B) 120 MeV, (C) 150 MeV, (D) 200 MeV, and (E) 240 MeV.

increased R100 and R80 values. The peak width of the depth-dose distribution also increases with energy due to greater energy range straggling at greater depths. At higher nominal energies, the peak-to-plateau ratio of the Bragg curve generally decreases, except for 100 MeV. This occurs because higher energy protons experience increased energy straggling, leading to a broader Bragg peak (Fig. 3.12) and a more pronounced buildup of dose in the plateau region. As a result, the contrast between the Bragg peak and the plateau is reduced.

3.3.2 Double Passive Scattering Characterization

Large Field Uniformity

The two-stage brass collimator system for the dual-ring passive scattering configuration provides field sizes from $2 \times 2\ \text{cm}^2$ up to $20 \times 20\ \text{cm}^2$ with both high and low dose rates.

TABLE 3.2: Values of nominal beam energy E_{nom} in MeV, measured energy at isocenter E_{iso} in MeV, FWHM in x ($FWHM_x$) and y ($FWHM_y$) based on equation 3.1, beam sport asymmetry AS (%) calculated at isocenter, transmission efficiency TE (%) and measured proton flux per nominal 1 nA beam current. TE is reported with its relative error calculated from the standard deviation of the measured values.

E_{nom} (MeV)	E_{iso} (MeV)	$FWHM_x$ (mm)	$FWHM_y$ (mm)	AS (%)	TE (%)	Flux/1nA
70	68.3	12.8	12.2	1.6	0.04±0.0024	$2.44 \cdot 10^6$
80	78.6	12.0	11.6	1.6		
90	88.9	11.4	11.0	1.7	0.071±0.0042	$4.44 \cdot 10^6$
100	99.0	10.9	10.6	1.5	0.114±0.003	$6.86 \cdot 10^6$
110	109.1	10.5	10.3	1.2		
120	119.2	10.1	9.8	0.8	0.16±0.01	$8.91 \cdot 10^6$
130	129.2	9.9	9.8	0.5		
140	139.4	9.7	9.7	0.2		
150	149.3	9.5	9.3	0.3	0.29±0.01	$1.78 \cdot 10^7$
160	159.4	9.3	9.3	0.0		
170	169.4	9.2	9.3	0.5		
180	179.4	9.1	9.2	0.4	0.63±0.01	$3.94 \cdot 10^7$
190	189.4	9.0	9.1	0.4		
200	199.4	8.9	8.7	0.1	1.01±0.02	$7.04 \cdot 10^7$
210	209.4	8.8	8.8	0.0		
220	219.4	8.8	8.7	0.3	1.84±0.02	$1.16 \cdot 10^8$
230	229.3	8.7	8.5	0.7		
240	239.7	8.6	8.1	1.6	5.49±0.26	$3.29 \cdot 10^8$

Figure 3.13 presents the 2D beam cross-sections along with their corresponding intensity profiles through the center x and y direction, for low dose rate field sizes of 4×4 cm^2, 10×10 cm^2 and 20×20 cm^2. The increased intensity at the edges is noticeable, however, the use of a larger aperture compared to the desired field size ensures dose homogeneity is maintained. All generated fields, produced using both the thick and thin ring systems, exhibit large field uniformity levels between 97% and 99%. The uniformity values for all available fields are summarized in Table 3.4.

TABLE 3.3: Parameters derived from the experimental depth-dose distributions measured with the Qubenext detector, fitted through the Bortfeld function: peak position (R100) expressed in cm Water-Equivalent (WE), peak width at R80 in cm WE, range (R80) and peak-to-plateau ratio at 70, 100, 130, 150, 180, 200 and 230 MeV.

E (MeV)	R100 (WE cm)	peak width (WE cm)	R80 (WE cm)	P-E ratio
70	3.62	0.41	3.76	3.9
100	7.29	0.55	7.42	3.7
130	11.66	0.75	12.05	3.9
150	15.04	0.91	15.52	3.9
180	20.87	1.17	21.39	3.7
200	25.25	1.30	25.68	3.6
240	34.28	1.32	34.79	3.7

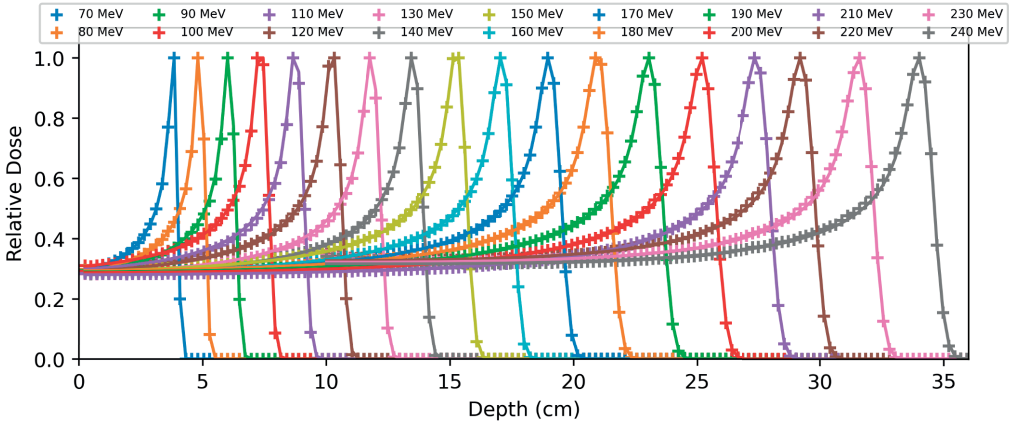

FIGURE 3.12: Depth-dose distributions in water (cm) obtained with the Qubenext detector for energies between 70 and 240 MeV with 10 MeV steps, measured at the isocenter.

TABLE 3.4: Available collimated field sizes and their large field uniformity according to Equation 3.4.

System	Field size (cm^2)	Uniformity (%)
Thick Ring (low dose rate)	2×2	99±1
	4×4	99±1
	10×10	98±1
	16×16	97±1
	20×20	97±1
Thin Ring (high dose rate)	2×2	99±1
	4×4	98±1
	8×8	98±1

Depth-Dose Distributions

The depth-dose distribution of the 150 MeV double passively scattered proton beam was measured in a water phantom (Fig. 3.6) using the Advanced Markus® chamber to record the dose at the center of a 10×10 cm^2 field. The resulting Bragg curve and SOBP curve for both the thin and thick ring systems are presented in Figure 3.14. The R80 of the Bragg curve was measured at 13.79 cm WE for the thin ring and 9.95 cm WE for the thick ring system. The P-E ratio was approximately 3 for both systems. The middle of the SOBP was located at 12.2 cm for the thin ring and 7.5 cm for the thick ring system. The ratio between the mid-SOBP dose value and the entrance value was 1.74 for the thin ring and 1.57 for the thick ring system. The SOBP width was 2.0 cm for the thin ring system with a longitudinal uniformity of 98% and 2.5 cm for the thick ring system with a longitudinal uniformity of 99%.

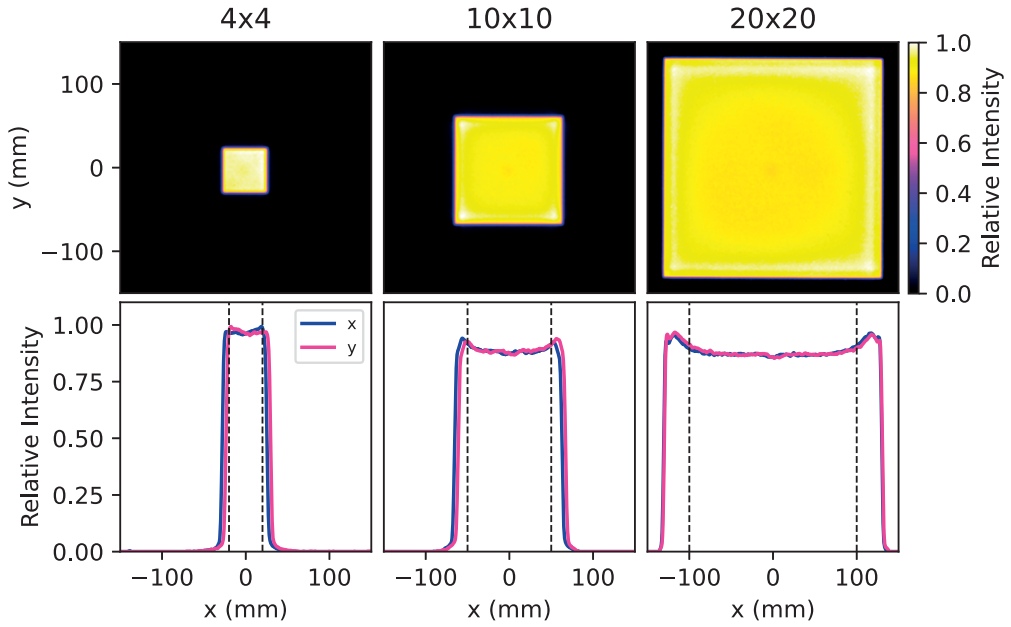

FIGURE 3.13: 2D beam cross-sections of the 150 MeV thick ring double passively scattered proton beam for field sizes of 4 × 4 cm^2, 10 × 10 cm^2, and 20 × 20 cm^2 are shown in the top panel. The intensity of the distributions are normalized to the maximum value. The bottom panel shows the x and y intensity profiles through the center of the large field.

Maximum Dose Rates

For the Bragg curve, for the thin ring configuration, dose rates of 3.8 Gy/min, 10.5 Gy/min, and 2.8 Gy/min were observed at the entrance, P80, and D20 positions, respectively. In contrast, for the thick ring configuration, dose rates of 0.9 Gy/min, 1.9 Gy/min, and 0.5 Gy/min were recorded at the same positions. For the SOBP, the maximum achievable dose rates in the mid-SOBP were found to be 9.9 Gy/min for the thin ring system, while a dose rate of 1.6 Gy/min was found for the thick ring system.

3D Depth-Dose Reconstruction

The 3D depth-dose reconstruction obtained using the OCTAVIUS Detector 1500XDR using RW3 slab phantoms for the thick ring system is shown in Figure 3.15. The beam profiles in x and y were combined, and the total dose was calculated at all depths to generate a 3D relative dose map for the SOBP, clearly visualizing the homogeneous dose region.

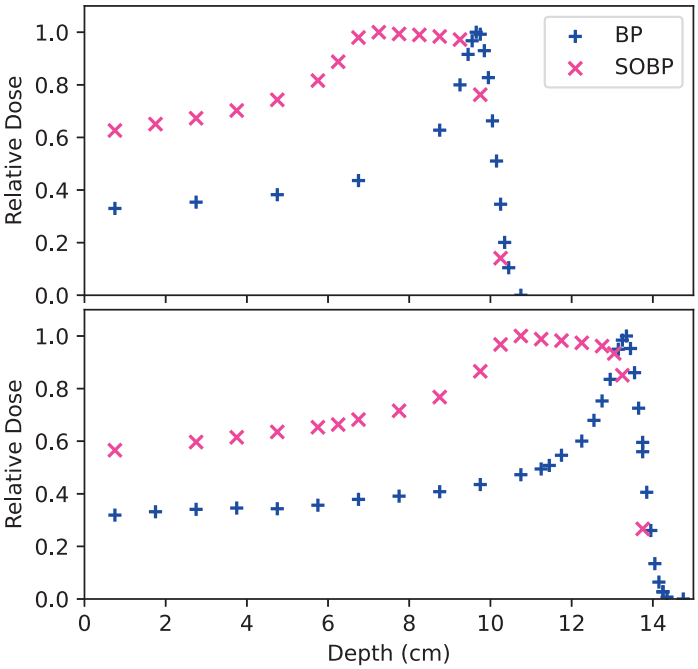

FIGURE 3.14: The 150 MeV double passively scattered BP and SOBP in a water phantom (Fig. 3.6) using the Advanced Markus® chamber at the center of a 10×10 cm^2 field. The top panel shows the result for the thick ring system, and the bottom panel shows the thin ring system.

3.4 Discussion

The characterization of the HollandPTC R&D experimental proton beamline revealed that the pencil beam configuration exhibited a reduction in beam spot size with increasing energy, accompanied by beam asymmetry, which was more pronounced at lower energies. The reduced beam spot size at higher energies is an expected effect of reduced multiple Coulomb scattering in air, which makes the beam more focused. In contrast to other studies where beam profiles were assumed to be symmetric and therefore analyzed using a 1D Gaussian fit [42, 133], this study employed a 2D Gaussian fit to capture the full spatial correlation between the x and y dimensions. This approach provided more accurate FWHM values by modeling the intensity distribution as a function of both x and y. Consequently, it allowed for an elliptical Gaussian representation to account for potential asymmetries in the beam profile. In contrast, fitting separate 1D Gaussians assumes that the x- and y-profiles are independent which can result in a less accurate understanding of the beam spot size. Furthermore, the observed difference between the FWHM$_x$ and FWHM$_y$ in the beam envelope measurements indicated non-linear beam

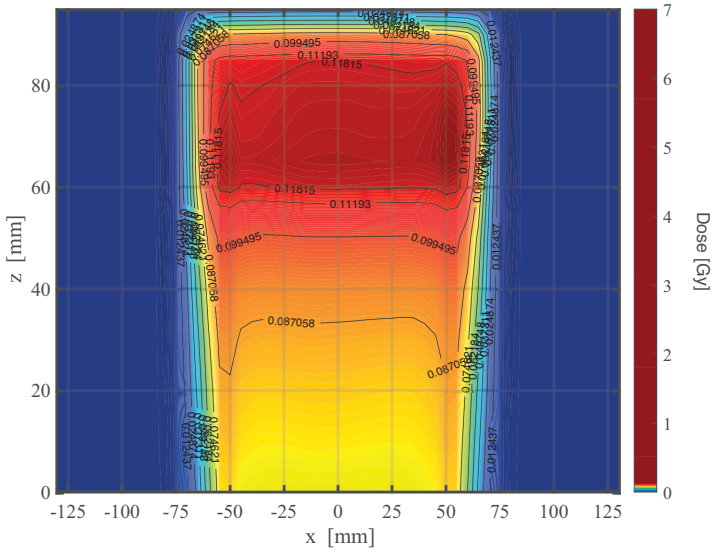

FIGURE 3.15: 3D integrated dose distribution as function of depth in water-equivalent (beam direction expressed in z mm), for the thick ring system. The x (mm) represents the field size around the center of the detector which correspond to the center of the field.

optics, a phenomenon common in proton therapy systems [28]. However, when utilizing a large field for radiobiological experiments, the deviations caused by the beam optics become less significant, as the broadening of the field averages out localized variations.

A fully characterized 150 MeV double passive scattering configuration was developed, which includes a scattering foil and a dual-ring system, based on the concept proposed by Tommasino et al. [43]. While field sizes ranging from 2 $\times$ 2 cm^2 to 20 $\times$ 20 cm^2 can be achieved by varying the brass collimator sizes, the configuration using a 10 $\times$ 10 cm^2 field at an energy of 150 MeV was optimized for radiobiological studies. This configuration demonstrated a field uniformity of 98%, a result that aligns well with studies at other proton therapy facilities [37, 38, 43]. Although the double passive scattering configuration offers great flexibility and versatility, it will not fully match the capabilities of a fully active scanning system. To address this, HollandPTC provides the option of utilizing its clinical gantry for research purposes. This approach enables HollandPTC to combine the advantages of both systems: the passive scattering system's ease of use, simple geometry, and well-defined dosimetry, alongside the benefits of an active scanning system, which fully replicates patient treatment, allows for the use of treatment planning systems, and supports complex geometries. This combination optimizes both practical simplicity and the advanced capabilities required for radiobiological research, making it a valuable tool for experimental studies in proton therapy.

3.5 Conclusion

This chapter presents the characterization of the HollandPTC R&D experimental proton beamline for both pencil beam and double passive scattering configurations. In the pencil beam configuration, the beamline is characterized in terms of beam spot size, beam envelope, beam asymmetry, and depth-dose characteristics, evaluated at various energies and different depths through air. In the double passive scattering configuration, which includes a scattering foil, dual-ring system, and two-stage brass collimation system, the characterization focused on large field sizes, their uniformity and depth-dose profiles. The development of these configurations has enabled the establishment of two specialized biological endstations, which, now fully characterized and tested, are available for high precision physics and radiobiological experiments.

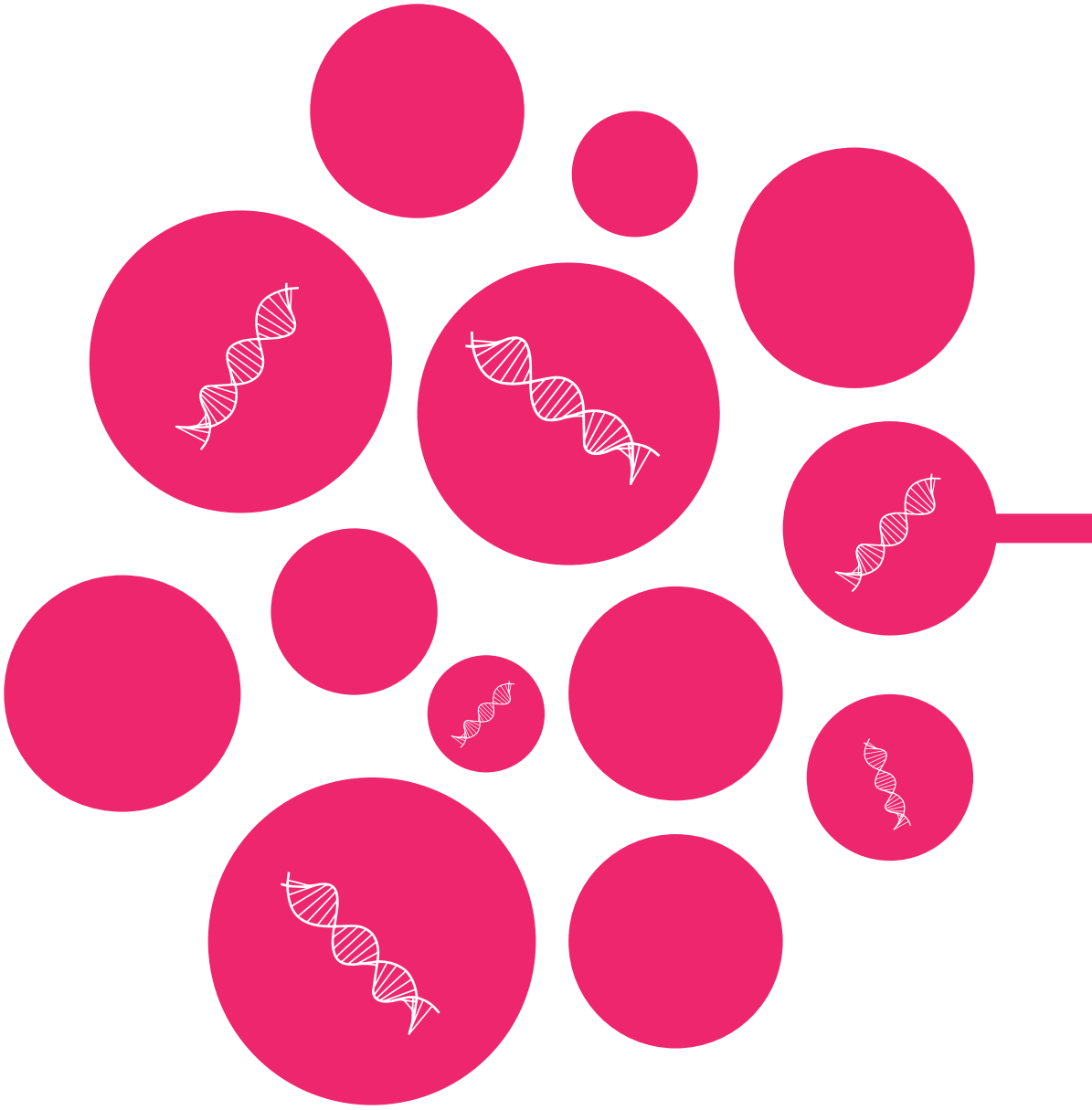

Chapter 4

The Development of a GEANT4 Based Simulation Platform

Parts of this chapter have been published as "Groenendijk, C. F., Rovituso, M., Lathouwers, D., & Brown, J. M. C. (2023). *A Geant4 based simulation platform of the HollandPTC R&D proton beamline for radiobiological studies*. Physica Medica, 112, 102643" [134].

4.1 Introduction

To ensure that every allocated experimental beamtime is used efficiently significant planning, workflow optimization, and pre-irradiation preparation is required. One useful way to ensure that each experimental configuration will yield the desired proton field shape, intensity, and incident energy spectra is to undertake in silico trials through the use of Monte Carlo radiation transport modelling toolkits such as GEANT4 [110, 111, 112], FLUKA [107, 108] and MCNP [105, 106]. This approach is standard for lower energy proton beamlines [135, 136, 137, 138, 139], and has been shown to be crucial for clinical energy proton passive scattering beamlines to enable accurate determination of delivered dose/LET in radiobiological studies [43, 140].

This chapter presents the development of a GEANT4 based simulation platform of the HollandPTC R&D experimental proton beamline (G4HPTC-R&D) to enable the planning, optimization, and advanced dosimetry for radiobiological studies in both a pencil beam and passively scattered field configuration. In contrast to past studies, this work implements a six parameter non-symmetrical Gaussian pencil beam surrogate model to simulate the pencil beam properties with only the ProBeam isochronous cyclotron mean extraction proton energy as input. Section 4.2 describes the development of the G4HPTC-R&D simulation platform and its individual parameter surrogate functions for non-symmetrical Gaussian pencil beam model through optimization with respect to three proton energy experimental datasets, and G4HPTC-R&D's benchmarking with respect to an additional three independent experimental datasets. The results of this process and an accompanying discussion can be found in Section 4.3, with an overall conclusion following in Section 4.4.

4.2 Methods

4.2.1 G4HPTC-R&D Simulation Platform Development

GEANT4 version 10.06.p01 was utilized to develop the G4HPTC-R&D simulation platform based on the experimental geometry of the HollandPTC R&D beamline in its passively scattered field configuration seen in Figure 4.1. A total of eight key geometric elements outlined in Table 4.1 were implemented in G4HPTC-R&D that could be enabled or disabled depending on the beamline operational mode (i.e. pencil beam or passively scattered field configuration). The scattering foil and dual-ring seen in Figure 4.1 facilitate the expansion and shaping of the initial proton pencil beam to generate a uniform intensity proton field. The expanded and shaped beam is collimated at two stages along

its path through the use of a first and second stage variable open cross-section brass collimator to produce square fields of up to 20 × 20 cm^2. At the irradiation/measurement stage where different radiobiological endstations are placed in Figure 4.1, a Lynx® detector (Ch. 3, Sec. 3.2.1) can be seen which is used to assess the shape and quality of the proton field. Finally, an additional geometrical element that is not show in Figure 4.1 was implemented: a water box that mimics the properties of the Qubenext detector (Ch. 3, Sec. 3.2.1). Table 4.1 outlines the dimensions and materials of the different elements, with additional information relating to their design and orientation along the beamline's path outlined in Chapter 3 [126].

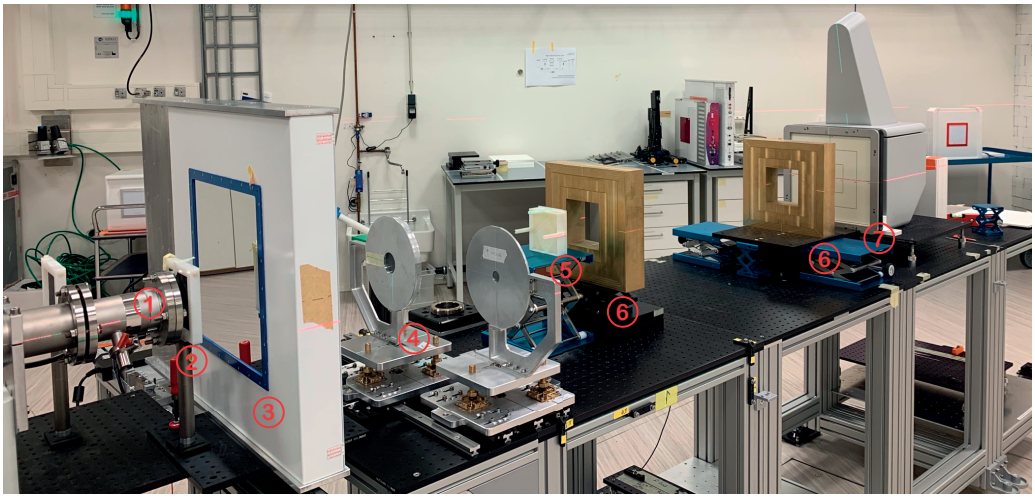

FIGURE 4.1: HollandPTC R&D beamline configured in its passively scattered field configuration. Seven of the eight implemented geometric elements in G4HPTC-R&D to mimic this experimental configuration, and their relative distances with respect to the Kapton vacuum pipe exit window in mm, can be seen in Fig. 3.5. Here the seven of the eight key geometric elements are: (1) the Kapton vacuum pipe exit window, (2) scattering foil, (3) beam monitor, (4) dual-ring, (5) first stage beam defining collimator, (6) second stage beam defining collimator, and (7) the front of the irradiation/measurement stage. Note that a Lynx® detector can be seen at the irradiation/measurement stage, and the Qubenext detector is not shown.

4.2.2 G4HPTC-R&D Proton Pencil Beam Model Optimization

The non-symmetrical Gaussian pencil proton beam of the HollandPTC R&D beamline was implemented in G4HPTC-R&D using a six parameter surrogate model emerging after the Kapton vacuum pipe exit window. These six parameters model three important characteristics of the proton beam at the Kapton vacuum pipe exit window: the 2D Gaussian lateral beam spot size (σ_x, σ_y), the 2D Gaussian beam spot angular deviation (θ_x, θ_y), and the 1D Gaussian energy spread of the cyclotron generated proton beam with initial mean energy E_0 and energy spread ΔE. Through the optimization workflow

outlined in Figure 4.2, a set of individual surrogate functions were developed for each of these parameters to enable the modelling of the Gaussian pencil beam properties using the ProBeam isochronous cyclotron mean extraction proton energy with respect to experimental measurements at 70, 150, and 240 MeV. For each combination of these six parameters and detection media (Lynx® detector or surrogate Qubenext detector water box) investigated with G4HPTC-R&D, a total of 10^6 primary protons were run and the transport of all particles was simulated using a combined GEANT4 "Standard EM Option 4" and "QGSP_BIC_HP" physics list [112, 141] with atomic deexcitation enabled, a particle production range cut of 200 µm, and a low-energy cut off of 250 eV.

TABLE 4.1: Name, dimensions, and materials of the geometric elements that were implemented in G4HPTC-R&D to mimic the experimental configuration seen in Figure 4.1.

Name	**Dimensions**	**Material**
Kapton Vacuum Pipe Exit Window	Disc (diameter,z): 100, 0.125 mm	G4_KAPTON
Scattering Foil	Box (x,y,z): 100, 100, 3.4 mm	G4_Pb
Beam Monitor	Surrogate Box (x,y,z): 400, 400, 0.6 mm	G4_WATER
Dual-Ring	Inner Disc (diameter,z): 45, 5.5 mm Outer Ring (inn., out., z): 45, 200, 16 mm	G4_Pb G4_Al
First Stage Collimator	Box Outer (x,y,z): 220, 220, 70 mm Inner Opening (x,y,z): 120, 120, 70 mm	Brass Cu:Zn:Pb 58%:39%:3% ρ = 8.7 g/cm^3
Second Stage Collimator	Box Outer (x,y,z): 220, 220, 70 mm Inner Opening (x,y,z): 120, 120, 70 mm	Brass Cu:Zn:Pb 58%:39%:3% ρ = 8.7 g/cm^3
Lynx® Detector	Front Box (x,y,z): 300, 300, 1 mm Back Box (x,y,z): 300, 300, 0.5 mm	G4_PLEXIGLASS G4_GADOLINIUM _OXYSULFIDE
Water Box (Qubenext Detector)	Box (x,y,z): 127, 127, 400 mm	G4_WATER

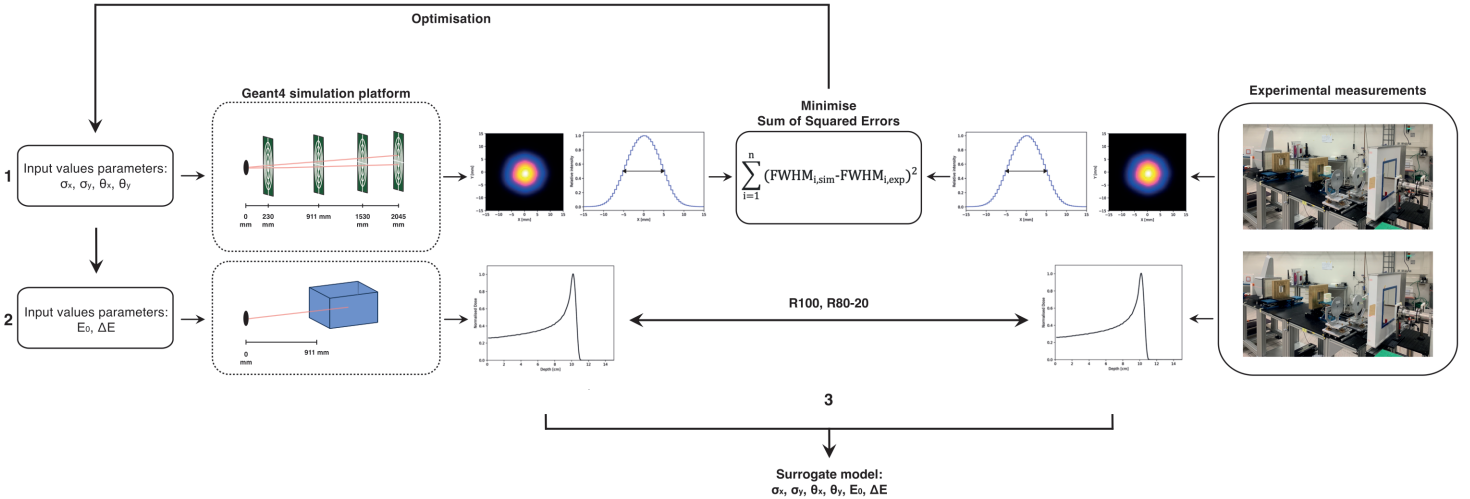

FIGURE 4.2: G4HPTC-R&D simulation platform six parameter non-symmetrical Gaussian pencil beam surrogate model optimization and individual parameter surrogate function mapping workflow with respect to experimental measurement at 70, 150, and 240 MeV. This parameter optimization and individual surrogate function mapping workflow is composed of three stages: (1) lateral beam spot size (σ_x, σ_y) and angular deviation (θ_x, θ_y) optimization with respect to the proton pencil beam envelope cross-sectionals evolution measurements in free air, (2) initial proton beam mean energy (E_0) and energy spread (ΔE) optimization with respect to proton pencil beam depth-dose distributions in water, and (3) mapping of each optimized parameter value to an individual parameter second-order polynomial surrogate function.

Beam Spot Size and Angular Deviation

In the first stage, the lateral beam spot size (σ_x, σ_y) and angular deviation (θ_x, θ_y) were optimized with respect to the proton pencil beam envelope cross-section measured with a Lynx® detector in free air at 230, 530, 911, 1230, 1530, 1830 and 2045 mm down-stream from the Kapton vacuum pipe exit window. Both sets of experimental and simulated Lynx® detector data 2D beam profiles were fitted with a 2D Gaussian function (Eq. 3.1) to obtain the Full Width at Half Maximum (FWHM) in x and y. The Full Width at Tenth Maximum (FWTM) was extracted from the central x- and y-axis planes to investigate the tails of the distributions as a second figure of merit. The agreement between experimental and simulated FWHM values as a function of the pencil beam energy was assessed through the use of the Sum of Squared Errors (SSE) metric:

$$\mathrm{SSE} = \sum_{i=1}^{n=7} (\mathrm{FWHM}_{\mathrm{sim},i} - \mathrm{FWHM}_{\mathrm{exp},i})^2 \tag{4.1}$$

where $\mathrm{FWHM}_{\mathrm{sim},i}$ is the simulated and $\mathrm{FWHM}_{\mathrm{exp},i}$ is the experimental FWHM summed over $n = 7$ distances. Starting with (predefined) initial values for σ_x, σ_y, θ_x and θ_y from Chapter 3, a two-step optimization with the SSE metric was undertaken. In the first step a $\pm$10% offset sweep around initial values was explored, and the combination that resulted in the smallest SSE was selected as an initial estimates for each parameter. A second parameter sweep of all four of the initial estimate for each parameter with a $\pm$5% offset was then undertaken to fine tune and ensure that each parameter value was not a local minimum in the optimization.

Mean Energy and Energy Spread

In the second stage, the two remaining beam parameters (E_0 and ΔE) that modeled the initial mean energy and energy spread of the cyclotron generated proton pencil beam were optimized with respect to the experimental proton pencil beam depth-dose distributions at 70, 150, and 240 MeV. Experimental measurements of the proton pencil beam depth-dose distributions at 70, 150, and 240 MeV were obtained with a Qubenext detector placed at the beam isocenter 911 mm from the Kapton vacuum pipe exit window[1]. Using the optimized lateral beam spot size (σ_x, σ_y) and angular deviation (θ_x, θ_y) values at each energy, the mean energy (E_0) was varied in steps of 0.1 MeV around the ProBeam isochronous cyclotron mean extraction proton energy and the energy spread (ΔE) in $\pm$5 steps of 0.05 MeV with respect to initial estimates taken from Chapter 3 to compare to

[1] The experimental 240 MeV proton pencil beam depth-dose profile was measured with a 100 mm thick and 300 $\times$ 300 mm^2 cross-sectional area slab of water equivalent plastic placed in front of the Qubenext detector.

the experimental proton pencil beam depth-dose distributions. Each proton pencil beam depth-dose profile data was fitted with a Bortfeld function [127], and the position of the 80% dose in the distal falloff (R80), the distance between the distal position of the 80% and 20% dose values (R80-R20 distal fall-off), and peak-to-entrance (P-E) ratio were extracted as figures of merit [142]. Comparison of the simulation and experimental results for these three figures of merit were used to optimise E_0, ΔE, and to provided a general figure of merit.

The set of six parameter values obtained in the first and second stages of the optimization workflow outlined in Figure 4.2 form the basis of the developed individual parameter surrogate functions (third stage). They were solved through the mapping of each parameter value at 70, 150 and 240 MeV to second-order polynomial functions. With these surrogate functions G4HPTC-R&D can model the non-symmetrical Gaussian pencil beam properties at the Kapton vacuum pipe exit window of the R&D beamline with only the ProBeam isochronous cyclotron mean extraction proton energy as input.

4.2.3 G4HPTC-R&D Independent Experimental Benchmarking

The refined non-symmetrical Gaussian pencil beam model and G4HPTC-R&D simulation platform was benchmarked with respect to three independent experimental datasets. Two of these experimental datasets were of the HollandPTC R&D beamline operating in its pencil beam configuration at 120 and 200 MeV, and the other was the HollandPTC R&D beamline operating in its passively scattered field configuration at 150 MeV to generate a 100 $\times$ 100 mm^2 field at the irradiation/measurement stage. Experimental measurements and G4HPTC-R&D simulations were undertaken at 120 and 200 MeV in an identical manner to that outlined above to obtain beam envelope evolution in free air and depth-dose distributions in water datasets. These experimental and simulated FWHM, FWTM, R80, R80-R20 distal fall-off, and P-E ratio results at each energy were compared to assess the validity of the refined non-symmetrical Gaussian pencil beam model and G4HPTC-R&D simulation platform.

Experimental measurement of the 100 mm $\times$ 100 mm field generated at the irradiation/measurement stage for the HollandPTC R&D beamline operating in its passively scattered field configuration was undertaken using the Lynx® detector at 150 MeV. Large field simulations were performed using the parameter values outlined in Table 4.2 (E_0 = 148.8 MeV, ΔE = 1.35 MeV, σ_x = 2.819 mm, σ_y = 2.100 mm, θ_x = 0.0028 rad, and θ_y = 0.0033 rad), with all beam elements implemented as shown in Figure 4.1 and for an inner open cross-section of the final stage beam defining brass collimator set to 100 mm $\times$

100 mm. A total of 4×10^7 primary protons were run, and the transport of all particles was simulated using the same physics configuration outlined above for the pencil beam configuration simulations.

Three figures of merit were utilized to assess the validity of the refined G4HPTC-R&D simulation platform operating in a passively scattered field configuration: (1) the field uniformity U, (2) the γ-index mean value, and (3) the γ-index global pass rate. The field uniformity (U) figure of merit across the field for both the experimental and simulation data was calculated by:

$$\mathrm{U}\,[\%] = \left(1 - \frac{I_{max} - I_{min}}{I_{max} + I_{min}}\right) \cdot 100\% \tag{4.2}$$

where I_{max} is the maximum intensity across the field, and I_{min} is the minimum intensity across the field. It should be noted that a uniformity of above 97% is required for radiobiological experiments [43, 126]. Whereas for the γ-index mean value and global pass rate figures of merit, the γ-index can be written as:

$$\gamma(\mathbf{r_E}) = \min\{\Gamma(\mathbf{r_E}, \mathbf{r_S})\} \forall \{\mathbf{r_S}\} \tag{4.3}$$

with:

$$\Gamma(\mathbf{r_E}, \mathbf{r_S}) = \sqrt{\frac{\Delta r^2(\mathbf{r_E}, \mathbf{r_S})}{\delta r^2} + \frac{\Delta D^2(\mathbf{r_E}, \mathbf{r_S})}{\delta D^2}} \tag{4.4}$$

where $\mathbf{r_E}$ is the spatial location in the experimental field, $\mathbf{r_S}$ is the spatial location in the simulated G4HPTC-R&D field, $\Delta r(\mathbf{r_E}, \mathbf{r_S})$ is the distance between the two locations, $\Delta D(\mathbf{r_E}, \mathbf{r_S})$ is the difference in dose between the two locations, δr is the distance difference criterion, and δD is the dose difference criterion [143, 144]. A total of three different δr and δD criterion combinations were assessed respectively: (1) 3 mm and 3%, (2) 4 mm and 4%, and (3) 5 mm and 5%.

4.3 Results and Discussion

4.3.1 G4HPTC-R&D Proton Pencil Beam Model Optimization

Table 4.2 presents the optimal values for the non-symmetrical Gaussian pencil beam surrogate model parameters σ_x, σ_y, θ_x and θ_y obtained through the optimization workflow outlined in Figure 4.2 at 70, 150 and 240 MeV. In the case of σ_x, σ_y, θ_x, θ_y and ΔE, all of these parameters decrease with increasing initial mean proton energy as expected [145, 146, 147]. Whereas for the E_0, the obtained values are within less than 2%

of the requested ProBeam isochronous cyclotron mean extraction proton energy. This small difference between experimental and G4HPTC-R&D value for the E_0 parameter can be attributed to: (1) generation of the non-symmetrical Gaussian pencil beam spot after the Kapton vacuum pipe exit window, (2) uncertainties in the alignment and the resolution of the Qubenext detector, and (3) uncertainties in relevant GEANT4 proton cross-sectional data and physics models which are on the order of ±10% [141, 147].

TABLE 4.2: Optimized non-symmetrical Gaussian pencil beam surrogate model parameters at 70, 150, and 240 MeV: lateral spread σ in x and y (mm) and angular spread θ in x and y (radians), initial mean energy E_0 (MeV) and energy spread ΔE (MeV).

E (MeV)	σ_x (mm)	σ_y (mm)	θ_x (rad)	θ_y (rad)	E_0 (MeV)	ΔE (MeV)
70	3.383	2.559	0.00371	0.00409	69.8	1.43
150	2.819	2.100	0.00280	0.00330	148.8	1.35
240	2.509	1.890	0.00273	0.00300	235.5	0.80

Beam Spot Size and Beam Envelope

Figure 4.3 presents a comparison between the fitted FWHM and FWTM extracted values from the experimental and G4HPTC-R&D proton pencil beam envelope cross-section measurements in free air at 70, 150, and 240 MeV using the optimal values for σ_x, σ_y, θ_x, and θ_y outlined in Table 4.2. The dotted lines represent a ±5% deviation with respect to experimental results to aid in assessing the accuracy of the G4HPTC-R&D results. For all energies the G4HPTC-R&D FWHM values in both x and y were reproduced to within less than 5% indicating a high level of correlation. With the FWTM values, the G4HPTC-R&D 70 and 150 MeV data is also within 5% of experimental results indicating a high level of correlation. However, at 240 MeV the G4HPTC-R&D 2D proton pencil beam envelope cross-section FWTM values increase as a function of distance in air with the furthest two distances having a difference of up to 9% relative to their respective experimental values. It should be noted that this level difference is still within the established uncertainties in relevant GEANT4 proton cross-sectional data and physics models which are on the order of ±10% [141, 147], and the fact that this difference is still on the order of 5% indicates a high level of correlation between the experimental and G4HPTC-R&D data.

Depth-Dose Distributions

The depth-dose distributions of experimental and G4HPTC-R&D results obtained with these optimized values of Table 4.2 are shown in Figure 4.4, and their corresponding proton range (R80), distal fall-off (R80-R20) and peak-to-entrance (P-E) ratio values are displayed in Table 4.3. The depth-dose distributions are normalized on the maximum

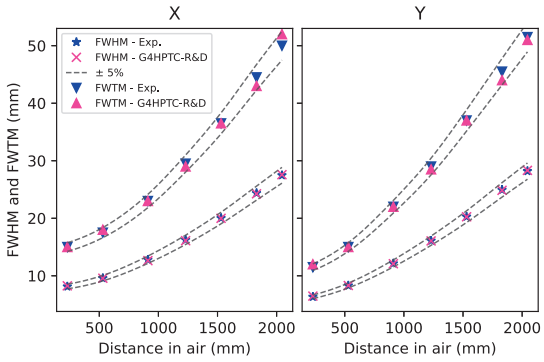

(A)

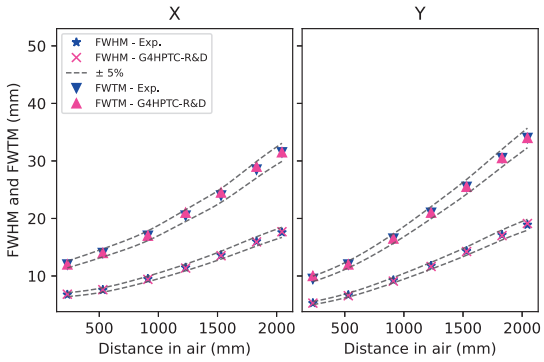

(B)

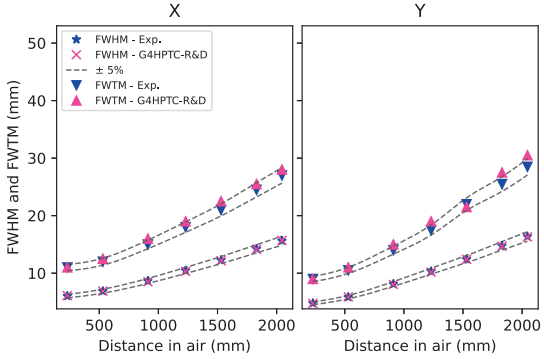

(C)

FIGURE 4.3: Experimental and G4HPTC-R&D 2D beam cross-section FWHM and FWTM values as a function of distance from the Kapton vacuum pipe exit window at (A) 70 MeV, (B) 150 MeV, and (C) 240 MeV. Here error bars representing the accuracy of FHWM data fitting cannot be resolved due to their scale being on the same order as FWHM data symbols.

dose, and show agreement in R80 and R80-R20 to within less than 0.5 mm (or 2%) for all energies. As for the P-E ratio, a difference on the order of 5% can be observed for all three energies. Again given that the difference for all figures of merit are on the order or less than 5%, a high level of correlation is present between the experimental and G4HPTC-R&D depth-dose distributions at 70, 150, and 240 MeV.

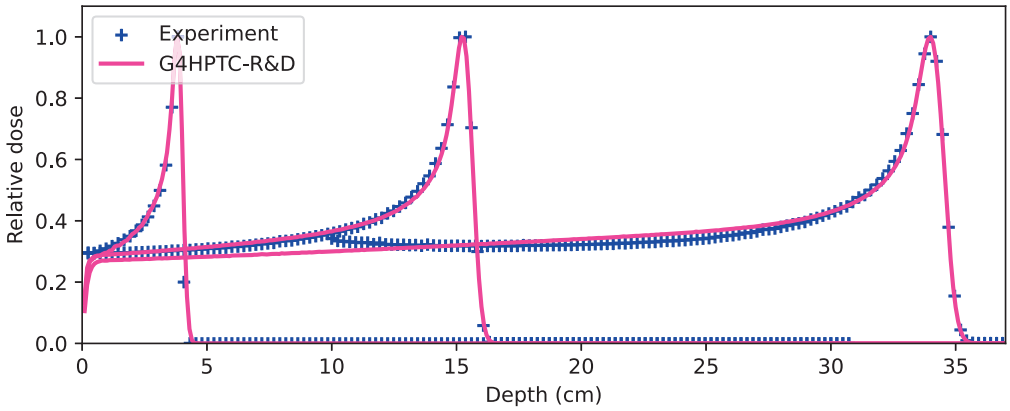

FIGURE 4.4: Experimental and G4HPTC-R&D relative depth-dose distributions in water (cm) at 70 MeV, 150 MeV, and 240 MeV (from left to right).

TABLE 4.3: Proton range R80 (mm), distal fall-off R80-R20 (mm) and peak-to-entrance P-E ratios of the experimental (exp) and G4HPTC-R&D (G4) of the 70, 150, and 240 MeV depth-dose distributions seen in Fig. 4.4.

	R80 (mm)		R80-R20 (mm)		P-E ratio	
E (MeV)	Exp.	G4	Exp.	G4	Exp.	G4
70	39.1	39.6	1.6	2.1	3.4	3.6
150	155.2	155.2	3.8	3.8	3.4	3.4
240	343.6	343.8	5.4	5.0	3.2	3.4

4.3.2 Refined G4HPTC-R&D Proton Pencil Beam Model Independent Experimental Benchmarking

Table 4.4 presents the second-order polynomial function constant values of the six refined non-symmetrical Gaussian pencil beam surrogate model parameters obtained via the optimization workflow outlined in Section 4.2.

Beam Spot Size and Beam Envelope

A comparison between the fitted FWHM and FWTM extracted values from the experimental and refined G4HPTC-R&D proton pencil beam envelope cross-section measurements in free air for a mean ProBeam isochronous cyclotron extraction proton energy of 120 and 200 MeV using these values can be seen in Figure 4.5. As in Figure 4.3, the dotted lines represent a $\pm$5% deviation with respect to experimental results to aid in assessing the accuracy of the G4HPTC-R&D results. Inspection of Figure 4.5 shows that the G4HPTC-R&D FWHM values in both x and y were reproduced to within 5% of the experimental data at 120 and 200 MeV. With the exception of a single outlier in the 120 MeV data at a distance of 1830 mm (7.6% difference in the y), it can be seen that the G4HPTC-R&D FWTM values in both x and y were reproduced again to within 5% of the experimental data at the 120 and 200 MeV.

TABLE 4.4: The second-order polynomial function constant values of the six refined non-symmetrical Gaussian pencil beam surrogate model parameters obtained via the optimization workflow outlined in Section 4.2. Here the second-order polynomial function is written Parameter(E) = $AE^2 + BE + C$ where E is the mean extraction proton energy of the ProBeam isochronous cyclotron.

Parameter	A	B	C
σ_x (mm)	2.121×10^{-5}	-1.172×10^{-2}	4.099
σ_y (mm)	2.003×10^{-5}	-1.014×10^{-2}	3.171
θ_x (rad)	6.234×10^{-5}	-2.509×10^{-2}	5.161
θ_y (rad)	3.848×10^{-5}	-1.834×10^{-2}	5.185
E_0 (MeV)	-1.561×10^{-4}	1.023	-1.151
ΔE (MeV)	2.043×10^{-5}	-3.574×10^{-3}	1.840

Depth-Dose Distributions

The depth-dose distributions of experimental and refined G4HPTC-R&D results for a mean ProBeam isochronous cyclotron extraction proton energy of 120 and 200 MeV are shown in Figure 4.6, and their corresponding proton range (R80), distal fall-off (R80-R20) and peak-to-entrance (P-E) ratio values are displayed in Table 4.5. For the 120 MeV depth-dose distribution data the G4HPTC-R&D R80 value agrees to within 0.5 mm (1%) of the experimental data, and R80-R20 value is the same as the experimental data. Whereas for the 200 MeV depth-dose distribution, the G4HPTC-R&D R80 value is within 1.5 mm (1%) to the experimental data and R80-R20 is on the order of 0.5 mm (11%) less than the experimental data. Furthermore, Table 4.5 also shows that a difference on the order or less than 5% is present in the experimental and G4HPTC-R&D P-E ratio values at both the 120 and 200 MeV.

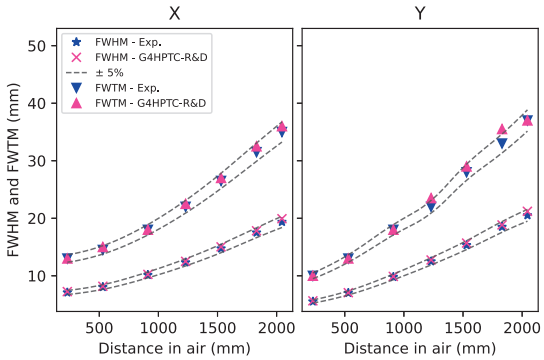

(A)

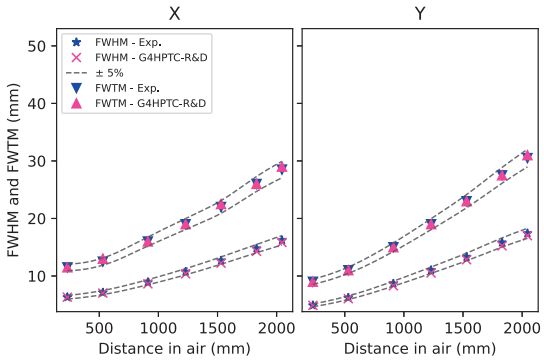

(B)

FIGURE 4.5: Experimental and G4HPTC-R&D 2D beam cross-section FWHM and FWTM values as a function of distance from the Kapton vacuum pipe exit window at (A) 120 MeV, and (B) 200 MeV. Here error bars representing the accuracy of FHWM data fitting cannot be resolved due to their scale being on the same order as FWHM data symbols.

4.3.3 Refined G4HPTC-R&D Large Field Validation

Figure 4.7 presents the experimental and refined G4HPTC-R&D 100 mm $\times$ 100 mm fields and their respective central x-axis lines profiles generated at the irradiation/measurement stage of the HollandPTC R&D beamline operating in its passively scattered field configuration. Both fields appear similar in shape and intensity, with their central x-axis lines profiles illustrating that the maximum difference in between the two is less than 5%. Assessment of the field uniformity in the x-axis yields a value of 97.4% and 96.7%, and in the y-axis yields a value of 97.7% and 96.9% for the experimental and G4HPTC-R&D data, respectively. This less than 1% field uniformity difference in along both axes indicates a good level of agreement between the experimental and G4HPTC-R&D data, and that the field quality is sufficient for radiobiological experiments [43, 126].

TABLE 4.5: Proton range R80 (mm), distal fall-off R80-R20 (mm) and peak-to-entrance (P-E) ratios of the experimental (exp.) and G4HPTC-R&D (G4) of the 120 and 200 MeV depth-dose distributions seen in Fig. 4.6.

	R80 (mm)		R80-R20 (mm)		P-E ratio	
E (MeV)	Exp.	G4	Exp.	G4	Exp.	G4
120	104.7	105.0	3.3	3.3	3.4	3.6
200	255.4	253.9	5.1	4.5	3.5	3.6

Table 4.6 presents the G4HPTC-R&D 100 mm $\times$ 100 mm field γ-index mean and γ-index global pass rate values with respect to the experimental 100 mm $\times$ 100 mm field for three different δr and δD criterion combinations. It can be seen that as the δr and δD combinations increase in value, the γ-index mean value decreases and the γ-index global pass rate increases. Under the most strict δr = 3 mm and δD = 3% criterion combination, the γ-index global pass rate is 96.6% and exceeds the clinically accepted pass rate threshold of 90% for this criterion combination [148, 149]. For δr = 4 mm and δD = 4% the γ-index global pass rate increases to 99.9%, and then to 100% for δr = 5 mm and δD = 5% criterion combination.

These three independent experimental benchmarking trials of the refined G4HPTC-R&D simulation platform illustrated that it is able to reproduce the physical characteristics of the HollandPTC R&D beamline operating in both its pencil beam and passively scattered field configurations to within an acceptable level of agreement for clinical and radiobiological applications. The slight differences observed between the refined

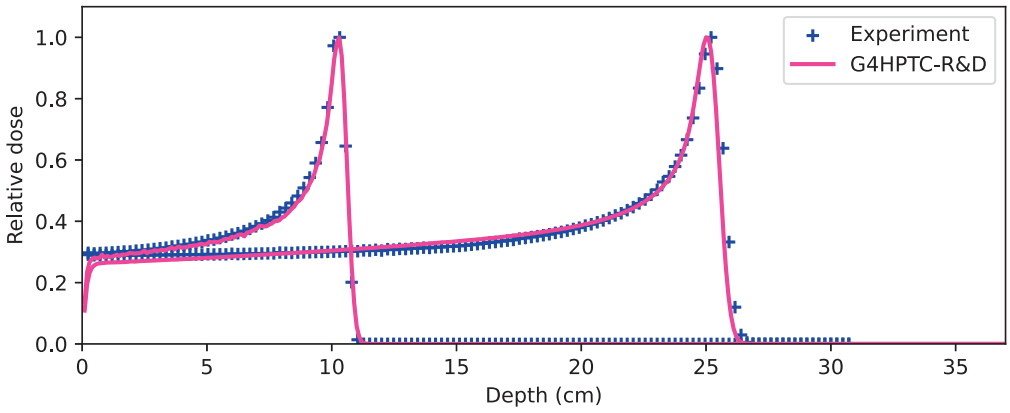

FIGURE 4.6: Experimental and G4HPTC-R&D relative depth-dose distributions in water (cm) at 120 MeV (left) and 200 MeV (right).

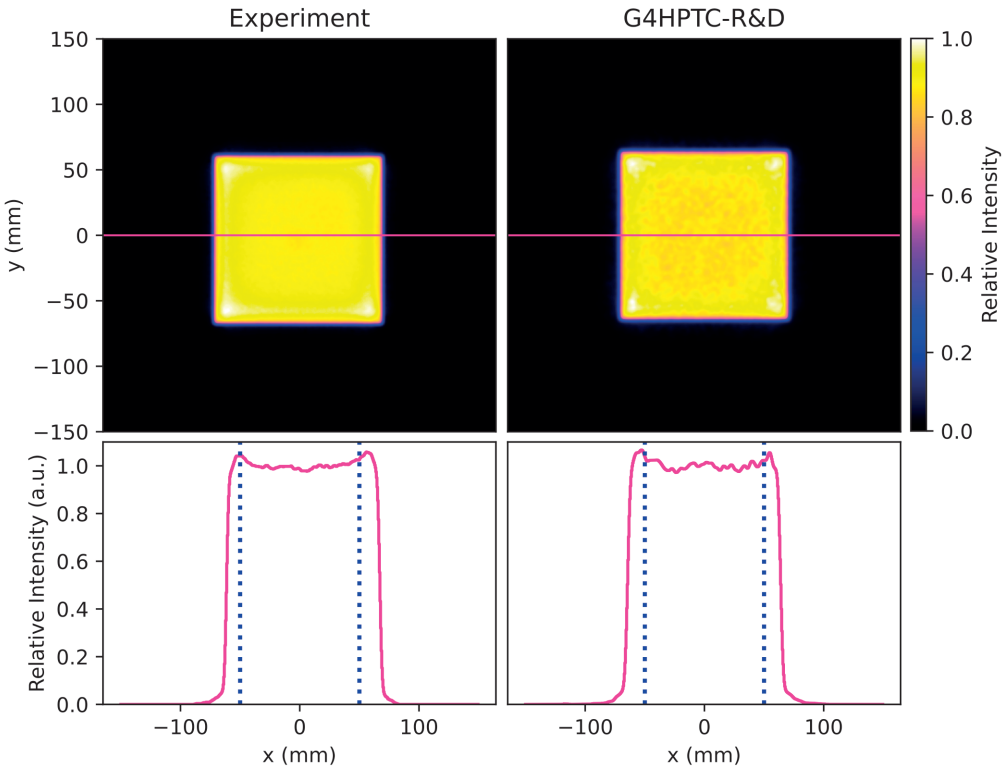

FIGURE 4.7: Experimental and G4HPTC-R&D 100 mm × 100 mm fields (top) and their respective central x-axis line profiles (bottom) generated at the irradiation/measurement stage of the HollandPTC R&D beamline operating in its passively scattered field configuration. The pink horizontal lines (top) represent where the central x-axis lines profiles were taken, and the blue dotted lines outline the target field 100 mm × 100 mm of interest.

G4HPTC-R&D and experimental data for these three independent experimental benchmarking trials can be attributed to two primary factors: (1) uncertainties in the alignment of each beamline element and the resolution of the Lynx®/Qubenext detector, and (2) uncertainties in relevant GEANT4 proton cross-sectional data and physics models which are on the order of ±10% [141, 147]. The impact of beamline geometric element alignment uncertainties is particular relevant in the case of the 100 mm × 100 mm passively scattered field data where misalignment on the level of a millimeter or two can cause excessive "haloing" around the edges of the field. Even under optimal alignment conditions, this "haloing" effect is still present and can be observed in both 2D field maps and central x-axis line profiles seen in Figure 4.7 via the increased in relative intensity at

TABLE 4.6: G4HPTC-R&D 100 mm × 100 mm field γ-index mean and γ-index global pass rate values with respect to the experimental 100 mm × 100 mm field for three different δr and δD criterion combinations.

δr (mm), δD (%)	γ-index mean	γ-index global pass rate
3, 3	0.49	96.6
4, 4	0.36	99.9
5, 5	0.29	100.0

the field edges and corners. Further work is already underway to explore the 3D proton lineal energy distributions at the cell/tissue surface for the different radiobiological endstations under development at the HollandPTC R&D beamline [126].

4.4 Conclusion

This chapter both developed and characterized the performance of a GEANT4 based simulation platform of the Holland Proton Therapy Centre R&D beamline (G4HPTC-R&D) to enable the planning, optimization, and advanced dosimetry for radiobiological studies in both a pencil beam and passively scattered field configuration. It implemented a six parameter non-symmetrical Gaussian pencil beam surrogate model to simulate the R&D beamline in both a pencil beam and passively scattered field configuration. Three different experimental proton datasets (70 MeV, 150 MeV, and 240 MeV) of the pencil beam envelope evolution in free air and depth-dose distributions in water were used to develop a set of individual parameter surrogate functions to enable the modelling of the non-symmetrical Gaussian pencil beam properties with only the ProBeam isochronous cyclotron mean extraction proton energy as input. This refined beam model was then benchmarked with respect to three independent experimental datasets of the R&D beamline operating in both a pencil beam configuration at 120 and 200 MeV, and passively scattered field configuration at 150 MeV. It was shown that the G4HPTC-R&D simulation platform can reproduce the pencil beam envelope evolution in free air and depth-dose distributions to within an accuracy on the order of $\pm$5% for all tested energies, and that it was able to reproduce the 150 MeV passively scattered field to the specifications need for clinical and radiobiological applications.

Chapter 5

3D Microdosimetric Characterization for Proton Energy Deposition Analysis

Parts of this chapter have been submitted as "Groenendijk, C. F., Tran, L. T., Rosenfeld, A. B., Rovituso, M., Van Burik, W., Lathouwers, D. & Brown, J. M. C. (2025). *3D Microdosimetric Characterization of the Double Passive Scattering Proton Beamline at the Holland Proton Therapy Centre*. Physics in Medicine and Biology."

5.1 Introduction

To understand varied biological outcomes and predict future cellular responses, accurate knowledge of cellular-level energy deposition patterns at the specific locations of irradiated tissues and cells throughout the Bragg curve is essential [150, 151, 152]. This work presents a novel spectral unfolding approach to analyze cellular-level energy deposition spectra, aiming to establish a 3D-LET classification system for various biological endstations at HollandPTC. Mapping LET in 3D offers a novel contribution to the scientific community by enabling more accurate and comprehensive evaluations of proton therapy's biological effects. Furthermore, the use of a double passively scattered Bragg peak in combination with 3D-LET exploration has not been studied before, making this study a significant contribution to the field of proton therapy and radiobiology. To establish the 3D-LET classification system, a combined experimental and simulation approach is employed. Data obtained using a high-resolution solid-state 3D silicon-on-insulator (SOI) Mushroom microdosimeter [97, 98, 153, 154] informs G4HPTC-R&D, enabling validation against experimental measurements. Validation is conducted at the three distinct positions along the BP, with subsequent mapping between these data points performed through simulations.

Despite the crucial role of detectors in microdosimetry, all detectors face limitations including low limit detection thresholds due to noise. These thresholds hinder the accurate capture of low-energy depositions in the microdosimeter's sensitive volumes (SVs), leading to a loss of spectral information and thus limiting precise analysis of energy deposition patterns. Furthermore, count losses due to pile-up, a common issue in all detector systems, further affect the measured energy spectra by the microdosimeter. Finally, the use of multichannel analyzers (MCAs) to obtain the radiation spectra results in binning spectral data into discrete intervals, causing the loss of actual energy spectral details and limiting the assessment of the true energy deposition spectrum. By addressing these detector constraints, the spectral unfolding approach offers a more accurate representation of the true energy deposition spectra at various depths and positions within the passively scattered proton beam. As a result, the novel 3D-LET classification system at HollandPTC enables precise assessment of spectra, thereby improving predictions of future biological outcomes.

This chapter presents the development of a 3D-LET classification system, achieved through microdosimetric spectral unfolding to map LET in three dimensions across two biological endstations at HollandPTC. This work aims to enhance the understanding of energy deposition patterns at the cellular level in proton therapy. Section 5.2 details

the LET characterization of the two biological endstations, including the experimental configurations and validation using G4HPTC-R&D. Additionally, the methodology for spectral unfolding and pile-up correction is introduced. Section 5.3 presents the results of the microdosimetric spectral unfolding of both endstations, along with the derived LET spectra. The chapter concludes with a discussion and conclusion of the findings in Section 5.4 and 5.5, respectively.

5.2 Methods

As detailed in Chapter 3, HollandPTC offers two unique and essential configurations for radiobiology studies: a water phantom configuration for positioning cell culture flasks in a water bath within a 10 $\times$ 10 cm^2 field, and water-equivalent polystyrene (RW3) slab phantom configuration for positioning cell culture plates in the same field size. The RW3 configuration includes a flipper system which allows the plates to be flipped back horizontally after vertical irradiation (Fig. 3.7). This possibility enables the irradiation of cells in a dry-state, with a minimal layer of medium present in the wells to ensure that the cells remain in a nutrient-rich environment before and after irradiation. Using the SOI Mushroom microdosimeter, which measures the lineal energy distribution in cell-sized volumes $\overline{y_D}$, was characterized across x, y, and through z (3D-$\overline{y_D}$). In the water phantom configuration, $\overline{y_D}$ was characterized along the BP (z) only (1D-$\overline{y_D}$). The validation in both configurations was conducted at three distinct positions along the BP: the plateau region, P_{36} (36% proximal to the maximum dose), P_{80} (80% proximal to the maximum dose), and D_{20} (20% distal to the maximum dose). Precise positions were determined through depth-dose measurements to ensure accuracy in these locations.

5.2.1 HollandPTC R&D Beamline and the G4HPTC-R&D Simulation Platform

The experimental setup of the HollandPTC R&D proton beamline was constructed in a double passively scattered configuration optimized for 150 MeV proton beams to achieve a 10 $\times$ 10 cm^2 field with a homogeneous dose distribution across the entire field. The use of a scattering foil and dual-ring expand the initial 150 MeV proton pencil beam and create a uniform field that gets shaped along its trajectory using a two-stage collimation system. This produces a field of 10 $\times$ 10 cm^2 at the irradiation stage, where various radiobiological endstations are positioned (Figure 5.1a). Full details of this experimental configuration and characterization can be seen in Chapter 3. G4HPTC-R&D was benchmarked experimentally within $\pm$5% to clinically relevant proton energies by employing a six parameter non-symmetrical Gaussian pencil beam surrogate model to accurately

replicate the R&D beamline in both pencil beam and double passively scattered field configurations (Ch. 4). The implementation of the experimental geometry used in this study for G4HPTC-R&D is illustrated in Figure 5.1b.

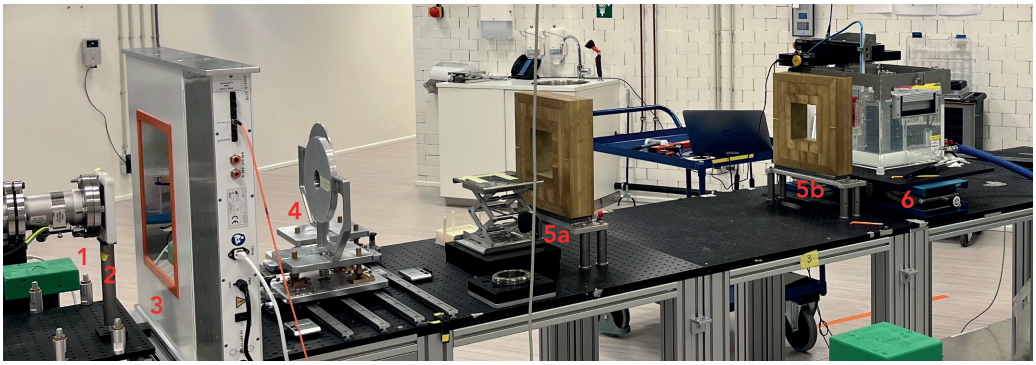

(A)

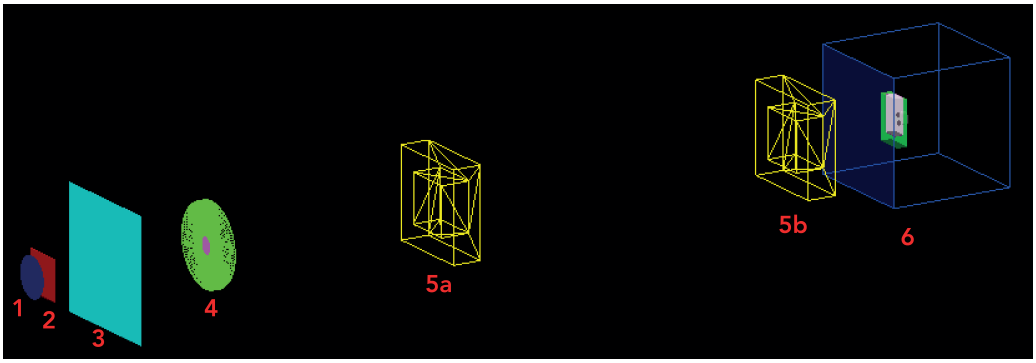

(B)

FIGURE 5.1: (A) A visual representation of the HollandPTC R&D proton beamline in its double passive scattering configuration optimized for 150 MeV proton beams. (B) The representation of the experimental geometry in the G4HPTC-R&D simulation platform [134]. The beamline elements are 1. Kapton vacuum pipe exit window, 2. Scattering foil, 3. Beam monitor, 4. Dual-ring, 5a. First stage beam defining collimator, 5b. Second stage beam defining collimator, 6. Irradiation/measurement stage with in this configuration a water phantom.

5.2.2 1D-$\overline{y_D}$ Characterization: Water Phantom Configuration

1D-$\overline{y_D}$: Experimental Configuration

The water phantom configuration is utilized to irradiate cell cultures in a cell culture flask at different positions along a passively scattered Bragg peak to study variability in biological outcomes. In this configuration, a water phantom ($30 \times 30 \times 30$ cm^3) filled with distilled water positioned at a distance of 2141 mm from the Kapton vaccuum

pipe exit window was utilized containing motorized linear stages facilitating movement in the z-direction. To ensure correct position of the flask along the Bragg peak, dose measurements were performed using an Advanced Markus® ionization chamber of type 34045 (Sec. 3.2.1). Through the fabrication of a custom 3D-printed holder, shown in Figure 5.2a, the Advanced Markus® chamber was positioned against the back wall of the flask. This configuration allowed for continuous dose monitoring directly behind the flask throughout the experiment.

Depth-Dose Measurements Both the flask and Advanced Markus® chamber were accommodated as shown in Figure 5.2b, altogether being able to move through the water phantom along z with sub-millimeter steps. Alignment was achieved using the room laser system in x and y to ensure that the center of the Advanced Markus® chamber aligned with the center of the 10×10 cm^2 field and is illustrated in Figure 5.3a. Additionally, the holder was placed against the phantom wall to ensure the incident beam entered the flask perpendicularly. Subsequent measurements were undertaken at various positions to acquire the complete depth-dose distribution throughout the water phantom and capture the P_{36}, P_{80} and D_{20} positions.

Microdosimetric Measurements A second 3D-printed holder was fabricated to hold the flask in the exact same position as described above, now with the μ^+ probe, housed within a watertight aluminum-coated PMMA sheath, placed behind it to be able to obtain lineal energy values (Figure 5.2c). The positioning of the holder containing both the flask and the sheath with the μ^+ probe can be seen in Figure 5.2d. Optimizing the holder's position in x and y ensured that the center of the μ^+ probe's detecting area aligned with the center of the 10×10 cm^2 field (Figure 5.3d) and the incident beam entered the flask perpendicularly. Figure 5.5a illustrates the 1D-$\overline{y_D}$ experimental configuration, showing the setup where the holder, containing the flask and μ^+ probe, is positioned within the water phantom. Three measurements were undertaken at P_{36}, P_{80} and D_{20} taking into account water-equivalent thicknesses of the phantom wall, protective PMMA cap of the Advanced Markus® chamber, water in between the flask and sheath, and the entrance window of the sheath to achieve equivalent effective points.

1D-$\overline{y_D}$: GEANT4 Simulations

The G4HPTC-R&D simulation platform (GEANT4 version 10.06.p01) [111, 112, 141], was utilized for conducting both depth-dose and microdosimetric simulations. In all simulations, the parameter values as outlined in Table 4.2 (E_0 = 148.8 MeV, ΔE = 1.35 MeV,

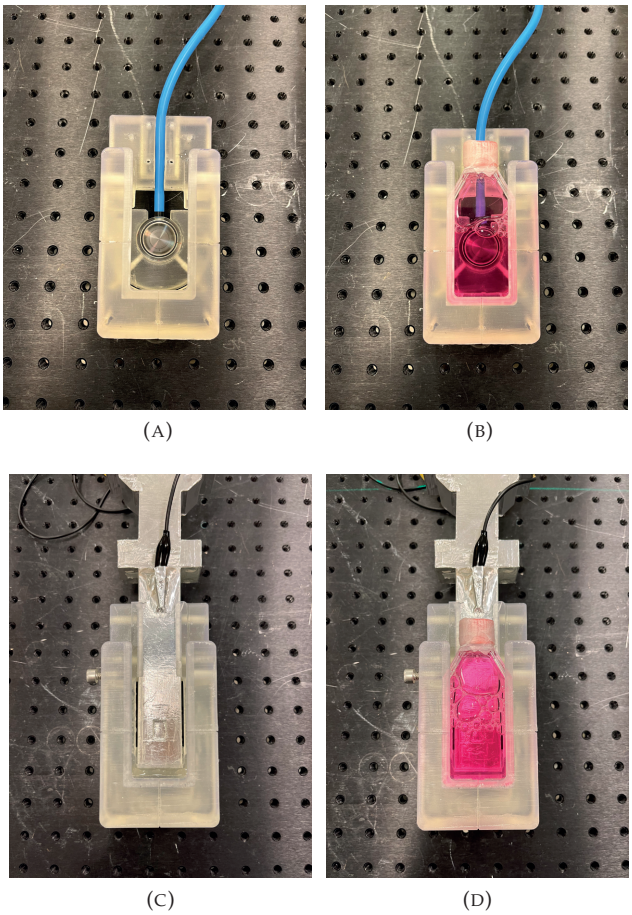

(A) (B)

(C) (D)

FIGURE 5.2: Two custom designed 3D-printed holders. (A) The holder that accomodates the Advanced Markus® chamber directly behind the cell culture flask, together shown in (B).(C) The holder that accommodates the μ^+ probe housed within a watertight aluminum-coated PMMA sheath, with the flask positioned in front of the sheath shown in (D).

σ_x = 2.819 mm, σ_y = 2.100 mm, θ_x = 0.0028 rad, and θ_y = 0.0033 rad) were used to define the proton source. Further information regarding simulation input parameters and beamline element characteristics can be found in Chapter 4 [134].

Depth-Dose Simulations The water phantom of 30 × 30 × 30 cm^3 was implemented with distilled water (ρ = 0.9982 g/cm^3). A cell culture flask (50 ml, Greiner) of polystyrene was modeled consisting of cell medium (10% FBS, ρ = 1.009 g/cm^3) surrounded by the 3D-printed material (clear resin). The Advanced Markus® chamber was implemented containing a 0.87 mm waterproof protective PMMA cap (ρ = 1.19 g/cm^3), a 0.4 mm thick

air cavity (ρ = 1.20 mg/cm^3), and a 0.03 mm polyethylene entrance foil (ρ = 0.92 g/cm^3) [155]. Each component had a diameter of 9 mm, followed by a 1 mm air cavity with a diameter of 2.5 mm ending with a disc-shaped graphite collecting electrode with a thickness of 0.03 mm (ρ = 0.44 g/cm^3). Encompassed by a 0.37 mm layer of air and a 2 mm guard ring, the air cavity and graphite collecting electrode formed the scoring volumes with the effective point of measurement situated 1.015 mm behind the protective cap. The simulated assembly comprising the holder, flask, and Advanced Markus® chamber is illustrated in Figure 5.3b with a close-up of the Advanced Markus® chamber implementation shown in Figure 5.3c. The assembly was moved as a single object throughout the water phantom (*z*-axis) whereupon simulations were performed using 10^7 protons at each experimental Advanced Markus® chamber position to obtain the depth-dose distribution. The "QGSP_BIC_HP" physics list was utilized combined with the "standard EM Option 4" [112, 141] with a low-energy cutoff of 100 eV and a particle production range cut of 0.01 µm. Subsequently, the deposited energy within the scoring volumes of the simulated Advanced Markus® chamber was compared to the dose values obtained in the experimental measurements.

Microdosimetric Simulations The incorporation of the μ^+ probe into G4HPTC-R&D was executed following the full 3D design of the SOI Mushroom microdosimeter to accurately mimic the experimental response. Figure 5.4a shows a photo of the microdosimeter used in this work, captured under a microscope to reveal the detailed structure of the 1520 (38 $\times$ 40) SVs. The implementation of these SVs into G4HPTC-R&D is depicted in Figure 5.4b. A closer examination of the array of cylindrical SVs shows the n^+ and p^+ electrodes (Fig. 5.4c), along with the other components of the individual SVs, as detailed in Figure 5.4d and outlined in Section 2.4. Additional components including the DIL package, probe, and sheath were also integrated into G4HPTC-R&D to further enhance the accuracy of G4HPTC-R&D. The whole simulated assemby, featuring the holder with the flask and μ^+ probe, is depicted in Figure 5.5b. Figure 5.5c shows the measurement point (position 1) which is the center of the 10 $\times$ 10 cm^2 field.

To acquire the energy deposition spectra and corresponding lineal energy spectra, a two-phase simulation approach was conducted to reduce computing time and increase statistics. In the first phase, the incident proton kinetic energies across the 10 $\times$ 10 cm^2 field were scored directly behind the back wall of the flask using 10^8 protons at P_{36}, P_{80} and D_{20}. Subsequently, an area three times the dimensions of the microdosimeter's detecting area was generated and used as squared input source in the second phase simulation located behind the back wall of the flask. This new input source location

was chosen to obtain charged particle equilibrium while traveling through water before reaching the detector. A probability density function was generated from the incident proton kinetic energy spectrum at position 1 and used as energy input array. The momenta of incident protons were determined in x and y and utilized as input parameters too. The second phase simulation employed the physics lists used in previous works [98, 100, 153] with G4EmStandardPhysics_option4 physics list for modeling electromagnetic interactions, *G4IonBinaryCascadePhysics* to describe hadronic interactions,

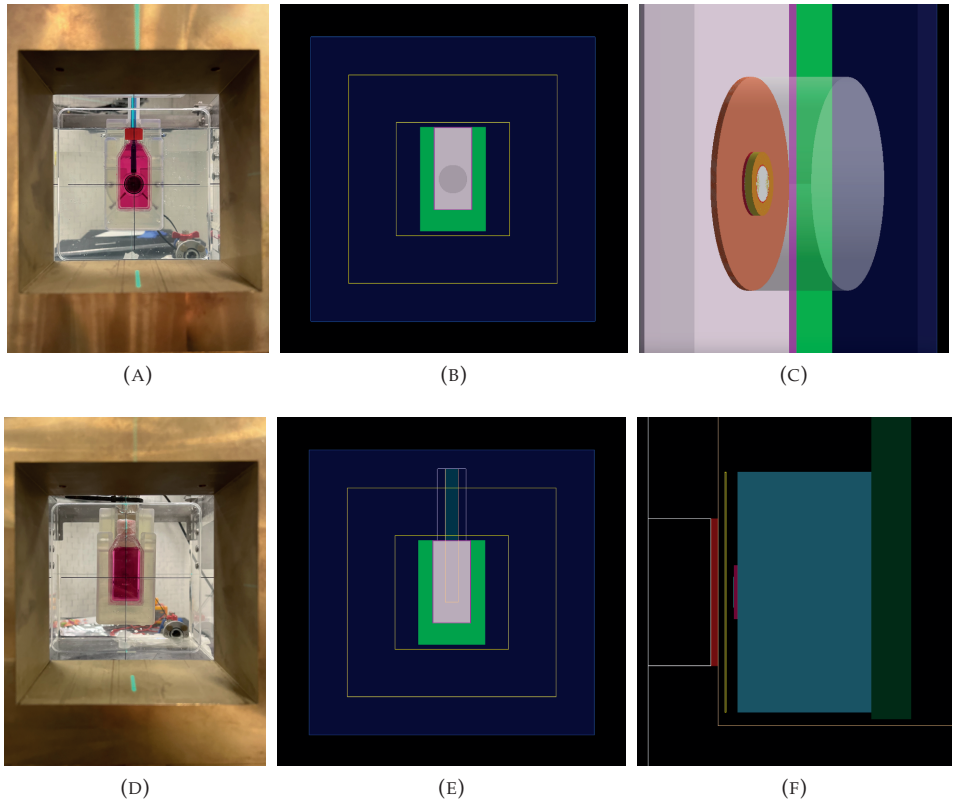

(A) (B) (C)

(D) (E) (F)

FIGURE 5.3: (A) Front-view through the second brass collimator of the holder featuring the flask and Advanced Markus® chamber in the water phantom, aligned with the room laser system in x and y. (B) Front-view of the same components implemented into G4HPTC-R&D showing the water phantom (dark blue), brass collimator contour (yellow), 3D-printed holder (green), flask walls (pink), cell medium (white) and Advanced Markus® chamber (gray). (C) A zoomed-in illustration of the Advanced Markus® chamber showing the elements including the waterproof protective PMMA cap (peach), air cavity (red), entrance foil (white), air cavity (yellow), graphite collecting electrode (white) surrounded by air (red) and guard electrode (orange). (D) Front-view of the holder featuring the flask and sheath in the water phantom, aligned in the center of the 10×10 cm^2 field. (E) Front-view of the same components implemented into G4HPTC-R&D. (F) A zoomed-in illustration of the watertight PMMA sheath contour with PMMA window (red), high-density polyethylene film (yellow), microdosimeter (pink) attached to the DIL package (blue) on the probe (green).

and *G4HadronElasticPhysicsHP* and *G4HadronPhysics* using *QGSP_BIC_AllHP* were used to describe the elastic and inelastic scattering of hadrons, respectively. The neutron High Precision (HP) model was employed to describe neutron interactions of energies up to 20 MeV. Finally, the energy depositions per proton within the silicon sensitive volumes were scored and summed using 10^7 protons per position, resulting in a collection of energy depositions. These values were then binned into a histogram based on the bin structure of the MCA (MCA-8000D, Amptek) used in the experimental configuration, together with the employment of the low limit detection threshold. From this histogram of binned energy depositions, the energy values corresponding to each bin center were extracted to realize the lineal energy spectrum (Ch. 2.4.3).

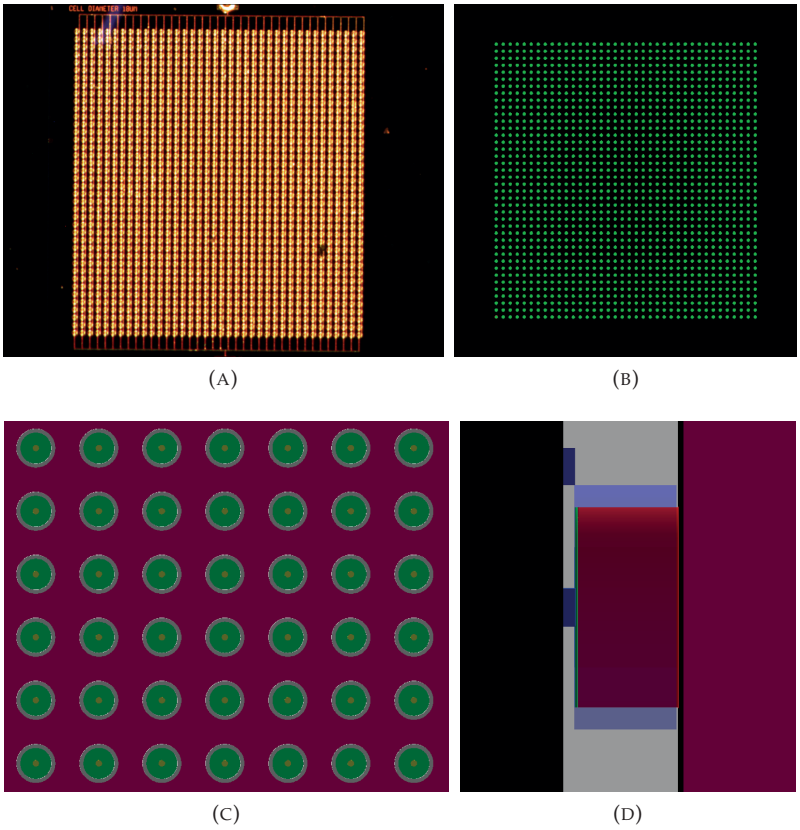

(A) (B)

(C) (D)

FIGURE 5.4: (A) Photo of the SOI Mushroom microdosimeter under the microscope. (B) The implementation of the microdosimeter into G4HPTC-R&D, with (C) a closer view of the array of cylindrical sensitive volumes, and (D) a side-view of a single sensitive volume.

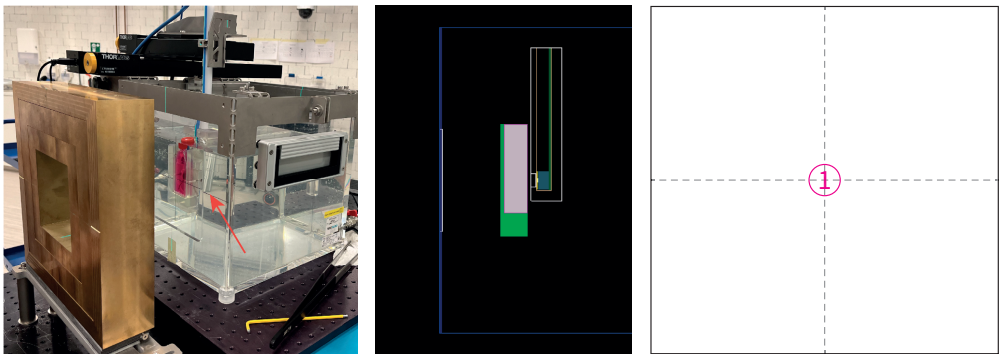

(A) (B) (C)

FIGURE 5.5: (A) A visual representation of the water phantom configuration and its linear stages holding the flask and μ^+ probe, positioned 12 cm away from the second stage beam defining collimator. (B) A side view of the implementation into G4HPTC-R&D: dark blue square is the water phantom, the holder in green with the flask walls in pink consisting of cell medium in gray. Behind, the PMMA sheath encompassing the μ^+ probe. And (C) the measurement position (1) within the 10 $\times$ 10 cm^2 field.

5.2.3 3D-$\overline{y_D}$ Characterization: RW3 Slab Phantom Configuration

3D-$\overline{y_D}$: Experimental Configuration

The RW3 slab phantom configuration was specifically used to irradiate cells in culture plates in a dry-state. To address this challenge, a 3D-printed flipper system (Fig. 3.7) was constructed to securely hold the plates in a horizontal orientation prior to irradiation, ensuring that a small layer of medium remains in the wells to keep the cells in a nutrient-rich environment. When the flipper system is rotated to a vertical orientation, the medium shifts to the bottom of the wells, leaving the cells dry. This ensures that the cells are not submerged during irradiation, which can be critical for certain experimental conditions. This configuration incorporated water-equivalent RW3 slab phantoms (PTW Freiburg, Germany), positioned at a distance of 2141 mm from the Kapton vaccuum pipe exit window, therefore replicating positions along the depth-dose distribution. The slabs' thicknesses ranged from 1 mm to 10 mm, facilitating incremental measurements with millimeter precision.

Depth-Dose Measurements The depth-dose distribution was determined by placing the OCTAVIUS detector 1500XDR (Sec. 3.2.1) behind various thicknesses of RW3 slabs, thereby measuring the dose across the 10 $\times$ 10 cm^2 field. The μ^+ probe, housed in its PMMA sheath, was mounted on two linear stages capable of moving in both x and y. The μ^+ probe was placed closely against the RW3 slab phantom and aligned with the

center of the 10 × 10 cm^2 field (position 1), as depicted in the side view seen in Figure 5.6a.

Microdosimetric Measurements To examine $\overline{y_D}$ in three dimensions, various locations in the middle and only right part of the 10 × 10 cm^2 field were selected assuming homogeneity across the field and are illustrated in Figure 5.6c. The locations were selected based on the dimensions of the well plate and the anticipated positions of cells within the large field, ensuring that the irradiation field accurately covered the regions where cells were most likely to be situated. Measurements were performed in the exact manner as was done in the 1D-$\overline{y_D}$ configuration and the acquired energy deposition spectra at these six locations were then utilized to derive the lineal energy spectra at each respective location. This process was repeated for P_{36} (30 mm RW3), P_{80} (96 mm RW3), and D_{20} (104 mm RW3), while maintaining a brass-to-RW3 distance of 12 cm.

3D-$\overline{y_D}$: GEANT4 Simulations

Depth-Dose Simulations To obtain the depth-dose distribution using G4HPTC-R&D, a 0.5 mm thick 10 × 10 cm^2 slab of water was simulated behind the RW3 slabs to mimic the response of the OCTAVIUS detector, and the deposited energy was scored and compared to the measured values. The water-equivalent RW3 slab phantoms were implemented as slabs of polystyrene (ρ = 1.045 g/cm^3) of 30 × 30 cm^2 with varying thicknesses.

Microdosimetric Simulations The simulated μ^+ probe was positioned directly behind the RW3 slabs as depicted in Figure 5.6b. Similar to the 1D-$\overline{y_D}$ characterization, a two-phase simulation approach was employed. In the first phase, the incident proton kinetic energy was scored across the 10 × 10 cm^2 field immediately behind the RW3 slabs at P_{36}, P_{80}, and D_{20} using 10^8 protons. This was done to derive the incident proton kinetic energy probability density function at the six specific locations within the field. At these locations, an area three times the dimensions of the microdosimeter's detecting area was defined, and the probability density functions were then utilized as input for the second phase simulation, alongside the determined proton momenta in x and y at those locations. The second phase simulation was conducted using 10^7 protons with the same physics list and secondary particle production cut as outlined in Section 5.2.2. By using the same approach as described in Section 5.2.2, the energy deposition and lineal energy spectra were obtained.

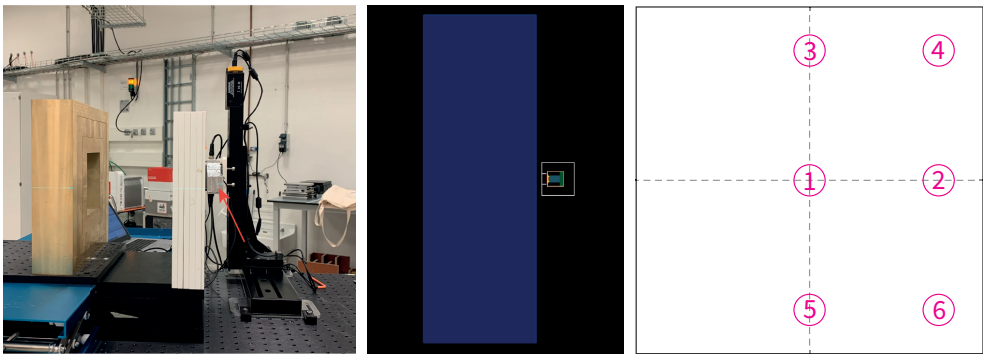

(A) (B) (C)

FIGURE 5.6: (A) A visual representation of the RW3 slab phantom setup positioned 12 cm away from the second brass collimator with the (90° rotated) μ^+ probe mounted to the linear stages 0.5 cm behind the RW3 slabs, (B) A side view of the implementation into G4HPTC-R&D with RW3 slabs in dark blue, and (C) The measurement positions in the 10×10 cm^2 field.

5.2.4 Spectral Unfolding Approach

Unfolding the true energy deposition spectrum was a detailed process that involved several critical steps:

1. Determination of the precise energy bin structure, which is essential for accurately categorizing the energy data. This was accomplished by applying a calibration file to the raw output spectrum from the MCA. This calibration aligned the raw data with the appropriate energy bins, ensuring that each bin corresponded to the correct energy range.

2. Identification of the low limit detection threshold, which varied with each measurement due to differences in background noise at the time of data collection. This threshold was the minimum energy level that the detector can reliably measure, and it must be accurately determined to avoid losing critical low-energy data.

3. Optimization of the energy deposition spectrum structure. This was done by using the same binned structure and detection threshold as those applied to the μ^+ probe measurements, allowing for a direct comparison between the G4HPTC-R&D simulations and experimental data.

During the optimization, adjustments were made to the simulation parameters, such as the depth of the water phantom, which may be varied by up to ± 2 mm. These adjustments helped to refine the simulation, ensuring that the binned data from the simulations aligned well with the experimental measurements. Once alignment was achieved, the actual full range of energy values recorded in the simulations, including those below

the detection threshold, could be used. This approach provided a more comprehensive representation of the true energy deposition spectrum, capturing details that would otherwise be missed due to detection limits. Following this, the lineal energy spectra were established as detailed in Section 2.4.3, followed by the computation of $\overline{y_D}$.

5.2.5 Pile-Up Correction Approach

All detector systems inherently experience count rate losses, primarily due to a phenomenon known as dead time (τ). Dead time refers to the minimum interval required between two consecutive events for them to be recorded as distinct and independent events [22]. This interval is crucial for ensuring accurate event detection and is often imposed by the electronic components associated with the detector, particularly during the pulse shaping stage in the amplifier [156]. During this stage, if the pulse shaping time is too long, the resulting amplified signal may develop a prolonged tail or a negative undershoot. This leads to closely spaced pulses merging into a single, combined pulse. This merging of pulses, a phenomenon termed pile-up, results in a combined pulse whose amplitude is equal to or less than twice the amplitude of the individual pulses that merged [22, 157, 158]. Such a combined pulse is then inaccurately recorded by the MCA in a higher energy channel, distorting the true energy spectrum and resulting in a loss of count rate. This distortion is particularly problematic because it can lead to an overestimation of high-energy events while underrepresenting lower energy events, thereby affecting the overall data interpretation. To address this issue, the approach undertaken in this study was to establish an upper limit for the pile-up estimation. While this method does not provide a perfect correction, it offers an informed approximation, as the expected impact of pile-up on the overall count rate was determined to be less than one percent. One effective method for estimating the pile-up fraction in measurements involves calculating the true count rate by applying a dead time correction approach and then comparing it to the measured count rate. Given that experimental count rates reflect the presence of a lower limit detection threshold, these rates were corrected for events falling below this threshold by utilizing the unfolded data from G4HPTC-R&D simulations.

Dead Time Correction Model

Over the past few decades, various dead time correction models have been proposed to address the described issues. The two primary types of idealized dead time models are those for a *paralyzable* system and *non-paralyzable* system. At low count rates ($<1/\tau$), both paralyzable and non-paralyzable systems yield equivalent results [156]. Since this condition applies to the current study, the true count rate n was determined using a

non-paralyzable system, which ensures that events occurring during dead time do not contribute to additional dead time, thereby providing a more accurate correction for count rate losses, defined by

$$n = \frac{m}{1 - m\tau}. \tag{5.1}$$

Here, m represents the measured count rate and τ denotes the dead time. To estimate τ, extensive inspection of a series of single pulse waveforms was conducted using an oscilloscope. The percentage difference between the threshold-corrected measured count rate and the true count rate was then calculated to indicate the pile-up fraction, which was assessed at all three positions along the Bragg curve. These pile-up fractions (%) were then excluded from the upper part of the spectrum.

5.3 Results

5.3.1 1D-$\overline{y_D}$ Characterization: Water Phantom Configuration

Depth-Dose Measurements & Simulations Figure 5.8a shows the depth-dose distribution obtained from the experimental configuration featuring the flask and Advanced Markus® chamber within the water phantom for the 150 MeV double passive scattering configuration (R_{80} = 103.4 mm). Each data point represents a measurement at that specific depth and alongside, the corresponding depth-dose distribution derived from G4HPTC-R&D (R_{80} = 103.6 mm) demonstrating accurate agreement in the proton range. The kinetic energy spectra of simulated primary protons at P_{36}, P_{80}, and D_{20} (Figure 5.8b) demonstrate a decrease in mean energy coupled with an increase in energy spread as the protons penetrate deeper into the water phantom. At P_{36}, the mean kinetic energy is 88.2 MeV with a relatively narrow energy distribution width of 2.4 MeV. In contrast, at

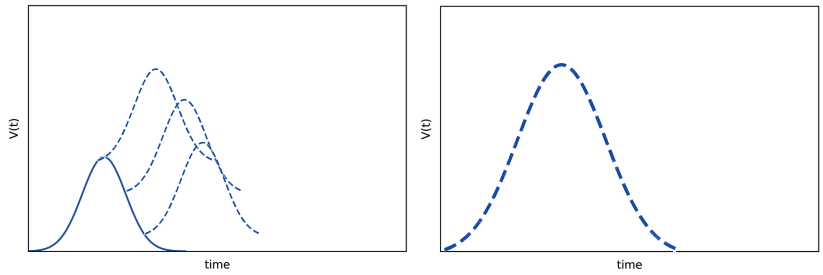

FIGURE 5.7: The effect of pile-up where multiple pulses within the pulse shaping time (left) can add up together to form one big pulse (right) with the amplitude equal or less than twice that of the individual pulses.

the distal end of the Bragg peak (D_{20}), the mean kinetic energy drops significantly to 12.9 MeV, while the energy distribution widens to 7.0 MeV. This broadening is due to energy straggling as the protons traverse through the matter, resulting in numerous low-energy contributions that are barely visible in the P_{36} spectrum. This pattern illustrates how the energy spread increases with decreasing kinetic energy at greater depths within the water phantom.

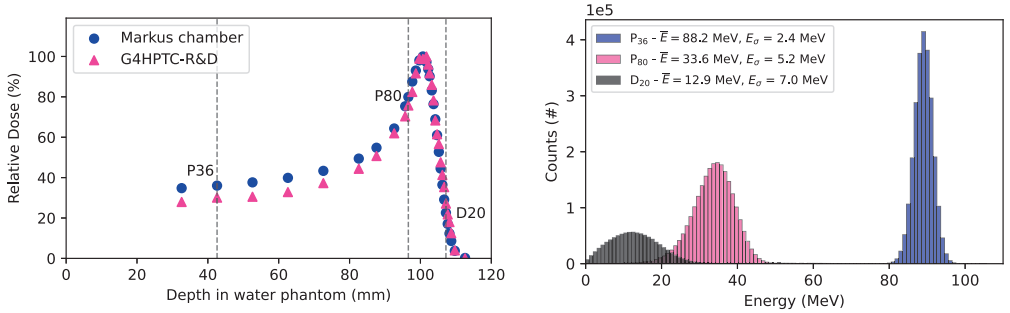

(A) (B)

FIGURE 5.8: (A) Normalized depth-dose distributions from the experimental configuration which includes the holder with the flask and Advanced Markus® chamber in the water phantom for the 150 MeV double passive scattering configuration, and the corresponding G4HPTC-R&D depth-dose distribution. Each data point represents a measurement at that specific depth. The P_{36}, P_{80}, and D_{20} positions of the depth-dose distribution are depicted by the dotted vertical lines. (B) Simulated kinetic energy spectra of primary protons at the P_{36}, P_{80} and D_{20} using a bin width of 1 MeV, describing the number of counts in each energy bin. The mean kinetic energy ($\overline{E}$) and corresponding energy distribution width (E_σ) are given for each position in the legend.

Microdosimetric Measurements & Simulations The top row of Figure 5.9 presents the acquired energy deposition spectra in silicon using the μ^+ probe of the 1D-$\overline{y_D}$ configuration at positions P_{36}, P_{80}, and D_{20} in the first, second and third column, respectively. Throughout the Bragg curve, the amount of energy deposited per event within the SVs increases and exhibits greater variation, leading to a broader spectrum towards the distal end of the BP. The G4HPTC-R&D energy deposition spectra with the low limit detection threshold of 11.65 keV, correlates strongly with the measured spectra at all positions. The corresponding unfolded spectra, indicated by the dotted black lines, illustrate the influence of the low limit detection threshold. This effect is most pronounced at P_{36}, which primarily consists of low-energy depositions within the SVs of the μ^+ probe caused by high energy protons. Disregarding the threshold at this position reveals a substantial portion of events with low y.

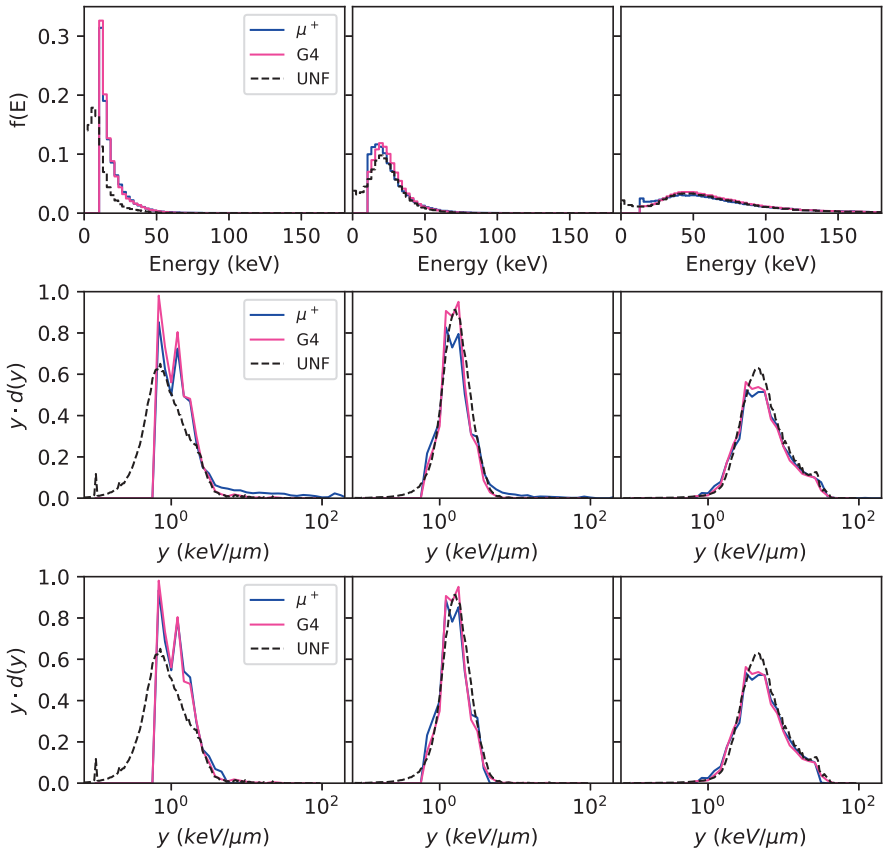

FIGURE 5.9: 1D-$\overline{y_D}$ configuration. First row: the energy deposition spectra measured by the μ^+ probe (μ), the G4HPTC-R&D simulation data (G4) and the unfolded result (UNF) for the P_{36}, P_{80}, and D_{20} position in the first, second and third column, respectively. All spectra are normalized by the sum. Second row: the corresponding lineal energy spectra at the three positions. The lineal energy spectra are plotted in a *semi-log* format, showing the fraction of dose ($y \cdot dy$) deposited by events with lineal energies (y) in a specific range. Third row shows the μ^+ probe pile-up corrected lineal energy spectra at the three positions after correcting for pile-up according to equation 5.1.

Through multiplication of the energy deposition spectra with the tissue conversion factor of 0.58, the spectra of lineal energies in tissue were obtained and are shown in the second row of Figure 5.9. There is a strong correlation between the general shape of the μ^+ probe spectra and the G4HPTC-R&D spectra. However, the μ^+ probe data exhibits a prolonged tail towards high y-values, primarily at P_{36} and P_{80}. This prolonged tail

may be attributed to pile-up occurrences during measurement. At P_{36}, with a threshold-corrected measured count rate m of 770.39 c/s and τ = 10 µs, the true count rate is 776.37 c/s according to equation 5.1. The pile-up fraction is then 0.78%. Excluding the upper 0.78% of the energy deposition spectrum results in the new lineal energy spectrum found in the third row of Figure 5.9. This spectrum clearly demonstrates the absence of the prolonged y-tail and correlates strongly with the G4HPTC-R&D spectrum. For P_{80}, a higher rate with m = 1298.84 c/s is observed, leading to a true count rate of 1319.41 c/s. At this position, the pile-up fraction was found to be 1.57% and demonstrates an improved match with the G4HPTC-R&D spectrum after pile-up correction. At D_{20}, despite the absence of a prolonged y-tail, the pile-up fraction was determined and equaled 0.22% with m = 185.84 c/s and n = 186.26 c/s. The pile-up corrected spectra does not show a notable difference. Overall, the lineal energy distributions clearly shift towards higher y-values as the penetration depth in the water phantom increases. $\overline{y_D}$ increases from 1.10 keV/µm in the plateau up to 7.25 keV/µm in the distal end of the BP, reflecting the accompanying rise in lineal energy as the protons reduce in energy and approach the end of their range. Table 5.1 summarizes derived $\overline{y_D}$ values from the μ^+ probe, G4HPTC-R&D and corresponding experimentally-informed simulated unfolded spectrum in the 1D-$\overline{y_D}$ configuration. At P_{36} and P_{80}, the μ^+ data is significantly affected by pile-up events, leading to elevated $\overline{y_D}$ values such as 4.89 keV/µm in the measurements compared to 1.40 keV/µm in GEANT4 simulations at P_{36}. This impact diminishes further along the Bragg curve. Furthermore, leaving out the low limit detection threshold at P_{36}, i.e. including all low-energy depositions, leads to a 21% lower $\overline{y_D}$ compared to G4HPTC-R&D with the threshold applied. This underscores the importance of unfolding the spectrum.

TABLE 5.1: $\overline{y_D}$ values at P_{36}, P_{80} and D_{20} using the 1D-$\overline{y_D}$ configuration in the 150 MeV double passive scattering configuration. $\overline{y_D}$ values are presented for measurements with the μ^+ probe (μ^+), pile-up corrected μ^+ data (μ^+_{PUC}), simulations with G4HPTC-R&D (G4) and the corresponding unfolded spectra (UNF).

	$\overline{y_D}$ (keV/µm)											
	P_{36}				P_{80}				D_{20}			
Location	μ^+	μ^+_{PUC}	G4	UNF	μ^+	μ^+_{PUC}	G4	UNF	μ^+	μ^+_{PUC}	G4	UNF
1	4.89	1.36	1.40	1.10	2.68	1.66	1.73	1.80	7.12	6.68	6.87	7.25

5.3.2 In-Between Mapping of Experimentally-Informed Simulated $\overline{y_D}$

The validation of G4HPTC-R&D against μ^+ probe measurements, followed by microdosimetric spectral unfolding, enabled the in-between mapping of experimentally-informed simulated $\overline{y_D}$ values along the Bragg curve and across the 10 × 10 cm^2 field

through the use of G4HPTC-R&D. This approach filled in the gaps, offering a more comprehensive understanding of the energy deposition patterns at different depths and positions in water. In the 1D-$\overline{y_D}$ configuration, intermediate μ^+ probe measurements were conducted. Applying microdosimetric spectral unfolding to all 17 measurement points resulted in the energy deposition and lineal energy spectra presented in Figure 5.10, with all $\overline{y_D}$ values found in Table 5.2. Furthermore, the simulated kinetic energy spectra of primary protons and the corresponding lineal energy spectra at all positions throughout the water phantom are shown in Figure 5.11. For the 3D-$\overline{y_D}$ configuration, no intermediate measurements were taken. Instead, G4HPTC-R&D simulations were utilized to estimate $\overline{y_D}$ at intermediate positions throughout the Bragg curve and across the 10×10 cm^2 field, effectively filling in the gaps between experimentally-informed simulated $\overline{y_D}$ values.

TABLE 5.2: The $\overline{y_D}$ values for the μ^+ probe, G4HPTC-R&D, and unfolded result, with the simulated mean proton kinetic energies ($\overline{E}$) in MeV and energy distribution width (E_σ) in MeV at all 17 positions along the 150 MeV double passively scattered Bragg curve of the water phantom configuration.

	$\overline{y_D}$				
	μ^+	G4	UNF	$\overline{E}$ (MeV)	E_σ (MeV)
Pos1	6.70	1.30	1.02	90.2	2.4
Pos2 (P_{36})	4.89	1.40	1.10	88.2	2.4
Pos3	7.57	1.31	1.06	82.4	2.6
Pos4	4.10	1.32	1.12	73.9	2.8
Pos5	3.26	1.27	1.13	65.5	3.1
Pos6	2.51	1.29	1.20	55.0	3.6
Pos7	2.53	1.38	1.36	43.7	4.3
Pos8	2.49	1.49	1.51	37.4	4.8
Pos9 (P_{80})	2.68	1.73	1.80	33.5	5.2
Pos10	2.61	1.76	2.07	30.8	5.5
Pos11	3.78	2.18	3.06	25.8	6.3
Pos12	4.68	3.64	4.23	20.9	7.1
Pos13	5.06	4.14	4.88	19.4	7.3
Pos14	5.76	5.51	5.84	16.3	7.5
Pos15	6.27	6.22	6.63	14.6	7.3
Pos16 (D_{20})	7.12	6.87	7.25	12.9	7.0
Pos17	7.68	7.63	8.03	11.8	6.6

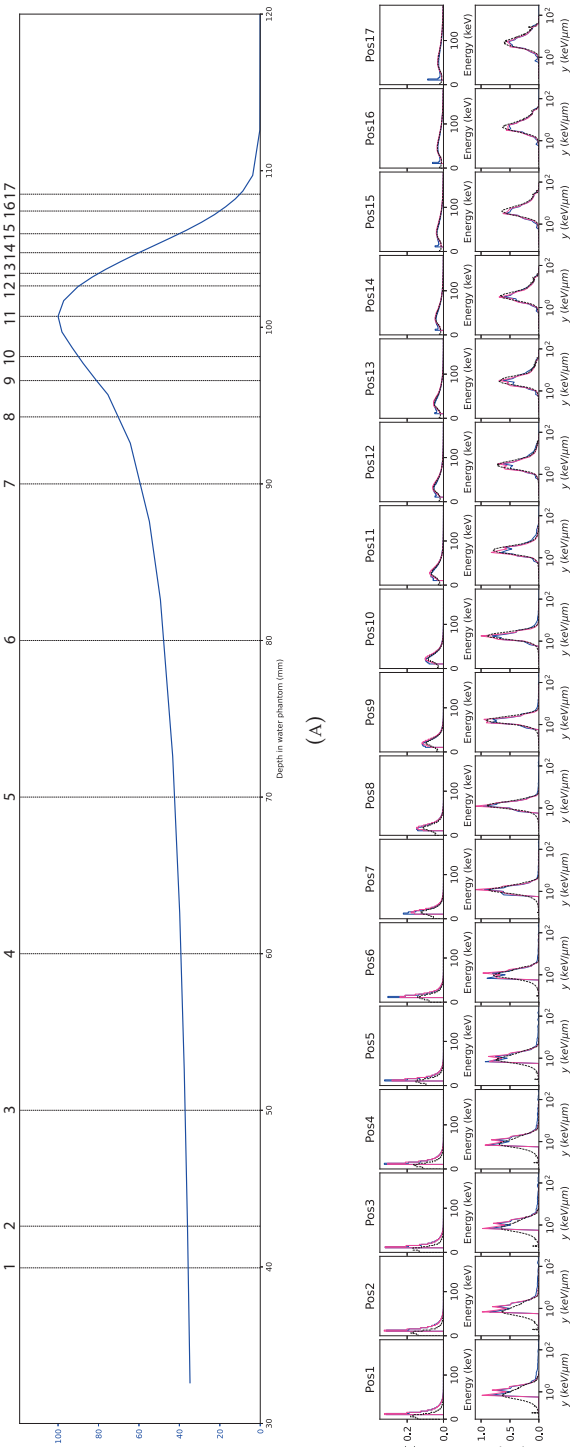

FIGURE 5.10: (A) The 17 measurements points denoted by vertical dotted black lines along the 150 MeV double passively scattered Bragg curve. (B) The energy deposition (top row) in keV and lineal energy spectra (bottom row) in keV/µm at all corresponding measurement points along the Bragg curve.

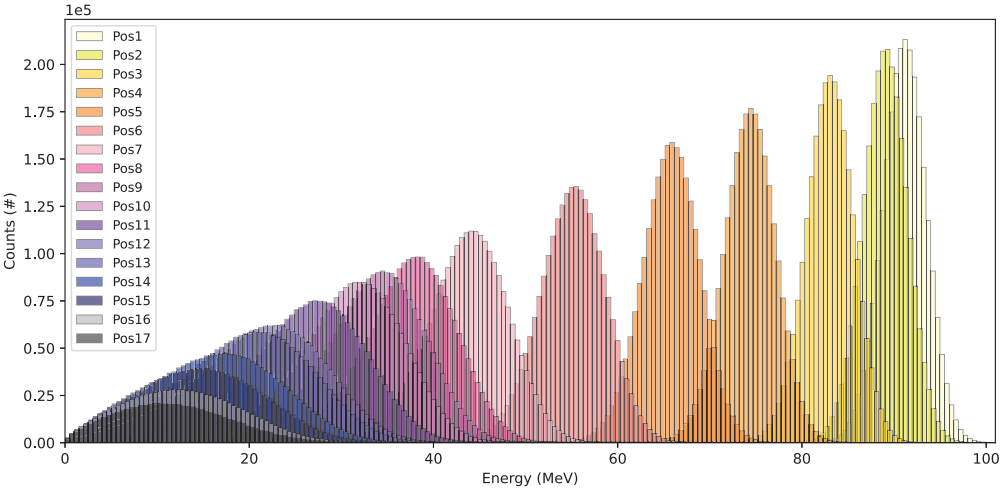

(A)

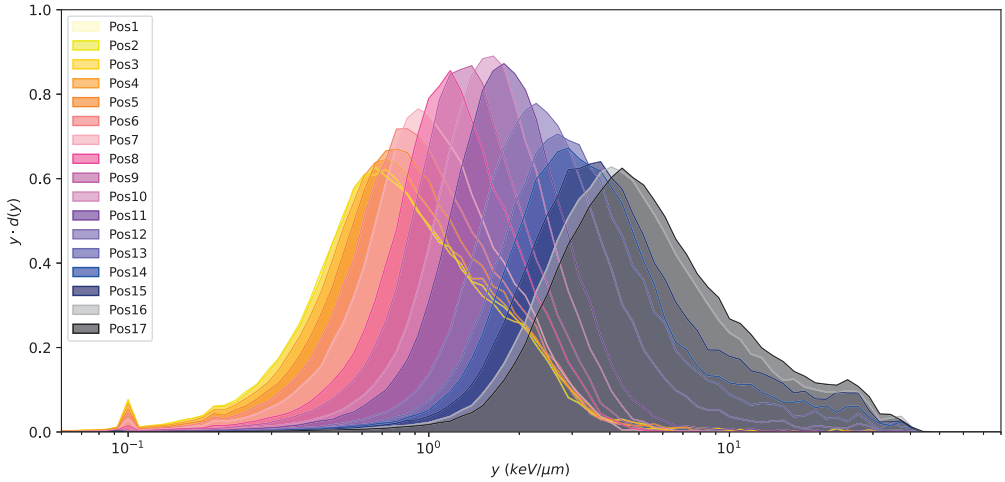

(B)

FIGURE 5.11: (A) Simulated kinetic energy spectra of primary protons at all positions throughout the water phantom. (B) The corresponding lineal energy spectra at all positions throughout the water phantom.

5.3.3 3D-$\overline{y_D}$ Characterization: RW3 Slab Phantom Configuration

Depth-Dose Measurements & Simulations The depth-dose distribution obtained using RW3 slab phantoms, measured with the OCTAVIUS detector in the 150 MeV double

passive scattering configuration (R_{80} = 99.6 mm) is shown in Figure 5.12. The corresponding G4HPTC-R&D depth-dose distribution (R_{80} = 99.7 mm) is presented as well and shows good agreement with the OCTAVIUS measurement. The proton kinetic energy spectra at all six locations within the 10 × 10 cm^2 large field at the P_{36}, P_{80} and D_{20} of the BP were analyzed too and are shown in Figure 5.13. Visually, there are scarcely any remarkable differences observed across the fields. Examination of the variances in mean energy and energy distribution widths across the fields show minimal variations (1-2%) at all BP positions and are listed in Table 5.3. However, deviations in energy distribution widths at the specific locations across the field slightly increase as one progresses further along the BP. For instance, at the D_{20}, comparing the center (position 1) to the corner positions (positions 4 & 6) reveals a percentage difference of 7.9% and 6.3%, respectively, in contrast to a 0% difference between these positions at P_{36}. Furthermore, as was observed in the 1D-y_D configuration, a closer examination of the proton kinetic energy spectra at the P_{36} position reveals the presence of various low-energy protons, likely originating due to scattering from the brass components of the double passive scattering system. These low-energy protons are consistently present in the spectra, but show no significant differences among the different positions.

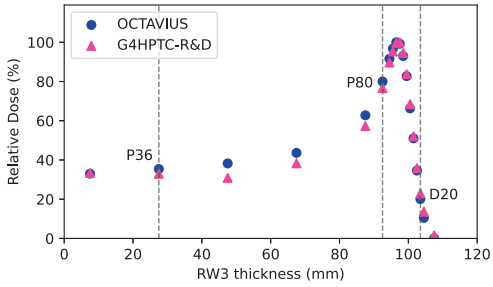

FIGURE 5.12: Normalized depth-dose distributions using the OCTAVIUS detector from the configuration using RW3 slab phantoms for the 150 MeV double passive scattering configuration, and the corresponding G4HPTC-R&D depth-dose distribution. Each data point indicates a measurement position using a certain thickness of RW3, with the dotted vertical lines in the figure representing the positions along the BP where the energy deposition and lineal energy spectra were obtained.

Microdosimetric Measurements & Simulations The energy deposition spectra and μ^+ probe pile-up corrected, G4HPTC-R&D, and unfolded lineal energy spectra at P_{36}, P_{80} and D_{20} using the RW3 slab phantoms are shown in each row respectively of Figure 5.14. At P_{36}, all six locations within the 10 × 10 cm^2 field show equivalent energy deposition spectra between the μ^+ probe and G4HPTC-R&D. Similar to observations at P_{36} of the 1D-$\overline{y_D}$ configuration, the spectra contain numerous high energy depositions, likely a result of pile-up. Correcting for pile-up (Eq. 5.1) was done for each location

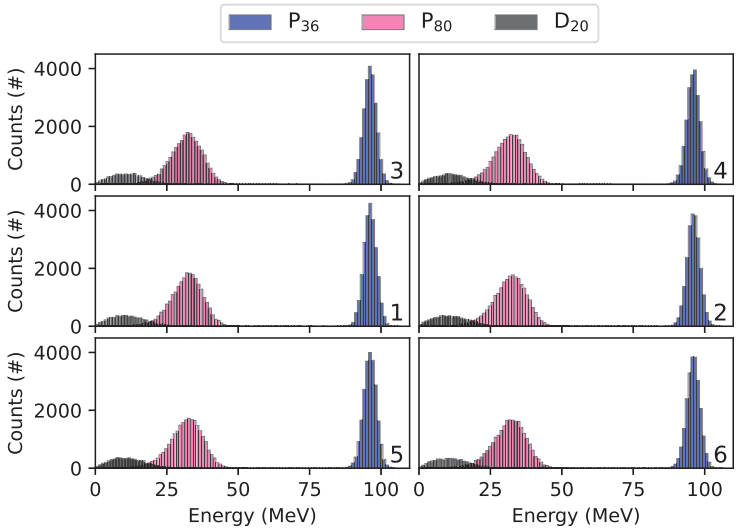

FIGURE 5.13: Simulated kinetic energy spectra of primary protons at the P_{36}, P_{80} and D_{20} using a bin width of 1 MeV, describing the number of counts in each energy bin. The location 1-6 are visualized following the representation in Figure 5.6c. The mean kinetic energy ($\overline{E}$) and corresponding energy distribution width (E_{σ}) at each location of each position are given in Table 5.3.

individually, with an average pile-up fraction of 0.90%. The original, non-corrected $\overline{y_D}$ values are listed in Table 5.4, alongside the pile-up corrected, G4HPTC-R&D, and unfolded $\overline{y_D}$ values. Analysis of μ^+ probe derived $\overline{y_D}$ across the field reveals significant deviations, ranging from 3.44 keV/µm to 8.14 keV/µm. After pile-up correction, a value of 1.16 keV/µm across the field is observed with the exception of position 4, being 10% lower than the other positions. Despite this, agreement within ±11% with the G4HPTC-R&D values is observed. The unfolded spectra highlight the impact of the low limit detection threshold (9.0 keV) across the field and reveal a significant portion of low lineal energy values. The unfolded $\overline{y_D}$ values vary within 7.5% across the field, with no discernible trend visible based on field position. Further along the BP, at both P_{80} and D_{20}, a wider range of energy depositions is observed, leading to a broader range of lineal energies. Overall, the energy deposition spectra obtained with G4HPTC-R&D match well with the measured data, except for the upper part of the spectra at P_{80} due to the occurrence of pile-up (visible upon zooming in the plots). At both positions, the pile-up fraction was determined at each location specifically within the field. Average pile-up fractions were 1.30% (P_{80}) and 0.13% (D_{20}). The pile-up corrected lineal energy spectra and the corresponding $\overline{y_D}$ show a high level of correlation for the lineal energy spectra compared to the uncorrected spectra, which showed comparable prolonged y tails at P_{80} as in the 1D-$\overline{y_D}$ configuration. At position 1, the non-corrected $\overline{y_D}$ (2.97 keV/µm)

TABLE 5.3: The simulated mean proton kinetic energies ($\overline{E}$) in MeV and energy distribution width (E_σ) in MeV at the six locations of the 10 × 10 cm^2 field of the RW3 slab phantom configuration in the double passive scattering configuration at the at the P_{36}, P_{80} and D_{20} of the Bragg peak.

	P_{36}		P_{80}		D_{20}	
Location	$\overline{E}$	E_σ	$\overline{E}$	E_σ	$\overline{E}$	E_σ
1	95.3	2.3	31.9	5.4	11.6	6.7
2	95.1	2.3	31.6	5.5	11.4	6.6
3	95.1	2.3	31.6	5.5	11.5	6.3
4	94.9	2.3	31.3	5.6	11.6	6.4
5	95.2	2.3	31.6	5.5	11.5	6.5
6	95.0	2.3	31.4	5.7	11.4	6.5

is 1.5 times higher than the G4HPTC-R&D result (1.92 keV/µm), whereas the pile-up corrected $\overline{y_D}$ (1.95 keV/µm) matches within 1.6% of the G4HPTC-R&D result. The other five positions, listed in Table 5.4, indicate comparable $\overline{y_D}$ values. Analyzing this effect at D_{20} reveals that the original μ^+ probe $\overline{y_D}$ values are up to 15% higher compared to the G4HPTC-R&D $\overline{y_D}$ values, while the difference is reduced to a maximum of 7.8% when correcting for pile-up. Furthermore, the unfolded $\overline{y_D}$ values vary from 8.17 keV/µm to 8.77 keV/µm, indicating a field variation of 7%. In general, throughout all positions of the Bragg curve, the $\overline{y_D}$ of μ^+ probe data at position 1 seems to be lower compared to the borders of the large field. However, this trend is not visible in the unfolded $\overline{y_D}$ values. Comparison of unfolded $\overline{y_D}$ values across the 10 × 10 cm^2 field throughout the three Bragg curve positions reveal deviations between 6.3% and 7.5%.

TABLE 5.4: $\overline{y_D}$ values at P_{36}, P_{80} and D_{20} using the 3D-$\overline{y_D}$ configuration in the 150 MeV double passive scattering configuration. $\overline{y_D}$ are presented for the measurements with the μ^+ probe (μ^+), the pile-up corrected (μ^+_{PUC}), G4HPTC-R&D (G4) and the unfolded lineal energy spectrum (UNF).

	$\overline{y_D}$ (keV/µm)											
	P_{36}				P_{80}				D_{20}			
Location	μ^+	μ^+_{PUC}	G4	UNF	μ^+	μ^+_{PUC}	G4	UNF	μ^+	μ^+_{PUC}	G4	UNF
1	3.44	1.16	1.20	1.05	2.97	1.95	1.92	2.04	8.32	8.03	7.90	8.43
2	4.54	1.16	1.22	1.06	2.73	1.98	1.95	2.07	8.89	8.36	7.75	8.27
3	5.82	1.16	1.29	1.12	3.12	1.99	1.97	2.09	8.75	8.31	8.04	8.57
4	3.60	1.05	1.21	1.06	3.22	2.04	1.99	2.11	8.50	8.12	7.65	8.17
5	5.45	1.17	1.21	1.06	3.32	1.91	1.96	2.07	8.61	8.29	8.22	8.77
6	8.14	1.16	1.25	1.09	3.13	2.01	2.01	2.13	8.52	8.20	7.71	8.22

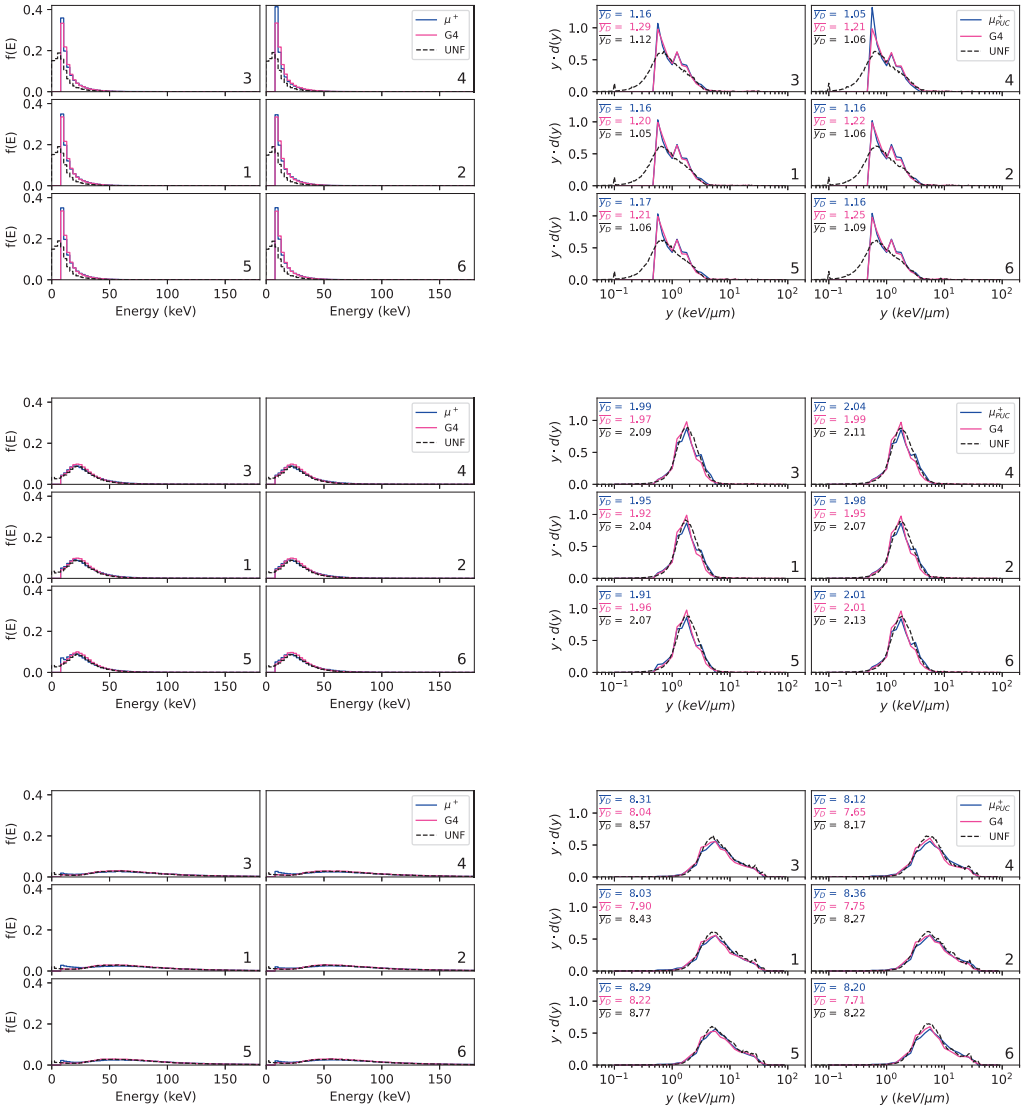

FIGURE 5.14: 3D-$\overline{y_D}$ configuration. First column: energy deposition spectra measured by the μ^+ probe, G4HPTC-R&D simulation data and the unfolded result for the P_{36}, P_{80}, and D_{20} position in the first, second and third row, respectively. Each figure consists of six sub-figures corresponding to the locations in the 10×10 cm^2 field (Fig. 5.6c). All spectra are normalized by the sum. Second column: the μ^+ probe pile-up corrected lineal energy spectra at the three positions after correcting for pile-up according to equation 5.1, together with G4HPTC-R&D and unfolded spectra. The lineal energy spectra are plotted in a *semi-log* format, the standard representation of lineal energy spectra, showing the fraction of dose ($y \cdot dy$) deposited by events with lineal energies (y) in a specific range. In each sub-figure the obtained $\overline{y_D}$ values are displayed to simplify comparison.

5.4 Discussion

The establishment of a 3D-LET classification system enabled the mapping of LET across a passively scattered proton beam in three dimensions. For the 1D-$\overline{y_D}$ configuration, the obtained experimentally-informed simulated $\overline{y_D}$ values, along with the remaining 14 validated positions and in-between LET values led to the result shown in Figure 5.15a. In contrast, the 3D-$\overline{y_D}$ configuration, which did not include intermediate measurements, relied solely on the G4HPTC-R&D simulations for estimating dose-mean lineal energy values at positions throughout the Bragg curve (Figure 5.15b) and across the 10×10 cm^2 field. G4HPTC-R&D simulations using the spectral unfolding approach can effectively fill in the gaps to create a continuous LET map that closely aligns with the experimentally-informed simulated data points. This comprehensive mapping provides a detailed representation of the spatial distribution of energy deposition in three dimensions, further validating the reliability and accuracy of the G4HPTC-R&D simulation platform.

In both the 1D-$\overline{y_D}$ and 3D-$\overline{y_D}$ configuration, deviations between the G4HPTC-R&D $\overline{y_D}$ values and those obtained from the μ^+ probe were most likely due to pile-up events during measurements. Pile-up is primarily associated with the electronics but can also be influenced by the proton beam current, with the likelihood of pile-up increasing as the proton beam current rises. Higher beam currents increase the proton flux, leading to more frequent interactions within the detector and thus a higher likelihood of pile-up, particularly at positions P_{36} and P_{80}. Reducing the beam current could mitigate pile-up, but such a reduction would result in impractically long measurement times given the available time frame. Although pile-up may affect the entire spectrum, this approach was designed to establish an upper limit for the pile-up approximation. While not a perfect solution, this method provided a reasonable estimate of the pile-up effect, ensuring that the impact on the overall results remains minimal. Additionally, while the pile-up correction inevitably removed some high LET values from the measured spectrum, the alignment with G4HPTC-R&D was still achieved, allowing these high LET events to be retained in the unfolded spectra. Given that the pile-up contribution appeared to be less than one percent, this approach offered a practical and sufficient means of addressing the issue within the context of the current study.

Removing the estimated pile-up fraction from the energy deposition spectra significantly improved the agreement of $\overline{y_D}$ values with G4HPTC-R&D results in both end-stations. This alignment between the portion of the energy deposition spectrum simulated by G4HPTC-R&D above the low limit detection threshold and μ^+ probe facilitated spectral unfolding. This approach allowed to use all energy deposition values from G4HPTC-R&D, rather than relying on binned values, by disregarding the low limit detection threshold. In the 1D-$\overline{y_D}$ configuration, the threshold concealed 65.3%, 17.9%, and 6.4% of the spectrum at P_{36}, P_{80}, and D_{20}, respectively. Furthermore, positioning uncertainties play a crucial role in this work due to the complexity of the experimental configurations. Positioning the μ^+ probe with a laser system in x, y and z is an accurate way to align but always comes with alignment uncertainties, especially crucial at the distal end of the BP where sub-millimeter alignment differences can lead to big changes in $\overline{y_D}$. However, during radiobiological experiments, the characterization of the BP using the configuration with the cell culture flask and Advanced Markus® chamber as one object allows the precise determination of the P_{36}, P_{80} and D_{20} positions before irradiation.

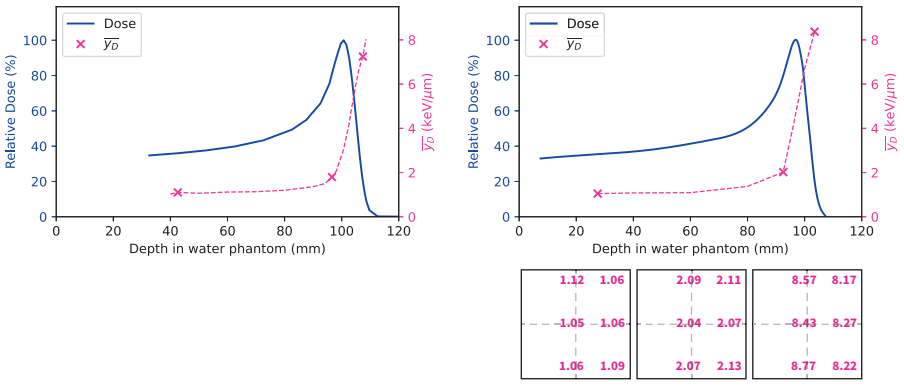

FIGURE 5.15: Result of the established 3D-LET classification system for the (A) 1D-$\overline{y_D}$ and (B) 3D-$\overline{y_D}$ configuration showing the depth-dose distribution in the water phantom configuration and RW3 slab phantom configuration, respectively, together with the corresponding experimentally-informed simulated $\overline{y_D}$ values shown as crosses. In (B), the fields are visualized at P_{36}, P_{80} and D_{20} indicating the mapped $\overline{y_D}$ values at the six locations across the 10×10 cm^2 field.

The 3D-$\overline{y_D}$ configuration has demonstrated results that are highly comparable to those obtained from the 1D-$\overline{y_D}$ configuration. Similarly, a prolonged y-tail is observed specifically at P_{36} and P_{80} in the obtained lineal energy spectra. Although the double passive scattering configuration is optimized for large fields to ensure dose homogeneity, mapping LET across the field remains crucial to detect any potential deviations. Given

that no significant deviations are observed, it appears that the center of the field (position 1) exhibits lower values compared to positions at the borders. Corner positions were selected taking into account the size of a culture plate well. Although placed at a significant distance from the field's actual border, placement of cells closer to these borders may result in $\overline{y_D}$ being influenced by Coulomb scattered low-energy protons and secondary particles originating from the brass collimator. Nevertheless, this effect is anticipated to have minimal impact on biological outcomes and is expected to remain within acceptable margins of error. The differences in $\overline{y_D}$ between the 1D-$\overline{y_D}$ and 3D-$\overline{y_D}$ configurations at D_{20} primarily stem from dissimilarities in their configurations. The 1D-$\overline{y_D}$ configuration utilizes water as the medium, whereas RW3 slabs are employed in the 3D-$\overline{y_D}$ configuration leading to different high LET secondaries affecting the spectra. Additionally, the 1D-$\overline{y_D}$ configuration offers sub-millimeter accuracy, whereas the 3D-$\overline{y_D}$ configuration provides millimeter accuracy.

Finally, inherent uncertainties in positioning also contribute to these observed differences. Comparing $\overline{y_D}$ with data from other facilities utilizing the Mushroom microdosimeter is challenging due to differing proton accelerators and beamline configurations, such as variations in proton energies, beam current and BP delivery. However, comparing $\overline{y_D}$ values with those obtained from a pencil beam configuration utilizing a different type of SOI microdosimeter (bridge microdosimeter) reveals comparable trends [56], including the rapid increase in $\overline{y_D}$ towards the distal end of the BP. Nonetheless, $\overline{y_D}$ values in the plateau region observed in this study are comparatively lower, which can likely be attributed to the unfolding of the spectrum. The study conducted by Missiaggia et al. also focused on the distribution of $\overline{y_D}$, specifically examining both in-field and out-of-field radiation quality within the context of a Spread-Out Bragg Peak (SOBP) in proton therapy [159]. Their in-field $\overline{y_D}$ results are comparable with those observed in this study. However, they utilized a walled Tissue Equivalent Proportional Counter (TEPC), which captures energy deposition across a larger volume. In contrast, the μ^+ probe employed in this work offers high-resolution insights into the energy deposition at the cellular level, which complicates direct comparison.

The presented results have demonstrated the experimental and simulated $\overline{y_D}$ exploration in 3D across a large field and through a passively scattered Bragg curve, alongside the unfolding of spectra to address inherent detector limitations, adding a novel dimension to LET studies. Looking forward, the integration of cellular responses, such as linking DNA damage complexity to survival fraction, is the next major challenge for HollandPTC. This will enhance the predictive capabilities of the 3D-LET classification system, advancing the ability to correlate $\overline{y_D}$ variations with biological effects.

5.5 Conclusion

This chapter presented a 3D spectral unfolding approach to analyze cellular-level energy deposition spectra within a double passive scattering configuration, aiming to establish a 3D-LET classification system for diverse biological endstations at the Holland Proton Therapy Centre. The combination of two unique radiobiological endstations allowed for detailed examination of LET across various depths and positions within a double passively scattered proton beam. The water phantom configuration provided precise one-dimensional characterization of energy deposition, essential for evaluating cellular responses in cell culture flasks. The RW3 slab phantom configuration facilitated three-dimensional analysis, offering insights into energy deposition variability across cell culture plates. The integration of high-resolution advanced LET dosimetry together with GEANT4 simulations has enabled accurate spectral unfolding. This addressed detector limitations and significantly improved the understanding of cellular-level energy deposition patterns. This combined experimental and simulation approach has not only further validated the G4HPTC-R&D simulation platform but also refined the understanding of LET distributions, providing valuable information for radiobiological studies. Overall, this work significantly advances the field by providing a framework for the 3D analysis of cellular-level energy deposition patterns in proton therapy. The novel system enables a deeper understanding of cellular energy deposition spectra, overcoming detector limitations and offering valuable insights into cellular responses under proton irradiation in a clinical setting.

Chapter 6

Mechanistic Proton Therapy Insights: Linking DNA Damage to Survival

Parts of this chapter have been published as "Heemskerk, T., Groenendijk, C., Rovituso, M., van der Wal, E., van Burik, W., Chatzipapas, K., Lathouwers, D., Kanaar, R., Brown, J. M. C., & Essers, J. (2025). *Position in Proton Bragg Curve Influences DNA Damage Complexity and Survival in Head and Neck Cancer Cells*. Clinical and Translational Radiation Oncology, 100908" [160].

6.1 Introduction

Proton radiotherapy induces tumor cell death by causing DNA damage. Recent radiobiological research has increasingly focused on understanding the complex relationship between proton irradiation and DNA damage. As the understanding of DNA damage complexity deepens, it becomes crucial to elucidate the structural yields of these damages and their implications for cellular survival. A critical aspect is the investigation of DSBs, which are among the most lethal forms of DNA damage, particularly when occurring as complex clustered DNA damage [161]. Complex clustered DNA damage involves a DSB along with multiple other lesions around the damaged site [162]. Studying these types of DSBs allows researchers to unravel the mechanism of DNA damage induction and its impact on cell survival.

To further understand the distribution of DSBs, in silico studies can offer valuable insights into the types and complexities of DNA damage. This requires a thorough understanding of the proton energy deposition pattern at the cellular level and the accompanying Linear Energy Transfer (LET) at the specific location of the irradiated tissue or cell. Since proton energy and energy spread vary along the Bragg curve, the energy deposition pattern at the cellular level also changes, affecting DNA damage induction and resulting DNA damage structures. Variations in the complexity and distribution of DSBs along the Bragg peak may lead to differences in cell survival fractions at different positions.

This work aims to study in vitro clonogenic survival and DNA damage foci kinetics of a head and neck squamous cell carcinoma cell line along the double passively scattered proton Bragg curve of HollandPTC. Complementary in silico studies - which involve computational simulations of proton energy deposition, DNA damage induction, and the resulting damage structure at the cellular level - will provide insights into the link between experimentally yielded foci and the number and complexity of DSBs. These computational models will help predict how different energy deposition patterns influence DNA damage and repair processes, enhancing the interpretation of experimental data. Understanding these interrelations and correlations is crucial for elucidating the complex mechanisms underlying proton-induced cellular responses. This integrated approach provides valuable insights into the effects of proton radiation at cellular and molecular levels, potentially enhancing the efficacy of proton therapy in cancer treatment.

6.2 Methods

The integrated approach of the study of *in vitro* clonogenic survival and DNA damage foci kinetics with the in silico study of proton energy deposition, DNA damage induction, and the resulting damage structure at the cellular level, was performed in two phases (Fig. 6.1) by the following sub-steps:

Phase I - Biological experiment:

- FaDu cell culture
- Clonogenic survival assay
- 53BP1 immunofluorescent staining
- Microscopy

Phase II - GEANT4-DNA Simulations

- Modified FaDu cell geometry development
- DNA damage complexity assessment

6.2.1 Phase I: Biological Experiment

A human cell contains a nucleus that houses DNA (deoxyribonucleic acid), which consists of two complementary strands linked by a sugar-phosphate backbone that provides structural stability [3]. DNA serves as the carrier of genetic information and is essential for cellular replication, making it the primary target of radiation therapy for tumor eradication [163]. Ionizing radiation damages DNA by inducing ionization and excitation of molecules, which can lead to strand breaks in the double helix. Single-strand breaks (SSBs), where only one strand is affected, are generally repairable. However, double-strand breaks (DSBs), where both strands are damaged, are significantly more challenging to repair. If multiple DSBs occur in close proximity, forming clustered DNA damage, they represent the most lethal form of radiation-induced damage, making the study of proton-induced DSBs essential for understanding cellular survival [164].

Due to cell's ability to repair strand breaks through DNA damage response (DDR) pathways, the cell is able to survive. One key biological endpoint to study the effect of different forms of radiation, i.e. different microscopic energy distributions, is cellular survival. Cellular survival refers to the ability to survive after a given radiation

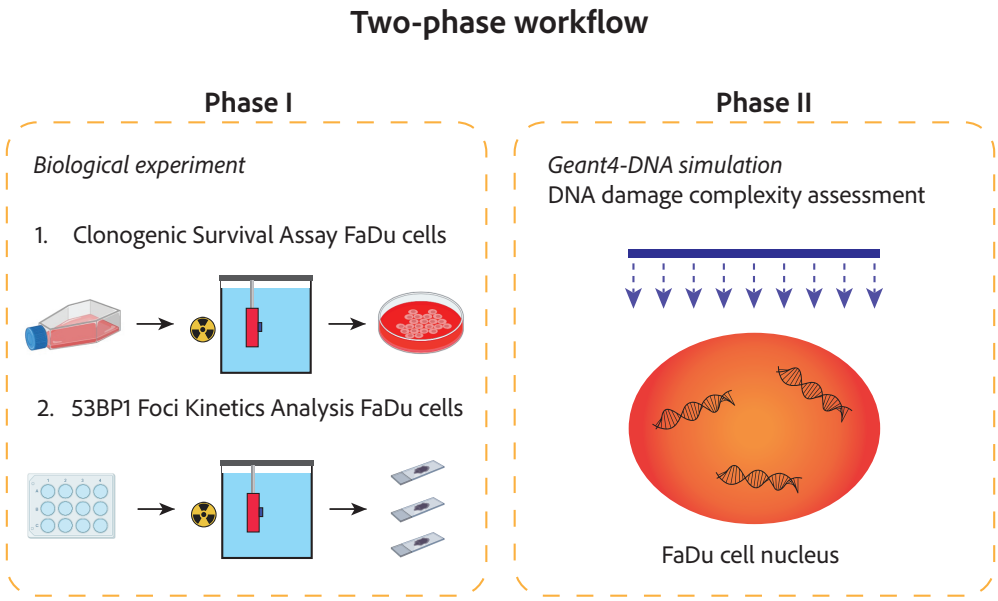

FIGURE 6.1: The two-phase workflow applied in this work. Phase I includes the biological experiment consisting of 1. The clonogenic survival assay of the FaDu cells at P_{36}, P_{80} and D_{20} of the 150 MeV passively scattered large field Bragg curve, and 2. The 53BP1 foci kinetics analysis at the same positions. Phase II includes the in silico assessment of DNA damage complexity using GEANT4-DNA simulations.

dose, quantified through a clonogenic survival assay. This assay evaluates a cell's ability to proliferate and form colonies after irradiation, comparing the number of resulting colonies to a non-irradiated control sample to determine the survival fraction S/S_0. The relationship between the surviving fraction of cells and the radiation dose can be fitted by a second-order polynomial, referred to as the linear-quadratic (LQ) model, described as

$$S/S_0 = \exp(-\alpha D - \beta D^2) \tag{6.1}$$

where S/S_0 is the surviving fraction, α represents the average number of lethal single-particle interactions per cell, proportional to absorbed dose D, and β represents the average number of lethal two-particle interactions per cell, proportional to the square of absorbed dose D^2. The surviving fraction following the LQ model is plotted in a cell survival curve following a logarithmic scale to easily assess the low cell survivals [3, 165].

To further investigate DSB formation, the dynamics of ionizing radiation-induced

foci can be analyzed. Following DNA damage, the DDR triggers the accumulation of DDR proteins at or near DSB sites, forming these foci. A key DDR protein is p53-binding protein 1 (53BP1). Examining the dynamics of 53BP1 foci enables the correlation between radiation-induced DSBs and subsequent cell survival outcomes [3].

Experimental Configuration at HollandPTC

The HollandPTC proton beamline was constructed using a 150 MeV double passively scattered configuration (Fig. 6.2a) delivering a 10 $\times$ 10 cm^2 large field. The biological experiment was conducted utilizing the water phantom configuration. Detailed descriptions of the experimental characterization of this configuration are available in Chapter 3 and 5. The water phantom configuration, including the custom-designed 3D-printed holder attached to motorized linear stages, accommodating the T25 cell culture flask and Advanced Markus® chamber is shown Figure 6.2b. Motorized linear stages enabled precise alignment of the T25 cell culture flask at the center of the 10 $\times$ 10 cm^2 field (Fig. 6.2c), and allowed submillimeter-precision movement through the water phantom along the passively scattered Bragg curve. The previously validated positions P_{36}, P_{80} and D_{20} along the passively scattered Bragg curve (Ch. 5) were selected for irradiation. To ensure accuracy and reproducibility, measurements were conducted prior to irradiation using the Advanced Markus® chamber and a cell flask filled with cell medium to validate the precise location of the Bragg peak. Subsequently, the positions P_{36}, P_{80} and D_{20} were determined, ensuring precise irradiation of the flask at the specified positions. Throughout the irradiation process, the Advanced Markus® chamber monitored the dose behind the T25 flask, ensuring adherence to the prescribed dose and precise positioning relative to the Bragg curve.

Cell Culture

FaDu cells (HTB-43, ATCC), derived from head and neck squamous cell carcinoma, were cultured in a 1:1 mixture of DMEM (4.5 g/L Glucose, with Ultraglutamine 1) and Ham's F-10, supplemented with 10% fetal calf serum and 1% penicillin/streptomycin. Cells were maintained in a humidified incubator at 37°C with 5% CO_2.

Clonogenic Survival Assay

The clonogenic survival assay workflow is presented in Figure 6.3. One day prior to irradiation, 1.5 $\times 10^6$ FaDu cells were seeded in T25 flasks and were allowed to attach overnight. Cells were irradiated with doses of 0, 2, 4 and 6 Gy at the three specified positions in the Bragg curve, with a dose rate of approximately 1.5 Gy per minute. Following irradiation, cells were trypsinized, counted and seeded in triplicates in six cm

(A)

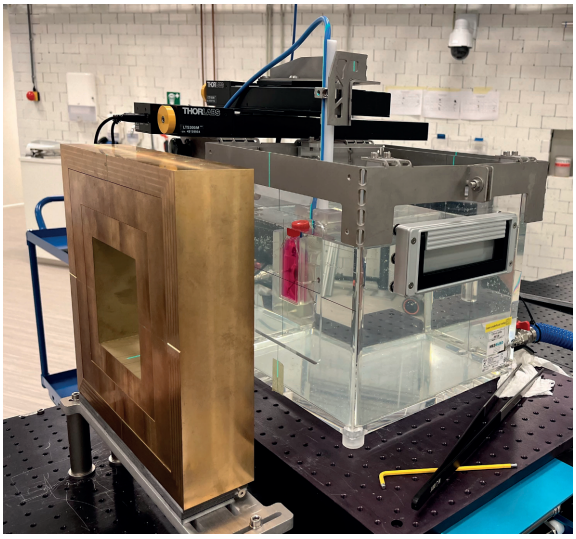

(B)

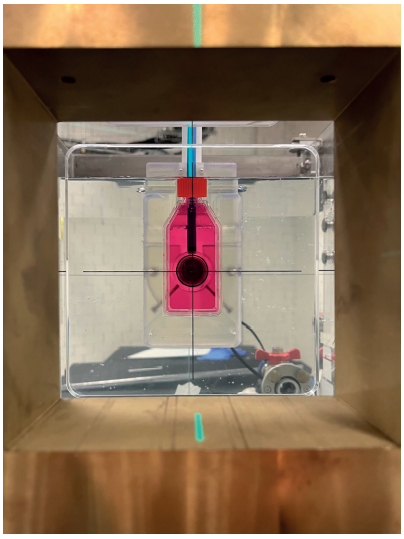

(C)

FIGURE 6.2: (A) Double passively scattered configuration utilizing the water phantom configuration at the HollandPTC R&D proton beamline, (B) the water phantom with the custom-designed 3D-printed holder mounted to two motorized linear stages, and (C) the positioning of the T25 cell culture flask and Advanced Markus® chamber directly behind it, within the center of the 10×10 cm^2 field.

dishes. The number of cells seeded depended on the dose administered, with 300, 600, 1200, and 2400 cells per dish for the doses 0, 2, 4, 6 Gy, respectively. Colonies were allowed to form for 14 days, fixed and stained in Coomassie Blue staining solution (50% methanol, 7% acetic acid, 43% demi water, 0.1% brilliant blue R). Colonies were counted

using the GelCount colony counter (Oxford optronic). To assess the relative sensitivity of cell survival curves, the data from three independent experiments were pooled and a linear-quadratic survival curve was fitted to the data points, using weighted least squares regression in GraphPad Prism 9. The doses required to achieve 37% survival ($D_{37\%}$ (Gy)) and 10% survival ($D_{10\%}$ (Gy)) were interpolated from the fitted curves. Both 37% and 10% survival fell within the range of the experimental data points, ensuring the reliability of the interpolation derived from the curve.

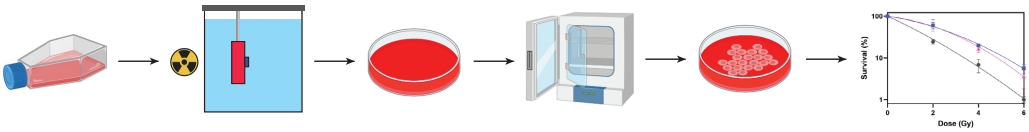

FIGURE 6.3: Clonogenic survival workflow: FaDu cells were seeded and allowed to attach in T25 flasks. The cells were then irradiated at P_{36}, P_{80} and D_{20} in the water phantom with doses of 0, 2, 4, and 6 Gy. Subsequently, cells were trypsinized, counted and seeded in triplicates in six cm dishes and then incubated for 14 days. Colonies were counted, and cell survival curves were generated by fitting the data to a linear-quadratic survival model.

53BP1 Immunofluorescent Staining

The p53-binding protein 1 (53BP1) immunofluorescent staining workflow is shown in Figure 6.4. One day prior to irradiation, cells were seeded on 18 mm coverslips in 6-well plates at a density of 500.000 cells per well and allowed to attach overnight. Coverslips were transferred to a 12-well plate. The coverslips were attached to the well using PNIPAAm-PEG 3D thermoreversible hydrogel in cell culture medium (MBG-PMW20-1001, Mebiol Gel). The wells were filled with medium and sealed with Microseal B seals (MSB1001, Bio-Rad). The samples were irradiated with 2 Gy and fixed at time points 15 minutes, 2, 6, 8, 15, 18 and 24 hours post-irradiation. Unirradiated coverslips were fixed after 15 minutes and 24 hours. Cells were washed with phosphate buffered saline (PBS), fixed with 4% paraformaldehyde (PFA) in PBS for 15 minutes at room temperature and washed again with PBS. Cells were permeabilized with 0.1% Triton X-100 in PBS for two times 10 minutes and blocked with PBS+ buffer (5 mg Bovine Serum Albumin and 1.5 mg glycine/mL PBS). Primary anti-53BP1 antibody (rabbit, 1:1000, NB100-304, Novus biologicals) was diluted in PBS+ buffer and cells were incubated with primary antibodies overnight at 4°C. After washing with PBS+ buffer, secondary antibodies (anti-rabbit Alexa488; Life Technologies) diluted in PBS+ buffer (1:1000) were applied, and cells were incubated in the dark for one hour at room temperature. Coverslips were mounted on microscope slides using Antifade mounting medium with DAPI (Vectashield) and sealed with nail polish.

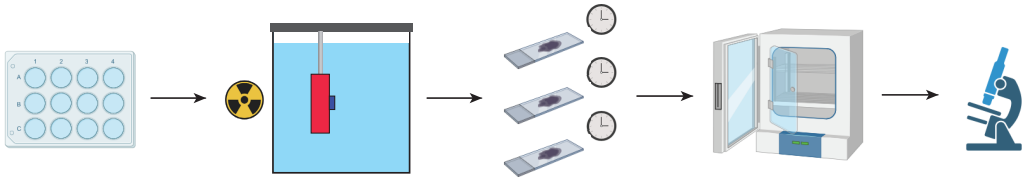

FIGURE 6.4: 53BP1 immunofluorescent staining workflow: FaDu cells were seeded and allowed to attached in 6-well plates. The cells were then irradiated at P_{36}, P_{80} and D_{20} in the water phantom with a dose of 2 Gy. Cells were fixed at time points 15 minutes, 2, 6, 8, 15, 18 and 24 hours post-irradiation. Following fixation, cells were incubated, and the coverslips were mounted on microscope slides for analysis.

Microscopy

Immunofluorescence in cells was visualized with a Leica STELLARIS 5 confocal microscope with the laser lines DAPI (405 nm) and Alexa 488 (488 nm). For each sample, four Z-stack images were captured using a 40x objective. Z-projections were generated and nuclear area, mean and integrated density of the DAPI signal were measured for each nucleus. Additionally, the number of 53BP1 foci, average focus size, and average focus intensity were analyzed for each nucleus using homemade ImageJ scripts. Cell nuclei were segmented based on the DAPI signal and nuclear area and integrated density of the DAPI signal were quantified using the measurement function within ImageJ. Foci within segmented nuclei were identified using thresholds based on the mean + factor $\times$ standard deviation of the 53BP1 signal [166]. The number, size, and intensity of segmented foci were measured using the measurement function within ImageJ. To assess the resolution rate of 53BP1 foci, a sum of two exponential curves was fitted to the data points, using least squares regression in GraphPad Prism 9. The fitted curve follows the form:

$$\#\,\text{Foci per nucleus} = C_1 \cdot e^{-\frac{t}{\tau_1}} - C_2 \cdot e^{-\frac{t}{\tau_2}} + C_3 \quad C_1, C_2 > 0 \tag{6.2}$$

where the parameters C_1, C_2, C_3 and τ are determined during the fitting process, with t representing the time after irradiation. C_1 and C_2 describe the magnitude of the rise or decline of the fit, respectively, while C_3 represents a constant offset. τ_1 is the exponential time constant for the decline, and τ_2 is the exponential time constant for the rise. The half-life of 53BP1 resolution, $\tau_{1/2}$ was subsequently calculated.

6.2.2 Phase II: GEANT4-DNA Simulations

The second phase of this work involved assessing DNA damage complexity using GEANT4-DNA [70, 71, 72, 73, 74, 110, 111, 112] (Fig. 6.1). Building on previous work (Ch. 5), proton kinetic energy spectra at the back of the flask – where the cells were located –

were obtained from G4HPTC-R&D for the three specified positions along the passively scattered Bragg curve [167]. Additionally, the FaDu cell nucleus dimensions in x, y and z were determined by fitting an ellipse onto the maximum projections of the microscopic z-projections of numerous FaDu cells, enabling extraction of the average semi-axes of the nucleus. These proton kinetic energy spectra and FaDu cell nucleus dimensions were then used as input for GEANT4-DNA to investigate DNA damage complexity along the 150 MeV passively scattered proton Bragg curve. The workflow is depicted in Figure 6.5. Simulations were conducted using the "moleculardna" example of the GEANT4-DNA toolkit (GEANT4 version 11.1.2), with the "human cell" geometry taken as starting point.

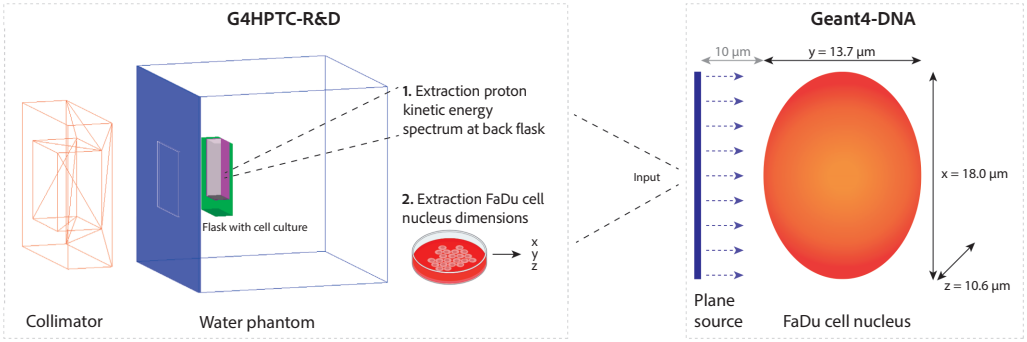

FIGURE 6.5: GEANT4 simulation workflow. The left panel displays part of G4HPTC-R&D with the second brass collimator visible along with the water phantom featuring the holder containing the flask with the FaDu cell culture. From here: 1. The proton kinetic energy spectra at the back of the flask for the P_{36}, P_{80} and D_{20} along the passively scattered Bragg curve were obtained. 2. The FaDu cell nucleus dimensions in x, y and z were determined by fitting an ellipse onto the maximum projections of the microscopic z-projections. Both were used as input for GEANT4-DNA, shown in the right panel. A squared 18 µm × 18 µm plane source was implemented and positioned 10 µm away from the FaDu cell's boundary. The semi-axes in x, y, z of the FaDu cell nucleus are 9.0 µm × 6.9 µm × 5.3 µm.

Human Cell Geometry in "moleculardna"

The modeling of DNA in GEANT4-DNA was initially developed by Lampe et al. [76, 168, 169]. The DNA fiber is composed of phosphate (H_3PO_4) and deoxyribose ($C_5H_{10}O_4$) molecules that formed its backbone. In this model, both phosphate and deoxyribose (sugar) molecules were approximated as spheres, supporting the nucleotide bases - guanine ($C_5H_5\ N_5O$), adenine ($C_5H_5N_5$), cytosine ($C_4H_5N_3O$), and thymine ($C_5H_6N_2O_2$) - which, due to their flatter structure, were represented as ellipsoids. The DNA fiber was further compacted into chromatin by folding around histones. Although the packing of DNA is highly complex, at larger scales, it follows a roughly fractal geometry that can be approximated by space-filling curves [168]. This meets two key requirements for

DNA packing: it must unfold without tangling for replication, and the packing method should require minimal information. Space-filling curves, a type of fractal, achieve this by enabling dense compaction without forming knots, and requiring minimal data to model due to their recursive nature. DNA was modeled using a large-scale fractal geometry based on the Hilbert curve (Fig. 6.6a) [170]. One iteration of the Hilbert curve is illustrated in Figure 6.6b, while two iterations are shown in Figure 6.6c. To achieve a sufficiently dense DNA structure, the Hilbert curve was iterated eight times [80]. This fractal DNA representation was divided into cubic regions (voxels) with 750 Å side lengths, each representing segments of chromatin. Three models of chromatin segments were used: straight, turned and turned-twisted DNA solenoids. These DNA solenoids were generated using the FractalDNA tool and were positioned to form a continuous DNA chain. The human cell geometry example within the "moleculardna" example application was implemented as an ellipsoid with dimensions 14.2 µm × 14.2 µm × 5 µm acting as a mask over the seeded Hilbert curve to define the chromosomal region. Cubic regions with centers inside this ellipsoid were included in the simulation. Within this ellipsoid, the fractal-based DNA chain structure comprised approximately 6.4 Gbp, typical of normal human cells [171], with an effective DNA density of ~ 0.012 bp/nm^3 [80]. Further details on DNA modeling are available in the work of Lampe et al. [76, 168, 169].

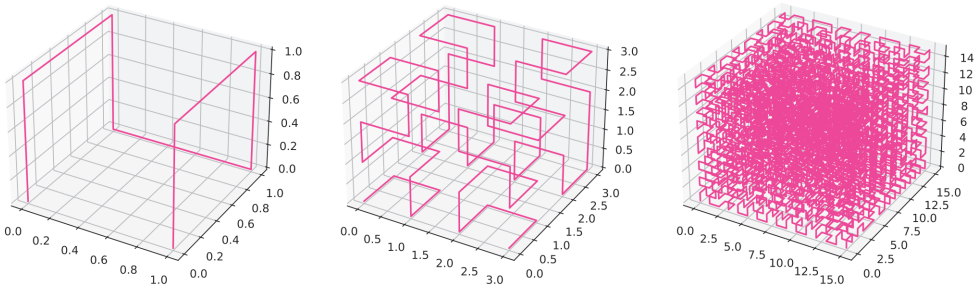

FIGURE 6.6: (A) 3D Hilbert curve, (B) one iteration of the Hilbert curve, and (C) two iterations of the Hilbert curve [168, 170].

Modified FaDu Cell Geometry Development

Given the difference in size between the FaDu cell nucleus (18.0 µm × 13.7 µm × 10.6 µm) compared to the human cell geometry in the "moleculardna" example (Sec. 6.2.2), and the requirement for a cell to contain approximately 6.4 Gbp [171], it was necessary to develop a modified geometry for the FaDu cell. To achieve this, the chromatin segments

(straight, turned and turned-twisted) were adjusted using the FractalDNA tool [172]. FractalDNA is a Python package designed to create DNA geometries that can be assembled like jigsaw puzzles. The tool enables the creation of both simple DNA segments and solenoidal DNA structures for DNA-level simulations in GEANT4-DNA. Modifications to the DNA solenoid structures were carried out by adjusting the voxel size and number of histones. Increasing the voxel size led to a more extended and less compact DNA solenoid. To maintain a constant linear density of histones and ensure chromosomal compaction without altering DNA damage sensitivity [173], the histone-to-voxel ratio was set at 0.05, corresponding to 51 histones per 1000 Å [172]. These modifications resulted in a voxel size of 1223 Å with 61 histones per voxel, compared to a 750 Å voxel size and 38 histones per voxel using the original human cell example. Using a chromosomal region of 18.0 µm × 13.7 µm × 10.6 µm led to 6406270100 base pairs within the FaDu cell, compared to 6405886128 base pairs using the original human cell example. Given the ellipsoidal volume of 1369.2×10^9 nm^3, this corresponded to a DNA density of $\sim$ 0.0047 bp/nm^3. Visual inspection ensured there were no overlaps in the DNA solenoid structure. The newly modified straight and turned chromatin are illustrated in Figure 6.7a and 6.7b, respectively, with a zoomed-in view presented in Figure 6.7c. The detailed structure of the chromatin segments are shown in Figure 6.7d, 6.7e and 6.7f, respectively.

Simulation Configuration in GEANT4-DNA

The right panel of Figure 6.5 presents the implementation of the FaDu cell nucleus in GEANT4-DNA. This model incorporated a modified FaDu cell geometry with an ellipsoidal chromosomal region defined by semi-axes of 8.974 µm, 6.857 µm, and 5.312 µm along the x, y and z axes, respectively. A squared plane source of 18 µm × 18 µm was positioned 10 µm from the nucleus' boundary, all surrounded by liquid water. This configuration was designed to achieve charged particle equilibrium, ensuring that secondary particle production occured before reaching the cell nucleus. The three proton kinetic energy spectra (Fig. 5.8b) were implemented as user-defined energy histograms with 0.5 MeV bins, each assigned a specific weight. Simulations were conducted at P_{36}, P_{80} and D_{20} with a total of 2×10^4 protons per position. The GEANT4-DNA *option4* physics list [70] was adopted to simulate both the physical and chemical interactions, including interactions of reactive species, which is the recommended physics list according to the GEANT4-DNA collaboration [121, 174, 175]. Additional parameters were set to model DNA damage, which are summarized in Table 6.1 and were optimized in the work of Sakata et al. [75]. The direct interaction range, defined as the radius within which energy depositions are assigned to a DNA molecule to induce direct strand breaks, was set to 3.5 Å. The energy threshold for direct damage induction followed a linear probability distribution, ranging from 0 to 1 for energy depositions between 5 eV and 37.5 eV,

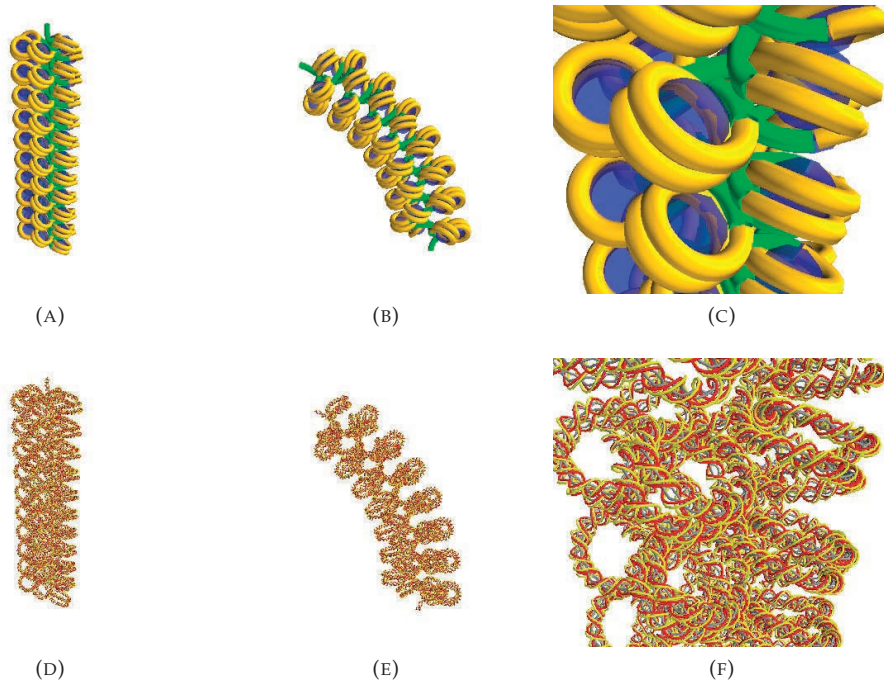

FIGURE 6.7: Modified FaDu cell geometry showing a (A) straight chromatin segment, (B) turned chromatin segment, and (C) a zoomed-in view of the chromatin segment with DNA shown in yellow, the protein core shown in blue and the linking sections shown in green which were calculated using 3D spline functions [80]. (D), (E), and (F) show the detailed structure of the DNA strands with yellow lines connecting the phosphate molecules and red lines connecting the sugar molecules.

respectively. The probability of a chemical reaction between a proton and an $OH^{\bullet}$ radical causing indirect strand breakage was set at 0.405. The chemical reaction simulations were limited to 5 ns, with a radical kill distance of 9 nm, beyond which chemical tracks were removed.

Defining and Scoring DNA Damage

The GEANT4-DNA simulations quantified DNA damage based on complexity and interaction type, adopting the damage classification scheme proposed by Nikjoo et al. [176]. This scheme includes single strand breaks (SSB), double strand breaks (DSB), and their more complex variants (DSB+, and DSB++), as well as by the source of damage (direct, indirect, mixed, and hybrid), as shown in Figure 6.8. A DSB refers to the occurrence of lesions at opposite DNA strands within 10 base pairs of each other. A more complex form, DSB+, denotes a DSB accompanied by an additional lesion on one of the DNA strands within 10 base pairs of the break site. An even more complex variant, DSB++,

indicates the occurrence of at least two DSBs within a segment of the chromatin fiber, with a default segment length of 100 base pairs. Additional lesions may include oxidized bases, cross-links, or further strand breaks [121]. Direct damage (DSB_D) is caused by the direct interaction of protons with the DNA molecule itself, while indirect damage (DSB_I) occurs as a result of interactions between protons and other cellular components, such as water, leading to the production of reactive oxygen species or other free radicals. Subsequently, these radicals interact with the DNA molecule, causing oxidative damage to the DNA bases or inducing strand breaks [80]. In cases where a DSB is attributed to both direct and indirect damage, it is classified as hybrid (DSB_{HYB}), and if the DSB is caused by direct damage, together with another lesion caused by indirect damage, it is defined as DSB mixed (DSB_M).

TABLE 6.1: GEANT4-DNA damage parameter values and chemistry limits used in the "moleculardna" example. R_{dir} is the direct interaction range in Å, E_{min}^{break} and E_{max}^{break} are the lower and upper values for direct damage in eV, P_{OH}^{break} is the probability of a chemical reaction to cause indirect strand damage, T_{chem} is the time limit of chemical diffusion in ns, and d_{kill}^{chem} is the radical kill distance in nm.

Parameter in "moleculardna" example	Value
R_{dir} (Å)	3.5
E_{min}^{break} (eV)	5
E_{max}^{break} (eV)	37.5
P_{OH}^{break}	0.405
T_{chem} (ns)	5
d_{kill}^{chem} (nm)	9

6.3 Results

6.3.1 Phase I: Biological Experiments

Irradiation at D_{20} Reduces Clonogenic Survival of FaDu Cells

The first aim of this study was to gain insights into the *in vitro* clonogenic survival of FaDu cells at different positions along the Bragg curve. A correlation is then sought between Bragg curve position associated FaDu cell survival and previously obtained experimentally-informed simulated $\overline{y_D}$ values at those positions [167]. By analyzing the clonogenic survival rates at these positions, it was intended to understand how variations in $\overline{y_D}$ affect cell survival. Figure 6.9a shows the yielded experimentally-informed simulated $\overline{y_D}$ values in keV/µm relative to the depth-dose distribution of the 150 MeV passively scattered proton Bragg curve, obtained from the work by Groenendijk et al.

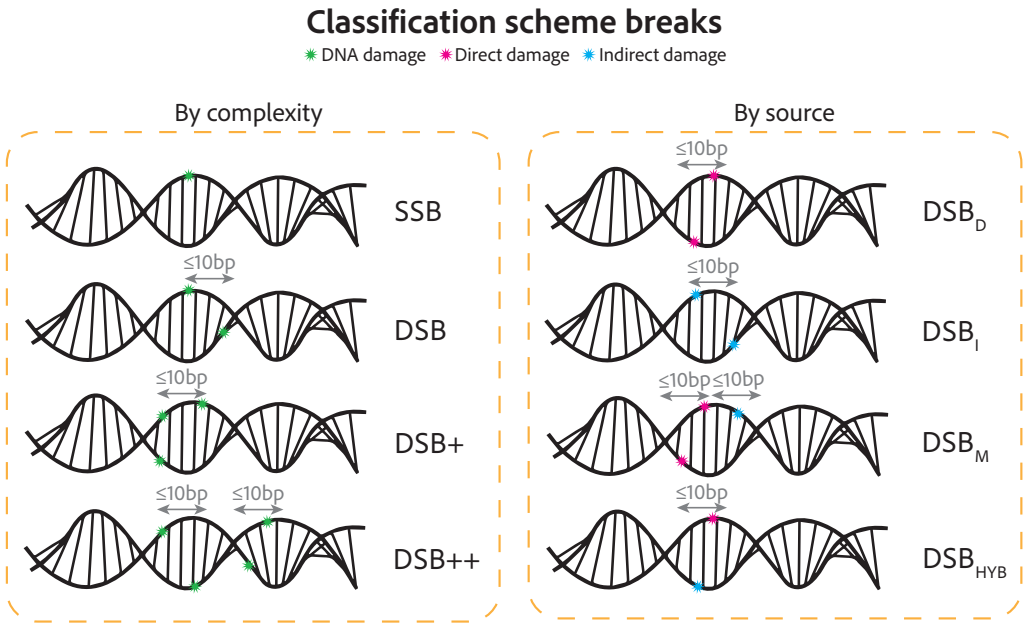

FIGURE 6.8: Classification scheme DNA breaks. DNA breaks are classified into single strand breaks (SSBs), double strand breaks (DSBs), and complex forms of DSBs (DSB+ and DSB++), along with classifications based on the damage source. A DSB refers to two lesions on opposite strands within 10 base pairs. DSB+ involves an additional lesion within 10 base pairs of the break site, while DSB++ indicates at least two DSBs within a 100-base-pair segment of chromatin. Direct damage (DSB_D) results from protons directly interacting with DNA, whereas indirect damage (DSB_I) arises from reactive species generated by proton interactions with other cellular components, such as water. Hybrid (DSB_{HYB}) occurs when both direct and indirect damage contribute to a DSB, while mixed (DSB_M) involves a combination of direct and indirect lesions.

[167], where the relative dose refers to the dose delivered at a given point along the passively scattered proton Bragg curve, expressed relative to the maximum dose at the Bragg peak. Figure 6.9b presents the results of the clonogenic survival assay after irradiation of the samples at the P_{36}, P_{80} and D_{20} positions. While the clonogenic survival of samples irradiated at P_{36} or P_{80} was not significantly different, a substantial reduction in the survival of FaDu cells was observed at the D_{20} position. Specifically, there was a 1.88-fold decrease in the dose required to induce 37% survival ($D_{37\%}$) for samples irradiated at the distal end compared to those irradiated at the plateau (Table 6.2). A slightly smaller decrease of 1.53-fold was observed for $D_{10\%}$. At this position, $\overline{y_D}$ was substantially higher (7.25 keV/µm) compared to P_{36} and P_{80} (1.10 keV/µm and 1.80 keV/µm, respectively). The marked rise in $\overline{y_D}$ at D_{20} indicates more localized energy deposition by protons, leading to increased DNA damage and, consequently, a significant decrease in cell survival.

TABLE 6.2: Overview of experimental and in silico results at the P_{36}, P_{80} and D_{20}, showing the $D_{37\%}$ and $D_{10\%}$ (Gy) determined from clonogenic survival, half-life of the 53BP1 foci $t_{1/2}$ (h), along with the experimental-informed simulated $\overline{y_D}$ values (keV/µm). The in silico results indicate the number of SSBs and DSBs per Gy per Gbp, the SSB/DSB ratio and the fraction of complex DSBs (DSB+ and DSB++) with respect to the total number of stand breaks (%).

	Experimental				in silico			
	$D_{37\%}$	$D_{10\%}$	$t_{1/2}$	$\overline{y_D}$	SSBs	DSBs	SSB/DSB	DSB+&++/SB
P_{36}	3.0	5.2	2.65±0.36	1.10	291.66	9.51	29.7	0.48%
P_{80}	2.9	4.8	2.97±0.01	1.80	282.91	10.02	27.2	0.55%
D_{20}	1.6	3.4	4.40±0.17	7.25	260.54	11.62	21.4	0.88%

Altered 53BP1 Foci Kinetics After Irradiation at D_{20}

The second aim of this study was to further comprehend the observed FaDu cell survival outcomes through examination of the kinetics of the DSB repair protein 53BP1 at the three different positions in the Bragg curve. Analyzing the number and size of 53BP1 foci provides insights into the extent and complexity of DSBs at the specific positions. Representative images of the samples stained for 53BP1 after irradiation at the three different positions in the Bragg curve and fixed at different time points are shown in Figure 6.10. The general trend in the number of 53BP1 foci per nucleus is the same for all three positions, with a strong increase in foci after 15 minutes and 2 hours, followed by gradual resolution of the 53BP1 foci, shown in Figure 6.11. For the P_{36} and P_{80} samples, the kinetics of 53BP1 foci per nucleus are similar. However, at the D_{20} position, where $\overline{y_D}$ is significantly higher, the number of 53BP1 foci is substantially greater after two hours

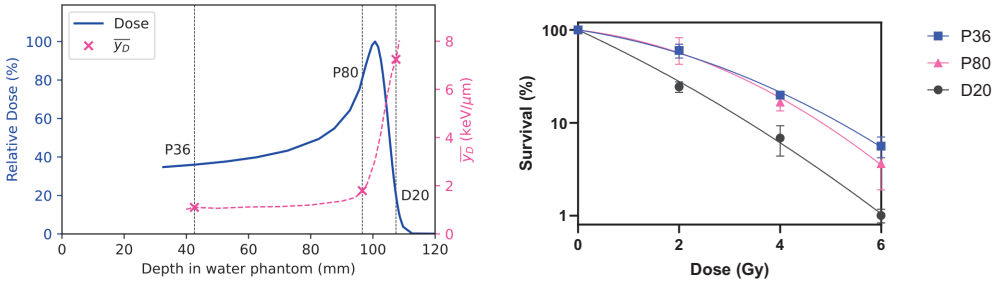

(A) (B)

FIGURE 6.9: (A) Depth-dose distribution of the 150 MeV passively scattered proton Bragg peak in the water phantom configuration, along with the experimentally-informed simulated $\overline{y_D}$ values throughout the Bragg curve. Positions used for the biological experiments are indicated by the vertical dotted black lines. (B) Clonogenic survival of FaDu cells irradiated with proton radiation at P_{36}, P_{80} and D_{20}. The mean survival of three replicate experiments was plotted. Error bars represent the standard error of the mean (S.E.M.).

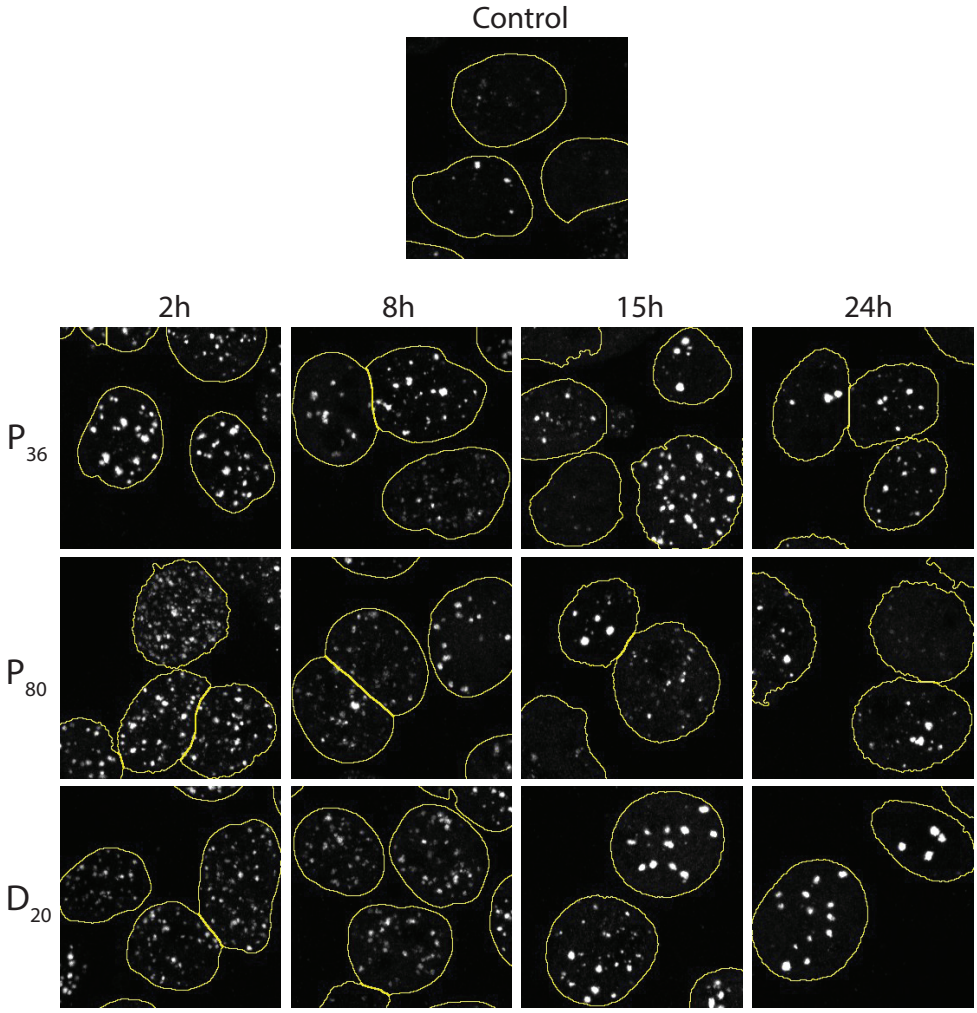

FIGURE 6.10: Representative images of immunofluorescent 53BP1 staining of FaDu cells irradiated at the P_{36}, P_{80} and D_{20} positions along the Bragg curve, at different time points indicated in the columns: at 2h, 8h, 15h and 24h post-irradiation. The FaDu nuclei are visualized with yellow contours. The bright spots indicate the 53BP1 foci.

post-irradiation and resolves more slowly compared to the P_{36} and P_{80} positions. This delay in foci resolution suggests that the DSBs are more complex and more challenging to repair. In addition to the increased number of 53BP1 foci observed at D_{20}, the size of these foci also shows notable differences. Directly after irradiation, the 53BP1 focus size decreases compared to the control sample. For the P_{36} and P_{80} positions, the foci size increases over time and aligns with the size observedin control samples after 24 hours. This indicates a similar repair response to the induced DNA damage at these positions. Conversely, samples irradiated at D_{20} exhibit a sustained increase in foci size at 18 hours

and 24 hours post-irradiation. The larger foci suggest the presence of more clustered DSBs, which requires a more intensive repair response. To determine whether there is a difference in the rate of 53BP1 resolution, the sum of two exponential curves was fitted to the 53BP1 foci per nucleus (Figure 6.11). This analysis allowed for the determination of the half-life of 53BP1 focus resolution at all three positions (Table 6.2). While the half-life is similar for the P_{36} and P_{80} samples (2.65 and 2.97 hours, respectively), the half-life of D_{20} irradiated samples is longer at 4.40 hours. These findings indicate that shortly after irradiation, D_{20} samples exhibit a higher number of 53BP1 foci that are resolved more slowly. 24 hours after irradiation at the D_{20} position, nearly all foci were resolved, however, the residual 53BP1 foci at this position were noticeably larger compared to those observed at the other two positions. The persistence and size of these foci, observed 24 hours post-irradiation, suggest the presence of complex DNA damage.

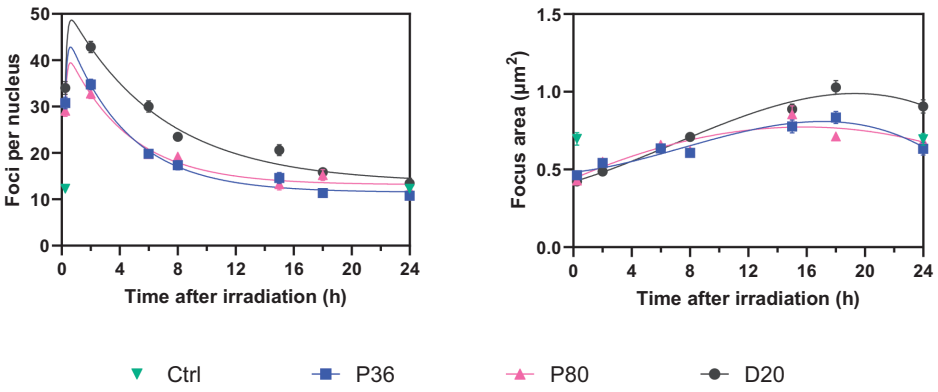

FIGURE 6.11: Quantification of the 53BP1 foci kinetics over time. The number of 53BP1 foci per nucleus (left) and the average focus size per nucleus (right) are plotted over time. Error bars represent S.E.M. Experiment was performed three times, representative data of 1 replicate is shown here.

6.3.2 Phase II: GEANT4-DNA Simulations

To evaluate the mechanistic processes underlying the observed experimental results, GEANT4-DNA simulations were used to explore the complexity of DNA damage and provide additional insights into the biological processes. Figure 6.12 illustrates the range of lineal energy values at each position along the Bragg curve, with $\overline{y_D}$ listed in Table 6.2. The corresponding proton kinetic energy spectra with mean energies of 88.2 MeV, 33.6 MeV and 12.9 MeV at P_{36}, P_{80} and D20, respectively, are presented in Chapter 5 [167]. Comparison of DNA damage yields by complexity and source following proton irradiation using three distinct proton kinetic energy spectra reveals several key insights into

the type and amounts of damage induced in the modeled FaDu cell nucleus. Analysis of break complexity, as depicted in Figure 6.13, demonstrates that while the number of SSBs decreases, the number of DSBs increases towards the distal end of the Bragg peak. Specifically, the contribution of DSBs to the total number of strand breaks is 3.3% at P_{36} and 3.5% at P_{80}, rising to 4.5% at D_{20}. This results in a reduction of the SSB-to-DSB ratio from 29.7 and 27.2 at P_{36} and P_{80}, respectively, to 21.4 at D_{20} (Table 6.2). Among the total DSBs induced, the fraction of complex DSBs (DSB+ and DSB++) is 15% at both P_{36} and P_{80} and rises to 20% at D_{20}. Relative to the total number of strand breaks, this represents a 1.7-fold increase in complex DSBs at the distal end of the Bragg peak compared to P_{36} and P_{80}. Furthermore, analysis of the source of DSBs reveals that the primary contribution to double strand breakage comes from indirect damage, although no specific trend is observed along the Bragg curve. DSBs induced through a combination of direct damage and other reactions (hybrid or indirect damage) are mostly present at D_{20}, supporting the observation of more complex DSBs at the distal end of the Bragg curve.

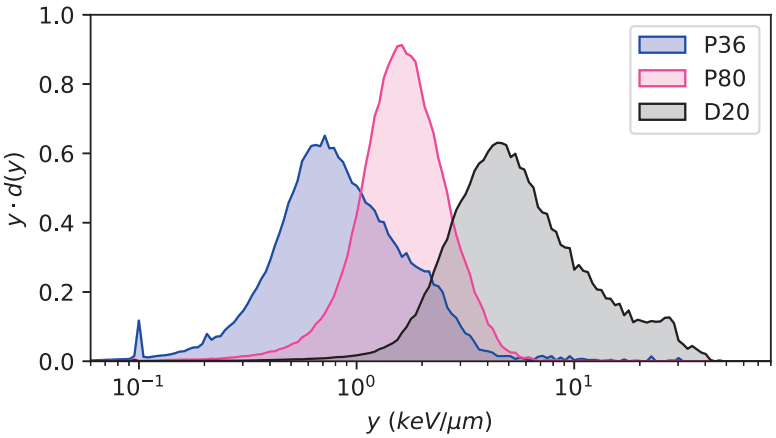

FIGURE 6.12: The acquired experimentally-informed simulated lineal energy spectra at the P_{36}, P_{80} and D_{20} positions of the Bragg curve.

6.4 Discussion

This chapter presents a novel approach by integrating experimental and in silico analyses to investigate the effects of proton irradiation along a passively scattered Bragg curve on cellular survival and DNA damage. While prior studies have focused primarily on single proton energies or broader LET ranges, this work uniquely combines: 1) biological experimental data: detailed analysis of clonogenic survival and 53BP1 foci kinetics

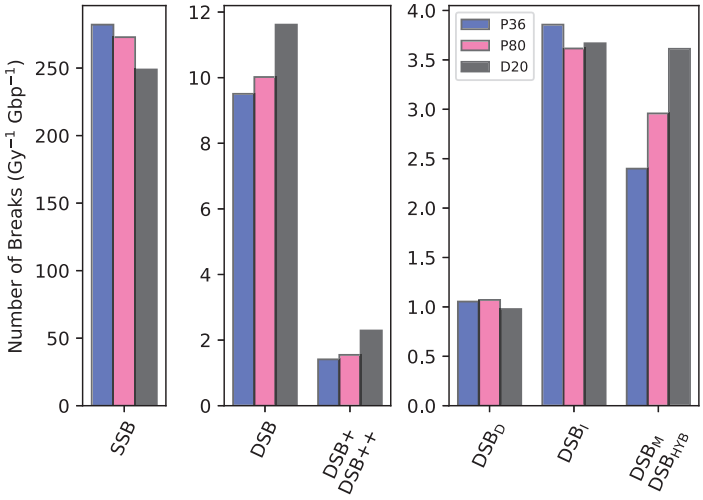

FIGURE 6.13: A bar plot of the acquired DNA damage yields using the "molecularDNA" example based on break classification (Fig. 6.8) showing single strand breaks (SSBs), double strand breaks (DSBs) and the more complex DSBs: DSB+ and DSB++. Additionally, DSBs based on source type are shown: DSBs as a result of direct damage (DSB_D), DSBs as a result of indirect damage (DSB_I) and hybrid or mixed DSBs (DSB_M / DSB_{HYB}).

across three distinct positions (P_{36}, P_{80}, and D_{20}) along the Bragg curve of a passively scattered 150 MeV proton beam, 2) simulated DNA damage complexity: experimentally-informed simulations of DNA damage complexity using GEANT4-DNA, which correlate mean lineal energy values with increased double-strand breaks (DSBs) and higher proportions of complex DSBs, and 3) integrated interpretation: directly linking experimental outcomes, such as reduced clonogenic survival and delayed 53BP1 foci resolution at D_{20}, with simulation-derived insights into DNA damage complexity at this position.

This integrated approach not only elucidates the biological effects of high LET at the distal end of the Bragg curve but also provides mechanistic insights into the increased radiobiological effectiveness observed in proton therapy. By directly correlating LET, DNA damage complexity, and cellular responses, this work advances the understanding of proton irradiation effects in a way that prior studies, limited to isolated experimental or simulation approaches, have not achieved. These findings underscore the importance of integrating experimental data with simulations to improve the understanding of proton therapy's efficacy, potentially informing treatment optimization strategies for cancer patients.

The FaDu cell line was selected as a well-established model for head and neck squamous cell carcinoma (HNSCC), a major indication for proton therapy. Focusing on a

single cell line enables us to analyze the relative effects of different positions along the Bragg curve without the confounding variability of inter-cell line differences, such as distinct radiation sensitivities and repair capacities.

A lower survival of FaDu cells is observed when samples are irradiated at the distal end of the Bragg curve, a result attributed to the higher $\overline{y_D}$ at this position, while the obtained $D_{37\%}$ and $D_{10\%}$ values for the P_{36} and P_{80} positions correlate well with other literature on X-ray and low-LET proton irradiation [177, 178, 179]. These results are consistent with previous research showing increased radiobiological effectiveness when LET increases. This has been demonstrated in various experimental models with protons of various energies, but also with heavier ions [180, 181, 182, 183, 184, 185]. The reduced survival of FaDu cells at D_{20} is accompanied by an increase in the number of 53BP1 foci and delayed foci resolution compared to P_{36} and P_{80}. This observation is supported by the simulations indicating an increased contribution of DSBs at D_{20}, which aligns with the observed experimental outcomes. In addition to the relatively increased DSBs at D_{20}, the contribution of complex DSBs increases as well, indicating greater DNA damage complexity at the distal end of the Bragg peak. These complex breaks are more challenging to repair, leading to residual damage, which manifests as persistent 53BP1 foci with increased size. Such residual breaks can eventually lead to cell death, thereby decreasing cellular survival at this position.

The increased damage complexity with higher LET is thought to contribute to the observed increase in radiobiological effectiveness. Studies on plasmid DNA irradiated with various LET have demonstrated that higher LET leads to more fragmented and complex damage, as shown by atomic force microscopy [186, 187], and electrophoresis [187]. This work focused on 53BP1 foci kinetics, which reflect complex DNA damage associated with high-LET radiation. Higher LET radiation induces more complex DNA damage, which takes longer to repair. This is consistent with previous studies on DSB induction and repair using γH2AX or 53BP1 as DSB markers, which demonstrated that higher LET results in increased break induction, followed by slower repair, with 53BP1 foci half-lives ranging from approximately 1 to 5 hours after proton irradiation [188, 189], and more residual breaks after 24 hours [188, 189, 190]. Additionally, higher LET can lead to increased 53BP1 focus size or intensity [191, 192]. The results presented here are consistent with these findings, as they align with the observed increase in simulated DNA damage complexity and residual breaks. This correlation is further supported by the in silico study, which also indicates elevated damage complexity at higher LET.

Previous research has utilized the GEANT4-DNA application to investigate DNA

damage yields induced by ionizing radiation in human fibroblasts cells, bacterial cells and human cells [76, 77, 78, 79, 80]. However, studies examining proton-induced DNA damage have primarily focused on single proton energies. This approach complicates direct comparisons with the current work, which incorporates three distinct proton energy spectra. The complexity is particularly evident at the distal end of the Bragg peak, which consists of a broad spectrum of LET values (0.08-40 keV/µm [167]), making direct comparisons with a single LET value challenging. Furthermore, when considering the mean LET values corresponding to the three proton energy spectra used in this study, as shown in Table 6.2, the available LET range is relatively narrow. This contrasts with all studies that examine a broad range of proton energies and LET values (from a few keV/µm up to 60-80 keV/µm or more), which tend to observe more pronounced differences in their results. Despite the narrower LET range, this work is unique in its detailed investigation of proton-induced DNA damage along a proton Bragg curve. Nevertheless, assuming the corresponding mean LET values to the three proton energy spectra, several comparisons can be made with other studies. Sakata et al. evaluated DNA damage in a human cell nucleus model induced by protons [75, 80]. Their findings indicated a decrease in SSB yield as a function of LET, a trend also observed in this study. Additionally, an increase in DSB yield with increasing LET was observed, and the corresponding decreasing SSB/DSB ratio. Similar trends regarding SSB and DSB yields have been observed in other studies as well [77, 78]. Chatzipapas et al. simulated DNA damage using the *moleculardna* example and analyzed DNA damage yield using the *human cell* example using mono-energetic proton energies varying between 0.15 and 66.5 MeV. They confirmed that the particle interactions become denser with increasing LET, therefore exhibiting a higher probability for DSB occurrence [193]. This observation is reflected in the SSB/DSB ratio which indicates that SSBs form DSBs more often, reflected by a DSB:SB fraction of 3.3%, 3.5% and 4.5% at P_{36}, P_{80} and D_{20}, respectively.

Additionally, the majority of the works that study proton-induced DNA damage have been limited to analyzing only SSBs and DSBs and their corresponding ratios at different proton energies. This research, however, extends beyond to explore the more complex forms of DSBs. Because of this, comparisons between DNA damage complexity and the associated source of the breaks are difficult to make. There have been studies on the contribution of indirect damage with increasing LET which stated that indirect damage decreased as LET increased, but this was only studies at higher LET values (20 to 2106 keV/µm) [194]. The discrepancy seen in this work could be attributed to the lower LET range examined, or differences in the specific conditions and models used. Finally, as highlighted in several studies, it is important to note that the quantification of SSBs and DSBs and their complexity is highly sensitive to the damage scoring parameters [75,

76, 77].

The integration of DNA damage simulations with radiobiological experiments has proven highly valuable, as it provides deeper insights into how variation in radiation quality affect biological outcomes. This approach facilitates a direct correlation between LET, DNA damage complexity and survival of FaDu cells across different positions along a passively scattered Bragg curve. Furthermore, the observed differences in 53BP1 foci kinetics and size correlate strongly with the increased DNA damage complexity identified in the simulations. Simulations alone cannot directly correlate with biological outcomes, such as cell survival or DNA damage repair kinetics, while experimental data often provides only indirect indicators of DNA damage complexity. Therefore, the integration of both approaches offers a more comprehensive understanding of the relationship between radiation quality and its biological effects.

The clear correlation between DNA damage complexity and cell survival opens up several interesting questions. One critical question is how increased DNA damage complexity affects the corresponding repair mechanisms. Cells have several DSB repair pathways available, including non-homologous end joining (NHEJ), homologous recombination (HR) and theta-mediated end joining (TMEJ), each of which plays a role depending on the structure of the break [164]. Research has shown that irradiation with high LET particles leads to increased DNA break end resection in both G1 and S/G2 cells, suggesting a reliance on TMEJ and HR. However, significant differences in resection were achieved only with heavy-ion radiation, which has much higher LET compared to protons [192, 195, 196]. While some studies show a stronger dependence on HR for repairing proton-induced DNA damage compared to photon-induced DNA damage [197, 198], others suggest this dependence is specific for high LET protons [199, 200] or occurs primarily after carbon-ion irradiation [201]. Other groups have not consistently demonstrated a stronger dependence on HR after proton radiation [202, 203]. While loss of NHEJ typically results in significant radiosensitization, this effect appears to be mostly independent of the type of radiation used [197, 198, 199, 201, 202, 203, 204]. Thus, the dominant repair pathway under different circumstances remains unclear.

The presented combination of biological experiments with simulation data presents a promising approach to unravel the mechanisms behind pathway choice. By combining radiobiological experiments with cells deficient in specific repair pathways, together with simulations, it may be possible to construct a comprehensive framework to gain more insight into the underlying mechanism of pathway choice. This approach could offer valuable insights into the mechanism guiding pathway selection and contribute to

optimizing proton therapy by enhancing the understanding of the cellular and molecular effects of proton radiation.

6.5 Conclusion

This chapter demonstrates the relationship between DNA damage complexity and the survival of head and neck squamous cell carcinoma cells irradiated at various positions along the Bragg curve. In vitro clonogenic assays and 53BP1 foci kinetics were employed to evaluate cell survival and the number and size of 53BP1 foci. These experimental observations were complemented by in silico studies to elucidate the relationship between increased $\overline{y_D}$, corresponding decreased cell survival and DNA damage complexity. The results indicate that cells irradiated at the distal end of the Bragg curve exhibit lower survival rates, increased 53BP1 foci, delayed foci resolution, and larger foci sizes compared to the plateau position and right before the Bragg peak. These findings are attributed to the higher lineal energy and increased complexity of DNA damage at D_{20}, as supported by simulation data showing a higher proportion of DSBs and complex DSBs at this location. These complex forms of DNA damage are more challenging for cells to repair efficiently, leading to persistent damage and reduced cellular survival. In contrast, irradiating cells at the plateau and at the P_{80}, where LET is lower, results in almost identical biological outcomes. This correlation between position in the Bragg curve, LET, and DNA damage complexity showed novel insights into the effects of proton radiation at cellular and molecular levels, which will be crucial to increase the efficacy of proton therapy in cancer treatment.

Chapter 7

Future Research Directions and Conclusion

This dissertation presents the development and establishment of a comprehensive radiobiological testing platform aimed at both enhancing the mechanistic understanding of biological outcomes following proton irradiation, and enabling ex vivo assessment of patient-derived tissue responses to proton irradiation, therefore facilitating a connection to clinical practice through clinical follow-up studies. The main finding of this dissertation are outlined in the following section.

7.1 Summary of Main Findings

1. The first major step in developing a radiobiological testing platform was the characterization of the HollandPTC R&D experimental proton beamline and the development of two proton irradiation platforms. This milestone was achieved and is described in Chapter 3, which presents the characterization of the beamline for both pencil beam and double passive scattering configurations. The characterization of the pencil beam configuration revealed a reduction in beam spot size at isocenter with increasing proton beam energies. At lower energies, greater beam asymmetry and a larger beam envelope in air were observed. Additionally, the Bragg peak width in water increased with higher proton beam energies, accompanied by a reduction in the peak-to-plateau ratio. With the development and optimization of a 150 MeV double passive scattering system featuring two dual-ring configurations and a two-stage brass collimator system, large fields with uniform dose distributions (98% uniformity) were achieved, enabling irradiation of biological samples. The developed proton irradiation platforms included a water phantom configuration, enabling precise irradiation of cell lines and patient-derived samples within a 10×10 cm^2 field, and an RW3 slab phantom configuration, which facilitated irradiation in a dry state using a flipper system. This well-characterized experimental environment served as a crucial first step in conducting radiobiological experiments.

2. The second step was the development of a simulation platform of the HollandPTC R&D experimental proton beamline using the Monte Carlo radiation transport modeling toolkit GEANT4: G4HPTC-R&D. This milestone was achieved and is detailed in Chapter 4. A refined beam model was developed using three experimental proton datasets to determine the non-symmetrical Gaussian pencil beam properties based on the ProBeam isochronous cyclotron's mean extraction energy. The model was benchmarked against three independent experimental datasets and demonstrated that the G4HPTC-R&D simulation platform was able to reproduce pencil beam and large field characteristics to within an accuracy on the order of

±5% at different proton beam energies. The G4HPTC-R&D platform played a crucial role in planning and optimizing radiobiological experiments by predicting beam characteristics that are difficult to measure experimentally and validating experimental results to ensure accuracy.

3. The third milestone was the 3D microdosimetric characterization of two proton irradiation platforms at the HollandPTC R&D experimental proton beamline. This milestone was achieved and is presented in Chapter 5. This step was critical for understanding cellular-level proton lineal energy distributions at the precise locations where cell lines or patient-derived samples were irradiated to understand biological outcomes. Initially, experimental microdosimetric measurements of both proton irradiation platforms were undertaken in three dimensions within the passively scattered proton Bragg curve using the 3D SOI Mushroom microdosimeter, the μ^+ probe. Subsequently, both irradiation platforms were simulated using G4HPTC-R&D, incorporating the detailed geometry and characteristics of the μ^+ probe. The application of a spectral unfolding approach, combined with a dead time correction model, enabled the generation of experimentally-informed simulated dose-averaged mean lineal energy values ($\overline{y_D}$). For the water phantom configuration, 1D-$\overline{y_D}$ characterization showed an increase from from 1.10 keV/µm in P_{36} to 1.80 keV/µm in P_{80}, reaching 7.25 keV/µm in D_{20} along the passively scattered proton Bragg curve. In the RW3 slab phantom configuration, 3D-$\overline{y_D}$ characterization exhibited a similar trend, with values increasing from 1.05 keV/µm in P_{36} to 2.04 keV/µm in P_{80}, and peaking at 8.43 keV/µm in D_{20}, with minimal variations across the 10×10 cm^2 field. These key findings offered insights into how $\overline{y_D}$ evolves along the Bragg curve across different irradiation configurations. This combined experimental and simulation approach not only validated the G4HPTC-R&D simulation platform but also enhanced the understanding of proton lineal energy distributions, supporting future correlations with biological outcomes at HollandPTC. This step represented the final stage in the establishment of a comprehensive radiobiological testing platform, enabling more precise investigations into proton effects at the cellular level.

4. The final milestone involved the application of the fully characterized radiobiological testing platform for proof-of-viability experiments with the FaDu HNSCC cell line to correlate mechanistic estimates of DNA damage and yield with biological outcomes. Clonogenic survival and DNA damage complexity, assessed by 53BP1 foci, were evaluated at various positions along the proton Bragg curve, corresponding to distinct $\overline{y_D}$ values. This milestone was achieved and is detailed

in Chapter 6. The irradiation of the FaDu HNSCC cell line in the water phantom configuration at P_{36}, P_{80}, and D_{20}, revealed that clonogenic survival correlates strongly with $\overline{y_D}$. Similar survival was observed at P_{36} ($D_{37\%}$=3.0 Gy) and P_{80} ($D_{37\%}$=2.9 Gy), but decreased survival for D_{20} ($D_{37\%}$=1.6 Gy). Assessment of 53BP1 foci showed a higher number of 53BP1 foci shorty after irradiation, slower foci resolution, and greater number of residual 53BP1 foci after 24 hours at D_{20} compared to P_{36} and P_{80}. This finding suggested the presence of unrepaired complex double-strand breaks (DSBs). To examine the mechanistic processes underlying the observed experimental results, a modified FaDu cell geometry was developed and incorporated into GEANT4-DNA. Combined with the experimentally-informed proton kinetic energy spectra at the irradiation sites from G4HPTC-R&D, this enabled the simulation of early DNA damage in FaDu cells. Irradiation at D_{20} resulted in a 1.7-fold increase in complex DSBs compared to P_{36} and P_{80}, highlighting the increased DNA damage complexity at the distal end of the Bragg curve due to increased $\overline{y_D}$. The correlation between Bragg curve position, $\overline{y_D}$, and DNA damage complexity provided novel insights into the cellular and molecular effects of proton radiation.

7.2 Future Research Directions

With the development and establishment of a comprehensive radiobiological testing platform, there is an opportunity to develop a framework for predicting individual tumor responses to radiotherapy. This can be pursued through three complementary approaches:

- A cellular mechanistic approach, which focuses on predicting radiation response at the molecular and cellular levels.
- A tissue biological approach, which utilizes patient-derived tissue samples and identified biomarkers to assess and predict radiation response.
- A patient clinical approach, which involves real-time irradiation of tumor biopsies before patient treatment to directly assess the individual tumor response and guide personalized treatment selection.

While the cellular mechanistic and tissue biological approaches are supported by a range of experiments conducted using the platform, the patient clinical approach operates independently of pre-conducted experiments. Crucially, all three approaches rely

on access to a clinical photon-based platform to enable direct proton-versus-photon comparisons. The following sections outline these approaches and their associated experiments.

7.2.1 Cellular Mechanistic Approach

Developing a predictive framework through a cellular mechanistic approach involves establishing clear links between physical characteristics – such as dose and lineal energy – and molecular and cellular processes, including DNA damage induction, protein interactions (e.g., foci kinetics), repair dynamics, and cell survival. A deeper mechanistic understanding of DNA damage types, their complexity, and the repair processes could be achieved through GEANT4-DNA simulations, providing insights into the biological effects at the molecular scale. To bridge these physical and biological factors, a series of radiobiological experiments would be required, advancing the development of a cellular mechanistic predictive framework.

Required Experiments

- The irradiation of additional HNSCC cell lines with both protons and photons and compare their survival fractions and 53BP1 foci dynamics (or other DSB markers such as γH2AX), in combination with modified GEANT4-DNA cell geometries. This would give information about variability in radiation sensitivity, enabling the assessment of inter-cell line differences in response at various positions along the Bragg curve and with different $\overline{y_D}$ values. This approach would provide a more comprehensive understanding of the biological effects of proton therapy on different tumor types.

- The creation of knockout HNSCC cell lines through the dissection of certain DNA damage repair dynamics by isolating specific molecular processes, such as homologous recombination (HR) and non-homologous end joining (NHEJ). By irradiating these knockout cell lines with protons and photons, and comparing their DNA damage response, repair kinetics, and cell survival to wild-type cell lines, these experiments provide critical insights into how different repair mechanisms influence biological outcomes following proton and photon irradiation.

- The proton and photon irradiation of DNA damage repair pathway deficient HNSCC cell lines using other methods, such as the study by Heemskerk et al., which examined the radiosensitivity of hyperthermia-induced HR-deficient FaDu cells to both protons and photons, as well as the effects of NHEJ pathway inactivation. A

key conclusion from these experiments was that HNSCC relies more on HR for repairing damage induced by proton radiation than by photon radiation [179].

The use of these radiobiological experiments could generate a comprehensive database of cell line data, serving as the foundation for developing a cellular mechanistic model capable of predicting tumor responses. Ultimately, this model could be translated into clinical practice to assess patient-specific radiosensitivity, and supporting the selection of the most appropriate radiation modality for HNSCC patients.

7.2.2 Tissue Biological Approach

The development of a predictive framework using a tissue biological approach moves a step closer to clinical relevance by employing patient-derived tissue samples to predict treatment responses. This approach necessitates a limited study in which biomarkers are identified from a large cohort of patient-derived tissue samples, irradiated with both protons and photons. In this study, the radiobiological testing platform would be utilized to conduct ex vivo assays for accurately assessing tissue radiosensitivity. The following experiments are essential for the development of a tissue biological predictive framework.

Required Experiments

- The proton irradiation of patient-derived HNSCC tumor slices. Together with the photon irradiation of patient-derived HNSCC tissue slices, this approach facilitates the evaluation of DNA repair dynamics, cell death induction, proliferation, and their relative sensitivity of these tissues to proton and photon therapy. The collaborating Department of Molecular Genetics at Erasmus MC has developed an ex vivo functional assay to evaluate the treatment response of HNSCC tissue slices ex vivo, i.e. outside the patient's body but in an environment that preserves their functionality [46].

- The proton irradiation of healthy tissue, including assessments at different positions along the proton Bragg curve, alongside photon irradiation studies at Erasmus MC. This provides critical information for determining the relative sparing of healthy tissue, thereby influencing the selection of proton or photon therapy based on the likelihood and severity of potential side effects. Pachler et al. utilized the established radiobiological testing platform to irradiate healthy oral mucosa using the ex vivo tissue culture system, investigating DNA repair dynamics, cell death induction, proliferation, and its radiosensitivity to proton and photon therapy [205].

- Investigation into the effects of ex vivo treatment on the tumor microenvironment, with a particular focus on immune cells. Radiation therapy partially modulates the immune response, particularly cytotoxic T cells and natural killer (NK) cells, which are critical for tumor cell killing. Given that the immune response may differ between proton and photon therapy, it is crucial to study how these immune cells react to each treatment modality.

During the ex vivo experiments with both proton and photon irradiation, a comprehensive analysis needs be conducted to identify potential biomarkers predictive of tumor response, focusing on DNA repair dynamics, cell death induction, proliferation, and DNA damage markers (e.g., γH2AX and 53BP1 foci) involved in HR and NHEJ pathways. These biomarkers need to be correlated with clinical outcomes, with the goal of developing a tissue biological predictive framework that facilitates the selection of the most effective radiation therapy for individual patients, based on their unique tissue profiles.

7.2.3 Patient Clinical Approach

The patient clinical approach would incorporate radiobiological testing into clinical practice to tailor treatment based on individual tumor responses, without relying on molecular or tissue models. By directly evaluating tumor radiosensitivity, this method could enable real-time treatment adjustments and could contribute to the development of a predictive model. Its implementation in clinical workflows would follow three key phases:

1. Pre-treatment phase. Tumor biopsies are collected during standard diagnostic procedures and stored in a controlled environment to maintain their viability. The radiobiological platform is then used irradiate the sample with protons, while a photon-based platform is employed for photon irradiation. Following irradiation, radiation sensitivity is assessed, and based on the response, clinicians can determine the most appropriate radiation modality.

2. Treatment phase. Throughout treatment, the radiobiological platform can be used to monitor tumor response, enabling real-time treatment adaptation. Follow-up biopsies can be analyzed to monitor changes in tumor response. If resistance develops, the radiation dose, fractionation scheme, therapeutic combinations or treatment plan can be adjusted in real time. This adaptive approach ensures therapy remains effective as the tumor evolves.

3. Post-treatment phase. The platform can contribute to ongoing patient monitoring by analyzing post-treatment biopsy samples to assess the risk of tumor relapse.

This continuous feedback loop allows for the integration of patient data into predictive models, refining future treatment strategies and advancing personalized radiotherapy.

While the concept of tailoring treatments based on individualized tumor responses is promising, it faces substantial logistical, infrastructural, and cost-related challenges. Additionally, the approach would require specialized personnel and the development of robust protocols to effectively manage and interpret the data, which may not be feasible in standard clinical settings.

7.3 Conclusion

This dissertation presents the development and establishment of a comprehensive radiobiological testing platform. It encompasses the development and characterization of two proton irradiation platforms at the HollandPTC R&D experimental proton beamline, the creation of the G4HPTC-R&D simulation platform, the 3D microdosimetric characterization of these irradiation platforms, and their successful application to irradiate FaDu HNSCC cells – demonstrating mechanistic links between proton radiation and biological outcomes. This platform not only deepens the mechanistic insight into the biological effects of proton irradiation but also facilitates ex vivo assays to evaluate patient-derived tissue responses to proton irradiation. Moreover, it offers several potential approaches for the development of a predictive framework. Most importantly, this work equips clinicians with the necessary tools to evaluate individual tumor sensitivity to proton versus photon therapy, enabling personalized radiotherapy selection for HNSCC patients and contributing to improved clinical outcomes.

Bibliography

[1] Freddie Bray et al. “Global cancer statistics 2022: GLOBOCAN estimates of incidence and mortality worldwide for 36 cancers in 185 countries”. In: *CA: a cancer journal for clinicians* 74.3 (2024), pp. 229–263. ISSN: 0007-9235.

[2] J Ferlay et al. *Global Cancer Observatory: Cancer Today. Lyon, France: International Agency for Research on Cancer*. 2024. URL: https://gco.iarc.who.int/today.

[3] Michael C Joiner and Albert J van der Kogel. *Basic clinical radiobiology*. CRC press, 2018. ISBN: 0429955405.

[4] Sara Lillo et al. “Current Status and Future Directions of Proton Therapy for Head and Neck Carcinoma”. In: *Cancers* 16.11 (2024), p. 2085. ISSN: 2072-6694.

[5] Tara A Water et al. “The potential benefit of radiotherapy with protons in head and neck cancer with respect to normal tissue sparing: a systematic review of literature”. In: *The oncologist* 16.3 (2011), pp. 366–377. ISSN: 1083-7159.

[6] Charles B Simone II et al. “Comparison of intensity-modulated radiotherapy, adaptive radiotherapy, proton radiotherapy, and adaptive proton radiotherapy for treatment of locally advanced head and neck cancer”. In: *Radiotherapy and oncology* 101.3 (2011), pp. 376–382. ISSN: 0167-8140.

[7] Sandra Nuyts et al. “Proton therapy for squamous cell carcinoma of the head and neck: early clinical experience and current challenges”. In: *Cancers* 14.11 (2022), p. 2587. ISSN: 2072-6694.

[8] Makbule Tambas et al. “Current practice in proton therapy delivery in adult cancer patients across Europe”. In: *Radiotherapy and Oncology* 167 (2022), pp. 7–13. ISSN: 0167-8140.

[9] Harald Paganetti. “Relative biological effectiveness (RBE) values for proton beam therapy. Variations as a function of biological endpoint, dose, and linear energy transfer”. In: *Physics in Medicine & Biology* 59.22 (2014), R419. ISSN: 0031-9155.

[10] Andrzej Niemierko et al. “Brain necrosis in adult patients after proton therapy: is there evidence for dependency on linear energy transfer?” In: *International Journal of Radiation Oncology* Biology* Physics* 109.1 (2021), pp. 109–119. ISSN: 0360-3016.

[11] Priyamal Silva et al. “Clinical and biological factors affecting response to radiotherapy in patients with head and neck cancer: a review”. In: *Clinical Otolaryngology* 32.5 (2007), pp. 337–345. ISSN: 1749-4478.

[12] Jean-Philippe Foy et al. “A 13-gene expression-based radioresistance score highlights the heterogeneity in the response to radiation therapy across HPV-negative HNSCC molecular subtypes”. In: *BMC medicine* 15 (2017), pp. 1–13.

[13] Paul Reid et al. “Diversity of cancer stem cells in head and neck carcinomas: The role of HPV in cancer stem cell heterogeneity, plasticity and treatment response”. In: *Radiotherapy and Oncology* 135 (2019), pp. 1–12. ISSN: 0167-8140.

[14] M Durante. “New challenges in high-energy particle radiobiology”. In: *The British journal of radiology* 87.1035 (2014), p. 20130626. ISSN: 0007-1285.

[15] Gro Elise Rødland et al. “Potential Benefits of Combining Proton or Carbon Ion Therapy with DNA Damage Repair Inhibitors”. In: *Cells* 13.12 (2024), p. 1058. ISSN: 2073-4409.

[16] Lan-ya Li et al. “DNA repair pathways in cancer therapy and resistance”. In: *Frontiers in pharmacology* 11 (2021), p. 629266. ISSN: 1663-9812.

[17] Johannes A Langendijk et al. “Clinical trial strategies to compare protons with photons”. In: *Seminars in radiation oncology*. Vol. 28. 2. Elsevier, 2018, pp. 79–87.

[18] Daniel E Johnson et al. “Head and neck squamous cell carcinoma”. In: *Nature reviews Disease primers* 6.1 (2020), p. 92. ISSN: 2056-676X.

[19] Dianne Pulte and Hermann Brenner. “Changes in survival in head and neck cancers in the late 20th and early 21st century: a period analysis”. In: *The oncologist* 15.9 (2010), pp. 994–1001. ISSN: 1083-7159.

[20] David Young et al. “Increase in head and neck cancer in younger patients due to human papillomavirus (HPV)”. In: *Oral oncology* 51.8 (2015), pp. 727–730. ISSN: 1368-8375.

[21] Harald Paganetti. *Proton beam therapy*. IOP Publishing Bristol, 2017. ISBN: 0750313706.

[22] Glenn F. Knoll. *Radiation Detection and Measurement*. Third Edition. John Wiley & Sons, 2010.

[23] Intensity Modulated Radiation Therapy Collaborative Working Group. “Intensity-modulated radiotherapy: current status and issues of interest”. In: *International Journal of Radiation Oncology Biology Physics* 51.4 (2001), pp. 880–914. ISSN: 0360-3016.

[24] Arnaud Beddok et al. "Proton therapy for head and neck squamous cell carcinomas: A review of the physical and clinical challenges". In: *Radiotherapy and Oncology* 147 (2020), pp. 30–39. ISSN: 0167-8140.

[25] Johannes A. Langendijk et al. "Impact of late treatment-related toxicity on quality of life among patients with head and neck cancer treated with radiotherapy". In: *Journal of Clinical Oncology* 26.22 (2008), pp. 3770–3776. ISSN: 0732183X. DOI: 10.1200/JCO.2007.14.6647.

[26] Annika Jakobi et al. "NTCP reduction for advanced head and neck cancer patients using proton therapy for complete or sequential boost treatment versus photon therapy". In: *Acta Oncologica* 54.9 (2015), pp. 1658–1664. ISSN: 0284-186X.

[27] Robert R Wilson. "Radiological use of fast protons". In: *Radiology* 47.5 (1946), pp. 487–491. ISSN: 0033-8419.

[28] Harald Paganetti. *Proton therapy physics*. CRC press, 2018. ISBN: 1351855751.

[29] Amy C Moreno et al. "Intensity modulated proton therapy (IMPT)-The future of IMRT for head and neck cancer". In: *Oral oncology* 88 (2019), pp. 66–74. ISSN: 1368-8375.

[30] Johannes A. Langendijk et al. "Selection of patients for radiotherapy with protons aiming at reduction of side effects: The model-based approach". In: *Radiotherapy and Oncology* 107.3 (2013), pp. 267–273. ISSN: 18790887. DOI: 10.1016/j.radonc.2013.05.007.

[31] Luca Cozzi et al. "A treatment planning comparison of 3D conformal therapy, intensity modulated photon therapy and proton therapy for treatment of advanced head and neck tumours". In: *Radiotherapy and Oncology* 61.3 (Nov. 2001), pp. 287–297. DOI: https://doi.org/10.1016/S0167-8140(01)00403-0.

[32] HollandPTC. *Research at HollandPTD*. URL: https://www.hollandptc.nl/research-at-hollandptc/.

[33] *Varian, A Siemens Healthineers Company*. URL: https://www.varian.com.

[34] HollandPTC. *First successful treatment with proton therapy in HollandPTC*. Sept. 2018. URL: https://www.tudelft.nl/en/2018/tu-delft/first-successful-treatment-with-proton-therapy-in-hollandptc.

[35] Johannes A Langendijk et al. "National protocol for model-based selection for proton therapy in head and neck cancer". In: *International journal of particle therapy* 8.1 (2021), pp. 354–365. ISSN: 2331-5180.

[36] A Peters et al. "Operational status and further enhancements of the HIT accelerator facility". In: *IPAC* 10 (2010), p. 73.

[37] S. Helmbrecht et al. “Design and implementation of a robust and cost-effective double-scattering system at a horizontal proton beamline”. In: *Journal of Instrumentation* 11.11 (Nov. 2016). ISSN: 17480221. DOI: 10.1088/1748-0221/11/11/T11001.

[38] Elke Beyreuther et al. “Research facility for radiobiological studies at the university proton therapy Dresden”. In: *International Journal of Particle Therapy* 5.1 (2018), pp. 172–182. ISSN: 2331-5180.

[39] E Griesmayer, T Schreiner, and Márius Pavlovič. “The MedAustron project”. In: *Nuclear Instruments and Methods in Physics Research Section B: Beam Interactions with Materials and Atoms* 258.1 (2007), pp. 134–138. ISSN: 0168-583X.

[40] Anders Tobias Frederiksen et al. “Evaluation of in vitro irradiation setup: Designed for the horizontal beamline at the Danish Centre for Particle Therapy”. In: *Acta Oncologica* 63 (2024), p. 19657.

[41] Neil G Burnet et al. “Proton beam therapy: perspectives on the National Health Service England clinical service and research programme”. In: *The British Journal of Radiology* 93.1107 (2020), p. 20190873. ISSN: 0007-1285.

[42] F. Tommasino et al. “Proton beam characterization in the experimental room of the Trento Proton Therapy facility”. In: *Nuclear Instruments and Methods in Physics Research, Section A: Accelerators, Spectrometers, Detectors and Associated Equipment* 869 (Oct. 2017), pp. 15–20. ISSN: 01689002. DOI: 10.1016/j.nima.2017.06.017.

[43] Francesco Tommasino et al. “A new facility for proton radiobiology at the Trento proton therapy centre: Design and implementation”. In: *Physica Medica* 58 (Feb. 2019), pp. 99–106. ISSN: 1724191X. DOI: 10.1016/j.ejmp.2019.02.001.

[44] Wojtek Hajdas et al. “The proton irradiation facility at the Paul Scherrer institute”. In: *Nuclear Instruments and Methods in Physics Research Section B: Beam Interactions with Materials and Atoms* 113.1-4 (1996), pp. 54–58. ISSN: 0168-583X.

[45] Manjit Dosanjh et al. “Overview of research and therapy facilities for radiobiological experimental work in particle therapy. Report from the European Particle Therapy Network radiobiology group”. In: *Radiotherapy and Oncology* 128.1 (2018), pp. 14–18. ISSN: 0167-8140.

[46] Marta E Capala et al. “Ex vivo functional assay for evaluating treatment response in tumor tissue of head and neck squamous cell carcinoma”. In: *Cancers* 15.2 (2023), p. 478. ISSN: 2072-6694.

[47] Dakota Horendeck et al. “High LET-like radiation tracks at the distal side of accelerated proton Bragg peak”. In: *Frontiers in Oncology* 11 (2021), p. 690042. ISSN: 2234-943X.

[48] Giuseppe A P Cirrone et al. “Clinical and research activities at the CATANA facility of INFN-LNS: from the conventional hadrontherapy to the laser-driven approach”. In: *Frontiers in oncology* 7 (2017), p. 223. ISSN: 2234-943X.

[49] Fada Guan et al. “Analysis of the track- and dose-averaged LET and LET spectra in proton therapy using the geant 4 Monte Carlo code”. In: *Medical Physics* 42.11 (Nov. 2015), pp. 6234–6247. ISSN: 24734209. DOI: 10.1118/1.4932217.

[50] Fada Guan et al. “RBE model-based biological dose optimization for proton radiobiology studies”. In: *International journal of particle therapy* 5.1 (2018), pp. 160–171. ISSN: 2331-5180.

[51] Mark Newpower et al. “Using the proton energy spectrum and microdosimetry to model proton relative biological effectiveness”. In: *International Journal of Radiation Oncology* Biology* Physics* 104.2 (2019), pp. 316–324. ISSN: 0360-3016.

[52] A Bertolet et al. “Dose-averaged LET calculation for proton track segments using microdosimetric Monte Carlo simulations”. In: *Medical physics* 46.9 (2019), pp. 4184–4192. ISSN: 0094-2405.

[53] Fada Guan et al. “Interpreting the biological effects of protons as a function of physical quantity: linear energy transfer or microdosimetric lineal energy spectrum?” In: *Scientific reports* 14.1 (Dec. 2024), p. 25181. ISSN: 20452322. DOI: 10.1038/s41598-024-73619-x.

[54] Sarah E Anderson et al. “Microdosimetric measurements of a clinical proton beam with micrometer-sized solid-state detector”. In: *Medical Physics* 44.11 (2017), pp. 6029–6037. ISSN: 0094-2405.

[55] A Bianchi et al. “Microdosimetric measurements for LET monitoring in proton therapy. The development of engineered mini-TEPCs for clinical applications: First results”. In: *Radiation Measurements* 177 (2024), p. 107271. ISSN: 1350-4487.

[56] Linh T Tran et al. “Characterization of proton pencil beam scanning and passive beam using a high spatial resolution solid-state microdosimeter”. In: *Med. Phys* 44.11 (2017). DOI: 10.1002/mp.12563. URL: https://doi.org/10.1002/mp.12563%5D.

[57] Oluwasayo Loto et al. “Simultaneous measurements of dose and microdosimetric spectra in a clinical proton beam using a scCVD diamond membrane microdosimeter”. In: *Sensors* 21.4 (2021), p. 1314. ISSN: 1424-8220.

[58] V. Conte et al. “Microdosimetry at the CATANA 62 MeV proton beam with a sealed miniaturized TEPC”. In: *Physica Medica* 64 (Aug. 2019), pp. 114–122. ISSN: 1724191X. DOI: 10.1016/j.ejmp.2019.06.011.

[59] Valeria Conte et al. "Microdosimetry of a therapeutic proton beam with a mini-TEPC and a MicroPlus-Bridge detector for RBE assessment". In: *Physics in Medicine & Biology* 65.24 (2020), p. 245018. ISSN: 0031-9155.

[60] Benjamin James et al. "In-field and out-of-field microdosimetric characterisation of a 62 MeV proton beam at CATANA". In: *Medical Physics* 48.8 (Aug. 2021), pp. 4532–4541. ISSN: 00942405. DOI: 10.1002/mp.14905.

[61] S. Agosteo et al. "A solid state microdosimeter based on a monolithic silicon telescope". In: *Radiation Protection Dosimetry* 122.1-4 (Dec. 2006), pp. 382–386. ISSN: 01448420. DOI: 10.1093/rpd/ncl468.

[62] C. Verona et al. "Toward the use of single crystal diamond based detector for ion-beam therapy microdosimetry". In: *Radiation Measurements* 110 (Mar. 2018), pp. 25–31. ISSN: 13504487. DOI: 10.1016/j.radmeas.2018.02.001.

[63] L De Nardo et al. "Mini-TEPCs for radiation therapy". In: *Radiation Protection Dosimetry* 108.4 (Apr. 2004), pp. 345–352. ISSN: 0144-8420. DOI: 10.1093/rpd/nch023. URL: https://doi.org/10.1093/rpd/nch023.

[64] Ioanna Kyriakou et al. "Review of the geant4-dna simulation toolkit for radiobiological applications at the cellular and dna level". In: *Cancers* 14.1 (Jan. 2022). ISSN: 20726694. DOI: 10.3390/cancers14010035.

[65] Werner Friedland et al. "Track structures, DNA targets and radiation effects in the biophysical Monte Carlo simulation code PARTRAC". In: *Mutation Research/Fundamental and Molecular Mechanisms of Mutagenesis* 711.1-2 (2011), pp. 28–40. ISSN: 0027-5107.

[66] Yusuke Matsuya et al. "Verification of KURBUC-based ion track structure mode for proton and carbon ions in the PHITS code". In: *Physics in Medicine & Biology* 66.6 (2021), 06NT02. ISSN: 0031-9155.

[67] Ianik Plante and Francis A Cucinotta. "Multiple CPU computing: the example of the code RITRACKS". In: *Computational Intelligence Methods for Bioinformatics and Biostatistics: 9th International Meeting, CIBB 2012, Houston, TX, USA, July 12-14, 2012 Revised Selected Papers 9*. Springer, 2013, pp. 12–25. ISBN: 3642383416.

[68] V A Semenenko, J E Turner, and T B Borak. "NOREC, a Monte Carlo code for simulating electron tracks in liquid water". In: *Radiation and environmental biophysics* 42 (2003), pp. 213–217. ISSN: 0301-634X.

[69] J Schuemann et al. "TOPAS-nBio: an extension to the TOPAS simulation toolkit for cellular and sub-cellular radiobiology". In: *Radiation research* 191.2 (2019), pp. 125–138. ISSN: 0033-7587.

[70] S. Incerti et al. "Geant4-DNA example applications for track structure simulations in liquid water: A report from the Geant4-DNA Project". In: *Medical Physics* 45.8 (Aug. 2018), e722–e739. ISSN: 24734209. DOI: 10.1002/mp.13048.

[71] Hoang Ngoc Tran et al. "Review of chemical models and applications in Geant4-DNA: Report from the ESA BioRad III Project". In: *Medical Physics* (2024). ISSN: 0094-2405.

[72] Mario A Bernal et al. "Track structure modeling in liquid water: A review of the Geant4-DNA very low energy extension of the Geant4 Monte Carlo simulation toolkit". In: *Physica Medica* 31.8 (2015), pp. 861–874. ISSN: 1120-1797.

[73] S Incerti et al. "The Geant4-DNA Project". In: *International Journal of Modeling, Simulation, and Scientific Computing* 01.02 (June 2010), pp. 157–178. ISSN: 1793-9623. DOI: 10.1142/S1793962310000122.

[74] S. Incerti et al. "Comparison of GEANT4 very low energy cross section models with experimental data in water". In: *Medical Physics* 37.9 (2010), pp. 4692–4708. ISSN: 00942405. DOI: 10.1118/1.3476457.

[75] Dousatsu Sakata et al. "Fully integrated Monte Carlo simulation for evaluating radiation induced DNA damage and subsequent repair using Geant4-DNA". In: *Scientific Reports* 10.1 (Dec. 2020). ISSN: 20452322. DOI: 10.1038/s41598-020-75982-x.

[76] Nathanael Lampe et al. "Mechanistic DNA damage simulations in Geant4-DNA Part 2: Electron and proton damage in a bacterial cell". In: *Physica Medica* 48 (Apr. 2018), pp. 146–155. ISSN: 1724191X. DOI: 10.1016/j.ejmp.2017.12.008.

[77] Konstantinos Chatzipapas et al. "Geant4-DNA simulation of human cancer cells irradiation with helium ion beams". In: *Physica Medica* 112 (Aug. 2023). ISSN: 1724191X. DOI: 10.1016/j.ejmp.2023.102613.

[78] Wook-Geun Shin et al. "A Geant4-DNA Evaluation of Radiation-Induced DNA Damage on a Human Fibroblast". In: (2021). DOI: 10.3390/cancers13194940. URL: https://doi.org/10.3390/cancers13194940.

[79] Sylvain Meylan et al. "Simulation of early DNA damage after the irradiation of a fibroblast cell nucleus using Geant4-DNA". In: *Scientific reports* 7.1 (2017), p. 11923. ISSN: 2045-2322.

[80] Dousatsu Sakata et al. "Evaluation of early radiation DNA damage in a fractal cell nucleus model using Geant4-DNA". In: *Physica Medica* 62 (June 2019), pp. 152–157. ISSN: 1724191X. DOI: 10.1016/j.ejmp.2019.04.010.

[81] Dieter Schardt, Thilo Elsässer, and Daniela Schulz-Ertner. "Heavy-ion tumor therapy: Physical and radiobiological benefits". In: *Reviews of modern physics* 82.1 (2010), pp. 383–425. ISSN: 1539-0756.

[82] Gabriel O Sawakuchi et al. "Density heterogeneities and the influence of multiple Coulomb and nuclear scatterings on the Bragg peak distal edge of proton therapy beams". In: *Physics in Medicine & Biology* 53.17 (2008), p. 4605. ISSN: 0031-9155.

[83] Wayne D. Newhauser and Rui Zhang. "The physics of proton therapy". In: *Physics in Medicine and Biology* 60.8 (Apr. 2015), R155–R209. ISSN: 13616560. DOI: 10.1088/0031-9155/60/8/R155.

[84] ICRU. "ICRU Report 19: Radiation Quantities and Units". In: *Journal of the ICRU* (1972).

[85] Harald H Rossi. "Specification of radiation quality". In: *Radiation Research* 10.5 (1959), pp. 522–531. ISSN: 0033-7587.

[86] Raymond E Zirkle, Dorothy F Marchbank, and Kathryn D Kuck. *Exponential and sigmoid survival curves resulting from alpha and x irradiation of Aspergillus spores*. Tech. rep. 1951.

[87] M A Hill. "Radiation damage to DNA: the importance of track structure". In: *Radiation measurements* 31.1-6 (1999), pp. 15–23. ISSN: 1350-4487.

[88] Jan J. Wilkens and Uwe Oelfke. "Analytical linear energy transfer calculations for proton therapy". In: *Medical Physics* 30.5 (May 2003), pp. 806–815. ISSN: 00942405. DOI: 10.1118/1.1567852.

[89] W Rosenzweig and H H Rossi. "Determination of the quality of the absorbed dose delivered by monoenergetic neutrons". In: *Radiation Research* 10.5 (1959), pp. 532–544. ISSN: 0033-7587.

[90] Marco Zaider and Harald H. Rossi. *Microdosimetry And Its Applications*. Springer Berlin, Heidelberg, Dec. 2011. ISBN: 978-3-642-85184-1. DOI: https://doi.org/10.1007/978-3-642-85184-1.

[91] ICRU. *Report No. 36, Microdosimetry*. 1983.

[92] L W Brackenbush. *Using tissue equivalent proportional counters to determine dose equivalent*. Tech. rep. 1991.

[93] Syed Naeem Ahmed. *Physics and engineering of radiation detection*. Academic Press, 2007. ISBN: 0080569641.

[94] Ugo Fano. "Note on the Bragg-Gray cavity principle for measuring energy dissipation". In: *Radiation Research* 1.3 (1954), pp. 237–240. ISSN: 0033-7587.

[95] M Missiaggia et al. "A novel hybrid microdosimeter for radiation field characterization based on the tissue equivalent proportional counter detector and low gain avalanche detectors tracker: A feasibility study". In: *Frontiers in Physics* 8 (2021), p. 578444. ISSN: 2296-424X.

[96] Linh T Tran. "Advanced semiconductor silicon detector for dosimetry and microdosimetry in radiation protection and hadron therapy". In: (Jan. 2014). URL: https://ro.uow.edu.au/articles/thesis/Advanced_semiconductor_silicon_detector_for_dosimetry_and_microdosimetry_in_radiation_protection_and_hadron_therapy/27660105.

[97] Anatoly B. Rosenfeld. "Novel detectors for silicon based microdosimetry, their concepts and applications". In: *Nuclear Instruments and Methods in Physics Research, Section A: Accelerators, Spectrometers, Detectors and Associated Equipment* 809 (Feb. 2016), pp. 156–170. ISSN: 01689002. DOI: 10.1016/j.nima.2015.08.059.

[98] Linh T. Tran et al. "Silicon 3d microdosimeters for advanced quality assurance in particle therapy". In: *Applied Sciences (Switzerland)* 12.1 (Jan. 2022). ISSN: 20763417. DOI: 10.3390/app12010328.

[99] S. Guatelli et al. "Tissue equivalence correction in silicon microdosimetry for protons characteristic of the LEO space environment". In: *IEEE Transactions on Nuclear Science* 55.6 (Dec. 2008), pp. 3407–3413. ISSN: 00189499. DOI: 10.1109/TNS.2008.2006894.

[100] D Bolst et al. "Correction factors to convert microdosimetry measurements in silicon to tissue in 12 C ion therapy". In: *Physics in Medicine and Biology* 62.6 (2017), pp. 2055–2069. URL: https://ro.uow.edu.au/eispapers/6635.

[101] S. Muraro, G. Battistoni, and A. C. Kraan. *Challenges in Monte Carlo Simulations as Clinical and Research Tool in Particle Therapy: A Review*. Nov. 2020. DOI: 10.3389/fphy.2020.567800.

[102] S. Ulam and J. Von Neumann. "On combination of deterministic and stochastic processes". In: *The Summer Meeting in New Haven*. Vol. 53. 1947, p. 1120.

[103] Hyojun Park et al. "Monte Carlo methods for device simulations in radiation therapy". In: *Physics in Medicine & Biology* 66.18 (2021), 18TR01. ISSN: 0031-9155.

[104] Walter R Nelson and Richard L Ford. *The EGS Code System: Computer Programs for the Monte Carlo Simulation of Electromagnetic Cascade Showers (version 3)*. Stanford Linear Accelerator Center, 1978.

[105] Laurie S Waters et al. "The MCNPX Monte Carlo radiation transport code". In: *AIP conference Proceedings* 896.1 (2007), pp. 81–90.

[106] T Goorley et al. "Features of MCNP6". In: *SNA+ MC 2013-joint international conference on supercomputing in nuclear applications+ Monte Carlo* (2014), p. 06011.

[107] Alberto Fasso et al. *FLUKA: a multi-particle transport code*. Tech. rep. 2005.

[108] T T Böhlen et al. "The FLUKA code: developments and challenges for high energy and medical applications". In: *Nuclear data sheets* 120 (2014), pp. 211–214. ISSN: 0090-3752.

[109] Francesc Salvat et al. "PENELOPE, and algorithm and computer code for Monte Carlo simulation of electron-photon showers". In: (1996).

[110] S. Agostinelli et al. "GEANT4 - A simulation toolkit". In: *Nuclear Instruments and Methods in Physics Research, Section A: Accelerators, Spectrometers, Detectors and Associated Equipment* 506.3 (July 2003), pp. 250–303. ISSN: 01689002. DOI: 10.1016/S0168-9002(03)01368-8.

[111] J. Allison et al. "Geant4 developments and applications". In: *IEEE Transactions on Nuclear Science* 53.1 (Feb. 2006), pp. 270–278. ISSN: 00189499. DOI: 10.1109/TNS.2006.869826.

[112] J. Allison et al. "Recent developments in GEANT4". In: *Nuclear Instruments and Methods in Physics Research, Section A: Accelerators, Spectrometers, Detectors and Associated Equipment* 835 (Nov. 2016), pp. 186–225. ISSN: 01689002. DOI: 10.1016/j.nima.2016.06.125.

[113] *Geant4 home page*. URL: http://cern.ch/geant4/.

[114] Geant4 Collaboration. "Physics reference manual". In: (2020).

[115] Jeremy M.C. Brown, David Boardman, and Alison Flynn. *A condensed overview of sub-geV hadronic physics in GEANT4*. Tech. rep. Lucas Heights: NSW: Australian Nuclear Science and Technology Organisation, 2022.

[116] Claudia Patrignani et al. "Review of particle physics". In: (2016). ISSN: 1674-1137.

[117] P F Rose. *ENDF-201: ENDF/B-VI summary documentation*. Tech. rep. 1991.

[118] S Chauvie et al. "Geant4 physics processes for microdosimetry simulation: design foundation and implementation of the first set of models". In: *IEEE Transactions on Nuclear Science* 54.6 (2007), pp. 2619–2628. ISSN: 0018-9499.

[119] C Villagrasa, Z Francis, and S Incerti. "Physical models implemented in the GEANT4-DNA extension of the GEANT-4 toolkit for calculating initial radiation damage at the molecular level". In: *Radiation protection dosimetry* 143.2-4 (2011), pp. 214–218. ISSN: 1742-3406.

[120] Z Francis et al. "Molecular scale track structure simulations in liquid water using the Geant4-DNA Monte-Carlo processes". In: *Applied radiation and isotopes* 69.1 (2011), pp. 220–226. ISSN: 0969-8043.

[121] Konstantinos P. Chatzipapas et al. "Simulation of DNA damage using Geant4-DNA: an overview of the "molecularDNA" example application". In: *Precision Radiation Oncology* 7.1 (Mar. 2023), pp. 4–14. ISSN: 23987324. DOI: 10.1002/pro6.1186.

[122] W-G Shin et al. "Evaluation of the influence of physical and chemical parameters on water radiolysis simulations under MeV electron irradiation using Geant4-DNA". In: *Journal of Applied Physics* 126.11 (2019). ISSN: 0021-8979.

[123] Ianik Plante and Luc Devroye. "Considerations for the independent reaction times and step-by-step methods for radiation chemistry simulations". In: *Radiation Physics and Chemistry* 139 (2017), pp. 157–172. ISSN: 0969-806X.

[124] *Geant4-DNA "molecularDNA" documentation*. URL: https://geant4-dna.github.io/molecular-docs.

[125] *Geant4-DNA home page*. URL: http://geant4-dna.org.

[126] M. Rovituso et al. "Characterisation of the HollandPTC R&D proton beamline for physics and radiobiology studies". In: *Physica Medica* 130 (Jan. 2025), p. 104883. ISSN: 11201797. DOI: 10.1016/j.ejmp.2024.104883.

[127] Thomas Bortfeld. "An analytical approximation of the Bragg curve for therapeutic proton beams". In: *Medical Physics* 24.12 (1997), pp. 2024–2033. ISSN: 00942405. DOI: 10.1118/1.598116.

[128] Yoshihisa Takada. "Dual-Ring Double Scattering Method for ProtonBeam Spreading". In: *Japanese Journal of Applied Physics To* 33 (1994), p. 353.

[129] Yoshihisa Takada. "Optimum solution of dual-ring double-scattering system for an incident beam with given phase space for proton beam spreading". In: *Nuclear Instruments and Methods in Physics Research Section A: Accelerators, Spectrometers, Detectors and Associated Equipment* 485.3 (2002), pp. 255–276. ISSN: 0168-9002.

[130] Yuri Simeonov et al. "3D range-modulator for scanned particle therapy: development, Monte Carlo simulations and experimental evaluation". In: *Physics in Medicine & Biology* 62.17 (2017), p. 7075. ISSN: 0031-9155.

[131] Yuri Simeonov et al. "Monte Carlo simulations and dose measurements of 2D range-modulators for scanned particle therapy". In: *Zeitschrift fur Medizinische Physik* 31.2 (May 2021), pp. 203–214. ISSN: 18764436. DOI: 10.1016/j.zemedi.2020.06.008.

[132] David J. Brenner et al. “Reduction of the secondary neutron dose in passively scattered proton radiotherapy, using an optimized pre-collimator/collimator”. In: *Physics in Medicine and Biology* 54.20 (2009), pp. 6065–6078. ISSN: 00319155. DOI: 10.1088/0031-9155/54/20/003.

[133] Yu-Mi Kim et al. “Beam characterization of the low-flux proton beam line at KOMAC for application to radiation effect testing”. In: *Nuclear Instruments and Methods in Physics Research Section A: Accelerators, Spectrometers, Detectors and Associated Equipment* 950 (2020), p. 162971. ISSN: 0168-9002.

[134] Celebrity F. Groenendijk et al. “A Geant4 based simulation platform of the HollandPTC R&D proton beamline for radiobiological studies”. In: *Physica Medica* 112 (Aug. 2023). ISSN: 1724191X. DOI: 10.1016/j.ejmp.2023.102643.

[135] Paola Scampoli et al. “Low-energy light ion irradiation beam-line for radiobiological studies”. In: *Nuclear Instruments and Methods in Physics Research Section B: Beam Interactions with Materials and Atoms* 174.3 (2001), pp. 337–343. ISSN: 0168-583X.

[136] J. Constanzo et al. “Radiograaff, a proton irradiation facility for radiobiological studies at a 4 MV Van de Graaff accelerator”. In: *Nuclear Instruments and Methods in Physics Research, Section B: Beam Interactions with Materials and Atoms* 334 (Sept. 2014), pp. 52–58. ISSN: 0168583X. DOI: 10.1016/j.nimb.2014.05.005.

[137] Tordis J Dahle et al. “Monte Carlo simulations of a low energy proton beamline for radiobiological experiments”. In: *Acta Oncologica* 56.6 (2017), pp. 779–786. ISSN: 0284-186X.

[138] Anna Baratto-Roldán et al. “Preparation of a radiobiology beam line at the 18 MeV proton cyclotron facility at CNA”. In: *Physica Medica* 74 (2020), pp. 19–29. ISSN: 1120-1797.

[139] Mihai Straticiuc et al. “New setup for basic radiobiology studies using a 3 MV TandetronTM: Design and developments”. In: *Nuclear Instruments and Methods in Physics Research Section B: Beam Interactions with Materials and Atoms* 528 (2022), pp. 45–53. ISSN: 0168-583X.

[140] Kento Nomura et al. “Biological effects of passive scattering and spot scanning proton beams at the distal end of the spread-out Bragg peak in single cells and multicell spheroids”. In: *International Journal of Radiation Biology* 97.5 (2021), pp. 695–703. ISSN: 0955-3002.

[141] P Arce et al. “Report on G4-Med, a Geant4 benchmarking system for medical physics applications developed by the Geant4 Medical Simulation Benchmarking Group”. In: *Med. Phys* 48.1 (2021).

[142] J Schuemann et al. "Site-specific range uncertainties caused by dose calculation algorithms for proton therapy". In: *Physics in Medicine & Biology* 59.15 (2014), p. 4007. ISSN: 0031-9155.

[143] Daniel A Low et al. "A technique for the quantitative evaluation of dose distributions". In: *Medical physics* 25.5 (1998), pp. 656–661. ISSN: 0094-2405.

[144] Mohammad Hussein, C H Clark, and Andrew Nisbet. "Challenges in calculation of the gamma index in radiotherapy–towards good practice". In: *Physica Medica* 36 (2017), pp. 1–11. ISSN: 1120-1797.

[145] H. Paganetti et al. "Accurate Monte Carlo simulations for nozzle design, commissioning and quality assurance for a proton radiation therapy facility". In: *Medical Physics* 31.7 (2004), pp. 2107–2118. ISSN: 00942405. DOI: 10.1118/1.1762792.

[146] F. Fracchiolla et al. "Characterization and validation of a Monte Carlo code for independent dose calculation in proton therapy treatments with pencil beam scanning". Oct. 2015. DOI: 10.1088/0031-9155/60/21/8601.

[147] Andreas F Resch et al. "Evaluation of electromagnetic and nuclear scattering models in GATE/Geant4 for proton therapy". In: *Medical Physics* 46.5 (2019), pp. 2444–2456. ISSN: 0094-2405.

[148] Gary A Ezzell et al. "IMRT commissioning: multiple institution planning and dosimetry comparisons, a report from AAPM Task Group 119". In: *Medical physics* 36.11 (2009), pp. 5359–5373. ISSN: 0094-2405.

[149] Leland Muller et al. "A complete workflow for utilizing Monte Carlo toolkits in clinical cases for a double-scattering proton therapy system". In: *Journal of applied clinical medical physics* 20.1 (2019), pp. 23–30. ISSN: 1526-9914.

[150] Mark A. Hill. "Track to the future: historical perspective on the importance of radiation track structure and DNA as a radiobiological target". In: *International Journal of Radiation Biology* 94.8 (July 2018), pp. 759–768. ISSN: 13623095. DOI: 10.1080/09553002.2017.1387304.

[151] Giorgio Baiocco et al. "A matter of space: how the spatial heterogeneity in energy deposition determines the biological outcome of radiation exposure". In: *Radiation and Environmental Biophysics* 61.4 (Nov. 2022), pp. 545–559. ISSN: 14322099. DOI: 10.1007/s00411-022-00989-z.

[152] Aimee L. McNamara, Jan Schuemann, and Harald Paganetti. "A phenomenological relative biological effectiveness (RBE) model for proton therapy based on all published in vitro cell survival data". In: *Physics in Medicine and Biology* 60.21 (Oct. 2015), pp. 8399–8416. ISSN: 13616560. DOI: 10.1088/0031-9155/60/21/8399.

[153] Linh T. Tran et al. "A novel silicon microdosimeter using 3D sensitive volumes: Modeling the response in neutron fields typical of aviation". In: *IEEE Transactions on Nuclear Science* 61.4 (2014), pp. 1552–1557. ISSN: 00189499. DOI: 10.1109/TNS.2014.2298461.

[154] Linh T. Tran et al. "Thin Silicon Microdosimeter Utilizing 3-D MEMS Fabrication Technology: Charge Collection Study and Its Application in Mixed Radiation Fields". In: *IEEE Transactions on Nuclear Science* 65.1 (Jan. 2018), pp. 467–472. ISSN: 00189499. DOI: 10.1109/TNS.2017.2768062.

[155] Jana Kretschmer et al. "Monte Carlo simulated beam quality and perturbation correction factors for ionization chambers in monoenergetic proton beams". In: *Medical Physics* 47.11 (Nov. 2020), pp. 5890–5905. ISSN: 24734209. DOI: 10.1002/mp.14499.

[156] Shoaib Usman and Amol Patil. "Radiation detector deadtime and pile up: A review of the status of science". In: *Nuclear Engineering and Technology* 50.7 (2018), pp. 1006–1016. ISSN: 1738-5733.

[157] Mohammad-Reza Mohammadian-Behbahani and Shahyar Saramad. "A comparison study of the pile-up correction algorithms". In: *Nuclear Instruments and Methods in Physics Research Section A: Accelerators, Spectrometers, Detectors and Associated Equipment* 951 (2020), p. 163013. ISSN: 0168-9002.

[158] Lucian Wielopolski and Robin P Gardner. "Prediction of the pulse-height spectral distortion caused by the peak pile-up effect". In: *Nuclear Instruments and Methods* 133.2 (1976), pp. 303–309. ISSN: 0029-554X.

[159] Marta Missiaggia et al. "Investigation of In-Field and Out-of-Field Radiation Quality With Microdosimetry and Its Impact on Relative Biological Effectiveness in Proton Therapy". In: *International Journal of Radiation Oncology Biology Physics* 115.5 (Apr. 2023), pp. 1269–1282. ISSN: 1879355X. DOI: 10.1016/j.ijrobp.2022.11.037.

[160] Tim Heemskerk et al. "Position in proton Bragg curve influences DNA damage complexity and survival in head and neck cancer cells". In: *Clinical and Translational Radiation Oncology* 51 (Mar. 2025), p. 100908. ISSN: 24056308. DOI: 10.1016/j.ctro.2024.100908.

[161] Konstantinos P Chatzipapas et al. "Ionizing radiation and complex DNA damage: quantifying the radiobiological damage using Monte Carlo simulations". In: *Cancers* 12.4 (2020), p. 799. ISSN: 2072-6694.

[162] Wei Liu et al. “Investigation on the correlation between energy deposition and clustered DNA damage induced by low-energy electrons”. In: *Radiation and Environmental Biophysics* 57.2 (May 2018), pp. 179–187. ISSN: 0301634X. DOI: 10.1007/s00411-018-0730-0.

[163] Stephen J McMahon and Kevin M Prise. “Mechanistic modelling of radiation responses”. In: *Cancers* 11.2 (2019), p. 205. ISSN: 2072-6694.

[164] Gerarda van de Kamp et al. “DNA Double Strand Break Repair Pathways in Response to Different Types of Ionizing Radiation”. In: *Frontiers in Genetics* 12 (Sept. 2021), p. 1771. ISSN: 16648021. DOI: 10.3389/fgene.2021.738230.

[165] J Donald Chapman and Colin J Gillespie. “Radiation-induced events and their time scale in mammalian cells”. In: *Advances in radiation biology* 9 (1981), pp. 143–198. ISSN: 0065-3292.

[166] Martin E. van Royen et al. “Compartmentalization of androgen receptor protein–protein interactions in living cells”. In: *The Journal of Cell Biology* 177.1 (Apr. 2007), pp. 63–72. ISSN: 1540-8140. DOI: 10.1083/jcb.200609178.

[167] Celebrity F. Groenendijk et al. “3D Microdosimetric Characterization of the Double Passive Scattering Proton Beamline at the Holland Proton Therapy Centre”. In: *Physics in Medicine and Biology* (2025).

[168] Nathanael Lampe. “The long term impact of ionising radiation on living systems”. PhD thesis. Université Clermont Auvergne [2017-2020], 2017.

[169] Nathanael Lampe et al. “Mechanistic DNA damage simulations in Geant4-DNA part 1: A parameter study in a simplified geometry”. In: *Physica Medica* 48 (Apr. 2018), pp. 135–145. ISSN: 1724191X. DOI: 10.1016/j.ejmp.2018.02.011.

[170] David Hilbert and David Hilbert. “Über die stetige Abbildung einer Linie auf ein Flächenstück”. In: *Dritter Band: Analysis· Grundlagen der Mathematik· Physik Verschiedenes: Nebst Einer Lebensgeschichte* (1935), pp. 1–2. ISSN: 3662376571.

[171] International Human Genome Sequencing Consortium. “Finishing the euchromatic sequence of the human genome”. In: *Nature* 431.7011 (2004), pp. 931–945. ISSN: 0028-0836.

[172] Nathanael Lampe. *FractalDNA*. 2021. URL: https://github.com/natl/fractaldna.

[173] N. Tang et al. “Influence of chromatin compaction on simulated early radiation-induced DNA damage using Geant4-DNA”. In: *Medical Physics* 46.3 (Mar. 2019), pp. 1501–1511. ISSN: 24734209. DOI: 10.1002/mp.13405.

[174] I Kyriakou et al. “The impact of new Geant4-DNA cross section models on electron track structure simulations in liquid water”. In: *Journal of Applied Physics* 119.19 (2016).

[175] I Kyriakou, S Incerti, and Z Francis. "Improvements in geant4 energy-loss model and the effect on low-energy electron transport in liquid water". In: *Medical physics* 42.7 (2015), pp. 3870–3876.

[176] H. Nikjoo et al. "Computational modelling of low-energy electron-induced DNA damage by early physical and chemical events". In: *International Journal of Radiation Biology* 71.5 (1997), pp. 467–483. ISSN: 09553002. DOI: 10.1080/095530097143798.

[177] Nathalie van den Tempel et al. "The effect of thermal dose on hyperthermia-mediated inhibition of DNA repair through homologous recombination". In: *Oncotarget* 8.27 (2017), p. 44593.

[178] Elisabeth Mara et al. "Investigating the impact of alpha/beta and LETd on relative biological effectiveness in scanned proton beams: An in vitro study based on human cell lines". In: *Medical physics* 47.8 (2020), pp. 3691–3702. ISSN: 0094-2405.

[179] Tim Heemskerk et al. "Enhanced radiosensitivity of head and neck cancer cells to proton therapy via hyperthermia-induced homologous recombination deficiency". In: *Clinical and Translational Radiation Oncology* 51 (2025), p. 100898. ISSN: 2405-6308.

[180] D. Bettega et al. "Radiobiological studies on the 65MeV therapeutic proton beam at Nice using human tumour cells". In: *International journal of radiation biology* 76.10 (2000), pp. 1297–1303. ISSN: 0955-3002.

[181] Kazufumi Kagawa et al. "Preclinical biological assessment of proton and carbon ion beams at Hyogo Ion Beam Medical Center". In: *International Journal of Radiation Oncology* Biology* Physics* 54.3 (2002), pp. 928–938. ISSN: 0360-3016.

[182] Richard A Britten et al. "Variations in the RBE for cell killing along the depth-dose profile of a modulated proton therapy beam". In: *Radiation research* 179.1 (2013), pp. 21–28. ISSN: 0033-7587.

[183] Anna Michaelidesová et al. "Relative biological effectiveness in a proton spread-out Bragg peak formed by pencil beam scanning mode". In: *Australasian Physical & Engineering Sciences in Medicine* 40 (2017), pp. 359–368. ISSN: 0158-9938.

[184] Fada Guan et al. "Spatial mapping of the biologic effectiveness of scanned particle beams: towards biologically optimized particle therapy". In: *Scientific reports* 5.1 (2015), p. 9850. ISSN: 2045-2322.

[185] Pankaj Chaudhary et al. "Relative biological effectiveness variation along monoenergetic and modulated Bragg peaks of a 62-MeV therapeutic proton beam: a preclinical assessment". In: *International Journal of Radiation Oncology* Biology* Physics* 90.1 (2014), pp. 27–35. ISSN: 0360-3016.

[186] Cara M Frame et al. “Proton induced DNA double strand breaks at the Bragg peak: Evidence of enhanced LET effect”. In: *Frontiers in oncology* 12 (2022), p. 930393. ISSN: 2234-943X.

[187] Maria P Souli et al. “Clustered DNA Damage Patterns after Proton Therapy Beam Irradiation Using Plasmid DNA”. In: *International Journal of Molecular Sciences* 23.24 (2022), p. 15606. ISSN: 1422-0067.

[188] Ana Belchior et al. “Repair Kinetics of DSB-Foci Induced by Proton and α-Particle Microbeams of Different Energies”. In: *Life* 12.12 (2022), p. 2040. ISSN: 2075-1729.

[189] Pankaj Chaudhary et al. “Variations in the processing of DNA double-strand breaks along 60-MeV therapeutic proton beams”. In: *International Journal of Radiation Oncology* Biology* Physics* 95.1 (2016), pp. 86–94. ISSN: 0360-3016.

[190] Otilija Keta et al. “DNA double-strand breaks in cancer cells as a function of proton linear energy transfer and its variation in time”. In: *International Journal of Radiation Biology* 97.9 (2021), pp. 1229–1240. ISSN: 0955-3002.

[191] Sebastian Oeck et al. “Relating linear energy transfer to the formation and resolution of DNA repair foci after irradiation with equal doses of X-ray photons, plateau, or Bragg-peak protons”. In: *International Journal of Molecular Sciences* 19.12 (2018), p. 3779. ISSN: 1422-0067.

[192] Stefan J Roobol et al. “Comparison of high-and low-LET radiation-induced DNA double-strand break processing in living cells”. In: *International Journal of Molecular Sciences* 21.18 (2020), p. 6602. ISSN: 1422-0067.

[193] Tran Ngoc Hoang et al. ““dsbandrepair”-An updated Geant4-DNA simulation tool for evaluating the radiation-induced DNA damage and its repair”. In: *Physica Medica* 124 (2024), p. 103422. ISSN: 1120-1797.

[194] Ryoichi Hirayama et al. “Contributions of direct and indirect actions in cell killing by high-LET radiations”. In: *Radiation Research* 171.2 (Feb. 2009), pp. 212–218. ISSN: 00337587. DOI: 10.1667/RR1490.1.

[195] Hirohiko Yajima et al. “The complexity of DNA double strand breaks is a critical factor enhancing end-resection”. In: *DNA Repair* 12.11 (Nov. 2013), pp. 936–946. ISSN: 15687864. DOI: 10.1016/j.dnarep.2013.08.009. URL: https://linkinghub.elsevier.com/retrieve/pii/S1568786413002140.

[196] Nicole B. Averbeck et al. “DNA end resection is needed for the repair of complex lesions in G1-phase human cells”. In: *Cell Cycle* 13.16 (Aug. 2014), pp. 2509–2516. ISSN: 15514005. DOI: 10.4161/15384101.2015.941743.

[197] Andrea O. Fontana et al. “Differential DNA repair pathway choice in cancer cells after proton- and photon-irradiation”. In: *Radiotherapy and Oncology* 116.3 (Sept. 2015), pp. 374–380. ISSN: 18790887. DOI: 10.1016/j.radonc.2015.08.014.

[198] Nicole Grosse et al. “Deficiency in homologous recombination renders mammalian cells more sensitive to proton versus photon irradiation”. In: *International Journal of Radiation Oncology Biology Physics*. Vol. 88. 1. Elsevier, Jan. 2014, pp. 175–181. DOI: 10.1016/j.ijrobp.2013.09.041.

[199] Scott J. Bright et al. “Nonhomologous End Joining Is More Important Than Proton Linear Energy Transfer in Dictating Cell Death”. In: *International Journal of Radiation Oncology Biology Physics* 105.5 (2019), pp. 1119–1125. ISSN: 1879355X. DOI: 10.1016/j.ijrobp.2019.08.011.

[200] Qin Zhou et al. “Inhibition of ATM Induces Hypersensitivity to Proton Irradiation by Upregulating Toxic End Joining”. In: *Cancer Research* 81.12 (June 2021), pp. 3333–3346. ISSN: 0008-5472. DOI: 10.1158/0008-5472.CAN-20-2960.

[201] Hongyu Ma et al. “Combining carbon ion irradiation and non-homologous end-joining repair inhibitor NU7026 efficiently kills cancer cells”. In: *Radiation Oncology* 10.1 (Nov. 2015), p. 225. ISSN: 1748717X. DOI: 10.1186/s13014-015-0536-z.

[202] Francisco D. C. Guerra Liberal, Jason L. Parsons, and Stephen J. McMahon. “Most DNA repair defects do not modify the relationship between relative biological effectiveness and linear energy transfer in CRISPR-edited cells”. In: *Medical Physics* 51.1 (Jan. 2024), pp. 591–600. ISSN: 0094-2405. DOI: 10.1002/mp.16764.

[203] Josephine Görte et al. “Comparative proton and photon irradiation combined with pharmacological inhibitors in 3D pancreatic cancer cultures”. In: *Cancers* 12.11 (Oct. 2020), pp. 1–15. ISSN: 20726694. DOI: 10.3390/cancers12113216.

[204] Ariungerel Gerelchuluun et al. “The Major DNA Repair Pathway after Both Proton and Carbon-Ion Radiation is NHEJ, but the HR Pathway is More Relevant in Carbon Ions”. In: *Radiation Research* 183.3 (Mar. 2015), pp. 345–356. ISSN: 0033-7587. DOI: 10.1667/RR13904.1.

[205] Katrin S. Pachler et al. “Development of an Ex Vivo Functional Assay for Prediction of Irradiation Related Toxicity in Healthy Oral Mucosa Tissue”. In: *International Journal of Molecular Sciences* 25.13 (July 2024). ISSN: 14220067. DOI: 10.3390/ijms25137157.

Acknowledgements

This thesis owes its existence to *"Jeremy settling an argument..."*, which I heard many times during my PhD. And I have tried to live up to it. Jeremy, we go way back, to September 2017, when you first got involved in my Master's thesis project and somehow ended up becoming my daily supervisor. It was a great project and I really enjoyed working with you. Afterwards, you helped me find an intership abroad and connected me to Kaye at the X-ray Imaging Group in the School of Physics and Astronomy at Monash University, Melbourne, Australia. That experience was incredible and I've always been deeply grateful to you for making it possible. After returning home seven months later, I started looking for a PhD. After many interviews at other institutions, you informed me about a PhD opening under your supervision at the TU Delft Reactor Institute. You convinced Danny that I could *"smash my head against the wall"*, so that I would be a great fit for the project. And that's how it all began: my PhD journey. After one year, you left TU Delft (not exactly by choice) and moved back to Australia. You had mentioned at the start of my PhD that this might happen, though I hadn't really been hoping for it. However, in the end we agreed on the positive impact it had: I grew as an independent researcher and took on more responsibility for the project. You were so involved in the first year that you nearly broke the microdosimeter, but let's keep that between us. And yes, I know I was being too direct. Even after you moved, you made yourself available to me every single week. Despite the massive time difference, you often stayed up late to meet with me (and Danny), and I have always appreciated that enormously. As you promised at the start of my PhD, you would let me visit wherever you ended up moving and you made that happen. I visited you in 2022 for three months at the Australian Nuclear Science and Technology Organisation (ANSTO), in Sydney. Thank you for making that possible, it was a fantastic experience. Later that year we went to the Geant4 International User Conference in Naples. I'll never forget that night when the fat Italian man at my Airbnb shouted at us to be quiet while rats as big as cats ran through the streets. Then, in 2024, my plan to have finished my PhD before going to Melbourne turned out to be way too ambitious. In the end, my time there turned into working with you for another six months at Swinburne University of Technology which I really enjoyed and I am grateful for how it all turned out including the thesis I ended up writing. Now, eight years later, our collaboration has come to an end, which, to be honest, makes me a bit sad. Although some might have found you a bit challenging person to work with and you often joked it's a miricle that I've managed to stick with you for such a long time, I've always enjoyed working with you. I want to thank you for everything: your supervision, support, patience, discussions, enthusiasm, jokes, swearing, understanding, and your knowledge. I have learned so much from you and was constantly amazed by how much you knew (I'll always keep on reading!). I've also appreciated all your advice on so many different areas, I'll always tell anyone with questions: Jeremy is the one to go to! Most of all, I deeply value the trust you had in me and how you supported my growth as a researcher and continuously looked for opportunities to help me develop professionally, this meant a lot to me. Last but not least, thank you for being not just a supervisor, but also a friend. It was a pleasure to work with you and I could never have done all this without you. Thanks for being the best supervisor I could have wished for.

The second person who played an important role in my PhD project is my promotor, Danny Lathouwers. Although my project probably wasn't fully aligned with your main research interests, I really appreciate that you took the time to supervise me over all these years. You always provided valuable feedback and were critical when needed. I've also appreciated your sense of humor, which I came to enjoy more and more as I got to know you better over the years. I really enjoyed being at your wedding and the trip to Maastricht with our bikes with the rest of your PhD students last summer! I'm very grateful to have worked with you Danny, and together with Jeremy, I feel truly lucky to have had both of you as supervisors. Thanks for all the support, trust and for always being there.

The collaboration with the Erasmus Medical Center in Rotterdam has always given me a lot of energy. I really enjoyed the discussions with the biology side of my project. It was very enriching to explore how to combine my physics work at TU Delft with the biological aspects at Erasmus MC within our project. A special thanks to Katrin Pachler, my colleague on this project. I truly enjoyed working with you; we made a great team. I would also like to thank Dik van Gent and Marta Capala for the collaboration and interesting discussions. Lastly, thanks to Tim Heemskerk, although you weren't officially part of my project, we found a very nice collaboration which resulted in the great work presented in Chapter 6. Furthermore, my PhD project was also conducted in collaboration with HollandPTC. For a substantial part of my project, I performed microdosimetric measurements in the experimental bunker. I spent many evenings figuring out how the microdosimeter worked, which was a really exciting challenge, as it allowed me to combine the practical and technical aspects of my project. I would like to thank Marta, Wouter and Ernst for their support and patience during those sessions. Finally, I would like to thank the funder of my project, Varian (a Siemens Healthineers company), for giving me the opportunity to carry out this research.

My time at the TU Delft Reactor Institute has been truly unforgettable. Starting in 2017 with my Master's thesis project, I really enjoyed my time with all the coffee breaks with the Applied Radiation & Isotopes group, the students involved at the time, and the people from the education group, especially Folkert, and not to mention all the drinks at 't Koepeltje! When I returned to the RID in 2020, COVID had just started. It was a strange experience not being able to get to know my colleagues, exchange the PhD life, or go out together. Fortunately, that time passed. Thanks, Marc, for being such a good friend, also outside of the RID, I really enjoyed having you as my desk neighbor. Also, Tibi, thanks for the nice conservations we had, I really appreciate how we could share our experiences, also you are an insanely good table tennis player. I would also like to thank all my fellow PhD colleagues: Mikołaj, Jelte, David, Oscar, Alessandro, Thomas, and everyone else for amazing dinners we had, the table tennis tournament, the coffee breaks, drinkt at 't Koepeltje and all other fun times.

Looking back, these five years have been full of learning and growth, and one of my propositions sums it up perfectly: *"A PhD is as much a journey of self-discovery as it is an academic pursuit, often shaping one's identity more than the research itself."* Throughout this journey I would like to thank everyone who has been involved. A huge thanks to my friends from INTENS: Mina, Lara, Marlijn, Nino, Emma, Evianne, Simone, Janine, and Ilse. Thanks for supporting me no matter what, thanks for a lot of useful advice, thanks for making me laugh, and most of all, thanks for all the amazing frietfeesten. I would also like to give a special mention to one of my best friends, whom I've known since we were four years old: Loes Priester. Loes passed away unexpectedly in January 2025, while she was so close to completing her PhD at Erasmus MC but had not yet had her defense. Big shout out to you Loes, I miss you.

Then, most importantly, my family. Although you didn't always fully understand what I was doing, and especially at the start loved the idea of me finding the cure for cancer, you did your best and gradually understood what my project was about and I always felt your support and encouragement. I want to start with thanking my mother-in-law, Annette (& Ruud), who has also completed a PhD, for the enjoyable conversations about my work and doing a PhD, it meant a lot to me to share those moments with you. Next, I would like to thank my aunt, Lia (& Frank), who also earned a doctorate, I have always loved our conversations about research and writing, and your understanding of the challenges of a PhD was very helpful. I would like to give a big thanks to my grandmother, Oma de Vos, who has always been incredibly supportive and stayed so involved during my journey.

An enormous thanks, mum & dad, for being the best. For always being by my side, loving me for who I am, and giving me unconditional love and support in everything. Your encouragement and belief in me have meant more than words can express. The same goes for you Dylhan (& Laura & your lovely son Elio), your love and support have always been invaluable.

Last but not certainly not least, my maatje and love Irene, you met me right in the middle of a stressful period, and from that moment on you were the one who kept me going. You helped me find the energy to continue my PhD and guided and supported me right up to the very last minute during our amazing adventure in Australia. Thanks for sitting through all the discussions and brainstorm sessions about my project, I'm sure you are a real expert now. I cannot imagine having completed my PhD without you by my side. Thanks for everything – I love you and you mean the world to me.

List of Publications

Journal Publications

4. Heemskerk, T.[1], **Groenendijk, C. F.**[1], Rovituso, M., van der Wal, E., van Burik, W., Chatzipapas, K., Lathouwers, D., Kanaar, R., Brown, J. M. C., & Essers, J. (2025). *Position in Proton Bragg Curve Influences DNA Damage Complexity and Survival in Head and Neck Cancer Cells*. Clinical and Translational Radiation Oncology, 100908. [1] *Shared first authorship.*

3. **Groenendijk, C. F.**, Tran, L. T., Rosenfeld, A. B., Rovituso, M., Van Burik, W., Lathouwers, D. & Brown, J. M. C. (2025). *3D Microdosimetric Characterization of the Double Passive Scattering Proton Beamline at the Holland Proton Therapy Centre*. Submitted to Physics in Medicine and Biology.

2. **Groenendijk, C. F.**, Rovituso, M., Lathouwers, D., & Brown, J. M. C. (2023). *A* GEANT4 *Based Simulation Platform of the HollandPTC R&D Proton Beamline for Radiobiological Studies*. Physica Medica, 112, 102643.

1. Rovituso, M., **Groenendijk, C. F.**, Van der Wal, E., Van Burik, W., Ibrahimi, A., Prieto, H. R., Brown, J. M. C., Weber, U., Simeonov, Y., Fontana, M., Lathouwers, D., & Hoogeman, M. (2025). *Characterisation of the HollandPTC R&D Proton Beamline for Physics and Radiobiology Studies*. Physica Medica, 130, 104883.

Conferences

4. **Groenendijk, C. F.**, Heemskerk, T., van Burik, W., Rovituso, M., Tran, L., Rosenfeld, A., Essers, J., Lathouwers, D., Brown, J. M. C. (2023). *Linking Linear Energy Transfer to the Surviving Fraction of FaDu Cells at HollandPTC*. European SocieTy for Radiotherapy and Oncology (ESTRO), Vienna, Austria.

3. **Groenendijk, C. F.**, Rovituso, M., Lathouwers, D., & Brown, J. M. C. (2022). *Development of a* GEANT4 *Simulation Platform of the HollandPTC R&D Proton Beamline for Radiobiological Studies*. IV GEANT4 International User Conference, Naples, Italy.

2. **Groenendijk, C. F.**, Rovituso, M., Lathouwers, D., van Burik, W., Tran, L., Rosenfeld, A., Brown, J. M. C. (2022). *Micron-scale Dosimetry for Radiobiological Studies at the Holland Proton Therapy Centre*. Particle Therapy Cooperative Group (PTCOG), Miami, USA.

1. **Groenendijk, C. F.**, Lathouwers, D., Rovituso, M., van Burik, W., Rosenfeld, A., Tran, L., Brown, J. M. C. (2022). *3D-LET Characterisation of the HollandPTC R&D Proton Beamline for Radiobiological Experiments*. Micro-Mini & Nano Dosimetry and Innovative Technologies in Radiation Oncology (MMND - ITRO), Wollongong, Australia.

About the author

Celebrity Felicia Groenendijk was born on April 22, 1993, in Rotterdam, the Netherlands. She grew up in Barendrecht, where she began her pre-university education at Calvijn Groene Hart and later continued at Calvijn Vreewijk in Rotterdam. After repeating her final year, she successfully completed her Gymnasium diploma in 2012.

In the same year, she began her studies in Nanobiology at Delft University of Technology, where she obtained her Bachelor of Science degree in 2016. Motivated by a strong interest in the intersection of physics and medicine, she pursued a Master's degree in Biomedical Engineering with a specialization in Medical Physics, also at Delft University of Technology. Her master's research project was carried out within the Medical Physics & Technology group at the TU Delft Reactor Institute. Following a six month internship at the X-ray imaging group in the School of Physics and Astronomy at Monash University, Melbourne, Australia, she successfully obtained her Master of Science degree in 2019.

In 2020, she started as a PhD candidate within the Medical Physics & Technology group of the Department of Radiation Science & Technology at the TU Delft Reactor Institute, the Netherlands, under the supervision of Dr. ir. Danny Lathouwers and Dr. J.M.C. Brown. During her PhD, she spent three months as a visiting researcher at the Australian Nuclear Science and Technology Organisation (ANSTO) in Sydney and six months at Swinburne University of Technology in Melbourne, Australia. The results of her PhD research are presented in this dissertation.